BULETINUL INSTITUTULUI POLITEHNIC DIN IAŞI

Publicat de
UNIVERSITATEA TEHNICĂ „GHEORGHE ASACHI”
DIN IAŞI

Tomul LVII (LXI)
Fasc. 4

Secţia
ŞTIINŢA ŞI INGINERIA MATERIALELOR

2011 **Editura POLITEHNIUM**

ISSN 1453-1690

BULETINUL INSTITUTULUI POLITEHNIC DIN IAŞI

Tomul LVII (LXI)

Fasc. 4

ŞTIINŢA ŞI INGINERIA MATERIALELOR

2011 **Editura POLITEHNIUM**

BULETINUL INSTITUTULUI POLITEHNIC DIN IAŞI
PUBLISHED BY
„GHEORGHE ASACHI" TECHNICAL UNIVERSITY OF IAŞI
Editorial Office: Bd. D. Mangeron 63, 700050, Iaşi, ROMÂNIA
Tel. 40-232-278683; Fax: 40-232 237666; e-mail: polytech@mail.tuiasi.ro

BULETINUL INSTITUTULUI POLITEHNIC DIN IAŞI
BULLETIN OF THE POLYTECHNIC INSTITUTE OF IAŞI
Tomul LVII (LXI), Fasc. 4 2011

ŞTIINŢA ŞI INGINERIA MATERIALELOR

SUMAR

BULETINUL INSTITUTULUI POLITEHNIC DIN IAŞI
BULLETIN OF THE POLYTECHNIC INSTITUTE OF IAŞI
Tomul LVII (LXI), Fasc.4 2011

MATERIALS SCIENCE AND ENGINEERING

CONTENTS

BULETINUL INSTITUTULUI POLITEHNIC DIN IAŞI
Publicat de
Universitatea Tehnică „Gheorghe Asachi” din Iaşi
Tomul LVII (LXI), Fasc. 4, 2011
Secţia
ŞTIINŢA ŞI INGINERIA MATERIALELOR

ELECTROCHEMICAL DEPOSITION OF CALCIUM PHOSPHATES BIOCERAMICS

BY

ADRIANA CHIVU*, SORIN CIUCĂ and DIONEZIE BOJIN

* POLITEHNICA University, Bucharest,
Faculty of Materials Science and Engineering

Received: April 14, 2011
Accepted for publication: June 27, 2011

Abstract. Calcium phosphate thin layer was achieved by electrochemical method on titanium substrate. The titanium discs were immersed in a supersaturated calcium phosphate electrolyte at 90°C, ranging the deposition time and the degree of electrolyte agitation. Using this method were achieved homogeneous and uniform calcium phosphate coatings with typical morphology. The obtained coating after 3 hours was considered having optimal characteristics. A surface treatment was then applied to the HA coating. The treatment applied was Ag^+ ion implantation, in order to improve coating adherence and also to refine its morphology. This study shows that the electrodeposition technology is a very efficient method to coat the titanium with osteoconductive calcium phosphate layers.

Key words: Hydroxyapatite, electrodeposition, coating, titanium, ion implantation.

1.Introduction

A biomaterial is considered biocompatible when the implant does not react and when are not released toxic products in the body. The main

* Corresponding author e-mail: adrianachivu@yahoo.com

requirements are corrosion resistance, biocompatibility, biofunctionality, bioadhesion, etc. Titanium and titanium alloys are used as biomaterials due to their mechanical properties, good corrosion resistance and high biocompatibility. Ti4Al6V is the most widely used titanium alloy for orthopedic and dental implants due to the fatigue resistance and its biocompatibility. These alloys have certain limitations because the metallic ions (Al and V) are released from the implant. To overcome this adverse effect, many surface treatment techniques like anodic oxidation, alkaline treatments, bioactive coating with hydroxyapatite (HA), and ion implantation are used.

Hydroxyapatite $Ca_{10}(PO4)_6(OH)_2$ has a chemical composition very similar to the inorganic part of the human bones and has an excellent biocompatibility. HA coatings have been successfully prepared by: plasma spraying (Yang Sen *et al.*), pulsed laser deposition (Koch *et al.*, 2007), electrochemical deposition (Eliaz Noam *et al.*, 2008), sol-gel coating (Eduardo Peon Aves *et al.*, 2009), biomimetic coating (Heimann *et al.*, 2008), electrophoretic deposition (Wei, 2001), etc. Electrochemical deposition of HA has attracted a particular interest because of the large variety of advantages, such as a low processing temperature, the ability to deposit on porous or complex shapes, simple control of deposition parameters etc. The adhesion strength of HA coatings produced by the electrochemical deposition, is lower than that produced by plasma spraying or pulsed laser deposition.

The aim of this paper is to carry out some different HA coatings using electrochemical techniques by studying the influence of time and electrolyte agitation.

2. Materials and Methods

For this study titanium alloy Ti6Al4V discs (dimensions Ø 20 mm x 2 mm) were used as a substrate. The discs were mechanically polished and ultrasonically cleaned with alcohol. Before the deposition the discs were pickled in NaOH for 12 minutes and then cleaned with distillated (DI) water. The electrochemical deposition of HA was achieved at 90°C using potentiostatic mode -1V, and also ranging the deposition time and the degree of electrolyte agitation. The electrolyte solution contained 0.0061 M $Ca(NO_3)_2 \cdot 4H_2O$ (analytical grade) and 0.0036 M $NH_4H_2PO_4$ (analytical grade), the pH value was 4,5. After deposition, the specimens were rinsed in DI water to remove residual electrolyte and dried at 100°C for 12 hours.

The phase composition of the as-prepared coatings was investigated by X-ray diffraction (XRD) type Siemens D5000, using Cu-Kα radiation operating at 40 kV and 30 mA. The coating microstructure was analyzed using a Scanning Electron Microscopy (SEM) type Philips XL 30 SEM.

3. Results and Discussion

3.1. Influence of Deposition Time on Calcium Phosphate Coating

HA coatings with application in bone implantology should have high crystallinity, proper stoichiometry, good control of density/porosity and excellent adherence to the metallic substrate (Nelea *et al*., 2004).

The study was focused on HA coatings, in this order the samples were analyzed by X-ray diffraction (XRD), Scanning Electron Microscopy (SEM).

Comparing the obtained XRD spectrum (Fig.1) with HA standard pattern we can say that deposited layers contained crystalline HA, demonstrating a good applicability of this method.

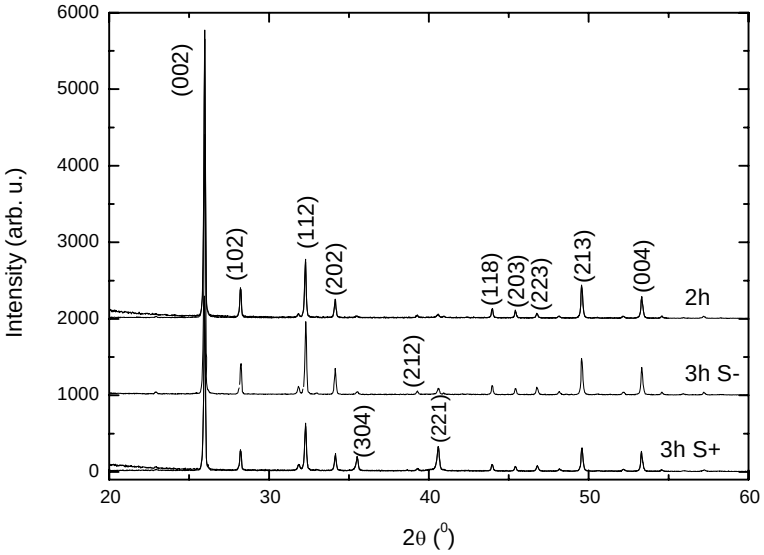

Fig. 1 – XRD spectrum of the coating prepared by electrodeposition at 90°C for 3 hours with and without stirring the electrolyte and after 2 hours.

The surface morphology was examined using Scanning Electron Microscopy. Fig. 2 shows that the electrochemical coatings of HA have an acicular morphology. A similar surface morphology has been previously reported in other published papers (Menghan Ma *et al*., 2008; Noam Eliaz & Sridhar, 2008).

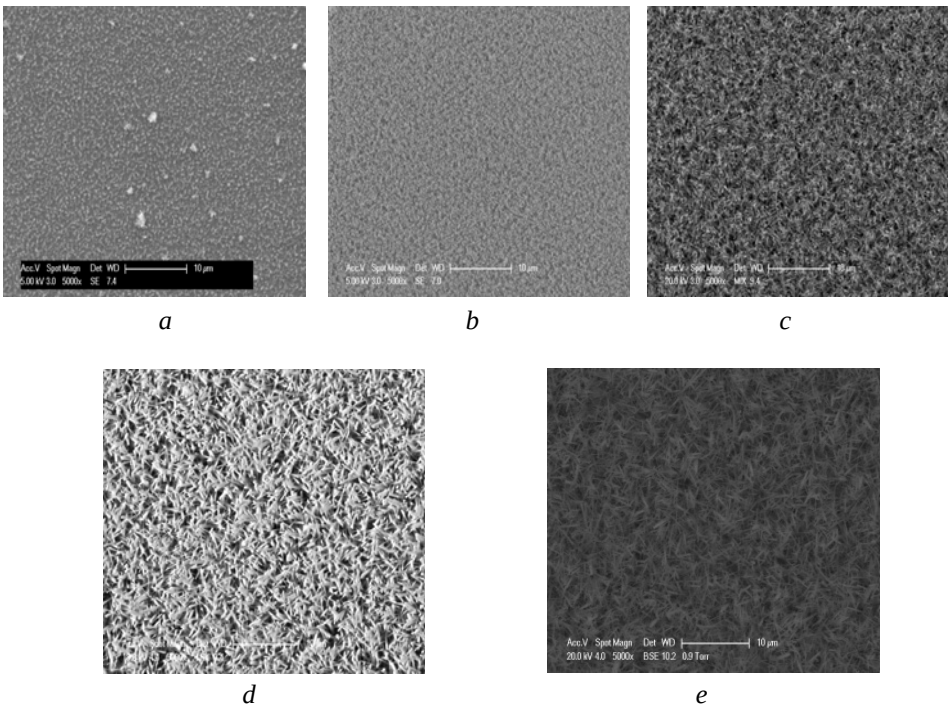

Fig. 2 – SEM micrographs of HA coatings on Ti6Al4V substrates obtained by electrochemical processing after: *a*) 5 minutes; *b*) 30 minutes; *c*) 1 hour; *d*) 2 hours and *e*) 3 hours.

After 30 minutes (Fig. 2*b*) we can see a thin and uniform layer deposited on the metallic surface. The morphology of the coating is highlighted after 1 hour (Fig. 2*c*) but the deposited layer is smaller/thinner compared to the coating achieved after 2 or 3 hours (Fig. 2*d*, *e*).

3.2. Kinetic Study Depending on Agitation of the Electrolyte

The influence of the electrolyte agitation during the deposition process has been observed for 1 and 3 hours.

In all situations the coatings morphology is homogenous and has a typical needle-like crystals (Fig. 3, Fig. 4). The achieved deposition using the stirrer device has induced in refined morphology (Fig. 3*b*, Fig. 4*b*), which suggests a better mechanical behavior. Also the increasing of maintaining time determines not only a longitudinal growth of crystals but also the densification of those.

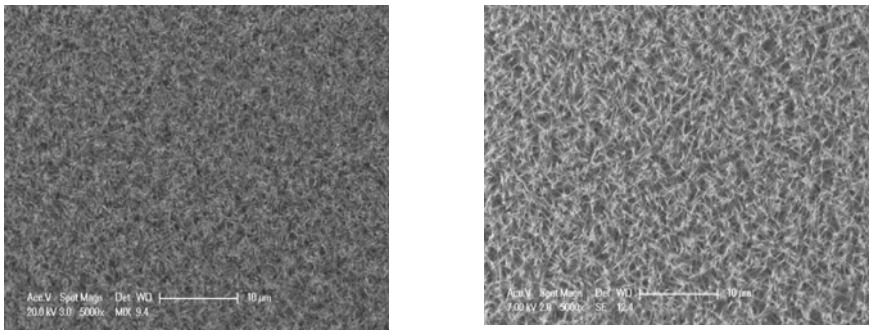

a *b*

Fig. 3 – SEM micrographs of the coatings obtained after 1 hour; *a* – without and *b* – with agitation of the electrolyte.

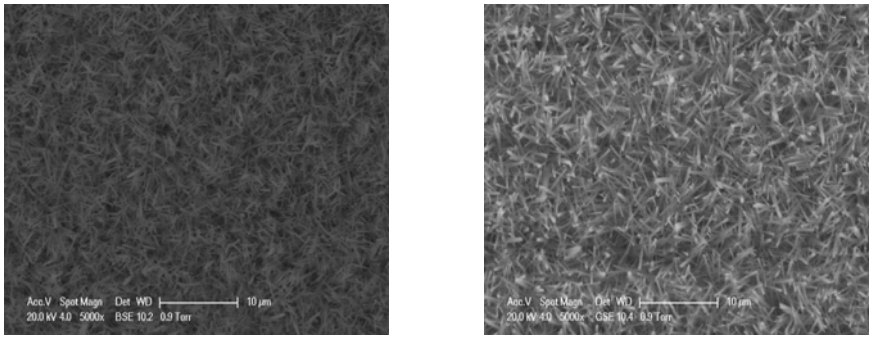

a *b*

Fig. 4 – SEM micrographs of the coatings obtained after 3 hour; *a* – without and *b* – with agitation of the electrolyte.

3.3. HA Reinforcement Layer by Silver Ion Implantation at Low Energy

The coatings obtained after 3 hours were considered having optimal characteristics. In this way, the layer was then subjected to a surface treatment. This treatment consisted in an ion implantation with Ag^+, in order to improve coating adherence and grain refining post-deposition. The Ag^+ ions were used due to the anti-bacteriological properties. Ion beam implantation is a non-conventional technique used for surface modification and thin films densification (Nelea *et al*., 2004).

The work parameters used in this procedure were: energy E= 160KeV; intensity of the beam I=28mA; ion density =$5 \cdot 10^{15} cm^2$.

The study of the coating morphology was carried out by SEM. In the Fig. 5 we have submitted the new micrography by comparison with the as

deposited sample. The typical morphology "needle-like" with pattern in "petals-flower-like" is maintained, but the refining level is very clear. It is marked by an obvious distribution of the crystals.

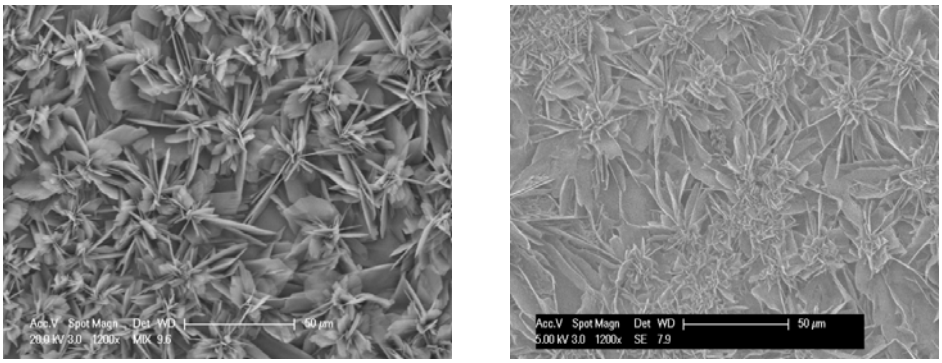

a *b*

Fig. 5 – SEM micrographs of (*a*) HA and (*b*) HA/Ag coating.

4. Conclusion

Using the electrochemical technique, uniform and homogeneous calcium phosphates layers, with characteristic morphologies were achieved, having a typical "needle-like" morphology.

The XRD analysis demonstrated that the coatings had a hydroxyapatite structure. This fact validates the electrochemical method as a technique able to obtain bioactive coatings, with a high biocompatibility.

The surface morphology of HA layer can be remarked after 30 minutes of deposition. This concludes that coating thickness is related to the deposition time.

A very important parameter which influences the HA electrochemical deposition is the electrolyte stirring. This factor has an important influence on the coating morphology.

The post deposition ion-beam implantation with Ag^+ ions contributes to the reinforcement and refining HA coating.

Acknowledgements. The work has been funded by the Sectoral Operational Programme Human Resources Development 2007-2013 of the Romanian Ministry of Labour, Family and Social Protection through the Financial Agreement POSDRU/88/1.5/S/61178.

The principal author gratefully acknowledges the help received from the Surface Engineering Laboratory from INSA Strasbourg, during her stage in this university.

REFERENCES

Blackwood D.J., Seah K.H.W., *Electrochemical Cathodic Deposition of Hydroxyapatite: Improvements in Adhesion and Crystallinity.* Materials Science and Engineering, **C 29**, 1233–1238 (2009).

Eduardo Peon Aves, Gaston Fuentes Estevez, Marcia Soares Sader, *Hydroxyapatite Coating by Sol–Gel on Ti–6Al–4V Alloy as Drug Carrier*. J. Mater Sci: Mater Med, **20**, 543–547 (2009).

Heimann R.B., Ntsoane T.P., Pineda-Vargas C.A., *Biomimetic Formation of Hydroxyapatite Investigated by Analytical Techniques with High Resolution*, J Mater Sci: Mater Med, **19**, 3295–3302 (2008).

Koch C.F., Johnson S., Kumar D., Jelinek M., Chrisey D.B., Doraiswamy A., Jin C., Narayan R.J., Mihailescu I.N., *Pulsed Laser Deposition of Hydroxyapatite thin Films*. Materials Science and Engineering, **C 27**, 484–494 (2007).

Menghan Ma, Wei Ye, Xiao-Xiang Wang*, Effect of Supersaturation on the Morphology of Hydroxyapatite Crystals Deposited by Electrochemical Deposition on Titanium.* Materials Letters, **62**, 3875–3877 (2008).

Nelea V., Pelletier H., Mille P., Muller D., *High-Energy Ion Beam Implantation of Hydroxyapatite Thin Films Grown on TiN and ZrO2 Inter-Layers by Pulsed Laser Deposition*. Thin Solid Films, 453 –454, 208–214 (2004).

Noam Eliaz, *Electrodeposition of Calcium Phosphates for Orthopaedic and Dental Implants*.

Noam Eliaz, Sridhar T.M., *Electrocrystallization of Hydroxyapatite and Its Dependence on Solution Conditions*. Crystal Growth & Design, **8**, *11*, 2008.

Noam Eliaz, William Kopelovitch, Larisa Burstein, Equo Kobayashi, Takao Hanawa, *Electrochemical Processes of Nucleation and Growth of Calcium Phosphate on Titanium Supported by Real-Time Quartz Crystal Microbalance Measurements and X-ray Photoelectron Spectroscopy Analysis.* Wiley InterScience 18 June 2008.

Sen Yang, H.C. Man, Wen. Xing, Xuebin Zheng: *Adhesion Strength of Plasma-Sprayed Hydroxyapatite Coatings on Laser Gas-Nitrided Pure Titanium*, Surface & Coatings Technology.

Wei M., *Electrophoretic Deposition of Hydroxyapatite Coatings on Metal Substrates: A Nanoparticulate Dual-Coating Approach.* J. of Sol-Gel Science and Technol., **21**, 39–48 (2001).

DEPUNEREA ELECTROCHIMICĂ A BIO-CEREMICELOR PE BAZĂ DE FOSFAŢI DE CALCIU

(Rezumat)

Folosind metoda de depunere electrochimică au fost obţinute straturi subţiri de fosfaţi de calciu pe substrat de titan. Probele (substratul) au fost imersate într-un electrolit de concentraţie 0,0061 mol/L $Ca(NO_3)_2 \cdot 4\ H_2O$ şi 0,0036 mol/L $NH_4H_2PO_4$, la

o temperatură de 90°C, variind timpul de proces şi gradul de agitare al electrolitului. În urma metodei studiate s-au realizat straturi uniforme şi omogene de fosfaţi de calciu, cu morfologii caracteristice. Acoperirile obţinute pentru o durată de menţinere de 3 ore, considerate optime calitativ, au fost ulterior supuse unui tratament de suprafaţă. Acesta a constat într-o implantare ionică cu Ag cu scopul de ameliorare a aderenţei şi de finisare a granulaţiei post-depunere. Studiul a demonstrat că metoda electrochimică este eficientă pentru obţinerea de acoperiri osteoconductive de fosfaţi de calciu, iar implantarea ionică conduce la o consolidare avansată a acoperirii.

BULETINUL INSTITUTULUI POLITEHNIC DIN IAŞI
Publicat de
Universitatea Tehnică „Gheorghe Asachi” din Iaşi
Tomul LVII (LXI), Fasc. 4, 2011
Secţia
ŞTIINŢA ŞI INGINERIA MATERIALELOR

BIOLOGICAL APATITES: A SHORT REVIEW

BY

GABRIELA CIOBANU[1*] and OCTAVIAN CIOBANU[2]

[1]“Gheorghe Asachi” Technical University of Iaşi,
Faculty of Chemical Engineering and Environmental Protection
[2]“Grigore T. Popa” Medicine and Pharmacy University of Iaşi,
Faculty of Medical Bioengineering

Received: April 15, 2011
Accepted for publication: June 27, 2011

Abstract. Currently, many natural or synthetic biomaterials are used to remedy the bone problems. The enhancement of the biological activity and performance of bone replacement materials is one of the mainly important concerns of orthopaedic and dental surgery specialists. This study present a short description of bone composition and structure, and finally, the properties of biological apatites are presented.

Key words: biological apatites, bone structure.

1. Introduction

Biomaterials have been defined as substances other than foods or drugs enclosed in therapeutic or diagnostic systems and in some cases have been described as materials composed of biologically derived components irrespective of their application (Peppas & Langer, 1994).

Currently, many natural or synthetic biomaterials are used to remedy the bone problems. The enhancement of the biological activity and performance of bone replacement materials is one of the mainly important concerns of orthopaedic and dental surgery specialists.

* Corresponding author e-mail: gciobanu03@yahoo.co.uk

This study reviews the structure and properties of bone and biological apatites. It discusses the various groups of calcium orthophosphates including hydroxyapatite.

2. The Structure and Bone Formation

Bone is a natural composite material. It is composed of organic matrix, inorganic mineral salts, water, support cells (osteoblasts and osteocytes) and remodelling cells (osteoclasts).

In the bone, these constituents are hierarchically disposed through five levels of organisation. At the molecular level, the triple helix of collagen molecules are grouped in microfibres. The small apatite crystals (about 5 x 30 nm sized) nucleate and grow in small cavities between microfibres edges. These microfibres bring together to form larger fibres that form the microscopic units of bone tissue. Next, these fibres are arranged in different structural distributions to form the full bone (Vallet-Regi & Arcos, 2008).

In the bone, in terms of chemical composition, the mineral phase (for almost 50% of the volume of bone) contain calcium orthophosphates, ***i.e.*** apatitic compounds (hydroxyapatite, HA: $Ca_{10}(PO_4)_6(OH)_2$), with low crystallinity and nanometric size, deposited in the organic matrix. The hydroxyapatite crystals are located in the spaces between the collagen fibrils. The organic phase (for almost 45% of the volume of bone) consists principally of 90% collagen (type-I collagen) fibres and other noncollageneous proteins (proteoglicans and glycoproteins).

In the case of vertebrates, the cells responsible with the production, preservation and modelling of the bone are (Fig. 1):

- *Osteoclasts*: are great multinucleated cells (like macrophages). Osteoclasts have role in resorption of mineralized tissue and are attached to the bone surface at sites of active bone resorption.

- *Osteoblasts*: are cells derived from mesenchymal stem cells; these cells are designed for bone matrix production and its following mineralization.

- *Osteocytes*: are osteoblasts cells that are included in the calcified bone matrix and in the new formed osteoid, which becomes new bone (Aubin, 1998; Heersche & Aubin, 1990).

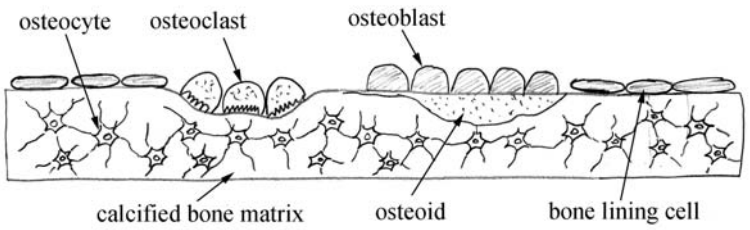

Fig. 1 – Cells responsible with the production, preservation and modelling of the bone.

Bone Modelling: this process takes place on different surfaces and involves both bone resorption and new bone formation (formation and resorption are not coupled). An example of bone modelling is the period of bone increases in length and diameter. Bone modelling occurs for the period of birth to maturity and is responsible for increase in skeletal mass and changes in skeletal shape (Aubin, 1998; Heersche & Aubin, 1990).

Bone Remodelling (*Fig. 2*): this process consists in the exchange of old by new bone tissue, and generally occurs in the adult skeleton to preserve bone mass.

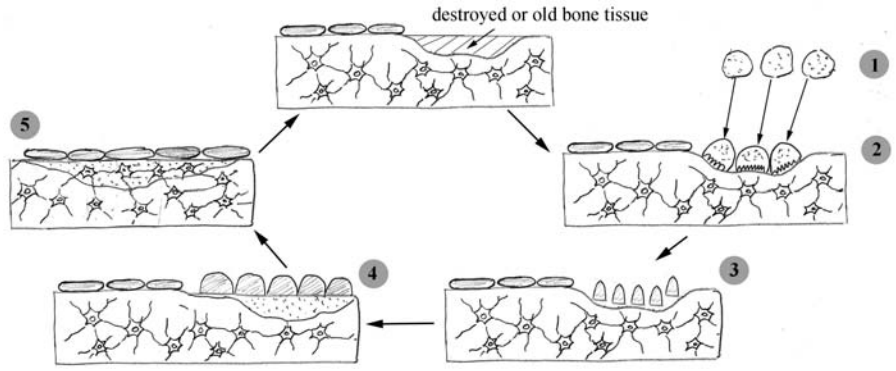

Fig. 2 – Bone remodelling.

Bone remodelling process implies the combination of bone formation and bone resorption (Fig. 2) and consists of five steps: (1) activation (in this step, under the influence of cytokines and growth factors, preosteoclasts are stimulated and differentiate into mature active osteoclasts), (2) resorption (osteoclasts absorb old bone), (3) reversal (closing stage of resorption), (4) formation (osteoblasts produce new osteoid, which becomes new bone) and (5) latent step (osteoblasts turn out to be resting bone lining cells on the new formed bone surface) (Aubin, 1998; Heersche & Aubin, 1990; Raisz, 2005).

Usually, modelling refers to the changing of the external form of the bone by the addition or removal of bone from external surfaces and internal remodelling refers to the production of new bone in the body of old bone.

3. Biological Apatites

As mentioned previously, the essential inorganic phase of bones and teeth are nanodimensional crystalline calcium orthophosphates (in the form of apatites, *i.e.* biological apatites). The uses of calcium phosphates in medical applications are due on the one hand the fact that the most important inorganic component of bone is hydroxyapatite (HA) and on the other hand the calcium

phosphates promote the movement of bone cells to the site and can also induce bone cell segregation.

Currently, in the ternary system $Ca(OH)_2$ (or CaO) – H_3PO_4 (or P_2O_5) – H_2O there are some known non-ion-substituted calcium orthophosphates with the Ca/P molar ratio within 0.5 and 2.0 (Table 1 and Table 2) (Brown, 1992; Dorozhkin, 2009).

Table 1

Calcium Orthophosphates Compounds (*Dorozhkin, 2009*)

Compound	Chemically correct name	Chemical formula
Monocalcium phosphate monohydrate (MCPM)	Calcium dihydrogen phosphate monohydrate	$Ca(H_2PO_4)_2 \cdot H_2O$
Monocalcium phosphate anhydrous (MCPA)	Calcium dihydrogen phosphate anhydrous	$Ca(H_2PO_4)_2$
Dicalcium phosphate dihydrate (DCPD), mineral Brushite	Calcium hydrogen phosphate dihydrate	$CaHPO_4 \cdot 2H_2O$
Dicalcium phosphate anhydrous (DCPA), mineral Monetite	Calcium hydrogen phosphate anhydrous	$CaHPO_4$
Octacalcium phosphate (OCP)	Octacalcium bis(hydrogenphosphate) tetrakis(phosphate) pentahydrate	$Ca_8(HPO_4)_2(PO_4)_4 \cdot 5H_2O$
α-Tricalcium phosphate (α-TCP)	Calcium phosphate tribasic alpha	$\alpha\text{-}Ca_3(PO_4)_2$
β-Tricalcium phosphate (β-TCP), mineral Whitlockite	Calcium phosphate tribasic beta	$\beta\text{-}Ca_3(PO_4)_2$
Amorphous calcium phosphate (ACP)	-	$Ca_xH_y(PO_4)_z \cdot nH_2O$, n = 3 – 4.5; 15 – 20 % H_2O
Calcium - deficient hydroxyapatite (CDHA)	-	$Ca_{10-x}(HPO_4)_x(PO_4)_{6-x}(OH)_{2-x}$ (0 < x < 1)
Hydroxyapatite or Hydroxylapatite (HA, HAp or OHAp)	Pentacalcium hydroxyl apatite	$Ca_{10}(PO_4)_6(OH)_2$ or $Ca_5(PO_4)_3(OH)$
Oxyapatite (OA or OAp)	-	$Ca_{10}(PO_4)_6O$
Tetracalcium phosphate (TTCP or TetCP), mineral Hilgenstockite	Tetracalcium phosphate monoxide	$Ca_4(PO_4)_2O$

In 1913, T. Gassmann was the first scientist who explained the calcium orthophosphate nature of the bones (Gassmann, 1913). This discovery was clarified later, suggesting that the bone mineral consist of biological apatite, which might be defined as a poorly crystalline (approximately amorphous), non-stoichiometric and ion substituted CDHA. Bone apatite nanocrystals exhibit a diversity of substitutions and vacancies that make the Ca/P molar ratio deviate from the stoichiometric HA ratio of 1.67 (Dorozhkin, 2009; Bredig, 1933; Omelon & Grynpas, 2008).

In bone and teeth, the mineral phases of the normal calcifications consist of only single type of calcium orthophosphate (biological apatite). Instead, the mineral phases of abnormal calcifications are found to occur as single or mixed phases of other types of calcium orthophosphates (ACP, DCPD, OCP) and/or other phosphatic or non-phosphatic compounds (*e.g.*, magnesium orthophosphates, calcium pyrophosphates, calcium oxalates etc.) in addition to or in place of biological apatite (Dorozhkin, 2009).

Hydroxyapatite is known as a representative apatite. Taking advantage of its bioactivity there have been efforts to replace impaired teeth and bones with HA. Presently, diverse methodologies have been proposed to prepare nanodimensional and/or nanocrystalline structures that mimic biological apatites.

Table 2

Some Properties of Calcium Orthophosphates Compounds (Dorozhkin, 2009)

Compound	Ca/P molar ratio	Solubility at 25 °C (g/L)	pH stability range at 25 °C	Characteristics / Applications
MCPM	0.5	~ 18	0.0 – 2.0	- never appears in calcified tissues; is not biocompartible due to its acidity. - applications: fertilizer, nutrient, acidulant and mineral supplement for dry baking powders, food, feed and some beverages (as additive E341).
MCPA	0.5	~ 17	-	- never appears in calcified tissues; is not biocompartible due to its acidity. - hydroscopic properties reduce its commercial applications.
DCPD	1.0	~ 0.088	2.0 – 6.0	- found in pathological calcifications (dental calculi, urinary stones etc.) and some carious lesions. - in medicine: used in calcium orthophosphate cements, intermediate for teeth remineralization, added to toothpaste for caries protection. - other applications: flame retardant, slow release fertilizer, glass production, pigment for some paints, calcium supplement in food (as additive E341) etc.
DCPA	1.0	~ 0.048	-	- in medicine: used in calcium phosphate cements. - other applications: polishing agent, source of calcium and phosphate in nutritional supplements, tabletting aid and toothpaste component, conditioner in the food industry.
OCP	1.33	~ 0.0081	5.5 – 7.0	- is one of the stable components of human dental and urinary calculi. - plays an important role in *in vivo* formation of apatitic biominerals. - in surgery: used for implantation into bone defects.

Table 2
Continuation

Compound	Ca/P molar ratio	Solubility at 25 °C (g/L)	pH stability range at 25 °C	Characteristics / Applications
α-TCP	1.5	~ 0.0025	-	- never occurs in biological calcifications. - in medicine: used in calcium phosphate cements. - can be used as a fertilizer.
β-TCP	1.5	~ 0.0005	-	- never occurs in biological calcifications. - in medicine: used in calcium orthophosphate bone cements, added to some toothpaste as a gentle polishing agent. - other applications: texturizer, bakery improver and anti-clumping agent for dry powdered food (flour, milk powder, dried cream, cocoa powder), dietary or mineral supplement (as E341) to food and feed, in porcelains, pottery, enamel etc.
ACP	1.0 – 2.2	-	~ 5 – 12	- biologically, ACP is found in soft-tissue pathological calcifications (e.g., heart valve calcifications of uremic patients). - in medicine: used in calcium orthophosphate cements and as a filling material in dentistry. - other applications: component for mordants and ackey, in glass and pottery production and as a raw material for production of some organic phosphates, for syrup clarification, inert filler in pelleted drugs etc.
CDHA	1.5 – 1.67	~ 0.0094	6.5 – 9.5	- in biological systems exist only ion-substituted CDHA. - other applications: are similar to those of ACP. CDHA was found to possess catalytic activity for the production of biogasoline.
HA	1.67	~ 0.0003	9.5 – 12	- occurs in biological systems, in teeth and bones. - in medicine: for implantation into bone defects, coating on orthopedic (e.g., hip joint prosthesis) and dental implants, added to some toothpaste, in liquid chromatography of nucleic acids, proteins and other biological compounds, for drug delivery purposes etc. - other applications: used as environmentally friendly filler for elastomers, sorbent of poisonous chemical elements, carrier for catalysts etc.
TTCP	2.0	~ 0.0007	-	- never found in biological calcifications. - in medicine: used for preparation of various calcium phosphate cements.

The literature shows various methods used to prepare apatites: wet chemical precipitation, sol-gel synthesis, co-precipitation, hydrothermal

synthesis, mechano-chemical synthesis, mechanical alloying, ball milling, radio frequency induction plasma, vibro-milling of bones, flame spray pyrolysis, liquid-solid-solution synthesis, electro-crystallization, microwave processing, hydrolysis of other calcium orthophosphates, double step stirring, emulsion-based or solvothermal syntheses and several other techniques are known (Dorozhkin, 2009; Drouet *et al*., 2009; Tanaka *et al*., 2003; Eichert *et al*., 2007; Cazalbou *et al*., 2004; Guo *et al*., 2004). The nanocrystalline forms of calcium orthophosphates have a great potential to develop the field of hard tissue engineering in bone repair, in augmentation, in controlled drug delivery devices and more.

REFERENCES

Aubin J.E., *Advances in the Osteoblast Lineage*. Biochem. Cell. Biol., **76**, *6*, 899-910 (1998).

Bredig M.A., *The Apatite Structure of Inorganic Bone and Tooth Substance*. H.-S. Z. Physiol. Chem. , *216*, 239-243 (1933).

Brown P.W., *Phase Relationships in the Ternary System CaO - P_2O_5 - H_2O at 25°C*. J. Am. Ceram. Soc., **75**, 17-22 (1992).

Cazalbou S., Combes C., Eichert D., Rey C., *Adaptative Physico-Chemistry of Bio-Related Calcium Phosphates*. J. Mater. Chem., *14*, 2148–2153 (2004).

Dorozhkin S.V., *Calcium Orthophosphates in Nature, Biology and Medicine*, Materials, *2*, 399-498 (2009).

Drouet C., Bosc F., Banu M., Largeot C., Combes C., Dechambre G., Estournes C., Raimbeaux G., Rey C., *Nanocrystalline Apatites: From Powders to Biomaterials*, Powder Technol., *190*, 118–122 (2009).

Eichert D., Drouet C., Sfihi H., Rey C., Combes C., *Nanocrystalline Apatite-Based Biomaterials: Synthesis, Processing and Characterization*. In *Biomaterials Research Advances*. Kendall, J.B., Ed.; Nova Science Publishers, Inc.: Hauppauge, NY, USA, Chapter , **5**, 2007.

Gassmann T., *The Preparation of a Complex Salt Corresponding to Apatite-Typus and its Relations to the Constitution of Bones*. H.-S. Z. Physiol. Chem., *83*, 403-408 (1913).

Guo X., Xiao P., Liu J., Shen Z., *Fabrication of Nanostructured Hydroxyapatite Via Hydrothermal Synthesis and Spark Plasma Sintering*. J. Am. Ceram. Soc., **88**, 1026–1029 (2004).

Heersche J.N.M., Aubin, J.E., *Regulation of Cellular Activity of Bone-Forming Cells*. In *The osteoblast and osteocyte*. Edited by B.K. Hal. Tilford Press, Caldwell, N.J., 1990.

Omelon S.J., Grynpas M.D., *Relationships Between Polyphosphate Chemistry, Biochemistry and Apatite Biomineralization*. Chem. Rev., *108*, 4694-4715 (2008).

Peppas N.A., Langer R., *New Challenges in Biomaterials*. Science, *263*, 1715-1720 (1994).

Raisz L.G., *Pathogenesis of Osteoporosis: Concepts, Conflicts, and Prospects*. J. Clinical Invesig., **115**, *12*, 3318-3325 (2005).

Tanaka Y., Hirata Y., Yoshinaka R., *Synthesis and Characteristics of Ultra-Fine Hydroxyapatite Particles*. J. Ceram. Proc. Res., *4*, 197–201 (2003).

Vallet-Regi M., Arcos D., *Biomimetic Nanoceramics in Clinical Use - From Materials to Applications*. RSC Publishing, Thomas Graham House, UK, 2008.

APATITE BIOLOGICE: O SCURTĂ ANALIZĂ

(Rezumat)

În prezent sunt folosite diverse biomateriale naturale sau sintetice pentru a remedia problemele osoase ale populaţiei umane. Consolidarea activităţii biologice şi performanţele materialelor utilizate în substituţia osoasă reprezintă una dintre principalele preocupări ale specialiştilor în intervenţii chirurgicale ortopedice şi dentare. În acest studiu se prezintă o scurtă trecere în revistă a materialelor apatitice, în special a apatitelor biologice.

BULETINUL INSTITUTULUI POLITEHNIC DIN IAŞI
Publicat de
Universitatea Tehnică „Gheorghe Asachi” din Iaşi
Tomul LVII (LXI), Fasc. 4, 2011
Secţia
ŞTIINŢA ŞI INGINERIA MATERIALELOR

CAD/CAM AND RAPID PROTOTYPING TECHNOLOGIES IN MEDICAL ENGINEERING

BY

OCTAVIAN CIOBANU[1*] and GABRIELA CIOBANU[2]

[1]“Gheorghe Asachi” Technical University of Iaşi,
Faculty of Chemical Engineering and Environmental Protection
[2]“Gr.T.Popa” University of Medicine and Pharmacy from Iaşi,
Department of Medical Bioengineering

Received: April 14, 2011
Accepted for publication: June 27, 2011

Abstract. The use of CAD/CAM and Rapid Prototyping technologies in medical industry, in association with other techniques such as 3D scanning and 3D reconstruction and visualization of anatomic surfaces have led to improvement in medical services offered to patients. The paper presents an overview of the various manufacturing technologies involved in medical industry and in medical engineering research for customized or large series production of medical equipments, medical devices, implants and prosthesis.

Key words: CAD/CAM, Rapid Prototyping, medical devices, manufacturing.

1. Introduction

CAD/CAM is considered as a powerful and modern tool in the manufacturing area, for technological improvement in the design and fabrication of the products in different domains. The use of CAD/CAM has recently extended into medical industry and services for the developing world.

* Corresponding author e-mail: oct.ciobanu@gmail.com

Rapid prototyping is another technology that can fabricate 3D objects directly from 3D CAD virtual model. Rapid prototyping (RP) technology has primarily been developed for the manufacturing industry to assist in speeding up the development of new products. Medical engineers and practitioners realized that the technology is also suitable for applications in the medical field and especially in the fabrication of customized medical devices.

Paper investigates the state of art in the application of various computer aided manufacturing technologies in medical engineering in connection with CAD/CAM and Rapid prototyping. Main approach is for the fabrication of prosthesis socket, the most important part of a prosthetic device, and the most individual and custom-made part of the prosthesis.

2. Customized and Large Series Fabrication

Initially, computer aided fabrication technologies were viewed as experimental by the medical engineers and orthopaedists and most CAD/CAM prosthesis sockets were not comfortable enough for long-term use. Today, CAD/CAM and Rapid Prototyping products in medical industry have very high-quality and relatively low cost. The methodology of the conception and fabrication of prosthesis depends on the production purpose and scale. There are four main directions in prosthesis fabrication (Ciobanu, 2007; Ciobanu, 2006; Ciobanu, 2007; Michael, 1989).

- Manual manufacturing of customized prosthesis (Fig.1);
- Manufacturing of customized prosthesis using CAD/CAM technologies (Fig. 2);
- Manufacturing of large series production of prosthesis, components and assisistive technology devices using CAD/CAM (Fig. 3)
- Manufacturing of customized prosthesis using Rapid Prototyping technologies (Fig. 4)
- Manufacturing of large series production of prosthesis, components and assistive technology devices using Rapid Prototyping technologies (Fig. 5).

Traditionally, the fabrication of the prosthetic socket has been a careful and handcrafted art attempting to create a comfortable and functional socket for the residual limb. The main phases in manual manufacturing of a socket are presented in Fig. 1. A plaster wrap cast of the stump is taken initially (the negative mould) and a positive mould is subsequently created. Currently exists a lot of techniques, styles and methods on how to create the socket.

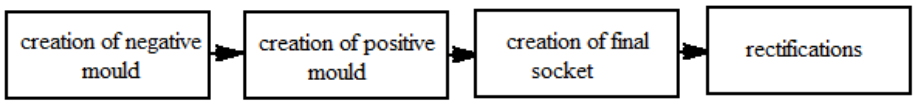

Fig. 1 – Manual manufacturing of customized prosthesis.

Customized fabrication through CAD/CAM techniques has next main phases similar as in the case of Rapid Prototyping (Fig. 3). The main CAD/CAM systems used in prosthetics were developed specifically for customized prosthesis and orthesis.

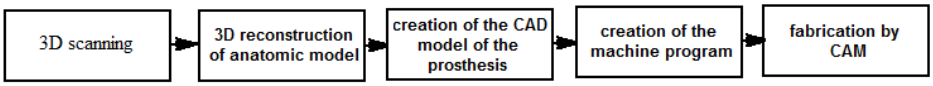

Fig. 2 – Phases of customized fabrication through CAD/CAM technologies.

The first CAD/CAM machines in prosthetics were special mills used for carving blanks made of plaster, foam blanks or plaster mixtures. These mills were used especially for: transfemoral sockets, transtibial sockets, knee orhesis, ankle foot orthesis, body jackets, socket liners, cosmetic covers, seat cushions etc. Fabrication through CAD/CAM techniques for large series production has fewer phases (Fig. 3) and some characteristic features. This type of production is for standardized prosthesis, typical medical devices, assistive devices and components. In clasic CAD/CAM technologies, the advantage is that any material can be worked, and the size range of the process is much larger than that of rapid prototyping.

CNC machining can make parts that range from nearly microscopic up to 30 m long. In general these raw materials are also much less expensive than the special materials needed by RP machines.

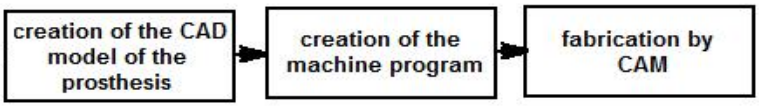

Fig. 3 – Phases of the CAD/CAM technologies for large series production.

Rapid Prototyping has revolutionized the way products are designed and manufactured (Chandra *et al*., 2005; Canciglieri *et al*., 2006). Customized fabrication through Rapid Prototyping requires next main steps: scanning the anatomic surface to determine anatomic surface forms, surface 3D reconstruction, and building of CAD model and converting to STL format and finally machining using a special machine controlled through computer (Fig. 4).

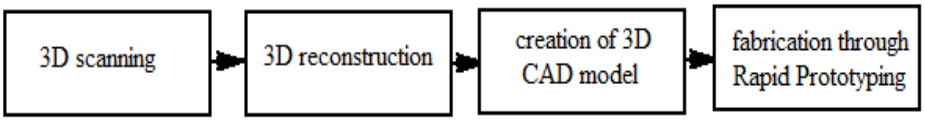

Fig. 4 – Phases of the Rapid prototyping technologies for large series production.

3. The use of Scanning Devices

Determination of anatomic forms can be done in two ways: through manually measuring and through scanning with special devices.

Usually, measuring in CAD/CAM is performed automatically using scanning devices based on X rays, video camera, laser or other techniques. Fig. 3 shows a scanning device used in orthopedics.

3D reconstruction of anatomic surfaces can be performed using different types of software, starting from CAD software (AutoCAD, Solid Works etc) or dedicated software (Mimics, 3D Doctor, In Vesalius etc).

Fig. 5 – Scanning the limb for anatomic dimensions determination.

Creation of the CAD *model* can be performed in two ways:

- generating the model starting from the 3D reconstruction model and using dedicated software in the case of customized prosthesis;
- generating the model using CAD software and starting from standard dimensions in the case of large series production of implants or prosthesis.

CAD models of prosthesis and especially the sockets have to be accomplished by surface adjustments. Once the model is captured and reassembled, the model is modified to achieve the desired design by using a variety of software tools.

Creation of the machine-program is necessary in order to transform the geometric data of prosthesis in commands compliable to Computer Numerical Control (***CNC***) machine tools.

CAD/CAM fabrication is the final processing phase and is based on the use of CNC machine tools, controlled through computers or numeric equipments (Canciglieri *et al*., 2006).

4. Rapid Prototyping Technologies

Rapid prototyping is a promising technology, ideal for conceptual models and functional testing prototypes. Rapid prototyping may help to construct a mock-up to improve the design.

New machines, known as 3D printers, will continue to expand as prices are lower and part quality better. Improvements in materials will maintain the expansion of emerging technologies.

Most 3D printers have prices between US $ 10.000 and US $ 20.000. Newest 3D miniature printer (Fig.6) costs about US $ 2600 (www.pp3dp.com.). It uses plastic fibres, has 0.2 mm accuracy and has 5 Kg weight

RP technologies have important applications in tissue engineering (Chandra *et al*., 2005). RP may control precisely some parameters of the artificial tissue scaffold: size, shape, interconnectivity, geometry and orientation (www.pp3dp.com.).

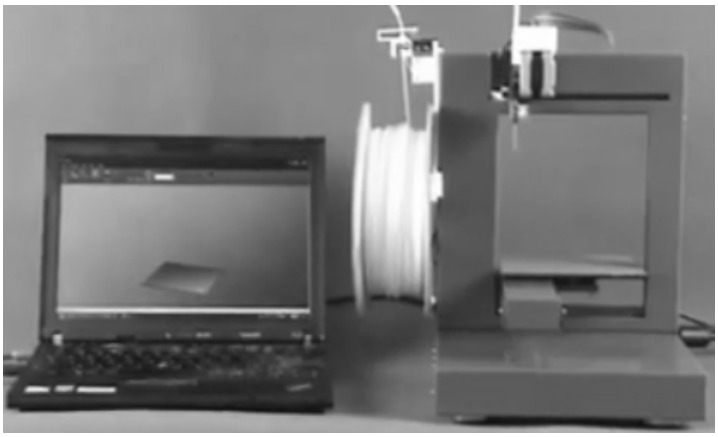

Fig. 6 – Last type of miniaturized 3D printer.

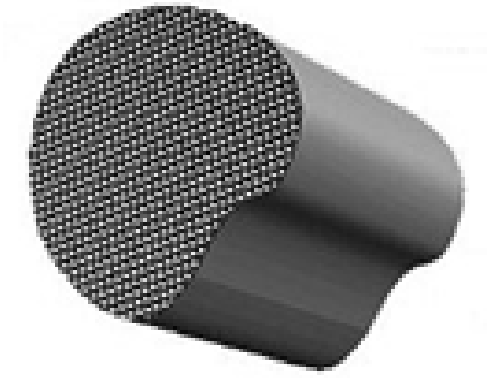

Fig. 7 – Application in bone tissue engineering.

Most of these techniques offer good to average control over microstructure with pore wall resolutions greater than 100 μm.

5. Discussion

Application of CAD/CAM and RP technologies in medical engineering can be divided in clinical applications (prosthetic laboratories) and manufacturing applications (manufacturing centers).

Today there are three main models of CAD/CAM and RP use in clinical practice (Canciglieri *et al*., 2006; Smith & Burgess 2001).

- Traditional prosthetic laboratory with no use of CAD/CAM or RP technologies. These types of laboratories are the most commonly used.
- Prosthetic laboratory with few CAD/CAM and RP tools (IT, 3D scanners, 3D reconstruction software and eventually a small 3D printer);
- Prosthetic laboratory fully equipped with CAD/CAM or Rapid Prototyping technologies. Users of full CAD/CAM laboratories have expressed concern that upgrading equipment and software might not be economical with today's decreasing economy

Manufacturing applications consist in centers for prosthesis manufacturing, fully equipped with CAD/CAM and Rapid Prototyping technologies (few contacts with patients)

The centers for prosthesis manufacturing receive manufacturing orders from prosthetic laboratories of a large geographic area. It is believed that the number of prosthesits who use a center for prosthesis manufacturing will grow more rapidly than the number of prosthesits who have a laboratory equipped with full CAD/CAM technologies (Smith & Burgess, 2001; Cheng *et al*., 1998).

Last years, 3D printers gain ground in both accuracy and material quality and they will take some of this market away from CAD/CAM technologies. The 3D printing technology has undergone huge developments and is the most promising technology in prosthesis and or thesis fabrication.

In Romania, main centers for Rapid Prototyping research and implementation are:

- National Center for Rapid Prototyping from Technical University of Cluj-Napoca;
- INCDMT (Institutul Naţional de Cercetare-Dezvoltare pentru Mecatronică si Tehnica Masurării) from Bucarest;
- MATRIS METAL PLAST S.A. Bucuresti, known for services and application of RP in production.

New Romanian research and service centre are planned to appear next years.

6. Conclusions

Although research continues into application of new CAD/CAM and Rapid Prototyping fabrication techniques, the prosthetics and orthotics industry has not yet taken full advantage of the possibilities in the computer-assisted manufacturing (Cheng *et al*., 1998; Gibson, 2005; Williams, 2003).

Rapid Prototyping and CAD/CAM technologies when implemented correctly, affords safety, consistency, repeatability and standardization of patient care.

The advent of new 3D tools and technologies could produce new ways of scanning, 3D reconstruction and manufacturing of prosthesis and or thesis.

REFERENCES

** www.pp3dp.com.

Canciglieri O., Lam A.E., J. de Oliveira Gomes, *A Methodology for Human Prosthesis Modeling in the CAD/CAM System*. Third International Conference on Production Research –Americas' Region 2006 (ICPR-AM06).

Chandra A., Watson J., Rowson J.E., Holland J.R. Harris A., Williams D.J., *Application of Rapid Manufacturing Techniques in Support of Maxillofacial Treatment: Evidence of the Requirements of Clinical Applications*. Proc. Int. Mech. Eng, **219**, Part B: J. Engineering Manufacture, 469 – 475 (2005).

Cheng T.K., Sin P.L.V., Fye T.K., Lin L.S., *Automation of Prosthetic Socket Design and Fabrication Using Computer-Aided-Design/Computer-Aided-Engineering and Rapid Prototyping Techniques*. The First National Symposium of Prosthetics and Orthotics, 28th October 1998.

Ciobanu O., *CAD Environment in 3D Anatomic Reconstruction*. Rev. Medico-Chirurgicala, **III**, *2*, SUPL. 2, 56-59 (2007).

Ciobanu O., *State of Art of CAD/CAM in Prosthetics*. Bul. IPI, **LIII (LVII)**, *2*, 273-280 (2007).

Ciobanu O., T*he Use of a Computer Aided Design (CAD) in 3D Reconstruction of Anatomic Surfaces*. Stud Health Technol Inform., *119*, 102-104 (2006).

Gibson I., *Advanced Manufacturing Technology for Medical Applications*. Reverse Engineering, Software Conversion and Rapid Prototyping, John Wiley & Sons Ltd, 2005.

Michael J.W., *Reflections on CAD/CAM in Prosthetics and Orthotics*. (J. of Prosthetics and Orthotics, **1**, *3*, 116-121 (1989).

Smith D.G., Burgess E.M., *The Use of CAD/CAM Technology in Prosthetics and Orthotics - Current Clinical Models and a View to the Future*. J. of Rehabilitation Research & Development, **38**, May/Jun 2001.

Williams G., *CNC Robotics*. McGraw-Hill, 2003.

TEHNOLOGII CAD/CAM ŞI PROTOTIPARE RAPIDĂ ÎN INGINERIA MEDICALĂ

(Rezumat)

Utilizarea în industria medicală a tehnologiilor CAD/CAM şi de fabricare rapidă a prototipurilor împreună cu alte tehnici, precum scanarea 3D, reconstrucţia 3D şi vizualizarea suprafeţelor anatomice au dus la îmbunătăţirea serviciilor medicale oferite pacienţilor. Lucrarea prezintă o trecere în revistă a diverselor tehnologii de fabricare utilizate în industria dispozitivelor medicale şi în cercetări de inginerie medicală în vederea producerii de echipamente, dispozitive medicale, implanturi şi proteze personalizate sau în serie mare.

BULETINUL INSTITUTULUI POLITEHNIC DIN IAŞI
Publicat de
Universitatea Tehnică „Gheorghe Asachi” din Iaşi
Tomul LVII (LXI), Fasc. 4, 2011
Secţia
ŞTIINŢA ŞI INGINERIA MATERIALELOR

THE MAINTENANCE, YESTERDAY AND TODAY, WITHIN WATER COMPANY S.C. APAVITAL S.A. IASI

BY

CIORBĂ FLORENTINA*, TOPLICEAN TIBE, VÂNCĂ SORIN, SANDU MARIUS and TUMURUG CIPRIAN

S.C. APAVITAL S.A. Iaşi

Received: April 14, 2011
Accepted for publication: June 27, 2011

Abstract. A proper maintenance is crucial for ensuring the safety and the reliability of equipment and of work environment. The maintenance itself is a high-risk activity and is to be carried in safe conditions. Thus, maintenance workers and the other persons that are on site have to be fitted with adequate protection gear. The lack of maintenance or an inadequate maintenance may cause work accidents and serious health problems.

Despite the fact that the pumping station has been upgraded the SC APAVITAL maintenance workers are always observing five key safety rules: 1. Planning; 2. Making the working area safe; 3. Adequate use of equipment; 4. Work in compliance to planning; 5. Final verification.

Key words: Apavital, maintenance, risks, comparative analysis.

1. Introduction

This paper makes reference to the upgrading of the Păcurari pumping station, facility belonging to company SC APAVITAL SA IASI and treats aspects related to maintenance, risks and dangers, in terms of health and work safety.

* Corresponding author e-mail: florentina.munteanu@apavital.ro

APAVITAL SA is a water-sewerage company that operates for the Iasi County, in the Northern-Eastern sector of Romania. Further data on the web pages from, www.apavital.ro.

Maintenance is a generic term designing various operations carried within all activity sectors, and within all types of work environments.

The equipment (*i.e.* work location-building, work equipment, transportation mean) is subject to technical, administrative or management measures implemented with the aim to keep it or reinstate it in that condition in which it can fulfill its designed primary function, and protecting it in the same time against failures or damages.

Maintenance, according to European Standard EN13306, is defined as „the combination of all tehnical, administrative and managing actions carried along the equipment's life span with the aim to keep it or reinstate it in the condition in which it can fulfill its designed main functions".

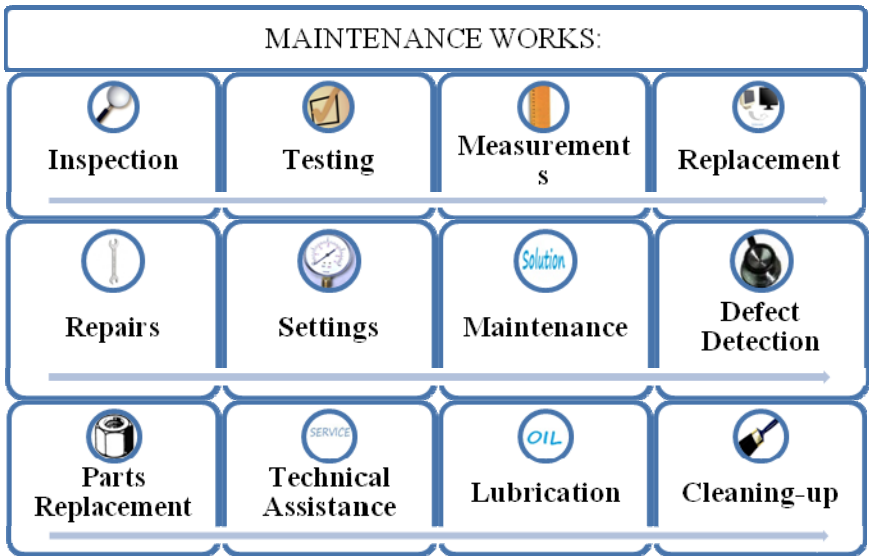

Types of maintenance:

- Corrective (reactive)
  - Based on elements of technical engineering: weariness, defects, material fatigue;
  - Unplanned, unprogrammed;
  - Repairing an equipment in order to make it operational;
  - Higher risks and hazards.
- Preventive (Pro-active)
  - Based on elements of economical engineering: efficiency,life-cycle;
  - Planned and programmed (manufacturer's instructions);

- Ensures the operational status of the equipment.

- Systemic (productive or total)
  - Based on the theory of quality, theory of design, systemic engineering, and human engineering.

Maintenance works are performed *in all sectors* and almost *by all employees* – hence, it is not a domain exclusively belonging to maintenance technicians and engineers. Due to this, the workers that carry maintenance works are exposing themselves to various hazards.

Risks:

- Physical: Accidents of all types, *e.g*. falls or detachments, the risk of being hit by machinery components
- Chemical: Exposure to chemical reagents, asbestos, by example during maintenance works in old buildings or industrial plants; fats, solvents, corrosive substances
- Biological: Exposure to biological hazards, *e.g.* Hepatitis A, Legionella, exposure to dusts, including carcinogen wooden powders
- Psycho-social: Exposure to stress (*e.g*. working against the clock)
- Musculo-skeletal conditions: Occur when workers work in vicious postures or in aggresive environments (in cold)

If no maintenance is performed: RISKS ARE INCREASING!

If maintenance is performed: RISKS FOR MAINTENANCE WORKERS!

If maintenance is inadequate: RISKS FOR MAINTENANCE AND OPERATING WORKERS!

Maintenance activities may harm all workers:

- The lack of maintenance

  - shortens the equipments' and buildings' life span

  - may generate accidents

  Example: The damaged flooring within a storage facility may lead to accidents

- During maintenance accidents or ilnesses my occur.
  - Examples:

  - Workers that repair an equipment may be injured if machinery gets accidentally started

  - Workers are exposed to hazardous substances

  - Workers are compelled to work in vicious postures (musculoskeletal diseases).

- Inadequate maintenance works.

Example: The use of unproper spare parts (replacement or repair) mai generate serious accidents.

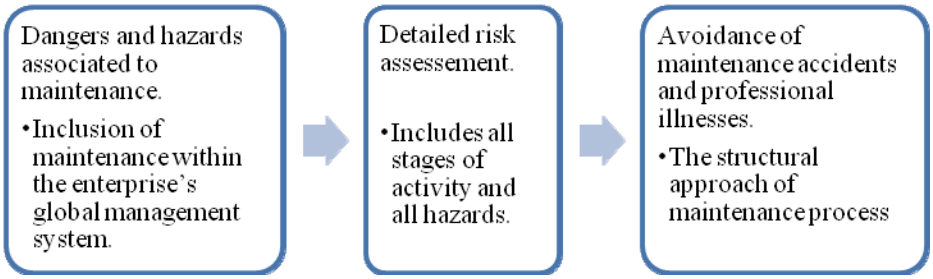

- The design-planning stage, with the next key-aspects:
  - Allotment of a sufficient period of time;
  - Allotment of a sufficient resources for the maintenance work.
- Developing the competences of the maintenance personnel.
- Implementing safe work systems, based on a sound risk assessment.
- An efficient communication.
  - Maintenance workers with the local work site chief;
  - Maintenance workers with the operational workers.

2. Experimental

The Păcurari Pumping Station.

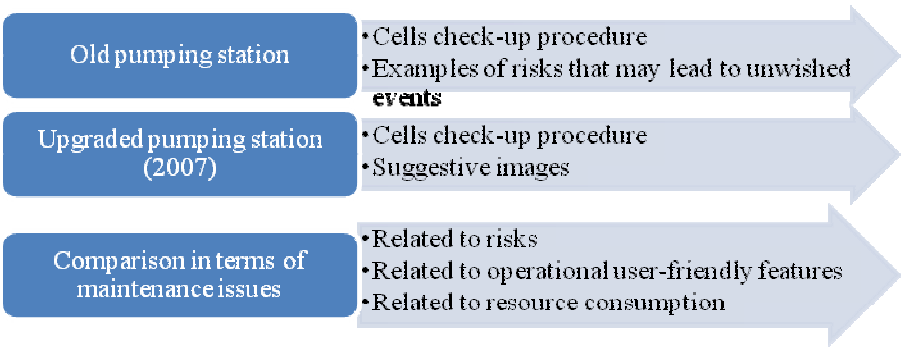

The old pumping station

- Risks of errors is higher than for the upgraded facility
- Access in cell is possible also via backsides („a worker hears what colleague is saying but cannot see what he is doing")
- Cell's door could be opened no matter if cell was operating or not
- No data base related to cells' operation was available
- No real time data flow was available (related to the machinery behavior and operational status)
- Lots of materials were used for cleaning-up (oil was used)
- Manual settings and adjustments, on a large number of gauges and devices, hence hard physical work of many workers

- Old cells did not have fuses
- In-door cleaning was performed with brushes

The upgraded pumping station

- Access in cell is possible only via frontside
- Cell's door cannot be opened if cell is in operation
- There is a data base that can be stored on a special software, anytime
- Real time data related to the machinery behavior and operational status are displayed
- Oil is not longer used (it was toxic and hazardous for workers)
- Now all settings are carried via computer (with special software)
- Material consumptions at repairs are much lesser
- Machinery and equipment check-ups are carried with computer (easier and cleaner)
- Duration of check-ups, rehaulings and repairs have been significantly decreased
- Reparations consisted in the changing of fuses shown by the computer soft and on the local cell's display
- In-door cleaning-up ca be carried with a simple small paintbrush and a rag with some alcohol in it (all materials used are in much lesser amounts)
- No more oil is used in cells, hence a much lesser cleaning time and a much more safe work environment

Old Station versus Upgraded Station; Comparison in images.

Fig. 1 – Higher error risk in the old station.

Fig. 2 – Access to cells: Old station - access possible via backside and frontside. New station - access possible only from frontside.

Fig. 3 – Opening the cell's door I.

Fig. 4 – Opening the cell's door II.

Fig. 5 – Real time data flow for machinery status. Old station: discontinous manual measurements. New station: real time continous displaying of data.

Fig. 6 – Maintenance materials: Oil. Old oil-based fuses have been replaced with oil-free modern fuses.

Fig. 7 – Dorso-lumbar illnesses.

Fig. 8 – Dorso-lumbar illnesses II.

Fig. 9 – Cleaning-up I.

Fig. 10 – Cleaning-up II.

Fig. 11 – Cleaning-up III.

Fig. 12 – Equipments during maintenance.

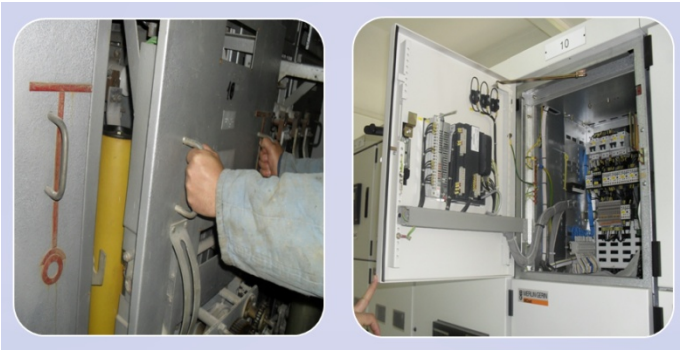

Fig. 13 – Cells' fuses.

Fig. 14 – Cells' fuses II.

1. Conclusion

Risks decreased for maintenance and operating workers.

In general the activity within the new pumping station takes place in better conditions, operating costs have decreased.

This upgrading is an example of good practice for the other pumping facilities managed by company SC APAVITAL, but also for all colleagues in Romania.

REFERENCES

[1]. *** *The European Campaign Regarding the Security of the Maintenance Workers – Healthy Work Places- Good for You. Good for Business.* http://hw.osha.europa.eu.

[2]. Eng D., Tanasievici G.D., *The Prevention of the Risks in the Maintenance Activity*.

[3]. *** Internal Documents S.C. APAVITAL S.A. IAŞI.

MENTENANŢA DE IERI ŞI DE AZI LA S.C. APAVITAL S.A. IAŞI

(Rezumat)

O bună mentenanţă este esenţială pentru menţinerea siguranţei şi fiabilităţii echipamentelor şi mediului de lucru. Mentenanţa în sine este o activitate cu risc ridicat şi trebuie efectuată în condiţii de siguranţă, cu o protecţie adecvată a lucrătorilor de mentenanţă şi a altor persoane prezente la locul de muncă. Lipsa mentenanţei sau o mentenanţă inadecvată poate da naştere unor accidente de muncă şi unor probleme grave de sănătate.

Chiar dacă staţia a fost modernizată, lucrătorii care execută lucrări de mentenanţă în cadrul companiei APAVITAL respectă cinci reguli de bază pentru securitatea lor: 1. Planificare; 2. Asigurarea securităţii zonei de lucru; 3. Utilizarea corespunzătoare a echipamentelor; 4. Lucrul conform planului; 5. Verificare finală.

BULETINUL INSTITUTULUI POLITEHNIC DIN IAŞI
Publicat de
Universitatea Tehnică „Gheorghe Asachi" din Iaşi
Tomul LVII (LXI), Fasc. 4, 2011
Secţia
ŞTIINŢA ŞI INGINERIA MATERIALELOR

RESEARCH ON DISTRIBUTION METHOD OF HEAVY METALS BY SOIL PROFILE FROM ROMPLUMB AREA, BAIA MARE

BY

CAMELIA COCIORHAN*, VALER MICLE and IOANA BERAR (SUR)

Technical University of Cluj-Napoca
Faculty of Materials and Environmental Engineering

Received: April 27, 2011
Accepted for publication: June 27, 2011

Abstract. Depression Baia Mare is an area with historical pollution, mainly from anthropogenic phenomena, phenomena that have their genesis pathways related to soil pollution from human activities predominantly. The paper made reference to the category of pollutants from direct deposit on the soil of minerals as raw materials and hazardous waste, involving the deflation of the particles on the surface of dumps, sewage infiltration locations, accidental discharges of sewage the site and crack pipes. Are present the way to choose the points of soil sampling and determination of heavy metal content of samples. The soil samples were taken from inside of the precinct Romplumb, Baia Mare in a number of 9 soil samples from three sampling points. Results on heavy metal concentrations are presented in histogram, according to depth, which allows assessment of heavy metal distribution in soil profile. Specific analysis on the determination of chemical elements were made by mineralization with royal water and then by atomic emission spectrometry in inductively coupled plasma (ICP – OES) were performed in specialized laboratories of Research Institute for Analytical Instrumentation - ICIA Cluj – Napoca. Through a comparative analysis between the concentrations of heavy metals in soil samples taken from inside of the precinct Romplumb in 2008, 2009 and 2010, it is formulate conclusions on changing the metals distribution from anthropogenic activities.

* Corresponding author e-mail: ccociorhan@yahoo.com

Key words: heavy metals, alert threshold, intervention threshold, soil samples.

1. Introduction

The mining activity, practices in Baia Mare for over 100 years, has led to pollution and economic sealing of large areas of land, it has adversely affected the environment and now poses a significant risk to human health. The actual sources of pollution, current or historical, in Baia Mare Depression are SC Romplumb SA, SC Cuprom SA and CNMPN Remin SA. The mining activities left over wide areas ponds, mine waste dumps and the underground waters that come across the existing mine galleries spring out contaminated and sometimes in an uncontrolled manner. Heavy metals are present in the environmental factors from this area and significantly affect local ecosystems and human health (Coman M. *et al*., 2010).

2. Materials and Methods

Soil sampling were taken in accordance with STAS no. 7184/1 – 84 and Order MAPPM no.184/1997, from inside precinct SC Romplumb SA, Baia-Mare, from three depth profiles determined in accordance with reference documents. Paper work, presents the evolution of heavy metals concentrations in soil samples. Taken near the former slag waste dump, the south side of the precinct, the depths of up to 5 cm, 30 cm and 100 cm. In years 2008 and 2009, the preparation and analysis of soil samples taken from that three depth profiles, from the precinct of SC Romplumb SA was performed by SC Prospecţiuni SA Bucharest, Geological Laboratory Division – Physico – Chemical Analysis Department, accredited RENAR, (Bilanţ de mediu nivel II, 2006). Analyses were conducted to determine the total concentration of chemical elements in soil samples taken, by spectrometry of atomic emission, in accordance with SR ISO 11047/1999.

Heavy metals concentrations in soil samples taken in 2010 were analyzed in specialized laboratories of Research Institute for Analytical Instrumentation - ICIA Cluj – Napoca, accredited RENAR according to SR EN ISO/CEI 17025:2005. The method used was atomic emission spectrometry with inductively coupled plasma (ICP-OES), made with spectrometer SpectroFlame FMD 07, in accordance with SR ISO 11047/1999.

In Fig. 1, are represented the sampling points from inside the precinct SC Romplumb SRL.

Concentrations value of pollutants was compared with reference values for traces of chemical elements in soil, according to Order MAPPM no. 756/1997, approving the Settlement about environmental pollution assessment, for less sensitive soils.

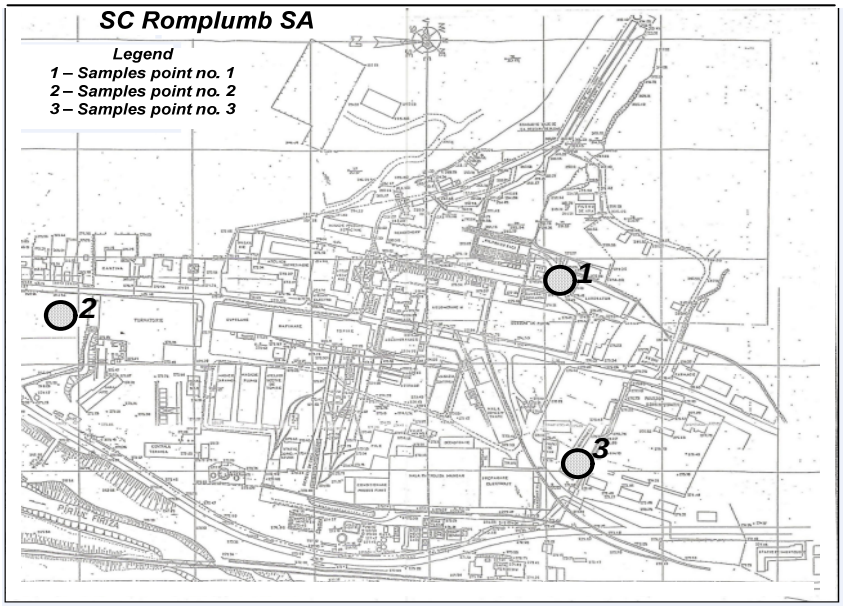

Fig. 1 – Soil sampling locations.

3. Results and Discussion

3.1. pH

Determination of pH was done in accordance with STAS 7184/13 – 88, soil in aqueous suspension. Aqueous suspension of soil has been prepared at ratio soil: water of 1 : 5 mass/volume for all sampling depths.

From Fig. 2, may specify that in the soil samples taken the pH ranges from strongly acid (at 5 cm depth) to moderately acid (in the sample taken from 30 cm depth), until neutral (at 100 cm depth).

- pH values determined for all sampling depths tend to increase proportionately with depth.

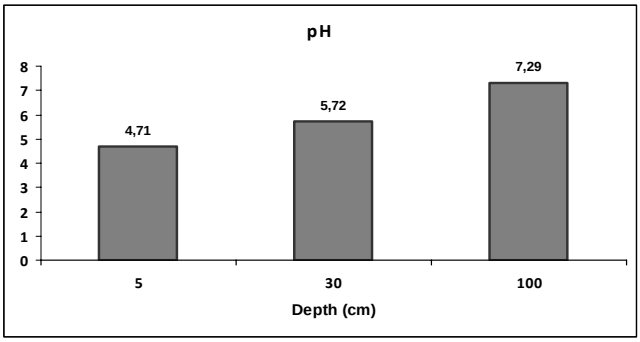

Fig. 2 – pH variation according to depth.

3.2. Determination of Heavy Metals Concentration in Soil Samples

Heavy metals concentrations were determined by extracting from soil of soluble microelements in royal water, under to SR ISO 11047/1999. Concentration values determined are presented in Table 1.

Table 1
Concentration of Heavy Metals, in Soil Laye

Parameters analyzed	Year	Assessed values mg/kgs.u.			Reference input according to Order 756/1997		
		Depth (cm)			Normal values	Alert threshold	Intervention threshold
		5	30	100			
Pb	2008	1127	14022	16907	20	250	1000
	2009	3423	25228	35375			
	2010	4668	24583	35400			
Zn	2008	140	1252	14014	100	700	1500
	2009	472	2221	6935			
	2010	1317	2369	6940			
Cu	2008	60	2505	5651	20	250	500
	2009	683	4428	7395			
	2010	1014	5106	7400			
Cd	2008	1,35	18	26	1	5	10
	2009	3,3	18	57			
	2010	12,8	14	46			

Lead, is found in nature as galena (PbS), andesite (PbSO4), cerussite (PbCO3), being covered by a protective oxide film (PbO). Is the most common pollutant, but also the most dangerous from the area investigated.

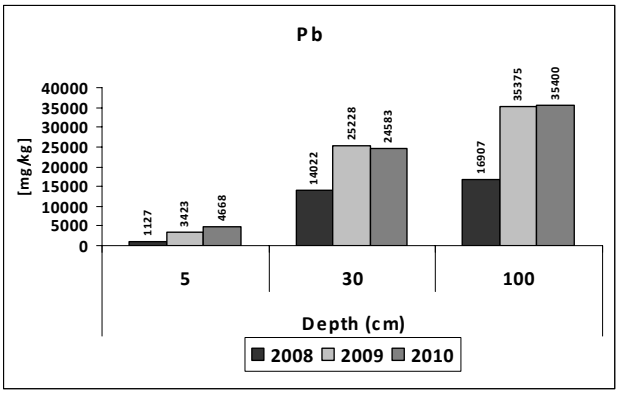

Fig. 3 – Pb variation according to depth.

His dangerousness is given of its specific properties, being invisible,

tasteless, colorless, odorless, all of this because they found it as very fine powder, being invisible to the naked eye. This chemical element is distributed at all depths of sampling as the main pollutant element. The levels of lead exceeding in whole volume of material investigated, (Bilanţ de mediu, nivel II, 2006) intervention threshold concentrations of 1 000 mg/kg s.u.

For all samples investigated, concentrations of lead ranging between 1127 – 35 400 mg/kg s.u. in year 2008 at 5 cm depth, in year 2010 at 100 cm, respectively. For details on the maximum, medium and minimum concentration of lead at 5, 30 and 100 cm depth, are interprets the values represented in the histogram from Fig. 3, column III, corresponding to each year.

Zinc, contrast to lead, has lower toxicity. This metal is enough wide-spread in nature, is used in industry and can be released into environment by mining activities and preparation of the ore. High concentrations of zinc in soil is due to the waste from metal manufacturing industries, from where reach surface waters at high concentrations. From the air can get in soil and water, where it settles on bottom of the channel.

Zinc concentration in soil samples taken shows high values (Fig. 4), except for samples taken from 5 cm depth in 2008 (140 mg/kg s.u.) and 2009 (472 mg/kg s.u.), which not exceed alert threshold (700 mg/kg s.u.), and samples from 5 cm depth in 2010 (1317 mg/kg s.u.), from the 30 cm depth (1252 mg/kg s.u.) in 2008, samples who do not exceed intervention threshold (1 500 mg/kg s.u.). For all samples investigated zinc concentrations varies from 140 mg/kg s.u. (in 2008, at 5 cm depth) and 14 014 mg/kg s.u. (in 2008, from depth of 100 cm). This distribution varies once with the increase of depth, can be explained by the specific properties of zinc, to concentrate in clays (present in this investigated area). Copper is among the first metals known and used by people in the state native. Copper and its salts are highly soluble and persistent in water. In soil, copper remains attached by the layer to the surface, but can occur depth migration at very high concentrations or by mixing soil in the soil profile.

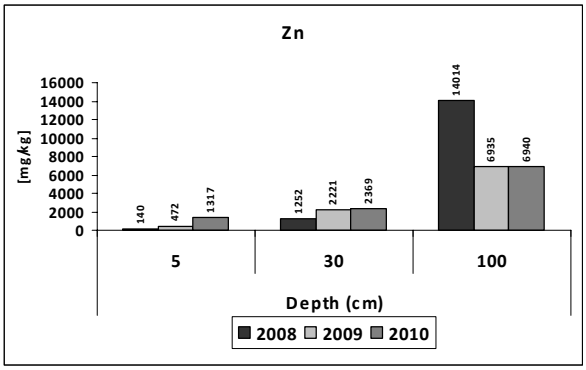

Fig. 4 – Zn variation according to depth.

For all samples investigated copper concentrations (Fig. 5) varies between 60 mg/kg s.u in year 2008 at 5 cm depth and 7 400 mg/kg s.u. in year 2010 at 100 cm depth. Distribution of copper in soil highlights a trend of increasing concentration with depth of sampling. The value obtained for copper concentrations, presents high values at all sampling depths except for samples from depth of 5 cm (60 mg/kg s.u.) in year 2008 which not exceeding the alert threshold (250 mg/kg s.u.).

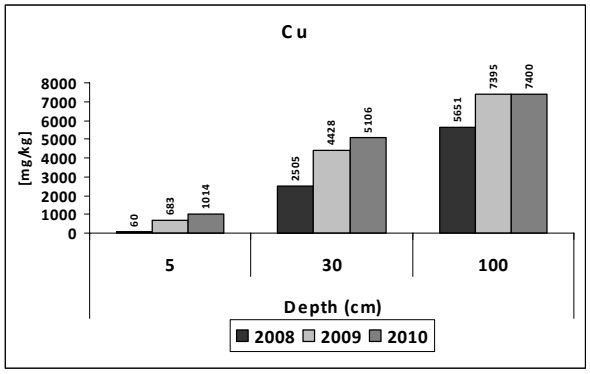

Fig. 5 – Cu variation according to depth.

Cadmium is known as one of the most toxic metal pollutants and just like lead, do not declare their presence.

The presence of cadmium in soils is due to both natural sources (includes parental rocks or the materials carried by alluvial type) and anthropogenic sources (submission from the atmosphere and from the animal manure and phosphate fertilizers). This chemical element is more stable in soils than in air and water. For the fixation, the absorption and the distribution in soils depend on: pH, metal oxide content, soluble organic matter content, type and clay content.

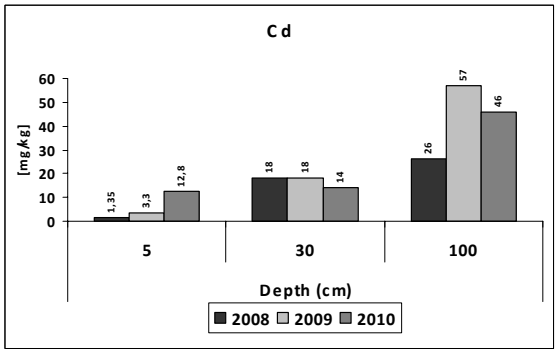

Fig. 6 – Cd variation according to depth.

Distribution of cadmium in soil (Fig. 6) is characterized by its concentration with the increasing depth, by the exceeding of intervention threshold 10 mg/ kg s.u., except of the concentrations at 5 cm depth in 2008 (1,35 mg/kg s.u.) and 2009 (3,3 mg/kg s.u.). The levels of cadmium present in soil samples taken, varies between 1,35 mg/kg s.u. at 5 cm depth in year 2008 and 57 mg/kg s.u. in year 2009 at 100 cm depth.

4. Conclusions

In soil layers, pH values tend to increase proportionately with depth.

Through a comparative analysis of the concentrations determined of the four elements (Pb, Zn, Cu, Cd) can specify that, proportionally, the concentrations increase with depth. At the same time, the variation of pollutants elements reported according to time, shows increases in concentrations of elements with its passage. Concentration value of lead exceeding in all samples of material investigated corresponding intervention threshold limits. Exceptions make the samples from 5 cm depth for all zinc concentrations, copper concentrations for the sample taken in year 2008 and cadmium concentrations for samples taken in year 2008 and 2009, which not exceed the limits of intervention threshold. Concentrations of samples from 30 and 100 cm depths, shows alarming levels, exceeding the limits imposed by the Order no. 756/1997, corresponding to alert threshold. In such conditions the remediation is becoming more expensive.

Acknowledgements. The financial support provided by the Romanian Ministry of Education and Research, PNCDI II Project RESOLMET no. 32161/2008 is greatly appreciated. This research was conducted within PRODOC, Contract POSDRU/6/1.5/S/5 ID7676, projekt co-founded from European Social Found through Sectorial Operational Program Human Resources 2007-2013.

REFERENCES

*** *Bilanţ de mediu nivel II pentru SC ROMPLUMB SA*.– Elaborat de SC. Envicons Consulting SRL – Centrul de cercetare şi consultanţă, 2006.

*** ORDIN nr. 756/1997, *Pentru aprobarea Reglementarii privind evaluarea poluării mediului*, 1997.

*** Ordinul MAPPM nr. 184/1997, *Pentru aprobarea procedurii de realizare a bilanţurilor de mediu*, 1997.

*** SR ISO 11047/1999, *Privind calitatea solului. Determinarea cadmiului, cromului, cobaltului, cuprului, plumbului, manganului, nichelului şi zincului din extracţie de sol în apă regală – Metodele prin spectrometrie de absorbţie atomică în flacără şi automizare electrotermică*, 1999.

* * * STAS 7184/13 – 88, *Privind determinarea pH-ului*.
* * * STAS 7184/1-84 *Privind recoltarea probelor de sol pentru studii pedologice şi agrochimice.*
Coman M., Oros V., Fălăuş B., Pop R., *Poluarea solului cu metale grele – probleme specifice pentru zona Baia Mare.* Proenvironmet, Cluj-Napoca, **3**, *5*, 155-158 (2010).

CERCETĂRI PRIVIND MODUL DE DISTRIBUŢIE A METALELOR GRELE PE PROFILUL DE SOL DIN ZONA ROMPLUMB, BAIA MARE

(Rezumat)

Depresiunea Baia Mare este o zonă cu poluare istorică, preponderent din fenomene antropice, fenomene care îşi au geneza legată de căile de poluare a solurilor din activităţi cu preponderenţă umane. În lucrare sunt făcute referiri la categoria de poluanţi care provin din depozitarea directă pe sol a minereurilor ca materii prime şi a deşeurilor periculoase, antrenarea prin deflaţie a particulelor de pe suprafaţa haldelor, infiltraţii de ape uzate de pe amplasamente, evacuări accidentale de ape uzate de pe amplasament şi fisurarea conductelor etc. Se prezintă modul de alegere a punctelor de prelevare a probelor de sol şi de determinare a conţinutului de metale grele din probele prelevate. Probele de sol au fost prelevate din interiorul incintei Romplumb, Baia Mare într-un număr de 9 probe de sol din 3 puncte de prelevare. Rezultatele privind concentraţiile de metale grele sunt prezentate sub formă de histograme, în funcţie de adâncime, ceea ce permite aprecierea distribuţiei metalelor grele pe profilul solului. Analizele specifice privind determinarea elementelor chimice au fost realizate prin mineralizare cu apă regală şi apoi prin spectrometria de emisie atomică în plasmă cuplată inductiv (ICP-OES), în cadrul laboratoarelor specializate ale Institutului pentru Instrumentaţie Analitică – ICIA, Cluj-Napoca. Printr-o analiză comparativă realizată între concentraţiile de metale grele prezente în probele de sol prelevate din interiorul incintei în anii 2008, 2009 şi 2010 se formulează concluziile privind modul de distribuţie a metalelor în urma activităţilor antropice.

BULETINUL INSTITUTULUI POLITEHNIC DIN IAŞI
Publicat de
Universitatea Tehnică „Gheorghe Asachi" din Iaşi
Tomul LVII (LXI), Fasc. 4, 2011
Secţia
ŞTIINŢA ŞI INGINERIA MATERIALELOR

DIE DESIGN AND PROCESS PARAMETERS FOR OPTIMAL WORKING LOAD IN EQUAL CHANNEL ANGULAR PRESSING

BY

ADRIAN COMĂNICI[1]* and RADU COMĂNECI[2]

[1]S.C. Aerostar S.A. Bacău,
[2]"Gheorghe Asachi" Technical University of Iaşi
Faculty of Materials Science and Engineering

Received: April 14, 2011
Accepted for publication: June 27, 2011

Abstract. As the most effective method for producing ultrafine grained/ nanostructured materials by severe plastic deformation (SPD), equal channel angular pressing (ECAP) has been the subject of intensive studies in the last decade. A successful ECAP process is mainly related to working load. Inherent failures of tools take place if load reaches a certain critical value. In this article, a tridimensional finite element analysis (FEA) was performed to study the influence of die design and friction condition on ECAP load. In order to validate the simulations, experimental tests were performed for 5052 Al-Mg alloy. In this study three design scenarios and separately, three coefficients of friction were considered. The results show a consistent influence of friction and especially of die design on load level.

Key words: severe plastic deformation, finite element, equal channel angular pressing.

1. Introduction

Equal channel angular pressing (ECAP) has been the subject of intensive study in recent years due to its capability of producing fully dense samples having ultrafine grain size (Umemoto, 2009; Furukawa *et al*., 2005). It

* Corresponding author e-mail: comaneci@tuiasi.ro

is generally accepted that if metals are deformed at room temperature, average subgrain/cell size decreases with strain. According to Hall-Petch relationship, it is well known that refining the grain size (d) increases yield strength (σ_y) and hardness (HV) of the materials (Furukawa *et al*., 2001):

$$\sigma_Y = \sigma_{Yo} + \frac{K}{\sqrt{d}} \tag{1}$$

where σ_{yo} is the intrinsic yield stress and K is a constant for the given material.

ECAP process involves large shear plastic deformation in a deforming layer of a workpiece by moving through a die containing two intersecting channels of identical cross-sections that meet at a predetermined angle (commonly 90 or 120°), Fig. 1. The metal is subjected to a simple shear strain along the bisect plane of the channels (Segal, 1995). The billet removal involves a new development of ECAP procedure. The introduction of a new sample returns the ECAP process to the initial configuration which permits the next pressing cycle to follow.

The theoretical effective strain according to the die geometry is given by Eq. (2), as formulated by Iwahashi *et al*. (1998):

$$\bar{\varepsilon} = \frac{1}{\sqrt{3}}\left[2\mathrm{ctg}\left(\frac{\phi}{2}+\frac{\psi}{2}\right) + \psi \cos\mathrm{ec}\left(\frac{\phi}{2}+\frac{\psi}{2}\right)\right] \tag{2}$$

where the significance of terms are revealed in Fig.1. For $\phi = 90°$, an equivalent strain of approximately 1 is achieved. Note that Eq. (2) was derived for ideal perfect-plastic behavior and frictionless conditions. The properties of the ECAPed materials are strongly dependent on the shear plastic deformation behavior during ECAP, which is controlled mainly by die geometry, material properties, and process conditions.

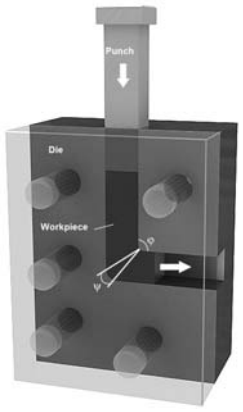

Fig. 1 – Principle of ECAP and die geometry components.

Die and process design starts from working load level which determines dimensions and component materials. From the technological point of view, a successful SPD process requires surpassing of two obstacles. First the load level (which directly affects the tool design, especially in large dimensions of the billet) and second an adequate formability of the material so that it can withstand high degrees of repeated deformation. Inherent failures of ECAP if not made a correct process design were reported. In this article, a tridimensional finite element analysis (FEA) was performed to study the influence of die design and friction condition on ECAP load. In order to validate the simulations, experimental tests were performed for 5052 Al-Mg alloy. Three design scenarios and separately, three coefficients of friction were considered in this study. The results show a consistent influence of friction and especially of die design on load level. Also it is shown that coefficient of friction has a different influence depending of die geometry: presence of corner channels make friction less important for load level.

1. Experimental Materials and Procedures

2.1. Processing Al-Mg Alloy by ECAP

There is considerable interest in using Al-Mg alloys for structural applications due to their good weld ability, moderate strength, but excellent corrosion resistance. Increasing strength by SPD without any supplementary alloying it's a convenient way to rise up the potential of the material with maintaining all other mechanical properties.

A commercial available aluminum AA 5052 alloy with a composition in wt.% of 2.8%Mg – 0.2%Cr and aluminum balance was used in this study. Specimens with dimensions of 10x10x60mm were machined from as-received alloy. A subsequently annealing at 723K for 1h was performed before ECAP. The ECAP process was conducted at room temperature with a constant speed of 8.75mm/s, using dies with $\phi = 90°$. All samples and inner walls of the dies channels were lubricated using zinc stearate. To confirm the modeling results of FEA, the evolution of working load vs. punch displacement in first ECAP pass was registered by data acquisition using National Instruments equipment.

2.2. Finite Element Analysis

Commercial finite element code DEFORM 3D was used to carried out the simulations. The workpiece (10x10x60mm) considered a plastic body in whole deformation process was discretized in 8000 tetrahedral elements. According to Figueiredo *et al*. (2007) a mesh of 8000 elements is sufficiently fine to reveal localized effects (this is equivalent to at least 36 elements across the width of the billet). The tolerance, positioning of the workpiece and top/bottom die, convergence criteria, re-meshing conditions, and boundary

conditions were specified before the execution of the simulation process. Adaptive meshing was used in the simulation. Poisson's ratio 0.33 and Young's modulus 69Gpa was assumed (Patil Basavaraj *et al.*, 2009). The hardening behavior is considered isotropic and independent of strain rate at room temperature. The simulation was performed for a stroke of 50mm under a constant speed of 8.75mm/s, which generates negligible heat during the plastic deformation. The processing takes place at room temperature.

The friction force along contact surfaces was modeled by constant shear friction law $F_r = m \cdot \tau_o$ where τ_o is the yield stress in shear and m, the shear friction coefficient which usually varies between 0.08 (carbide dies) and 0.12 (steel dies). To depict the influence of friction conditions, three different values for friction coefficient were considered: 0.08, 0.10, and 0.12. These values have been used by other authors (Figueiredo *et al.*, 2009).

Three design scenarios (symbolized 90_R_r) are analyzed by FEA to reveal the deformation behavior and its relationship with the design configuration: A - there is no arc transition, the channels are intersected at a sharp corner; R, r = 0 mm (**90_0_0**); B - there is one arc transition at the outer side of the channels; R = 2 mm; r = 0 mm (**90_2_0**); C - there is one arc transition at the inner side of the channels; R = 0 mm; r = 2 mm (**90_0_2**).

3. Results and Discussion

3.1. Working-load. Validation of Modeling

Matching of simulates with experimental load results is compulsory to validate the modeling. Fig. 2 shows load – displacement curve during the ECAP process of AA5052 using a die with channel angle of $\phi = 90°$ and no outer/inner arc of curvature between channels. The maximum level of working-load and the general evolution are in good agreement with experimental results, confirming the validity of ECAP modeling.

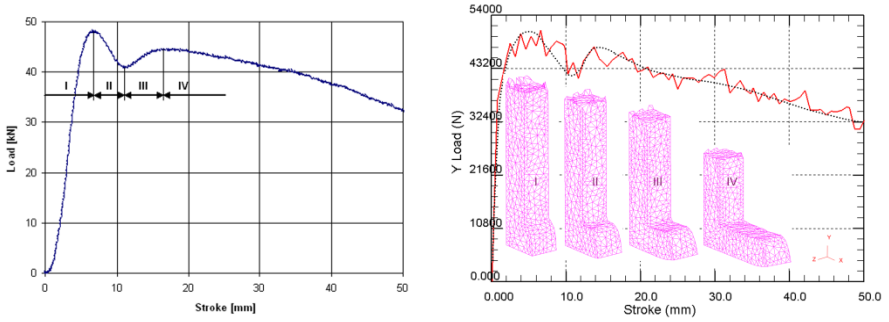

a *b*

Fig. 2 – Experimental (*a*) and simulated (*b*) load – stroke curve (AA 5052, ECAP 90_0_0, m = 0.12).

For die with sharp inner and outer corner, four distinguished stages can be identified. The dashed line highlights the evolution of load and helps identify the four stages. Different simulated steps of ECAP corresponding to the four stages were superimposed over graph (Fig. 2*b*).

In Stage I, the load increases rapidly with the ram displacement, reaching a maximum. This stage begins when the head of the billet first touches the bottom wall of the die channel at the outer corner and ends when the workpiece head bends over the corner. In Stage II the load decreases until the upper surface of the billet begins to touch the upper wall of the outlet channel.

In the next stage (Stage III), a slowly increase in load marks the period from the moment the billet head touches the upper wall (end of Stage II) to the moment that sufficient contact is established between the upper surface of the billet head and the upper wall of the outlet channel. Load increases because of deformation in the billet head. The load decreases gradually with the displacement in Stage IV because the contact area in the inlet channel and plastic deformation in the billet head decreases (Li *et al*., 2004).

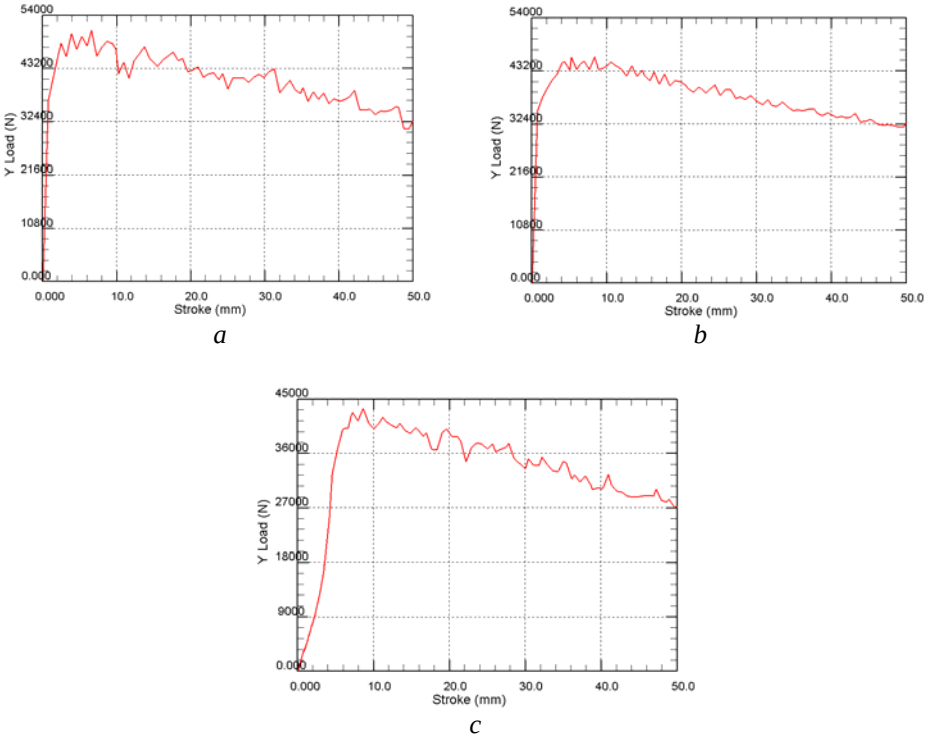

Fig. 5 - Load prediction for the first pass
μ = 0.12: *a*) 90_0_0; *b*) 90_0_2; *c*) 90_2_0.

The load decreases gradually with the displacement in Stage IV. The decrease of load in the steady state region is related to the dependence of

frictional forces on gap formation in the outlet channel. In general, the billet is in full contact with the die wall in the inlet channel, but only partially in contact with the wall in the outlet due to the formation of gaps. When the billet is pressed from the inlet channel to the outlet channel through the die corner, the contact area in the inlet channel decreases and in the meantime the length of the gap in the outlet channel grows until the head of the billet comes out of the outlet channel. As a result, the total contacting area between the billet and the die wall always decreases with the ram displacement, and so when we have real friction, the response is visible in load versus displacement curve.

The magnitude of the maximum load is most interesting from the viewpoint of die designs. The present results show that the peak load is reached prior to achieving the steady state and it is higher than the steady state load. This is a normal feature for a strain hardenable material (Li *et al*., 2004). For AA5052 alloy, the maximum ECAP working-load for the first pass is around 40-50kN. For 90_0_0 load is bigger due to high constraint of the sharp die corners. Obviously, the friction coefficient has an important influence on working-load level, as we can see in Figs. 3,...,5.

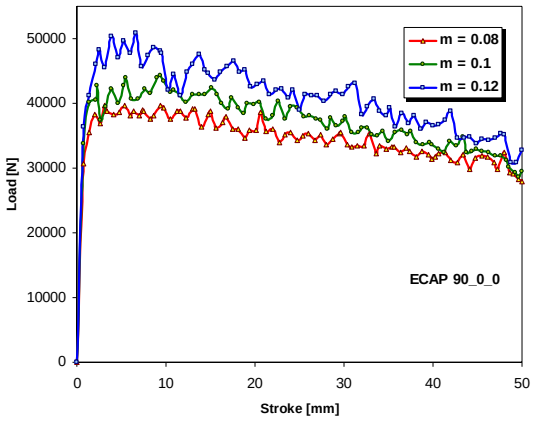

Fig. 3 – Simulated load for 90_0_0 scenario.

Furthermore, for dies with round corners of the channels, three stages in load evolution can be distinguished. That might be explained by the lack of constraint on the billet head.

It was demonstrated that the lesser shear zone in the outer part of the workpiece occurs because of shorter travel path of the outer part compared to the inner part within deformation zone when the inner corner angle of die is non-zero (Yoon & Kim, 2008).

As we can see from the comparison of Figs. 3,…,5, the decrease of load in the steady-state stage is associated with friction coefficient. Obviously, in all cases,

working load for every scenario tends to a certain value at the end of the process and that is a normal thing indicating the level of real friction during the process.

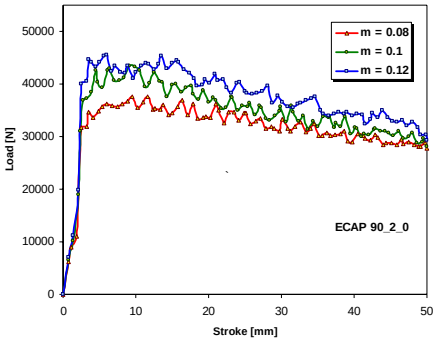

Fig. 4 – Simulated load for 90_2_0 scenario.

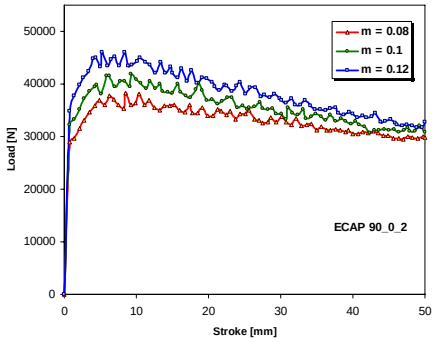

Fig. 5 – Simulated load for 90_0_2 scenario.

4. Conclusion

FEA was performed to predict working-load level for an Al-Mg alloy during ECAP. Three design scenarios which included outer and/or inner corner radius of die channels were analyzed. Die design with outer or inner corner radius provides the minimum loads during ECAP. FEA suggests there will be no spectacular changes of working-load determined by friction conditions for dies with round corner channel while the main influence on load during ECAP belongs to die design. The study of deformation load for a specify design can give both the necessary level of the forces in the severe plastic deformation process and important information for die design.

REFERENCES

Figueiredo R.B., Cetlin P.R., Langdon T.G., *The Evolution of Damage in Perfect-Plastic and Strain Hardening Materials Processed by Equal-Channel Angular Pressing*. Mater. Sci. Eng. A, *518*, 124–131 (2009).

Figueiredo R.B., Cetlin P.R., Langdon T.G., *The Processing of Difficult-To-Work Alloys by ECAP With an Emphasis on Magnesium Alloys.* Acta Mater., *55*, 4769-4779 (2007).

Furukawa M., Horita Z., Langdon T.G., *Processing by ECAP: Applications to Grain Boundary Engineering.* J. Mat. Sci,, *40*, 909-917 (2005).

Furukawa M., Nemoto M., Horita Z., *Processing of Metals by Equal-Channel Angular Pressing.* J. Mat. Sci, *36*, 2835-2843 (2001).

Iwahashi Y., Furukawa M., Horita Z., Nemoto M., Langdon T.G., *Microstructural Characteristics of Ultrafine-Grained Aluminum Produced Using Equal-Channel Angular Pressing. Metall*. Mater. Trans., **29**, *9*, 2245-2252 (1998).

Li S., Bourke M.A.M., Beyerlein I.J., Alexander D.J., Clausen B., *Finite Element Analysis of the Plastic Deformation Zone and Working Load in Equal Channel Angular Extrusion*. Mater. Sci. Eng. A, *382*, 217–236 (2004).

Patil Basavaraj V., Chakkingal Uday, Prasanna Kumar T.S., Study of Channel Angle *Influence* on *Material Flow* and *Strain Inhomogeneity* in *Equal Channel Angular Pressing Using* 3D *Finite Element Simulation*. J. Mater. Process. Technol., *209*, 89–95 (2009).

Segal V.M., *Materials Processing by Simple Shear*. Mater. Sci. Eng. A, *197*, 157–164 (1995).

Umemoto M., *Nanocrystallization of Steels by Severe Plastic Deformation*. Mater. Trans., **44**, *10*, 1900-1911 (2009).

Yoon S.C., Kim H.S., *Finite Element Analysis of the Effect of the Inner Corner Angle in Equal Channel Angular Pressing.* Mater. Sci. Eng. A, *490*, 438–444 (2008).

MATRIŢĂ ŞI PARAMETRI DE PROCES ÎN OPTIMIZAREA FORŢEI DE LUCRU ÎN PROCESUL PRESĂRII UNGHIULARE ÎN CANALE EGALE

(Rezumat)

Fiind cea mai eficientă metodă de obţinere a materialelor ultrafinisate/ nanostructurate prin deformare plastică severă, presarea unghiulară în canale egale a fost subiectul unor studii amănunţite în ultimul deceniu. Succesul procesului ECAP este în principal legat de forţa necesară. Eşecuri inerente ale sculelor de deformare au loc dacă valoarea forţei depăşeşte un anumit nivel critic. În această lucrare a fost realizată o analiză cu element finit tridimensională pentru a studia influenţa construcţiei matriţei şi a condiţiilor de frecare asupra forţei în procesul ECAP. Pentru a verifica rezultatele simulărilor s-au efectuat încercări experimentale pe un aliaj Al-Mg 5052. Au fost luate în considerare trei variante de matriţe şi separat trei coeficienţi de frecare. Rezultatele arată influenţa consistentă a frecării şi în special a configuraţiei matriţei asupra nivelului forţei.

BULETINUL INSTITUTULUI POLITEHNIC DIN IAŞI
Publicat de
Universitatea Tehnică „Gheorghe Asachi" din Iaşi
Tomul LVII (LXI), Fasc. 4, 2011
Secţia
ŞTIINŢA ŞI INGINERIA MATERIALELOR

EXPERIMENTAL MODEL FOR THE ASSEMBLY AND TESTING SYSTEM SHRINK

BY

SANDA CREŢU*, DAN-GELU GĂLUŞCĂ and IRINA-ELENA SURDU

"Gheorghe Asachi Technical University" of Iaşi,
Faculty of Materials Science & Engineering

Received: April 14, 2011
Accepted for publication: June 27, 2011

Abstract. This paper presents an experimental model assembly/ disassembly systems shrink, study on the surface shrink and the results obtained by processing and finite element results obtained on the strength of shrink systems subjected to torque.

Key words: stand assembly/disassembly, system shrink.

1. Introduction

Systems Shrink (Shrink assembling) assemblages are those which, for the sale of parts is necessary to partially or completely destroying the fastener or the parts that make up the assembly. The fasteners used to intercourse assemblies that make up a car or parts, namely the components parts of a mechanism, device or a metal.

The building shape, the constituents of technological operations preparatory nature, with the possibility of mechanization and automation of the execution process, permanent joining are generally cheaper.

* Corresponding autor e-mail: cretu.sanda@yahoo.com

2. Experimental Model for the Assembly and Testing System Shrink

Assembling and testing in order to achieve shrink, we designed a device that will achieve both a hub assembly by pressing an axial shaft and applying a torque shaft shrink resistance to demands in order to study the assembly. Device is based on four legs (*8*) arranged in a tapered pipe 2 inches to ensure stability throughout the whole which is fixed construction.

The lower frame (*7*) made of pipe with dimensions 100x60x6 mm and a support plate 20 mm thick welded over the frame itself is fitted with four removable legs. In this framework, welding and fastening elements for assembly directions shrink which must be applied torque. And at the same time are based on Crick's settlement with which the assembly will exert the necessary force.

Laying and fixing of the hub shaft shrink is done with the help with a support block (*11*) and demote screw clamps (*12*). Once seated and secured against rotation and motion through a lever, 6, which ends a pregnancy there will exert a torque shaft. Assembly, once positioned and fixed against rotation and motion through a washer (*14*) at the end there is a task which will exert a torque shaft.

Framework (*4*) is an intermediate unit that has the possibility to move vertically. It is built of 100x60x6 mm pipe, a disc diameter of 300 mm and 20 mm thick, two bracket fixing (*3*) and four screws (*2*) M22 which provides for raising hub in shrink. These clamps are secure and catching a larger diameter hub because we predicted two more threaded nuts on each side, allowing movement of the two clamps at a greater distance between them.

In the top of the device are no top frame (*1*), fixed, pipe made of 60x40x3 mm rectangular cross-section of the assurance role and parallel columns perpendicularly (*6*), a pipe 1 and ¼ inches.

The four columns are provided with Φ 16 sites with step 50 mm between them, a certain distance from the lower frame which ensures the positioning of the intermediate frame to frame at different heights and thus can lower shinrk several sizes of trees.

Fixing the convenient size of the intermediate frame columns is done with four bolts of the Φ 16.

For disassembly system shrink shaft-hub we proceed as follows: laying shrink system created in the block bearing arm (*11*). Clamp (*12*) fixed with screws to the body block bearings provide better reinforcement of the hub into place and avoid moving it. The key moment (*13*) is inserted along the shaft shrink in the two parallel sides milled. With a washer (*14*) and an M10 screw that is screwed along the longitudinal axis of the shaft to prevent slipping milled key moment in the shaft portion. In this way it made the whole hub-shaft fixing key moment in the disassembly.

Above the key point is "U" (*15*) which serves as mounting support for two-wheel-type belt. Small wheel, driven wheel (*16*) serves as a pulley wheel bigger role conductors (*17*). The latter is fixed to a steel cable that passes over the driven wheel, and lies at the end of a maximum weight of 13 kg (*19*). By rotating the lever (*21*) in clockwise or counterclockwise, weight (*19*) moves vertically upward. The sudden release lever provides a free fall until stop weight (*20*) hits the key moment. Thus, the weight acting on the time scales for exerting a torque shaft, disassembly necessary.

The proposed experimental realization and testing of assemblies is shown in Fig. 1 shrink.

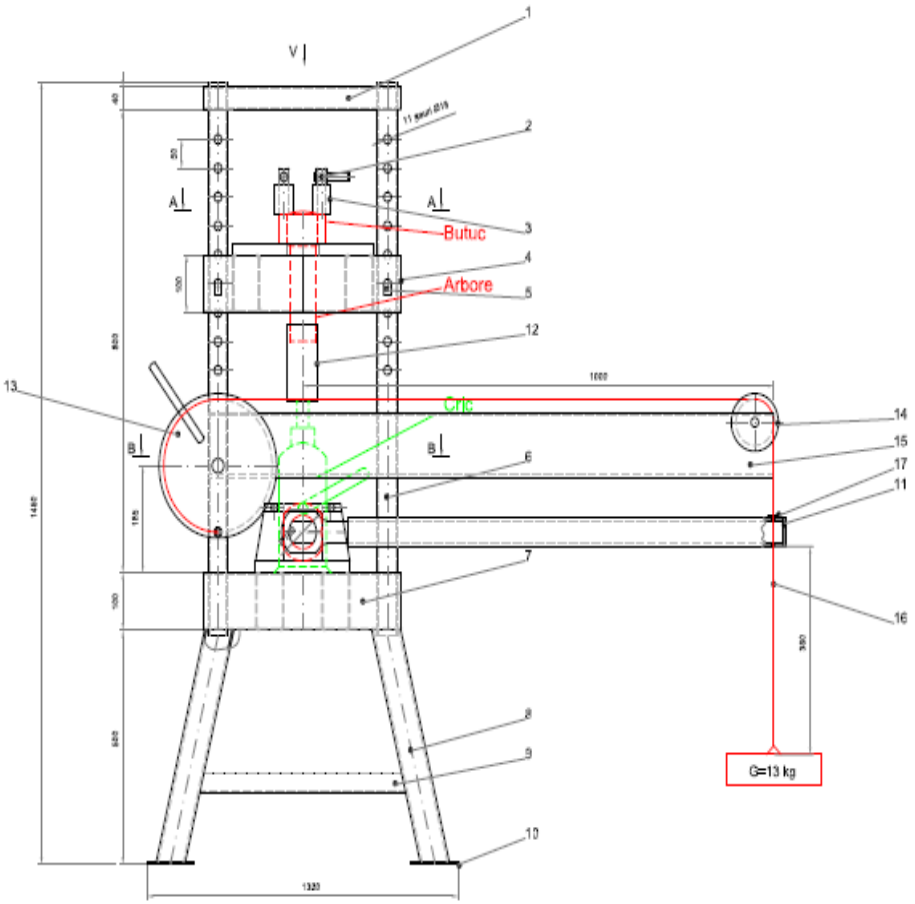

Fig. 1 – Stand assembly systems shrink: *1*-top frame, *2*-screw M22, *3*-bracket fixing, *4*-furniture frame, *5*-fixing bolt, *6*-column directions, *7*-lower frame, *8*-leg, *9*-contact, *10*-base, *11*-support block, *12*-bracket, *13*-key moment, *14*-washer, *15*-U profile, *16*-driven wheel, *17*-wire wheel, *18*-steel cable, *19*-weight, *20*-pawl, *21*-lever.

3. Experimental Results

Fig. 2 shows the parts ready for assembly by relieving the pieces being adjusted prior to tightening the tolerances of the type suitable mainly as a result of calculations made in the report II PhD, milled on two sides parallel (hub for mounting the assembly and the shaft and positioning key for determining the time at which ends there weight). Fig. 3 shows the assembly is performed by finite element method in Solidworks taken as a result of the application assembly torque.

Fig. 2 – Parts ready for assembly with shrink.

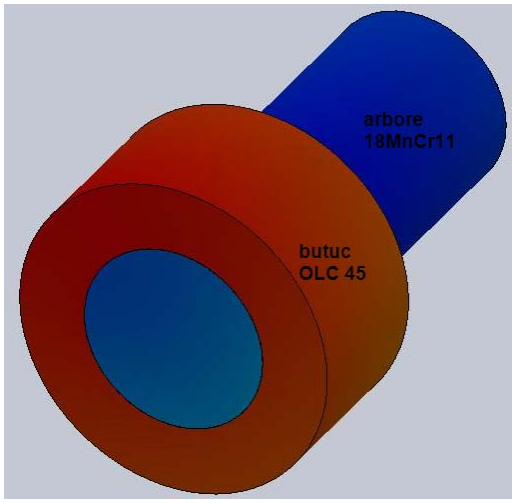

Fig. 3 – Assembling the finite element method over in Solidworks.

Submission during a time when assembly occurs as a result of the effort applied voltage. Note that the assembly area, near the junction of the two components are more intense because the tension by applying weight on the outer end of the shaft to be transmitted in the joint efforts, these are marked in red to green depending on the intensity of pistachio production them (color-scale is decreasing from red to blue).

In Figs. 4 and 5 shows a stress distribution in contact area during application assembly and a torque.

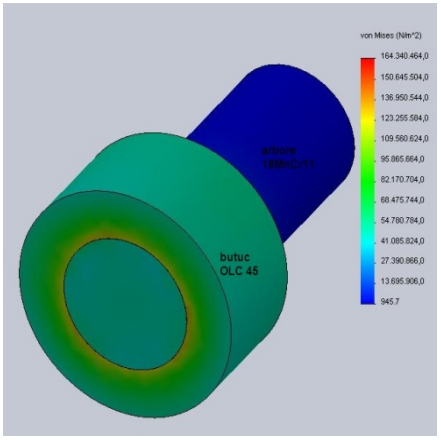

Fig. 4 – Assembly stress distribution.

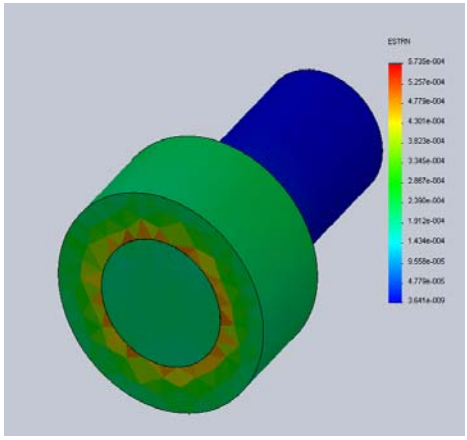

Fig. 5 – Torque stress distribution.

Observe the distribution of specific strains in tension due to the production assembly area and areas defined by the nodes of these formats.

The area marked in red represents the maximum effect of stresses and strains given set of nodes that achieves these areas, but decreasing intensity distributing these trips on larger areas (area defined by the distribution of yellow nodes) and going to the outside of the hub area (area defined The pistachio green nodes).

3. Conclusion

1. By design, the experimental model is more suitable size pieces.

2. Constructed so as to allow both assembly and disassembly in the same place, which gives a more effective solution.

3. Tension at the contact surface varies and is closely related to the torque produced in assembly.

4. Distribution after the application of torsion deformation is different in the contact area.

REFERENCES

[1] Budinski G.K., *Surface Engineering for Wear Resistance*. Prentice Hall, 1987.
[2] Comandar C., *Relaxation Gathering Force in Joints with Flanges and Bolts*. Publishing „Gh. Asachi" to Iasi, 2001.
[3] Creţu S., *Report II Doctorate, Experimental Model for Obtaining and Related Technologies Systems Assembled by Shrink with Increased Resistance Assembly to the Surface by Heating with Zinc Deposit.* September 2010.
[4] Sofonea G., Frăţilă M., *Resistant Materials*. Publishing University "Lucian Blaga" of Sibiu, 1998.
[5] Soporan V, Vermeşan H., *Considerations on Modeling the Processes Occurring in Surface Engineering, Chapter XVI, Appeared in the Volume of Advanced Surface Engineering Processes.* UTPRES Publishing of Cluj-Napoca 1998.

MODEL EXPERIMENTAL PENTRU REALIZAREA ŞI TESTAREA ASAMBLĂRILOR FRETATE

(Rezumat)

Lucrarea prezintă un model experimental de asamblare/dezasamblare a sistemelor fretate şi studiul asupra suprafeţei de fretare, rezultate obţinute prin prelucrarea cu element finit şi rezultate obtinute privind rezistenţa sistemelor fretate supuse unui moment de torsiune.

BULETINUL INSTITUTULUI POLITEHNIC DIN IAŞI
Publicat de
Universitatea Tehnică „Gheorghe Asachi" din Iaşi
Tomul LVII (LXI), Fasc. 4, 2011
Secţia
ŞTIINŢA ŞI INGINERIA MATERIALELOR

RESEARCH REGARDING THE STATIC BEHAVIOR OF LAYERS FROM STRUCTURE OF ROVING AND MAT COMPOSITE

BY

IOAN CURTU[1*], ANCA STANCIU[1], MARIANA DOMNICA STANCIU[1], ADRIANA SAVIN[2] and RAIMOND GRIMBERG[2]

[1] Transilvania University of Brasov,
[2] Nondestructive Testing Department,
National Institute of R&D for Technical Physics, Iasi

Received: April 14, 2011
Accepted for publication: June 27, 2011

Abstract. Composite materials are used in a variety of applications being appreciated for their superior properties. However, their use in aggressive environmental conditions, lead to damage and breakage of fibers, matrix fissure, damage of the bond between fiber and matrix. In this respect, the paper presents research on the values of the deformations and stresses of roving and mat composite layers, carried out by numerical methods (FEM) and experimental (TER). Between layers of composite samples were mounted resistive strain transducers (TER) since the fabrication of composites. The samples were subjected to bending, as measured the specific strains and determination of tension for each layer. Theoretical and experimental investigations revealed the static behavior of ROVING and MAT composite microstructure.

Key words: composite, specific strain, resistive strain transducer, FEM.

1. Introduction

Composite materials have a wide use in various applications: in the aviation industry, marine structures, transport, etc. One of the areas composite

* Corresponding author e-mail: curtui@unitbv.ro

materials can be used is represented by panels structures with some soundproofing characteristics, like acoustic barriers (Stanciu, 2010). Given the variety of static, dynamic, variable requests, aggressive environmental factors that the panels structures are subjected to, it is necessary to know the stress and strains, especially their size for each lamina (layer) of the composite structure (Cerbu, 2010; Motoc, 2010). Thus, the paper aims to present theoretical and experimental results on strains from the composite layers of Mat and Roving type composite, in case of static bending in four bearing points. Although the materials comprising the composite material can be isotropic, due to their layout, material can be, on average anisotropic. Materials that are operating in practice may be homogeneous or inhomogeneous. Internal stress and strain field, at the microscopic level, is locally influenced by the relative difference between the local properties of structural elements (matrix and reinforcement elements), their size, shape and relative orientation, and the geometry of the reinforcing elements (Curtu, 2009).

2. Materials and Method of Investigation

During the research, the composite materials performed by MAT and Roving materials, both in layered structures of each type of material and in laminated composite structures of both materials were analyzed. In this way, MAT type is the most commonly used form of reinforcement material, consisting of a layer of fibers with lengths ranging between 3.2 and 50 mm randomly oriented. The fibers are bound fibers together by an epoxy resin binder type (Fig. 1). The ROVING type consists of a collection of parallel fibers or filaments, bundled without an intentional twisting fabric type (Fig. 1). It is used to reinforce those structures where high strength is desired in the direction of fibers.

Table 1
Characteristics of the Samples

Type of samples, material	Code	Width mm	Thickness mm	Area mm^2
RT samples 800 in the warp, 4 layers	E U1	9,8	4,3	42,14
	E U2	9	4,3	38,7
	E U3	9	4,4	39,6
	E U4	10	4,4	44
	E U5	9,3	4,3	39,99
RT samples 800 in the woof, 4 layers	E B1	9,8	4,5	44,1
	E B2	9	4,4	40,92
	E B3	9	4,5	45
	E B4	10	4,3	42,57
	E B5	9,3	4,3	43

Continuation Table 1

Type of samples, material	Code	Width mm	Thickness mm	Area mm^2
MAT450-RT800 samples in the warp - MAT600, 8 layers	E 1	10	7	70
	E 2	9,5	7,2	68,4
	E 3	9,3	7,6	70,68
	E 4	9	7,1	63,9
	E 5	9,5	7,2	68,4
MAT samples 450, 4 layers	E M1	9	4	43,1
	E M2	9,4	4,1	44,92
	E M3	9	3,9	41
	E M4	9,2	4,1	42,57
	E M 5	9.6	4.2	43

- RT 800 in the warp-glass fiber composite material in epoxy resin matrix 4x with specific mass of 4x 800 g/m^2, 3.2 to 3.6 mm thickness.
- RT 800 woof-fiberglass composite material (fabric) in epoxy resin matrix, with 4x specific mass of 800 g/m^2, 3.2 to 3.6 mm thickness.
- MAT 450 - fiberglass composite material (short FIBERS) in epoxy resin matrix, having a specific mass of 4x450 g/m^2, 1,6 to 2 mm thickness.

Fiberglass - short fibres (MAT)

Roving fabric

Fig. 1 – The structure of studied composites.

The investigations were based on two methods: both the theoretical one using the finite element method (FEM) by applying the program MSC Nastran, and the experimental one, with the help of the Spider 8 device, which determine the specific strains of the layers of material through resistive electric transducer (TER), the samples being subjected to four point bending. Applied load was 600 N for specimens made of four layers, while for MAT-Roving composite material of eight layers, the sample was tested at a force of 1000 N. To determine the strains with the help of tensometry method, among the layers samples it were pasted TER from the manufacture, as shown in Fig. 2.

To capture the measured signal, it was necessary to apply the connection scheme, in order to achieve half of the bridge. The samples were subjected to four points bending. The signal was captured from electrotensometric resistive transducers with electronic measuring system Spider 8, set for half-bridge connection and device HBM Kompensator MK

Hottinger Baldwin Messtehnic. In Fig. 3 there are presented stages of testing, measurement and data processing.

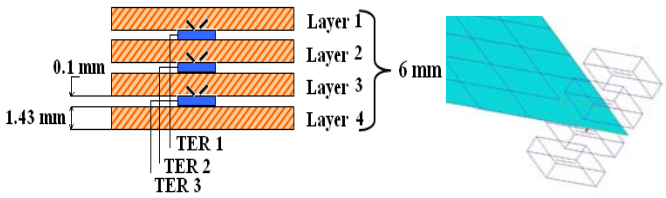

Fig. 2 – Representing a sample with TER among layers.

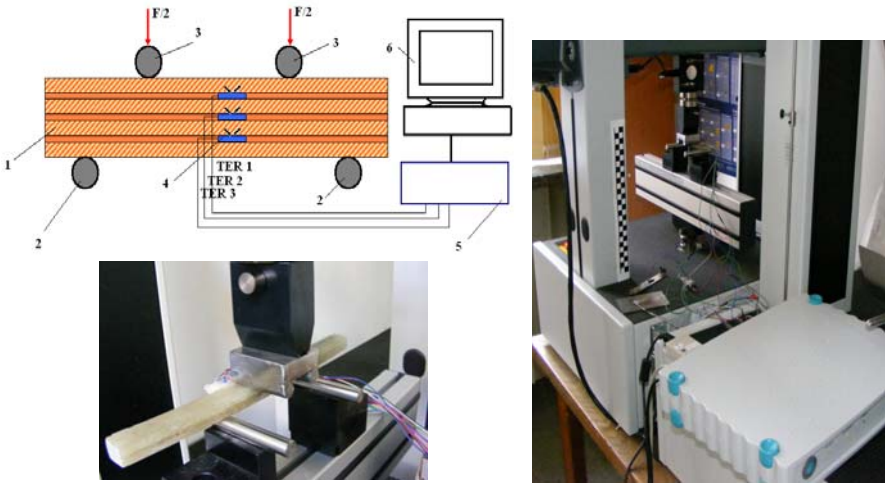

Fig. 3 – Test and Measurement Equipment (*1* - sample, *2* - bearing, *3* - point of force application, *4* - electrotensometrice resistive transducers, *5* - signal acquisition device, *6* - data processing unit).

After bending tests, we determined the variation of specific strains of the layers of the samples. In Table 2, there are summarized the average values of maximum specific strains for the samples tested obtained experimentally.

Table 2

The Strains Values Through Experimental Method

	RT 800 U	RT 800 B	Mat 450	Mat-Rov U 8 layers	Mat-Rov B 8 layers
TER 1	0.02565	0.01744	0.03355	0.01719	0.01953
TER 2	0.00235	0.00255	-0.00058	0.00902	0.01220
TER 3	-0.02336	-0.01616	-0.03318	0.00394	0.00615
TER 4				-0.00117	-0.00186
TER 5				-0.00470	-0.01107
TER 6				-0.00922	-0.01372
TER 7				-0.01512	-0.01816

The data acquired in the form of graphs of variation of strains of each layer, with respect to time of application, are presented in Fig. 4. Analyzing the behavior of the layer from the sample structure, it was found that the values of the strains are approximately symmetrical to the neutral axis, the layers being stressed to tension and compression.

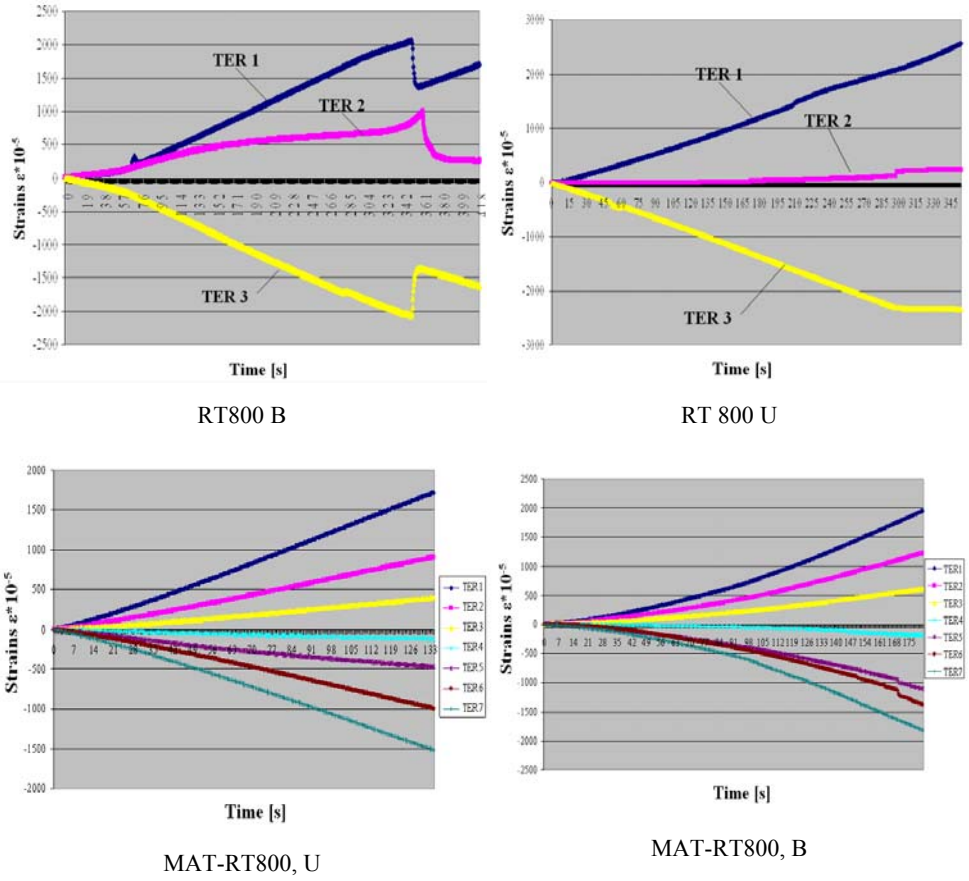

Fig. 4 – Variation of strains for each type of material tested.

Comparing the values of the strains of the outer layers (face contact with layer 2, Fig. 2) of the most requested composite samples with different composite structures (Fig. 5), it's revealed that the highest strains are obtained in the case of MAT 450 material type, with four layers, and the lowest strains are obtained in the case of eight layers composites, obtained by combining the MAT 450a with ROV 800.

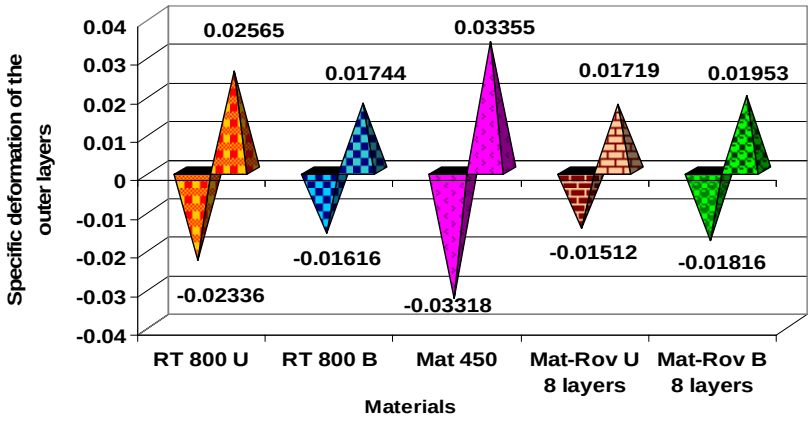

Fig. 5 – The strains determined in the outer layers.

In the final phase of the composite bearing capacity loss, destruction of the composite is achieved through: large delamination among layers, destroying large areas of the matrix, flaming fiber local in comprised areas, phenomena that may occur simultaneously or sequentially (Fig. 6).

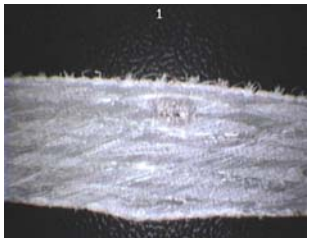

U3 RT 800 sample increased 5 times with camera

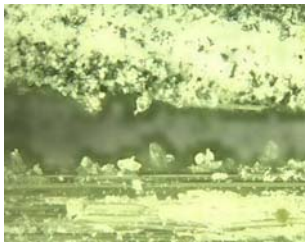

RT 800 sample U3 microscope magnified 500 times, 2D

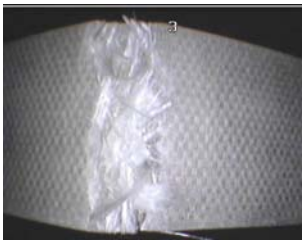

Sample 8 bending requested, 5 times larger with video camera

Fig. 6 –Images captured with a 2D camera and microscope during the failure of samples.

Since experimental measurements involve consumption of materials, TER, workmanship, in the study it was followed the possibility of using finite element method in determining the stresses and strains at the microstructural level, so that future studies should focus on several simulations.

Thus, shaped layers of material and strain gauge, each layer being characterized by specific properties of constituent materials, there were established the shape and type of stress, as shown in Fig. 7. Material properties (elasticity, Poisson's coefficient, density, etc.) were experimentally determined according to European standards.

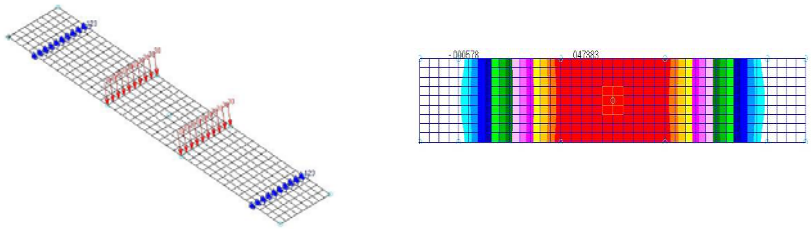

Fig. 7 – Stages of the FEM modeling of composite samples.

After running the program NASTRAN, FEM results were compared with experimental ones. It was found that the experimentally determined specific strains have higher values than those calculated by FEM (Fig. 8). To obtain experimental data with calculations based on FEM, these are amplified by a factor of 1.21....1.45. Minimum values of the coefficient refer to composites with several layers: 6, 8, 10, and maximum values in composites with fewer layers: 3.4, 5.

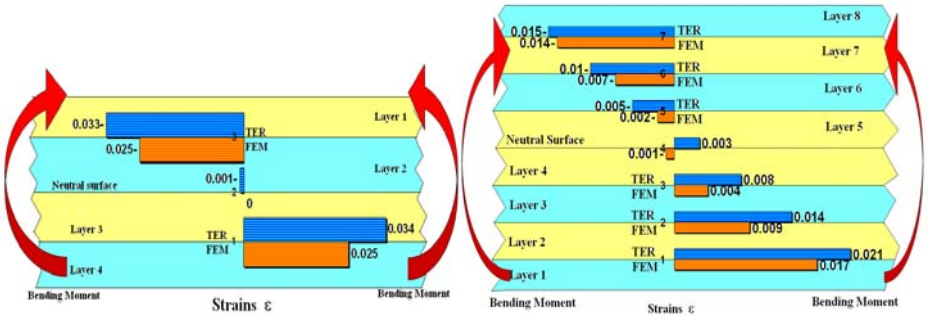

Mat 50 Mat - Roving

Fig. 8 – Specific deformation diagram obtained by FEM and TER.

3. Conclusion

The study presented in this paper contributes to knowledge of the properties of composite MAT 450 type, 800 Roving and combinations of these materials and to characterize the macroscopic behavior of composites, mechanical phenomena developed among the layers of materials. Analysis of strain gauge results makes a contribution in addition to experimental tests and finite element contributing to the validation of experimental research. So numerical calculations performed with FEM, amplified by a factor equal to 1.21 to 1.45, lead to values comparable with real ones. The originality of the research consisted in measuring the specific strains among the layers.

Acknowledgments. This paper is supported by the Sectoral Operational Programme Human Resources Development (SOP HRD), financed from the European

Social Fund and by the Romanian Government under the contract number POSDRU POSTDOC-DD, ID59323.

Some of the studies presented in the paper were the research subject of the PhD thesis: Contribution to the Mechanical Properties Determinations for the MAT - Roving Composite Materials used at Cylindrical containers, made by Anca Stanciu Eng.

REFERENCES

*** SR EN ISO 14125, *Compozite de materiale-plastice armate cu fibre. Determinarea proprietăţilor de încovoiere*, 2000.

Cerbu C., Curtu I., Ciofoaia V., Rosca I.C., Hanganu L.C., *Effects of the Wood Species on the Mechanical Characteristics in Case of Some E-Glass Fibres/Wood Flour/Polyester Composite Materials.* Rev. Materiale Plastice, MPLAAM, **47**, *1*, Bucuresti, Romania, 109-114 (2010).

Curtu, I., Luca Motoc, D., *Micromecanica materialelor composite*. Ed. Universităţii Transilvania, Braşov, 2009.

Motoc Luca, D., Curtu I., *A Micromechanical Based Approach for Dynamical Properties Evaluation in Case of Polymeric Composite Materials*. Proceedings of the 7th International Conference of DAAAM Baltic Industrial Engineering, Tallin Estonia, 423-428, 22-24 aprilie 2010.

Stanciu M., Timar J., Curtu I., Rosca I.C., *Evaluation of Acoustics Properties of Composite Materials with Potential Application in the sound Barriers Structures*. Proceedings–Advanced Transport Systems and Road Traffic of the 11th International Congress on Automotive and Transport Engineering CONAT, **IV**, 91 – 96 (2010).

CERCETĂRI PRIVIND COMPORTAREA STATICĂ A STRATURILOR COMPOZITELOR DE TIP ROVING ŞI MAT

(Rezumat)

Materialele compozite sunt utilizate pentru o serie de aplicaţii fiind apreciate pentru proprietăţile lor. Cu toate acestea, utilizarea lor în condiţii agresive de mediu, duce la distrugerea şi ruperea fibrelor, microfisurarea matricei, distrugerea legăturii dintre fibră şi matrice. În acest sens, lucrarea prezintă cercetările privind mărimea deformaţiilor şi tensiunilor dintre straturile compozitelor de tip ROVING şi MAT, realizate prin metode numerice (FEM) şi experimentale (TER). Între staturile epruvetelor din material compozit au fost montate traductoare electrotensometrice rezistive (TER) încă din procesul de fabricaţie al compozitelor. Epruvetele au fost supuse la încovoiere în patru puncte, fiind măsurate deformaţiile specifice şi determinarea tensiunilor pentru fiecare strat. Investigaţiile teoretice şi experimentale au permis stabilirea comportării statice a microstructurii compozitelor de tip ROVING şi MAT.

BULETINUL INSTITUTULUI POLITEHNIC DIN IAŞI
Publicat de
Universitatea Tehnică „Gheorghe Asachi" din Iaşi
Tomul LVII (LXI), Fasc. 4, 2011
Secţia
ŞTIINŢA ŞI INGINERIA MATERIALELOR

IMPEDANCE APPROACHES TO MOTOR OILS

BY

PEEV IV. DARIN*

University of Ruse, Bulgaria

Received: April 14, 2011
Accepted for publication: June 27, 2011

Abstract. In this paper are investigated variety of concepts and methods for impedance characterization of motor oils. Their abilities to estimate the lubricant properties and to detect chemical composition changes are analyzed. The general impedance methods and complex electrochemical impedance spectroscopy (EIS) techniques are discussed. A detail survey of Differential Impedance Analysis (DIA) is conducted. The virtues and the disadvantages of these concepts are listed.

Key words: Differential Impedance Analysis, Motor Oil, Quality Control

1. Introduction

One of the important machine maintenance tasks is the determination of the accurate oil change intervals. Using oil beyond its effective useful life can lead to an excessive friction and machine wear. Also the effect of the increased heat and decreased performance can cause component failure and therefore to high cost losses. On the other hand too frequent oil changes result to extra expenses, inappropriate material consumption and eventually to environmental changes.

Normally the mileage criterion is used to determine the oil change interval. But this criterion is often hard to formulate objectively because of the

* Corresponding author e-mail: dpeev@uni-ruse.bg

various factors such as work conditions, machine health, outside environment etc. Also the unforeseen conditions can dramatically reduce the oil life. A fuel dilution, water or coolant contamination, high temperatures and revolutions would make the oil unusable far before the mileage criterion is fulfilled.

One possible solution is the utilization of the known laboratory oil tests. The used oil samples are examined and the standard characteristics such as total acid/base number, viscosity and amount of oxidation products indicate the condition of the lubricant. But these methods normally require at least twenty-four hour time and are very resource consuming. For this reason the systems for fast oil condition estimation find a wide application.

The paper is dedicated to the comparison of the different electrical impedance methods and particularly to a Differential Impedance Analysis (Vladikova, 2004) of motor oils.

2. Results and Discussion

2.1. Capacitive and Resistive Conductance Method

Usually the electrical characteristics of the oil are extracted measuring the complex Impedance of an electrochemical cell. Between the two parallel electrodes of the cell is the lubricant which acts as a dielectric medium. Therefore the impedance typically has a resistance-capacitive character and generally can be expressed by an equivalent circuit composed of a parallel combination of capacitance Ceff and resistance Reff (Fig.1). Several versions of the method are based on the relative permittivity. As the relative dielectric constant of water is around $\varepsilon_r^{water} = 81$ and more than decade bigger than the constant of the fresh motor oil $\varepsilon_r^{fresh\cdot oil} \leq 4.5$, the presence of water can be easily detected. The ethylene glycol which is widely used as automotive antifreeze has $\varepsilon_r^{glycol} = 37$ and also strongly affects the relative permittivity of the oil.

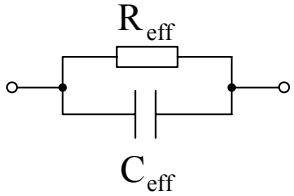

Fig. 1 – Equivalent circuit.

Some systems use an empirical dependency of dielectric constant from the driving distance (Kim). After certain threshold value is exceeded an alarm for oil change is turned on. The change of this parameter is not more then 10% at the whole driving range so the precision is controversial.

The resistive part of the impedance is highly affected by the soot and metal particles percentage and could partake in the analysis.

Other method is to measure the quality factor (Q-factor) or loss tangent $tg\delta$ (Dikarev, 1997). It is found that the loss tangent increases depending on the presence of mechanical impurities as is shown on the Fig 3. The curves 1 to 4 indicate the purification through a filter with an increasing density (Dikarev, 1997).

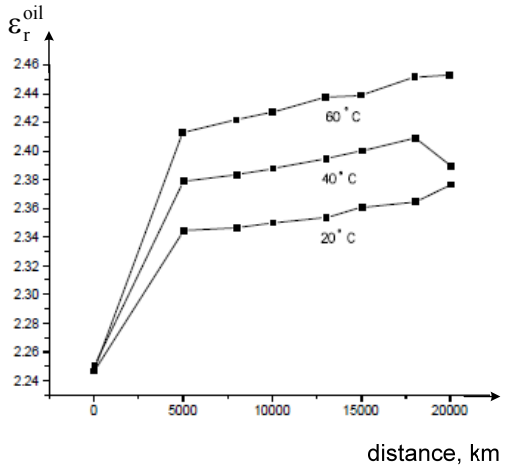

Fig. 2 – Dependency of the dielectric constant from the driving distance.

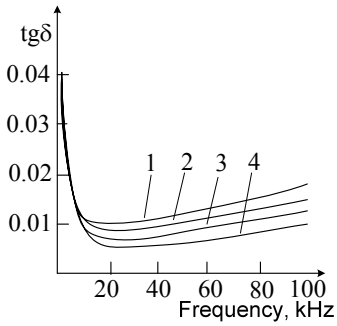

Fig. 3 – Loss tangent dependence on the presence of mechanical impurities.

In this method no frequency dependence is considered and it relies only on four values – Ceff and Reff of fresh and drain oil.

2.2. Applying Electrochemical Impedance Spectrometry (EIS)

That is the second stage of the oil analysis systems. According to the method one or more hypothetical equivalent models are determined and after model validation one of them is chosen. Another way is to build the model knowing some information about the electrochemical nature of the oil-electrode system. Two possible models are shown on the Figs. 4, 5. In the first the R_1 and

R_2 represent the charge transfer resistance at the two electrodes, while the C_{d1} and C_{d2} characterize the double layer capacitance at the electrodes (http// www.patentstorm.us). The R_{bulk} is the bulk layer resistance of the lubricant. The C_p is a physical capacitance of the sensor.

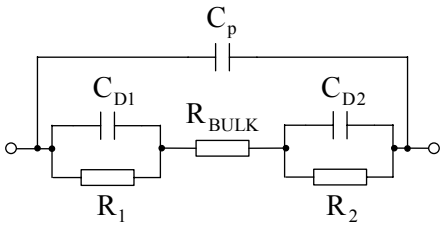

Fig. 4 – Equivalent model.

If the frequency range is extended – 1mHz to 10MHz and the measurement is very precise the second model could be used (Fig. 5).

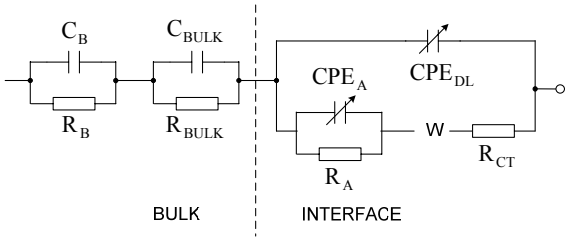

Fig. 5 – Extended equivalent model.

It was developed by M. Smiechowski (2005) and takes into account the relaxations of surfactant micelles in the solution, the double layer on the electrode, charge transfer, materials adsorbing on the electrode surface and impedance associated with diffusion. In the quoted study is analyzed the value of the R_{BULK} depending on the TAN (total acid number) and TBN (total base number) values of the certain oil. In such a way it could be developed a tabular register consisted of combinations of values of the equivalent model and the known exploitation characteristics of the certain oil brand (such as viscosity).

As the equivalent models have several groups of components each of them could serve as a recognition element for the oil condition analysis. Because of the frequency dependence estimation of the system response is considered more promising results can be expected in this method.

2.3. Differential Impedance Analysis

The DIA analysis as opposed to EIS does not require an initial working hypothesis and the information about the object is extracted from the experimental data (Vladikova, 2004). The DIA applies the algorithm of the scanning local analysis. The used local estimator, called Local Operating Model

(LOM) is shown on Fig. 6. The effective time constant T = RC is also regarded as a LOM's parameter (Vladikova, 2004). The characterization of the oil is based on the temporal or spectral analysis of the effective time-constant $\tau = \lg T = F\left(\lg T_f\right)$, where T_f is the period of the stimulus signal.

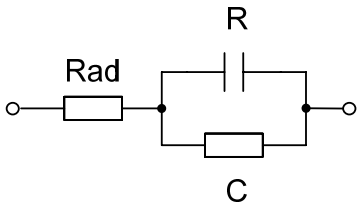

Fig. 6 – Local operating model.

The method doesn't rely on any equivalent circuit model or hypothesis about the oil degradation mechanisms. The mathematical model or algorithm of this technique is given on the Fig. 7. It involves the components of complex impedance as a function of frequency, calculation the effective time-constant, converting the analysis to a spectral form, extracting the basic parameters of the specter as initial values for the further analysis (m, s, h values – peaks, combs etc.), calculating the *quality factor* of the used oil toward to a fresh oil, categorize the used oil sample into one of the n-quality categories. The oil's quality is estimated in respect to its lubricating ability. As the main purpose of the oil is to reduce the wear of the friction surfaces the DIA method estimates the real exploitation characteristics of the oil.

The impedance of the LOM can be presented by:

$$Z_{LOM}(j\omega) = R_{ad} + \frac{R}{1+\omega^2 T^2} - j\frac{\omega RT}{1+\omega^2 T^2} \tag{1}$$

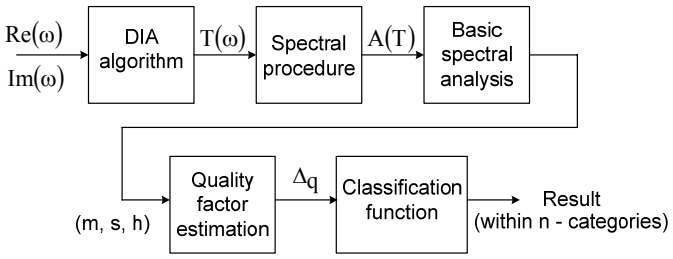

Fig. 7 – Mathematical model.

The calculation of the effective time-constant for specific frequency is based on (Vladikova, 2004):

$$T(\omega) = dL_{eff}(\omega)/dR_e(\omega) \tag{2}$$

where L_{eff} is the effective inductance, R_e - the real part of the impedance.

As the $T(\omega)$ can vary within several decades the form $\tau(\omega) = \lg T(\omega)$ is more appropriate.

The conversion the analysis from temporal to spectral representation the scope of values for $\tau(\omega)$ is separated into k-equal intervals $\Delta\tau$. For the first, second and n-th interval the $\tau(\omega)$ corresponds to the following conditions:

$$\begin{aligned} &\tau_{min} < \tau_i < \tau_{min} + \Delta\tau \\ &\tau_{min} + \Delta\tau < \tau_i < \tau_{min} + 2\Delta\tau \\ &\tau_{min} + (n-1)\Delta\tau < \tau_i < \tau_{min} + n\Delta\tau \end{aligned} \tag{3}$$

The amplitude for the i-th interval is:

$$A_i(\tau) = \text{const}.K_\tau^i \tag{4}$$

where K_τ^i is the number of time-constant values which belong to the i-th interval.

The values $A_1(\tau)$, $A_2(\tau)$ … , $A_k(\tau)$ at the Y-axis and the values τ_i at the X-axis form a spectral histogram. The artificially extension of the experimental points can be achieved through a *cubic splines* interpolation (http://www.physics.utah.edu). This interpolation is a piecewise continuous curve, passing through a set of m control points. That makes m-1 intervals between them. The curve satisfy the table of control points $[x_i, y_i]$, for the $i = 1,...,m$. There is a separate cubic polynomial for each interval, each with its own coefficients:

$$\begin{aligned} &S_i(x) = a_i(x - x_i)^3 + b_i(x - x_i)^2 + c_i(x - x_i) + d_i \\ &\text{for} \quad x \in [x_i, x_{i+1}] \end{aligned} \tag{5}$$

Among the parameters that define the spline $S(x)$ are some conditions that depend on the user's choice. If the curves are so called "natural" splines then the conditions are:

$$S_1''(x_1) = 0, \quad S_{m-1}''(x_m) = 0 \tag{6}$$

where x_1 and x_m are the two endmost points; S_1'' and S_{m-1}'' are the second derivatives at the first and the last interval.

The artificially created points could be chosen on each spline at regular intervals between the control points (Fig.8).

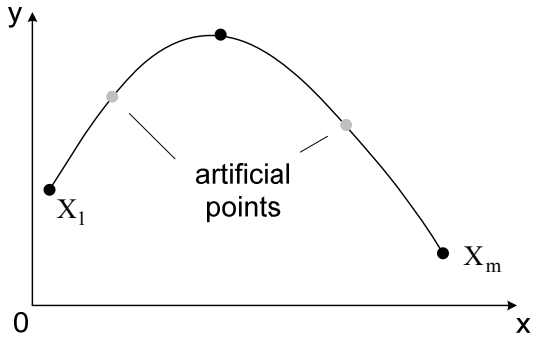

Fig. 8 – Artificially created points on the splines.

The extended number of experimental points improves the density of the histogram both at the amplitude and the time-constant axis (Vladikova, 2004).

3. Conclusion

The capacitive and resistive conductance method has simplicity and the connection between the condition of the oil and the system output is straightforward. As the oil covers more mileage the dielectric permittivity increases and this indicates the oil deterioration. The results are unreliable. The method provides information only in a qualitative manner.

Applying Electrochemical Impedance Spectrometry could lead to more promising results as it extracts maximum impedance information of the lubricant. The equivalent models have several groups of components and using additional measurements of certain exploitation characteristic empirical connections could be found. The result of the analysis has a quantitative significance.

The Differential Impedance Analysis has higher information potential, it does not require an initial working hypothesis and the information about the model's structure is extracted from the experimental data. As the method offers structural identification the more objective results are achievable. It could estimate the oil's quality directly from the lubricating characteristic. This ensures the knowledge of the oil's lubricating ability which is significant for exploitation.

Acknowledgements. The study was supported by contract № BG051PO001-3.3.04/28, "Support for the Scientific Staff Development in the Field of Engineering

Research and Innovation". The project is funded with support from the Operational Programme "Human Resources Development" 2007-2013, financed by the European Social Fund of the European Union.

REFERENCES

*** http://www.physics.utah.edu/~detar/phys6720/handouts/cubic_spline/cubic_spline/node1.html, *Cubic Spline Interpolation*.

*** http://www.patentstorm.us/*On-line Oil Condition Sensor System for Rotating and Reciprocating Machinery*. Patient number: US 7 043 402 B2.

Dikarev B., *Conduction Currents and Dielectric Properties of Engine Oils*. Seoul, Korea, 1997.

Kim W., *Development of a Coil-Typed Oil Senor System for the Automobile Engine Oil on the Dielectric Constant*.Chungnam, Korea.

Smiechowski M., *Electrochemical Characterization of Lubricants for Microfabricated Sensor Applications*. PhD Thesis, Department of Chemical Eng., Case Western Reserve University, 2005.

Vladikova D., *The Technique of the Differential Impedance Analysis*. part 1-2, Proceedings of the International Workshop "Advanced Techniques for Energy Sources Investigation and Testing", Sofia, Bulgaria, 2004.

ABORDAREA PRIN METODA IMPEDANŢEI A ULEIURILOR DE MOTOR

(Rezumat)

În această lucrare sunt studiate diferite concepte şi metode pentru caracterizarea prin impedanţă a uleiurilor de motor. Sunt analizate capacitatea acestora de estimare a proprietăţilor lubrifiante şi de detectare a compoziţiei chimice. Sunt discutate tehnicile generale cu metode de impedanţă şi spectroscopia de impedanţă electrochimică complexă (EIS). S-a realizat o observare detaliată a Analizei cu Impedanţă Diferenţială (DIA). Sunt prezentate avantajele şi dezavantajele acestor concepte.

BULETINUL INSTITUTULUI POLITEHNIC DIN IAŞI
Publicat de
Universitatea Tehnică „Gheorghe Asachi" din Iaşi
Tomul LVII (LXI), Fasc. 4, 2011
Secţia
ŞTIINŢA ŞI INGINERIA MATERIALELOR

CONSIDERATIONS REGARDING EQUAL CHANNEL ANGULAR EXTRUSION PROCESS OF MAGNESIUM ALLOYS

BY

FLORINA-DIANA DUMITRU[*1], BRÂNDUŞA GHIBAN[1], NICOLAE GHIBAN[1], GHEORGHE GURĂU[2] and MIHAI MARIN[1]

[1] Politehnica University from Bucharest,
Faculty of Materials Science and Engineering
[2]Dunărea de Jos University of Galaţi,
Faculty of Metallurgy, Material Science and Environment

Received: April 14, 2011
Accepted for publication: June 27, 2011

Abstract. In recent years, an ever-expanding volume of research has been conducted on studying the effects of equal channel angular extrusion processing. Equal channel angular extrusion (ECAE) is one of the severe plastic deformations (SPD) methods that improves the mechanical properties of the processed materials because of the ultrafine grained structures resulted. ECAE produces significant deformation strain without reducing the cross sectional area.

This paper takes into account different articles in order to explain both the mechanism of ECAE and how this SPD method influences the properties of magnesium alloys. The ECAE experiments have confirmed that this tehnique may be used to attain improved mechanical properties, like high superplastic elongations, high yield strength, large tensile elongation and a low mechanical anisotrop.

Key words: severe plastic deformation method, equal channel angular extrusion, processing techniques, magnesium alloys.

[*] Corresponding author e-mail: dianadumitru1986@yahoo.com

1. Introduction

Since the concept of nanocrystalline materials (ultrafine grained materials with a grain size under 100 nm) was presented in 1989 by Herbert Gleiter, these materials have known a rapid development because of its technological and scientific importance (Mueller & Mueller, 2007). The ultrafine grained materials can be obtained through a variety of methods, but in recent years, severe plastic deformation (SPD) techniques have been the focus of intense research (Segal, 2008; Wu *et al*., 2006), because they can produce metallic materials which have grain sizes ranging from 50 to 500 nm (Valiev *et al*., 2000; Ferrasse *et al*., 2008) and thus enhancing material properties such as improved tensile strength, hardness, toughness, fatigue life, and the optical and electrical related properties (Tham *et al*., 2007). The interest in grain-size reduction is driven by the possibility to produce ultrahigh strength metals and high strain rate superplasticity.

Due to the SPD methods a number of difficulties connected with residual porosity in compacted samples, processing of large scale billets, impurities from ball milling, and practical application of the given materials were overcome (Dumitru *et al*., 2010). The SPD methods developed and used are: accumulative roll bonding (Saito *et al*., 1999; Saito *et al*., 1998), severe torsion straining under high pressure (Valiev *et al*., 1993; Mishin *et al*., 1996), repetitive corrugation and straightening (Lowe & Valiev, 2004), multiple forging (Imayev *et al*., 1992; Salishchev *et al*., 1993), twist extrusion (Beygelzimer, Orlov and Varyukhin, 2002; Beygelzimer, Varyukhin, Orlov, Efros, Stolyarov and Salimgareyev 2002), and equal channel angular pressing or extrusion (Segal, 1995, 1999).

Presently, among the methods of SPD, equal channel angular extrusion (ECAE) is considered as the most promising for industrial applications.

Equal channel angular extrusion (ECAE) developed by Segal, in 1974 (Segal *et al*., 1981; Segal, 1974) is widely known as one of the techniques to impose severe plastic deformation on bulk materials to produce ultra-fine grained materials, without causing a significant change in the dimensions of the processed parts. In this regard, the ECAE process is similar to torsion, which was also used for the study of strain hardening and hot working. Also, some researchers noted a similarity between the geometry of the ECAE process and metal cutting (Agnew *et al*., 2005).

It has been suggested that this technology has great advantages over the conventional mechanical attrition of ball milling because it can produce large sized samples free of any residual porosity.

The aim of the process is to impart high deformation to the processed materials as they cross the channel. Until now four types of approaches have been proposed to describe the deformation field during the ECAE process: the

simple shear model (Segal, 1995) and applies at the intersection plane of the two channels, the second type calls for the experimental flow lines from which the deformation gradient is calculated, and then the strain field is obtained in a completely experimental way (Gholinia *et al*., 2002), the fan model, proposed by Beyerlein and Tome (2004), where the plastic zone has a fan-like form and the flow lines are circular within the fan and the last model approaches the whole flow line with a relatively simple analytic function from which the velocity field and all components of the strain rate tensor can be readily obtained (Tóth *et al*., 2004).

The process also leads to the formation of strong crystallographic texture in the material.

During the ECAE process, it can be observed a significant strain hardening (together with the grain refinement) resulting in remarkable enhancement of strength in many engineering materials (Richert *et al*., 2003; Segal, 2003; Stolyarov & Lapovok, 2004; Vinogradov *et al*., 1999).

2. Mechanism of ECAE

Equal channel angular extrusion (ECAE) is a deformation technique resulting in a large grain refinement through severe plastic deformation (Eivani, Karimi Taher, 2008). During ECAE processing the material is subjected to an intense plastic straining through simple shear without any corresponding change in the cross-sectional dimension of the sample (Eivani, Karimi Taheri, 2008). Simple shear can be considered a near ideal deformation method for structure refinement and texture formation in metal working.

Large and uniform strain intensity per pass can be reached in material under low pressure and load without a reduction of the initial billet cross-section. The process can be repeated a number of times in the die because the billet cross-section remains constant (Tham *et al*., 2007).

In ECAE process, a metal billet is pressed through a die having two channels of equal cross-section intersecting at an internal angle, Φ (Kim J.K. & Kim W.J., 2006; Zhao *et al*., 2009), which is usually between 60º and 160º (Liu *et al*., 1998; Furuno *et al*., 2004). Another important feature of the die is the existence of an additional angle Ψ that defines the arc of curvature at the outer point of intersection of the two channels (Spuskanyuk *et al*., 2008), as showed in Fig. 1.

The billet undergoes simple shear deformation when it is pressed through the intersecting corner. High plastic deformations lead to an improvement in the dislocations density in ductile crystalline materials and this improvement of the dislocation density is followed by an increase in the strength. Hence with enough accumulation of plastic strain a new structure of submicrometer or even nanometer grain size replaces the former grain size (Sevillano *et al*., 1980).

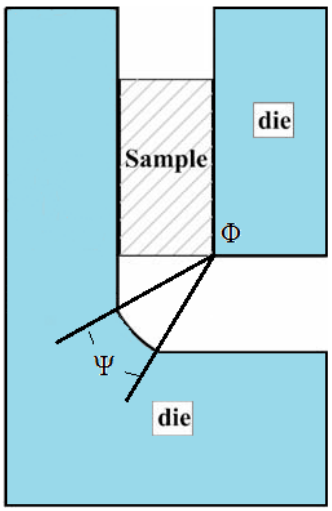

Fig. 1 – Front view of an ECAE die.

Because the channels of the die are of equal cross section, the cross-sectional shape of the specimen does not change during the process. This enables the process to be repeated several times, with each run called a pass. There are several possible sequences of passes, or routes, which differ on the re-orientation of the specimen's shear plane relative to the die's shear plane (Sivakumar & Ortiz, 2004).

During ECAE, the processing route is one parameter which can effectively change the strain path of the deformation. A nornenclature has evolved in the literature referring to the major variants as Route A - meaning no rotations between passes, Route B_A - meaning 90º back-and-forth rotations, Route B_C – meaning 90º continuous rotations and Route C meaning 180º rotations (Iwahashi *et al*., 1998; Aour *et al*., 2009).

The amount of plastic strain introduced in the materials after ECAE processing depends on the die angle and the number of passes.

The exit channel of the die is usually manufactured with the same diameter as the entrance channel and hence cross-section of the processed material is not modified and so, there is no geometrical limitation to the deformations that is possible to impart to the processed materials (Luis *et al*., 2005).

The ECAE die is manufactured with two channels that usually intersect at an angle with the same cross-section. The material is extruded through the die and it is mainly deformed by a shear mechanism combined with a high pressure, which exists within the die channels (Ghiban *et al*., 2010).

3. ECAE Process of Magnesium Alloys

Due to their high specific properties (superior specific stiffness and strength over many structural materials (Stalmann *et al*., 2001; Kainer, 2003), magnesium alloys are being viewed as the future materials for automobile, aerospace and electronics industries. However, their application potential is impeded by poor formability and limited ductility at room temperature, which is attributed to the hexagonal crystal structure and consequent non-availability of adequate numbers of independent slip systems (Patridge, 1967).

Grain refinement is an important practice to magnesium alloys because it improves their mechanical properties. Through ECAE process, ultrafine grain magnesium alloys with grain sizes of 0.5–5 μm have been obtained.

A parameter that can change the strain path of the deformation is the processing route. For magnesium alloys, processing route is more effective due to their intensive anisotropy. Different routes would result in an evident difference of grain orientations corresponding to the shear direction in each extrusion (Wu *et al.,* 2010).

There exists the continuity of the accumulated deformation in ECAE. For all the 4 routes, the strain rises straightly. Route B_C has the greatest increasing rate of strain, and its effective strain can reach the value of 3.8 by 5 passes. There exists different tendency of strain uniformity in multi-pass extrusion, the effective strains of Route A, Route B_C and Route B_A become more homogeneous with the increase of extrusion pass, but that of the Route C becomes worse (Zhang *et al*., 2008).

Several authors have described the microstructure evolution and mechanical properties of ECAE magnesium alloys (Jin *et al*., 2005; Yoshida *et al.,* 2003). The processing temperature is an important factor that affects the microstructure and mechanical properties of the AZ31 magnesium alloy by ECAE. At a processing temperature to 453 K, ultrafine grain of 0.5 μm were obtained, and both the ductility and strength of the alloy were improved significantly after the processing, which can be explained by grain refinement as well as incomplete dynamic recovery and recrystallization during the processing (Jin *et al*., 2005).

Mukai *et al.* have reported a potentially positive impact on the mechanical behavior of magnesium alloys, managing to develop a unique texture using ECAE processing (Mukai *et al*., 2001), and obtained a two to three times improvement in the tensile elongation of the magnesium alloy AZ31 processed by ECAE.

Also, there were found significant improvements in the yield strength and ductility of the conventionally extruded Mg–3.3%Li alloy after 4-pass ECAE at 523K with Route A and Route Bc (Liu *et al.,* 2004).

In contrast to these findings, for the AZ31 alloy after 8-pass ECAE at 473K with Route Bc, the tensile yield strength of the magnesium alloy was

slightly lower than the conventionally extruded counterpart, although its elongation to failure was twice as large as that of the conventionally extruded alloy. Similar results were obtained from the tensile tests of the AZ61 alloy after the conventional extrusion and then ECAE at 548K with Route Bc (Kim *et al*., 2002).

The maximum elongation achieved in ZK60, processed by ECAE, did not exceed 800% (Chuvil'deev *et al*., 2004).

The peculiar mechanical behaviour of these magnesium alloys was attributed to the strong texture developed during the ECAE process. Each route of ECAE gives rise to a characteristic texture. The textures carry the signatures of the corresponding strain path and sharpen with the number of ECAE passes. Route C gives rise to the sharpest texture (Suwas *et al*., 2007).

Primary processing, like hot rolling and hot extrusion, generally develops a strong basal texture in magnesium alloys. An ECAE processing on AZ31 magnesium alloy lead to the fabrication of ductile AZ31, which has basal plane orientation, inclined 45° to the extrusion direction. Because of the texture development, the material exhibited high ductility of 45% even at room temperature (Watanabe *et al*., 2004).

Recent research regarding ECAE of magnesium alloys towards high room temperature ductility by texture control (Kim *et al*., 2003; Agnew *et al*., 2004) is based on this result.

The deformation behavior of ECAE processed AZ31 alloy is dominated by magnesium small grains rotation and parallel wrinkled deformation type, and the mechanical properties of the ECAE processed AZ31 alloy are affected not only by the grain size but also by the transformations of the deformation types in the micro scale (Wang *et al*., 2008).

4. Conclusion

The hcp structure of magnesium limits the industrial applications of its alloys, because of the low ductility at a low forming temperature. In recent years, there were several attempts to enhance the ductility of magnesium alloys using grain refinement technology by deformation.

Equal-channel angular pressing (ECAP) imparts an intense plastic strain to a sample through simple shear but without any change in the cross-sectional dimensions. Thus, repetitive pressings may be conducted to achieve very high total strains.

In conclusion, the magnesium alloys produced through ECAE exhibits mechanical properties which show superior performance compared to the conventional magnesium alloys. ECAE offers the potential to induce crystallographic textures, previously unobserved, which may be of significant interest for modifying the properties.

Because of the fine sizes of the grains, it has been achieved, a high yield strength combined with large tensile elongation and low mechanical anisotrop. Further reduction of the grain size to the submicrometer level generates an increase in yield strength, a negligible mechanical anisotropy and an only slightly decreased elongation to fracture. At elevated temperatures, magnesium alloys show superplastic formability.

Acknowledgement. The work has been funded by the Sectoral Operational Programme Human Resources Development 2007-2013 of the Romanian Ministry of Labour, Family and Social Protection through the Financial Agreement POSDRU/88/1.5/S/60203.

REFERENCES

Agnew S.R., Horton J.A., Lillo T.M., Brown D.W., *Enhanced Ductility in Strongly Textured Magnesium Produced by Equal Channel Angular Processing*. Scripta Materialia **50**, 377–381 (2004).

Agnew S.R., Mehrotra P., Lillo T.M., Stoica G.M., Liaw P.K., *Texture Evolution of Five Wrought Magnesium Alloys During Route A Equal Channel Angular Extrusion: Experiments and Simulations*. Acta Mater., **53**, 3135-3146 (2005).

Aour B., Zaïri F. Boulahia, R., Naït-Abdelaziz M., Gloaguen J.M., J.M. Lefebvre, *Experimental and Numerical Study of ECAE Deformation of Polyolefins*. Computational Materials Science, *45*, 646–652 (2009).

Beyerlein I.J., Tome C.N., *Analytical Modeling Of Material Flow In Equal Channel Angular Extrusion (ECAE)*. Mater. Sci. Eng., **A 380**, 171-190 (2004).

Beygelzimer Y., Orlov D., Varyukhin V., *A New Severe Plastic Deformation Methd: Twist Extrusion*. TMS Annual Meeting, 297–302 (2002).

Beygelzimer Y., Varyukhin V., Orlov D., Efros B., Stolyarov V., Salimgareyev H., *Microstructural Evolution of Titanium Under Twist Extrusion*. TMS Annual Meeting, 43–46 (2002).

Chuvil'deev V.N., Nieh T.G., Yu M.. Gryaznov Sysoev, A.N., Kopylov V.I., *Low-Temperature Superplasticity and Internal Friction in Microcrystalline Mg Alloys Processed by ECAP.* Scripta Mater., **50**, 861–865(2004).

Dumitru F.-D., Ghiban B., Ghiban N., Marin M., Şaban R., Bane M., *Studies Considering die Design for Equal Channel Angular Extrusion (ECAE) Process,* Buletinul Ştiinţific Al Universităţii „Politehnica" din Timişoara, Seria Mecanică, **55(69)**, 45-48 (2010).

Eivani A.R., Karimi Taher A., *Effective Strain Based on Shear and Principal Strains in Equal Channel Angular Extrusion with Outer Curved Corner*. Computational Materials Science, **41**, 409–419 (2008).

Eivani A.R., Karimi Taheri A., *The Effect of Dead Metal Zone Formation on Strain and Extrusion Force During Equal Channel Angular Extrusion*. Computational Materials Science, **42**, 14–20 (2008).

Ferrasse S., Segal V.M., Alford F., Kardokus J., Strothers S., *Scale up and Application of Equal-Channel Angular Extrusion for the Electronics and Aerospace Industries*. Materials Science and Engineering, **A 493**, 130–140 (2008).

Furuno K., Akamatsu H., Oh-ishi K., Furukawa M., Horita Z., Langdon T.G., ActaMater., *52*, 2497–2507 (2004).

Ghiban B., Dumitru F.-D., Ghiban N., Saban R., Semenescu A., Marin M., *Consideration Regarding die Design for Equal Channel Angular Extrusion*. 21st International DAAAM Symposium "Intelligent Manufacturing & Automation: Focus on Interdisciplinary Solutions", **21**, 0189-0190 (2010).

Gholinia A., Bate P., Prangnell P.B., *Modelling Texture Development During Equal Channel Angular Extrusion of Aluminium.* Acta Mater., **50**, 2121-2136 (2002).

Gil, Sevillano J., Van Houtte P., Aernoudt E., *Large Strain Work Hardening and Textures.* Progress in Materials Science*, 25*, 69-134 (1980).

Imayev R.M., Imayev V.M., Salishchev G.A., *Formation of Submicrocrystalline Structure in TiAl Intermetallic Compound*. J. Mater. Sci., **27**, 4465–4471 (1992).

Iwahashi Y., Horita Z., Nemoto M., Langdon T.G., *The Process of Grain Refinement in Equal-Channel Angular Pressing*. Acta Mater., **46**, 3317-3331 (1998).

Jin L., Lin D.L., Mao D.L., Zen X.Q., Ding W.J., *Mechanical Properties and Microstructure of AZ31 Mg Alloy Processed by Two-Step Equal Channel Angular Extrusion*. Mater. Lett., **59**, 2267- 2270 (2005).

Kainer K.U., *Magnesium Alloys and Technology*. Weinheim: DGM, 2003.

Kim J.K., Kim W.J., *Analysis of Deformation Behavior in 3D During Equal Channel Angular Extrusion*. J. of Materials Processing Technology, **176**, 260–267 (2006).

Kim W.J., An C.W., Kim Y.S., Hong S.I., *Mechanical Properties and Microstructures of an AZ61 Mg Alloy Produced by Equal Channel Angular Pressing*. Scripta Mater., **47**, 39–44 (2002).

Kim W.J., Hong S.I., Kim Y.S., Min S.H., Jeong H.T. Lee, J.D., *Texture Development and its Effect on Mechanical Properties of an AZ61 Mg Alloy Fabricated by Equal Channel Angular Pressing*. Acta Mater., **51**, 3293 -3307 (2003).

Liu T., Wang Y.D., Wu S.D., Peng R.L., Huang C.X., Jiang C.B., Li S.X., *Textures and mechanical Behavior of Mg–3.3%Li alloy after ECAP*. Scripta Mater., **51**, 1057–1061 (2004).

Liu Z.Y., Liang G.X., Wang E.D., Wang Z.R., *The Effect of Cumulative Large Plastic Strain on the Structure and Properties of a Cu–Zn Alloy*. Mater. Sci. Eng. , **A 242**, 137–140 (1998).

Lowe T.C., Valiev R.Z., *The use of Severe Plastic Deformation Techniques in Grain Refinement*. JOM, **56**, *10*, 64–68 (2004).

Luis C.J., Luri R., Léon J., *Strain and Temperature Analysis of AA-1370 Processed by ECAE at Different Temperatures*. J. of Materials Processing Technology, *164–165*, 1530–1536 (2005).

Mishin O.V., Gertsman V.Y., Valiev R.Z., Gottstein G., *Grain Boundary Distribution and Texture in ultrafine-Grained Copper Produced By Severe Plastic Deformation*. Scripta Mater., **35**, 873–878 (1996).

Mueller K., Mueller S., *Severe Plastic Deformation of the Magnesium Alloy AZ31*. Journal of Materials Processing Technology, *187–188*, 775–779 (2007).

Mukai T., Yamanoi M., Watanabe H., Higashi K., *Ductility Enhancement in AZ31 Magnesium Alloy by Controlling its Grain Structure.* Scripta Mater., **45**, 89–94 (2001).

Patridge P.G., *Magnesium Alloys and its Applications*. Met Rev, 118-169 (1967).

Richert M., Richert J., Zasadzinski J., Hawryłkiewicz S., Długopolski J., *Effect of Large*

Deformations on the Microstructure of Aluminium Alloys. Mater. Chem. Phys., **81**, 528–530 (2003).

Saito Y., Tsuji N., Utsunomiya H., Sakai T., Hong R.G., *Ultra-Fine Grained Bulk Aluminum Produced by Accumulative Roll-Bonding (ARB) Process*. Scripta Mater., **39**, *9*, 1221–1227 (1998).

Saito Y., Utsunomiya H., Tsuji N., Sakai T., *Novel Ultra-High Straining Process for Bulk Materials-Development of the Accumulative Roll-Bonding (ARB) Proces.*, Acta Mater., **47**, *2*, 579–583 (1999).

Salishchev G.A., Valiakhmetov O.R., Galeyev R.M., *Formation of Submicrocrystalline Structure in the Titanium Alloy VT8 and its Influence on Mechanical Properties*. J. Mater. Sci., **28**, 2898–2902 (1993).

Segal V.M., *Equal Channel Angular Extrusion of Flat Product.* Materials Science and Engineering **A**, *476*, 178–185 (2008).

Segal V.M., *Equal Channel Angular Extrusion: from Macromechanics to Structure Formation*. Mater. Sci. Eng. **A 271**, 322–333(1999).

Segal V.M., *Materials Processing by Simple Shear*. Mater. Sci. Eng., **A 197**, 157–164 (1995).

Segal V.M., Ph.D thesis, Minsk, Russia, 1974.

Segal V.M., Reznikov V.I., Drobyshevskiy A.E., Kopylov V.I., *Plastic Working of Metals by Simple Shear.* Russian Metall., **1**, 99–105 (1981).

Segal V.M., *Slip Line Solutions, Deformation Mode and loading History During Equal Channel Angular Extrusion*. Mater. Sci. Eng., **A 345**, 36–46 (2003).

Sivakumar S.M., Ortiz M., *Microstructure Evolution in the Equal Channel Angular Extrusion Process*. Comput. Methods Appl. Mech. Engrg., *193*, 5177–5194 (2004).

Spuskanyuk V., Spuskanyuk A., Varyukhin V., *Development of the Equal-Channel Angular Hydroextrusion*. J. of materials processing technology, **203**, 305–309 (2008).

Stalmann A., Sebastian W., Friedrich H., Schumann S., Droder K., *Properties and Processing of Magnesium Wrought Products for Automotive Applications*. Adv Eng Mater, **3**, 969-974 (2001).

Stolyarov V.V., Lapovok R., *Effect of Back Pressure on Structure and Properties of AA5083 Alloy Processed by ECAP*. J. Alloys Compd., **378**, 233–236 (2004).

Suwas S., Gottstein G., Kumar R., *Evolution of Crystallographic Texture During Equal Channel Angular Extrusion (ECAE) and its Effects on Secondary Processing of Magnesium*. Materials Science and Engineering, **A 471**, 1–14 (2007).

Tham Y.W., Fu M.W., Hng H.H., Yong M.S., Lim K.B., *Study of Deformation Homogeneity in the Multi-Pass Equal Channel Angular Extrusion Process.* Journal of Materials Processing Technology *192–193*, 121–127 (2007).

Tham Y.W., M Fu.W., Hng H.H., M Yong.S., Lim K.B., *Study of Deformation Homogeneity in the Multi-Pass Equal Channel Angular Extrusion Process*. J. of Materials Processing Technology, *192-193*, 121-127 (2007).

Tóth L.S., Arruffat-Massion R., Germain L., Baik S.C., Suwas S., *Analysis of Texture Evolution in equal Channel Angular Extrusion of Copper Using a New Flow Field*. Acta Mater., **52**, 1885-1898 (2004).

Valiev R.Z., Islamgaliev R.K., Alexandrov I.V., *Bulk Nanostructured Materials from Severe Plastic Deformation*. Prog. Mater. Sci., **45**, 103 –189 (2000).

Valiev R.Z., Korznikov A.V., Mulyukov R.R., *Structure and Properties of Ultrafine-Grained Materials Produced by Severe Plastic Deformation*. Mater. Sci. Eng.,

A 168, 141–148 (1993).

Vinogradov A., Nagasaki S., Patlan V., Kitagawa K., Kawazoe M., *Fatigue Properties of 5056 Al–Mg Alloy Produced by Equal Channel Angular Pressing*. Nanostruct. Mater. **11**, *7*, 925–93 (1999).

Wang X.-S., Jin L., Li Y., Guo X.-W., *Effect of Equal Channel Angular Extrusion Process on Deformation Behaviors of Mg-3Al-Zn Alloy*. Materials Letters, **62**, 1856–1858 (2008).

Watanabe H., Mukai T., Sugioka M., Ishikawa K., *Elastic and Damping Properties from Room Temperature to 673 K in an AZ31 Magnesium Alloy*. Scripta Mater, **51,** 291-295 (2004).

Wu B.L., Wan G., Zhang Y.D., Du X.H., Wagner F., Esling C., *Fragmentation of Large Grains in AZ31 Magnesium Alloy During ECAE Via Route A*. Materials Science And Engineering **A 527**, *15*, 3365-3372 (2010).

Wu P.D., Huang Y., Lloyd D.J., *Studying Grain Fragmentation in ECAE by Simulating Simple Shear.* Scripta Materialia, **54**, 2107-2112 (2006).

Yoshida Y., Cisar L., Kamado S., Kojima Y., *Effect of Microstructural Factors on Tensile Properties of ECAE-Processed AZ31 Magnesium Alloy*. Materials Transactions, **44**, *4*, 468-475 (2003).

Zhang X., Luo S., Du Z., *Uniformity and Continuity of Effective Strain in AZ91D processed by Multi-Pass Equal Channel Angular Extrusion*. Trans. Nonferrous Met. Soc. China, **18**, 92-98 (2008).

Zhao Z., Chen Q., Wang Y., Shu D., *Microstructural Evolution of an ECAE-Formed ZK60-RE Magnesium Alloy in the Semi-Solid State*. Materials Science and Engineering, **A 506,** 8–15 (2009).

CONSIDERAŢII PRIVIND PROCESUL DE EXTRUDARE UNGHIULARĂ ÎN CANALE EGALE PE ALIAJE DE MAGNEZIU

(Rezumat)

În ultimii ani, s-a realizat o cercetare, în continuă creştere, privind efectele prelucrării prin extrudare unghiulară în canale egale. Extrudarea unghiulară în canale egale (EUCE) este una dintre metodele de deformare plastică severă (DPS), care îmbunătăţeşte proprietăţile mecanice ale materialelor prelucrate din cauza grăunţilor ultrafini rezultaţi. EUCE produce tensiuni de deformare semnificative, fără a modifica secţiunea transversală.

Această lucrare ia în considerare diferite articole în scopul de a explica atât mecanismul de EUCE, precum şi modul în care această metodă de DPS influenţează proprietăţile aliajelor de magneziu. Experimentele EUCE au confirmat că această tehnică poate fi utilizată pentru atingerea unor proprietăţi mecanice îmbunătăţite, cum ar fi alungiri mari superplastice, limita de curgere ridicată, alungire mare la întindere şi o anizotropie scăzută a proprietăţilor mecanice.

BULETINUL INSTITUTULUI POLITEHNIC DIN IAŞI
Publicat de
Universitatea Tehnică „Gheorghe Asachi” din Iaşi
Tomul LVII (LXI), Fasc. 4, 2011
Secţia
ŞTIINŢA ŞI INGINERIA MATERIALELOR

INFLUENCE OF CLOSED CELL ELASTOMER SCALE FACTOR ON THE PASSING POWER FLOW TRANSFORMATION

BY

G. DUNCHEVA*, P. NENCHEV, A. ANCHEV

Technical University Gabrovo, Bulgaria

Received: April 14, 2011
Accepted for publication: June 27, 2011

Abstract. The object of study is an elastomer in a closed cell, through which power flows. FEM approach has been applied to solve the problem. An axisymmetrical FEM model has been developed in which the model of elastomer material employs the Arruda-Boyce model. It is based on the specific potential strain energy which is the energy accumulated per unit of volume. For a selected optimized cell geometry the emphasis is laid on the influence of the scale factor, respectively, the elastormer volume impact upon the transformation of the power flow. The obtained results are visualized by graphics and relevant conclusions have been made.

Key words: scale factor optimization, closed cell, hyperelastic material, finite element simulations.

1. Introduction

The hyperelastic materials belong to the polymer materials group. Depending on the nature of the matter which builds these materials, they can be hydroplastic, rubber like, foam like and other polymers. In the machinery

* Corresponding author e-mail: nenchev@tugab.bg

construction the components made of hyperelastic materials are known as elastomers. As a part of machine-building products, the elastomers perform various functions: vibro-insulation, as congestion elements, as components in tightening mechanisms, for compensating the deflection of the mutual position of connected shafts. Analyzing the elastomer applications in the tightening mechanisms, a practical and scientific interest is the case when a force flow passes through the elastomer, *i.e*. when the elastomers perform basic role in the tightening process. Simultaneously, elastomer applications in tightening mechanisms where the transformation of the force flows to be at hand are not known.

The present investigation basis is the idea for an optimization of the application of elastomers made of rubber mixes as a medium for transferring of a pressure in the tightening mechanisms in a such manner that the force flow to be increased to direction of the workpiece to be fixed. For that purpose the elastomer is fit in a closed cell having the form of a truncated cone and two short cylindrical sections (Maximov & Nenchev, 2003).

The main objective of this work is to obtain quantitative estimation of the influence of the scale factor, respectively the elastomer volume on the force flow transformation. The problem has been solved by means of finite element (FE) approach.

2. Nature of the Technical Solution

The principle scheme of the technical solution is presented in Fig. 1. To reach an intensification of the force flow from piston 1 to piston 2 it is necessary elastomer Poisson ratio to be $\approx 0{,}5$, *i.e.* the elastomer to be almost incompressible. For that purpose, on the basis of experimental studies it is chosen a rubber-like material with Shore hardness of 55 (Duncheva *et al*., 2008). In order to receive a quantitative assessment of the passing force flow transformation, the coefficient of the force intensification k is introduced as (Maximov & Nenchev, 2003):

$$k = F_2 / F_1 \tag{1}$$

where F_1 and F_2 are respectively the input and the output forces, relative to the top of the elastomer's contact surfaces.

3. Organization of the Study

In order to make an optimization of the elastomer geometry, a multi-objective optimization is carried out by means of numerical simulations. In the condition of a constant volume and when $d = const$ and $h_1 = const$ (Fig. 1),

all the rest parameters depend on only angle β. It is established that when $\beta = 70^0$ the coefficient k is the biggest and the losses are the smallest. The objects of this study are the elastomers having optimal geometry but having different scale factors. The variation of its geometrical parameters depending on the scale factor, respectively depending on the elastomers volume, is shown in Table 1.

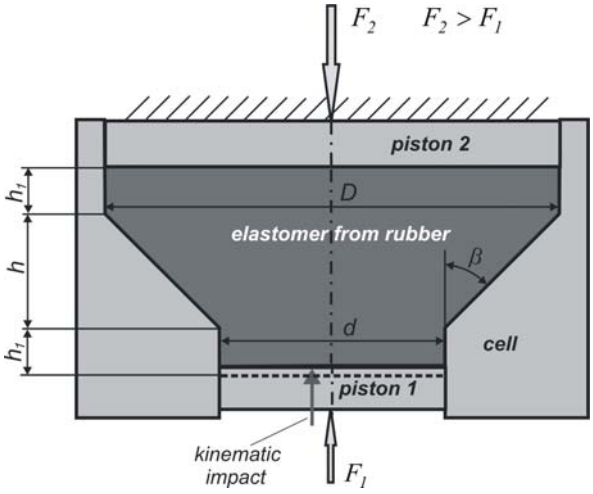

Fig. 1 – Principle scheme.

Table 1
Geometrical Parameters of Elastomers

Scale factor	d, mm	D, mm	h, mm	h_1, mm	V, mm^3
0.5	12.5	34.426	3.99	2.5	4484.644
0.75	18.75	51.639	5.985	3.75	15135.677
1	25	68.852	7.98	5	35877.16
1.25	31.25	86.065	9.975	6.25	70072.578
1.5	103.278	103.278	11.97	7.5	121085.412

4. Finite Element Model

4.1. General Characteristic

In view of the nature of the problem to be studied, an axisymmetrical FE model has been developed (Fig. 2 *a*, *b*). The pistons 1 and 2, and the cell are modeled as analytical rigid and the elastomer is modeled as deformable body.

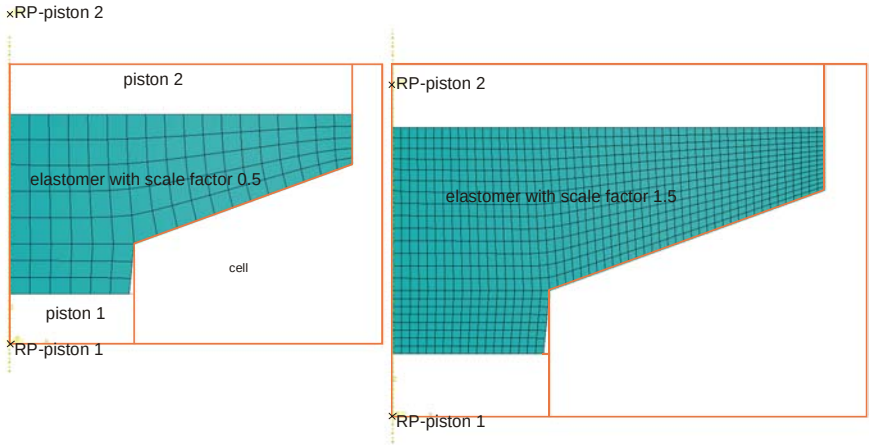

Fig. 2 – Axisymmetrical finite element model, *a* - scale factor 0.5; *b* - scale factor 1.5.

According to the construction of the closed cell, FE model consist of three parts –piston-1, piston-2 which simulate respectively small piston and big piston and cell. Tangential and normal contact between the elastomer and components of the cell allowing a separation are defined as the technique "master" and "slave" surfaces is applied (Hibbit *et al*., 2004). According to experimental results obtained (Petkov *et al*., 2007), for the rubber to be studied the friction coefficient 0.8 is assigned.

The kinematic impact applied on the piston 1 is assigned by means of a rectilinear translation with amplitude defined by means of tabulation. The input and the output forces, relative to the piston-1 and piston-2 are obtained by reactions in Reference point (RP) of their models (Fig. 2*a*, *b*).

The elastomer FE model is built from quadratic quadrilateral FE, type CAX8R. In order to obtain correct FE results the geometric similar elastomers are built with equal average size of the FEs - $1\ mm$ (Fig. 2*a*, *b*).

4.2. Constitutive Model of the Elastomer

On the basis of a comparison between experimental and FE results, it is proved that the Arruda-Boyce constitutive model is the most appropriate for describing the behavior of the investigated rubber mix [3-UNITECH'2008]:

$$\Omega = G[\frac{1}{2}(\bar{I}_1 - 3) + \frac{1}{20\lambda_m^2}(\bar{I}_1^2 - 9) + \frac{11}{1050\lambda_m^4}(\bar{I}_1^3 - 27) + \frac{19}{7000\lambda_m^6}(I_1^3 - 81) + \\ + \frac{519}{673750\lambda_m^8}(\bar{I}_1^5 - 243)] + \frac{1}{D}(\frac{J_{el}^2 - 1}{2} - \ln J_{el}) \quad (2)$$

the first deviatoric strain invariant

where G, λ_m and D are temperature dependent material parameters; $\bar{I}_1$ is the first deviatory strain invariant defined as:

$$\bar{I}_1 = \bar{\lambda}_1^2 + \bar{\lambda}_2^2 + \bar{\lambda}_3^2 \tag{3}$$

$\bar{\lambda}_i$ are the deviatory stretches: $\bar{\lambda}_i = J^{-\frac{1}{3}} . \lambda_i$; J is the total volume ratio (ratio of current volume to initial); J_{el} is the elastic volume ratio; λ_i are the principal stretches ($\lambda_i = 1 + \varepsilon_i$; ε_i are the principal linear strains).

The initial shear modulus G_0 is related to G with the expression:

$$G_0 = G(1 + \frac{3}{5\lambda_m^2} + \frac{99}{175\lambda_m^4} + \frac{513}{875\lambda_m^6} + \frac{42039}{67375\lambda_m^8}). \tag{4}$$

A typical value of λ_m is 7, from where $G_0 = 1{,}0125G$. The initial bulk modulus K_0 is related to D with the expression: $K_0 = 2/D$.

The following material constants are obtained: $G = 1{,}8516824$; $G_0 = 1{,}87480038$; $\lambda_m = 7{,}00020847$; $D = 0{,}0432$.

5. Finite Element Results and Discussions

The equivalent von Misses stress distribution for elastomers having scale factors respectively 0.75 and 1.25 and corresponding to the maximum displacement of the small piston are shown in Fig. 3. For each studied case the maximum displacement is conformable to the condition the maximum equivalent stress to be less than $\approx 5\ MPa$. In the field surrounding small piston the deforming process is the most intensive because of that the stresses are maximum in this zone.

The generalized results obtained from the numerical simulations for different scale factors are shown in Fig. 4-8. For the elastomers from Table 1, the output force F_2, N and the coefficient of the force intensification depending on the small piston displacement are graphically visualized.

On the basis of the graphical dependences obtained, the following comments can be made:

- With increasing of the output force F_2, the coefficient of the force intensification k decreases because of the bigger friction forces between the elastomer and the cell;

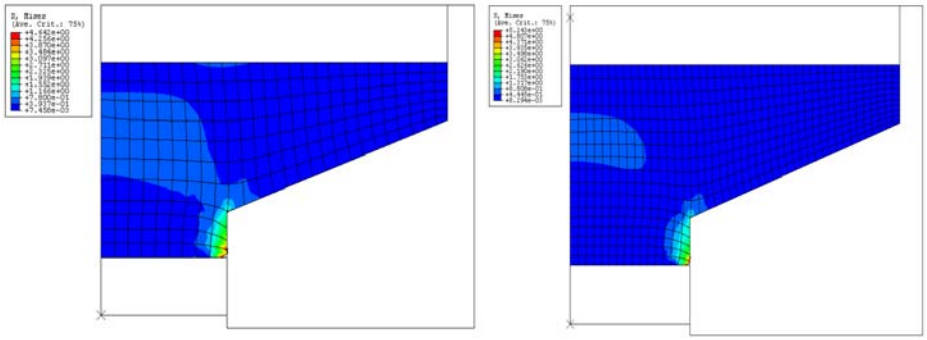

a *b*

Fig. 3 – Equivalent stress distribution; *a* - scale factor 0.75; *b* - scale factor 1.25.

- The dependence between the applied kinematics influence (the small piston axial displacement) and the output force F_2 has almost linear character. This gives a possibility comparatively easily to control the force applied to workpiece to be fixed by means of a control on the small piston displacement;

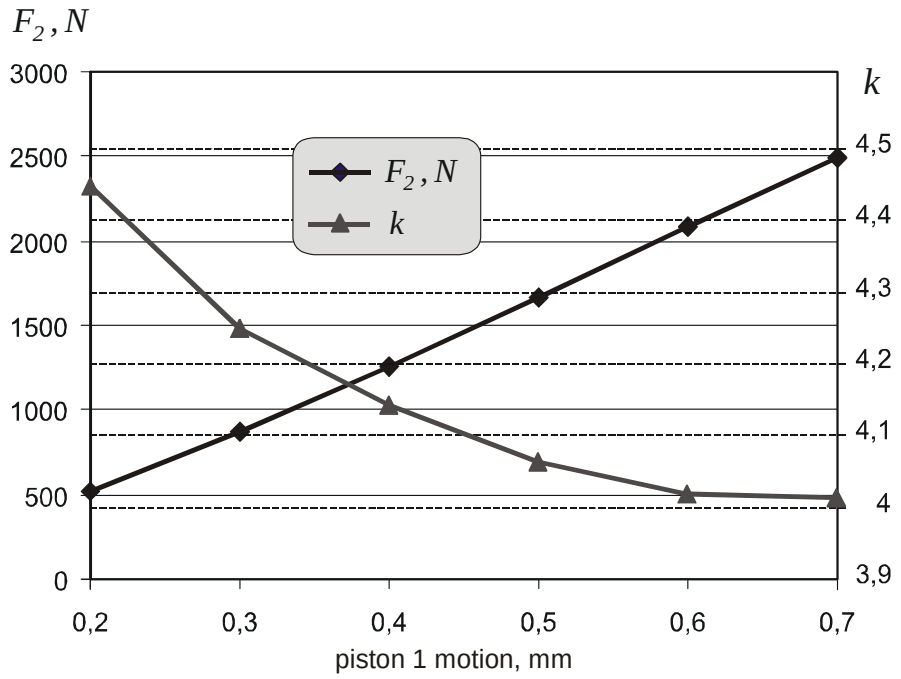

Fig. 4 – Power flow transformation in elastomer with scale factor 0.5.

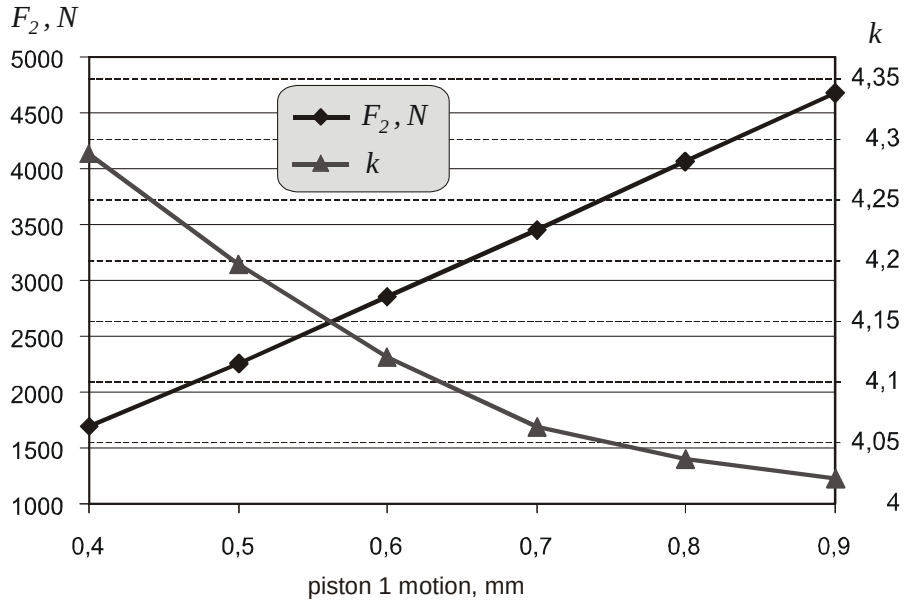

Fig. 5 – Power flow transformation in elastomer with scale factor 0.75.

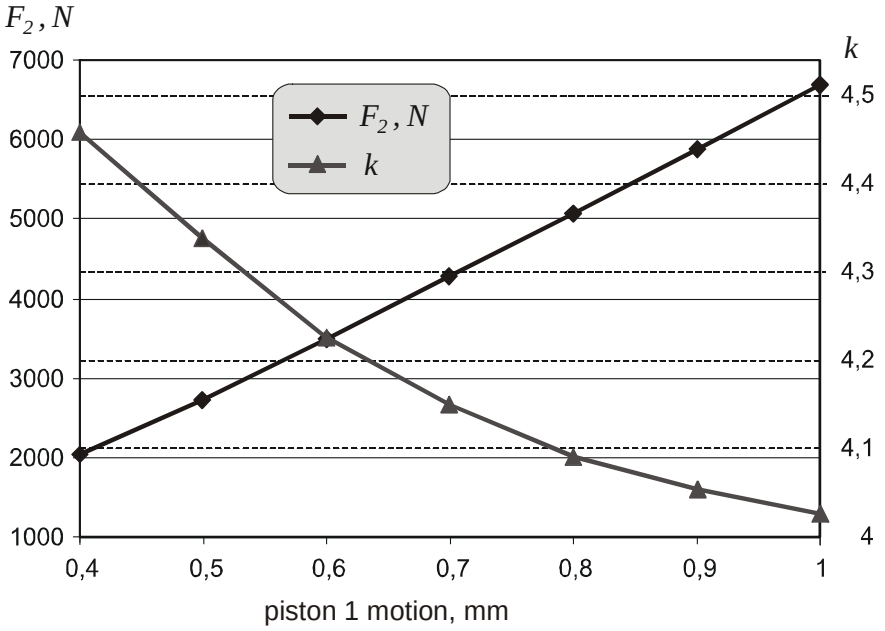

Fig. 6 – Power flow transformation in elastomer with scale factor 1.

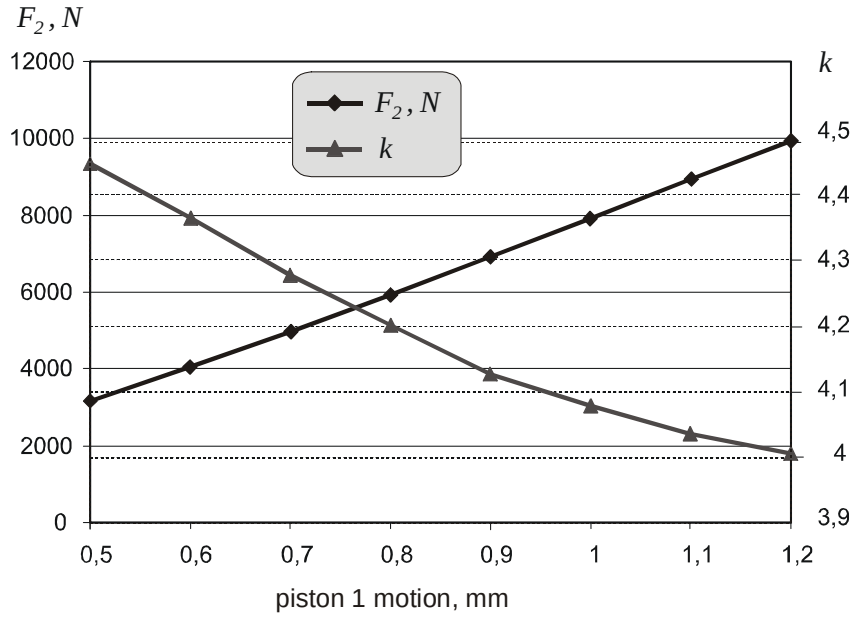

Fig. 7 – Power flow transformation in elastomer with scale factor 1.25.

- With increasing the small piston displacement, the coefficient of the force intensification decreases with changeable rate. It is observed that the scale factor leads to relatively little dispersing of k in the conditions of the maximum displacement for a given elastomer.

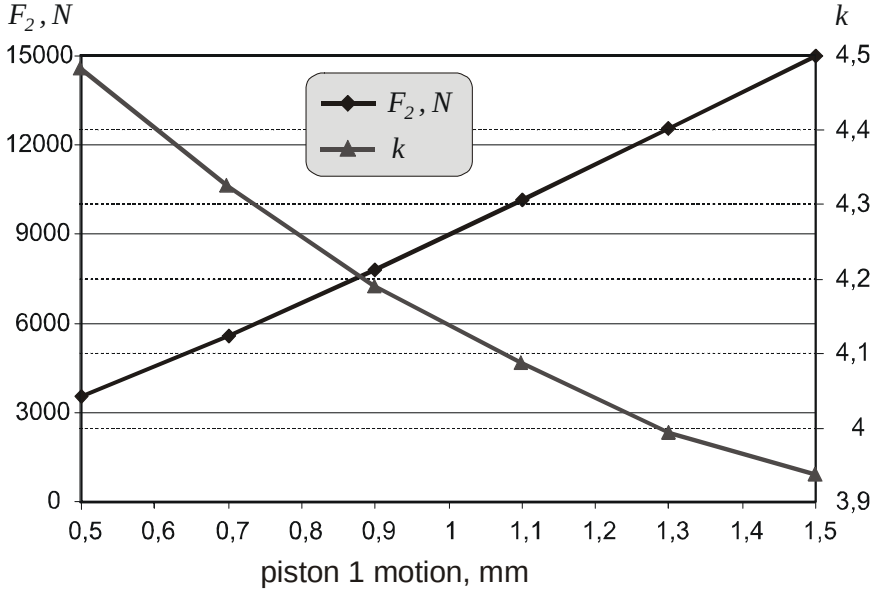

Fig. 8 – Power flow transformation in elastomer with scale factor 1.5.

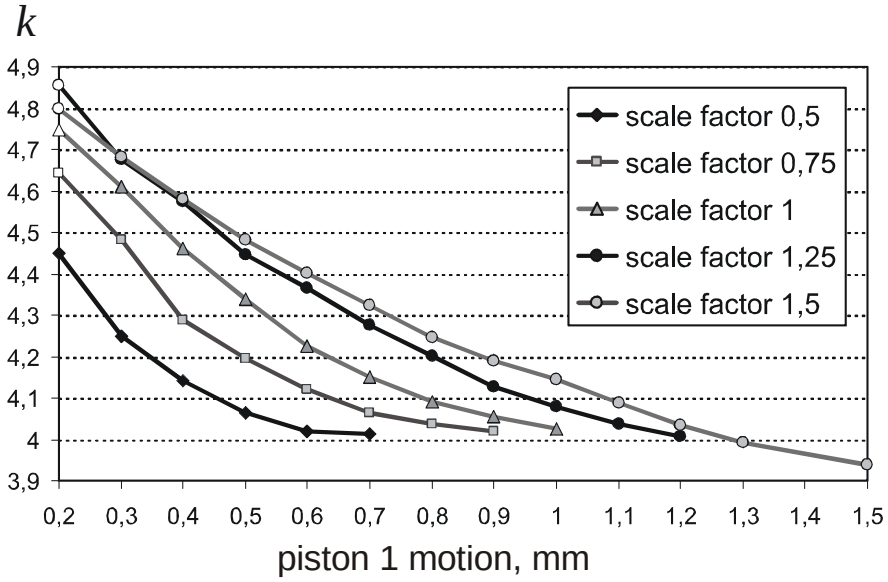

Fig. 9 – Variation of k from scale factor and kinematic impact.

Fig. 9 shows the variation of the coefficient of the force intensification of elastomers having different scale factors depending on the small piston displacement. Obviously, for one of the same kinematic impact the coefficient of the force intensification increases with increasing the scale factor. This can be explained by relatively smaller losses causal by external friction for elastomers having larger volume.

6. Conclusion

A generalized FE model of the elastomer in a closed cell has been developed, trough which force flow passes so that it is intensificated.

The influence of the scale factor on the flow force transformation has been studied by means of numerical simulations of the geometric similar elastomers.

The quantitative dependences between elastomers power characteristic and admissible values of the applied upon them kinematic impacts are obtained.

The results obtained can be used for design of tightening mechanisms based on the studied technical solution.

Acknowledgement. The study was supported by contract № BG051PO001-3.3.04/28, "Support for the Scientific Staff Development in the Field of Engineering Research and Innovation". The project is funded with support from the Operational Programme "Human Resources Development" 2007-2013, financed by the European Social Fund of the European Union.

REFERENCES

Duncheva G.V., Nenchev P.N., Maximov J. ., Anchev A.P., *Finite Element Investigation of the Behaviour of the Rubber Like Materials in a Closed Cell*. In: UNITECH'08 International Scientific Conference, Gabrovo, Bulgarian, **II**, 87-98 (2008).

Hibbit, Karlsson, and Sirensen Inc. ABAQUS/CAE Theory Manual, Version 6.5, ABAQUS Inc. Rising Sun Mills, 166 Valley Street Providence, RI 02909-2499, 2004.

Maximov J.T., Nenchev P.N., *Concerning the Possibility of Using Rubber Like Materials as Medium for Pressure Transferring in a Closed Cell*. In: AMTECH'03 International Scientific Conference, Varna, Bulgarian, **II**, 126-129 (2003).

Petkov S., Nenchev P.N., Anchev A.P., Duncheva G.V., *Experimental Investigation of the Friction Coefficient Between Steel and Hyperelastic Materials*. Mechanics of Machines, Bulgarian, **73**, 15-19 (2007).

INFLUENŢA FACTORULUI DE SCARĂ A UNEI CELULE ÎNCHISE DE ELASTOMER ASUPRA TRANSFORMĂRII UNUI FLUX DE FORŢĂ

(Rezumat)

Obiectul de studiu este un elastomer într-o celulă închisă, supus unui flux de forţă. S-a apelat la metoda elementului finit pentru rezolvarea problemei. A fost creat un model FEM în care modelul materialului elastomer foloseşte modelul Arruda-Boyce. Se bazează pe energia potenţială care este acumulată pe unitatea de volum. Pentru o geometrie optimizată a geometriei celulei se pune accent pe influenţa factorului de scală, respectiv, volumul elestomerului la impact la transformarea fluxului de putere. Rezultatele obţinute sunt prezentate vizual prin grafice şi au fost trase concluzii relevante.

BULETINUL INSTITUTULUI POLITEHNIC DIN IAŞI
Publicat de
Universitatea Tehnică „Gheorghe Asachi” din Iaşi
Tomul LVII (LXI), Fasc. 4, 2011
Secţia
ŞTIINŢA ŞI INGINERIA MATERIALELOR

EQUAL STRENGHT SHAPE MEMORY ALLOY (SMA) LAMELLA ACTUATOR

BY

ALEXANDRU ENACHE*, MIHAI AXINTE and ION HOPULELE

“Gheorghe Asachi” Technical University of Iaşi

Received: April 20, 2011
Accepted for publication: June 27, 2011

Abstract. In practice, the shape memory alloys lamellas are used to obtain actuators or sensors items. Elements of SMA transmitters are designed to convert thermal energy into mechanical energy. Mechanical energy act on a component in a mechanic assembly, changing its position or shape.

For lamellar shape actuators with constant section, it is noted that the maximum torque is restraint foreground. Bearing section supports all elastic deformations. The deformations can become residual strain if it exceeds the elastic range for material. If it is desirable that the maximum bending stress is the same in all sections of the beam, this is why equal bending strength bar is preferred. This bar is trapezoidal with constant thickness. Dimensions can be derived by computer simulation by finite element method CATIA module.

Key words: shape memory, alloys lamella, computer simulation

1. Introduction

1.1. Slide Actuator of Shape Memory Alloy (SMA) with Constant Section

The determination efforts in a constant lamella section are shown in Fig. 1. It is noted that maximum moment is close to the bearings. Section close

* Corresponding author e-mail: sandu_enache2006@yahoo.com

to the bearings supports all elastic deformations. These strains can become the residual strains if it exceeds the elastic range of material.

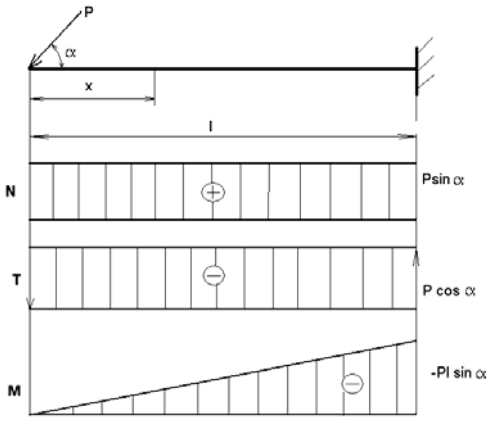

N = Psinα
P = concentrated force
α = angle of the force
T= - P·cosα
At the x distance the moment becomes:
M= -P·x·sinα
For α=90°:
N= P
M= -P·x

Fig. 1 – The effort determination in a constant lamella section.

1.2. Analysis of the S.M.A. Lamella Actuator Tensions with Constant Section by Computer Simulation by Finite Element Method CATIA V5 R17 Module

Finite element method (FEM) is one of the best existing methods for engineering calculations and simulations. This method, of course, which incorporates programs have become essential parts of modern computer aided design. Engineer will design a virtual system and will study the behavior.

Strength, stability, sustainability are all part of the required characteristics of a piece or assembly composed of parts or subassemblies. Finite element analysis of a resistance structure model is, in fact, numerical calculation verification. Thus, for a given dimensional defined geometry, for a given load and well-defined conditions (constraints) bearing, are achieved: offset values, tensions, the bearings reactions, own frequencies etc.

The finite element analysis purpose is, first, discretizing the transformation of the real structure, continuous, in a discrete model with a number of points called nodes.

The finite element method defines the unknown (displacements and stresses) only in created model nodes and calculates their respective point's values. Number of nodes must be large enough in the areas of interest to obtain a satisfactory approximation of the geometry structure, the edge areas and loading conditions.

Discretization process results in dividing the structure model in a finite but unspecified number of elements. Thus, any model can be discretized into a

number of elements known as prismatic or tetrahedral finite elements. These nodes are connected by through tetrahedrons or prisms vertices.

2. Results and Debates

Analysis of stress and strain for the uneducated lamella actuator S.M.A. is enlightening also for the educated shape memory actuator.

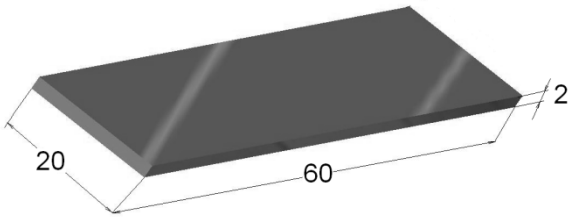

Fig. 2 – Rectangular section lamella.

Fig. 3 – Concentrated load (10N) 1000g.

Analysis is done on a rectangular section lamella S.M.A. Cu-Zn-Al, uneducated, with dimensions of 60 mm x 20mm x 2mm (Fig. 2) is 2400 mm^2 plate volume and mass of 20 g (Fig. 2).

In Fig. 3 minimum stress is shown in blue (right) and its value is 4.83 $x10^5$ N/m^2 and the maximum stress is shown in red (left) and its value is 2.95 $x10^7$ N/m^2.

On the lamella actuator S.M.A. of equal strength with variable width (Fig. 4) elastic stresses and strains are distributed evenly throughout the volume of material.

The S.M.A. lamella actuator with variable width and equal strength produces more mechanical work than a constant section actuator after a thermal cycle.

The virtual sample 1 is presented in Fig. 4. This sample is a S.M.A. isosceles trapezoid with the peak angle with the value 9.4.

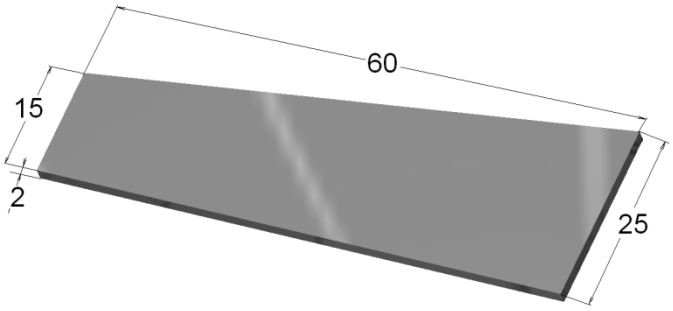

Fig. 4 – Virtual isosceles trapezoid shaped S.M.A. lamella.

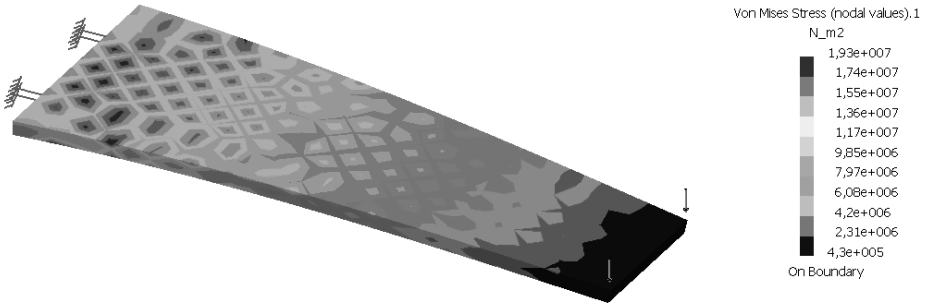

Fig. 5 –Virtual isosceles trapezoid shape S.M.A. lamella
10N applied force.

In Fig. 5 minimum stresses are shown in blue (positioned at the outer edge) and its value is 4.3 x10^5 N/m^2, and the maximum stress is shown in red (positioned closer to the support edge) and its value is 1.93 x10^7 N/m^2.

Note that maximum moment is near embedded section. Section near bearing, rendered in red, is one that supports all elastic deformations. These strains can become the residual strains if it exceeds the elastic range of material. In S.M.A. actuators or sensors case this phenomenon is undesirable because it leads to the destruction of shape memory effect.

The virtual sample 2 is presented in Fig. 6. This sample is a S.M.A. isosceles trapezoid with the dimensions presented in Fig. 6 and the peak angle with the value 47° Fig. 7.

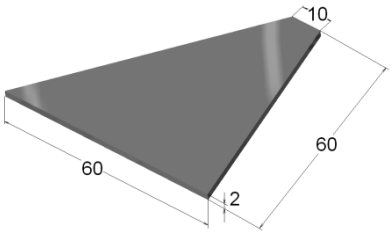

Fig. 6 – Virtual isosceles trapezoid shaped S.M.A. lamella.

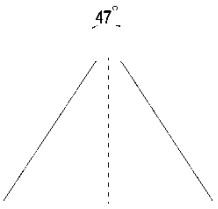

Fig. 7 – The peak angle is 47.°

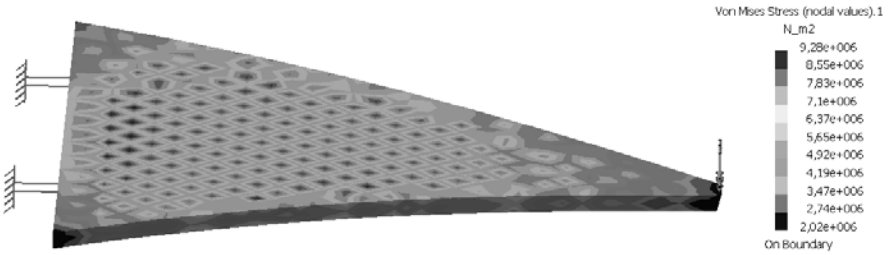

Fig. 8 – Virtual isosceles trapezoid shape S.M.A. lamella 10N applied force.

In Fig. 8 minimum stress is shown in blue and its value is 2.02 x10^6 N/m^2 and the maximum voltage is shown in red and its value is 9.28 x10^6 N/m^2. It is noted that the minimum stress and maximum stress have the same order of magnitude. Also the distribution for the stress is even on the surface and in material volume.

3. Conclusion

1. On the virtual samples Fig. 3 and Fig. 5, it is noted that the maximum tensions represented in red are concentrated near bearings.

2. Virtual sample of figure 8 is an equal strength distribution sample because the maximum stress resistance as represented in red is distributed uniformly throughout the section. Angle peak is about 47. This angle depends on the modulus of brass.

3. If the cross section is constant throughout the bar, then the material is not used to its maximum capacity. It used to its maximum capacity only near the bearings.The other sections are oversized. In case of expensive S.M.A. the use of material is unjustified. The S.M.A. lamella actuator with variable width and equal strength produces more mechanical work than a constant section

actuator after a thermal cycle. The entire volume participates in equal measure and not just the part near the section bearings.

REFERENCES

[1]. Dia V., Bujoreanu L.G., Stanciu S., Munteanu C., *Study of the Shape Memory Effect in Lamellar Helical Springs Made From Cu–Zn–Al Shape Memory Alloy*. Proceedings of the 7th European Symposium on Martensitic Transformations, ESOMAT 2006, **481-482**, 25 May 2008, 697-701.

[2]. Stanciu S., Bujoreanu L.G., Cimpoeşu N., Ioniţă I., Moldoveanu V., *Shape Memory Effect and Related Characteristics of Helical Springs Made From Cu-Al-Ni Alloy by Investment Casting*. Optoelectronics and Advanced Materials-Rapid Communications, **3**, *6*, 581-585 (2009).

[3] Ghionea I.G., *Proiectare asistată în Catia V5, elemente teoretice şi aplicaţii*. Editura Bern, 2007.

ACTUATORUL DIN LAMELĂ DIN ALIAJ CU MEMORIA FORMEI (A.M.F.) DE EGALĂ REZISTENŢĂ

(Rezumat)

În practică, lamelele din AMF sunt folosite pentru obţinerea de elemente actuatoare sau senzori. Elementele actuatoare din AMF au rolul de a transforma energia termică în energie mecanică. Această energie mecanică acţionează asupra unei componente dintr-un ansamblu mecanic modificând poziţia sau forma acestuia.

Pentru actuatorii de formă lamelară cu secţiune constantă, se observă că, momentul este maxim în planul apropiat încastrării. Secţiunea din planul apropiat încastrării este cea care suportă toate deformaţiile elastice. Aceste deformaţii pot deveni remanente dacă se depăşeşte domeniul elastic al materialului respectiv. Dacă se urmăreşte ca nivelul tensiunilor maxime de încovoiere să fie acelaşi în toate secţiunile grinzii, se preferă bara de egală rezistenţă la încovoiere. Această bară este de formă trapezoidală cu grosime constantă. Dimensiunile pot fi deduse prin simulare pe calculator cu modulul CATIA prin metoda elementelor finite.

BULETINUL INSTITUTULUI POLITEHNIC DIN IAŞI
Publicat de
Universitatea Tehnică „Gheorghe Asachi" din Iaşi
Tomul LVII (LXI), Fasc. 4, 2011
Secţia
ŞTIINŢA ŞI INGINERIA MATERIALELOR

NUNUMERICAL MODELS FOR URANIUM PURIFICATION BY LIQUID-LIQUID EXTRACTION

BY

A. FILCENCO-OLTEANU[1*], E. PANTURU[1], L. GRIGORAS[1] and R. I. PANTURU[2]

[1]Research & Development National Institute for Metals and Radioactive Resources Bucharest
[2]Politehnica University of Bucharest

Received: April 14, 2011
Accepted for publication: June 27, 2011

Abstract. The paper presents a study on the statistical modeling of the results obtained in experimental uranium purification by liquid-liquid extraction. In order to achieve the mathematical model, the following parameters were varied: the uranium contents in the aqueous phase, the acidity of the aqueous phase, the TBP concentration in kerosene, the aqueous: organic phase's ratio and the number of extraction steps, using a factorial experiment 2^{5-2}. The mathematical model obtained by the processing of experimental data describes the dependence of yield on technically and economically significant operational parameters and is able to calculate the extraction efficiencies in the range of studied experimental values, with a precision of 95%. The general effect of the optimization consists in decreasing the uranium technological losses, by avoiding the third phase formation. The formation of stable emulsions in the uranium extraction - re-extraction operations is caused by: impurities in the aqueous phase; impurities in the organic phase and operating conditions. The statistical model obtained by the processing of experimental data is able to calculate the extraction efficiencies in the range of studied experimental values, with a precision of 95%.

Key words: uranium, extraction, TBP, kerosene, third phase.

* Corresponding author e-mail: tonyfil2002@yahoo.com

1. Introduction

Technological processes based on uranium acid or alkaline leaching and subsequent extraction by precipitation, ion exchange sorption or organic solvents, finally lead to enriched chemical concentrates which, besides (50-70%) uranium, also contain impurities that make them incompatible for use as nuclear fuels (Panturu *et al*., 2008). The optimum purification process, the only one applied on industrial scale, is the liquid – liquid extraction, using a solution of tri-butyl phosphate (TBP) in kerosene as an extracting reagent (Patent RO 120630).

Uranium purification by extraction from the aqueous phase in the organic phase is achieved by the selective transfer of uranyl nitrate ($UO_2(NO_3)_2$) from the aqueous phase into the organic phase, under the form of a solvating complex with TBP, $UO_2(NO_3)_2 \cdot 2TBP$, during which the other inorganic nitrates remain in the aqueous phase. Specialized literature reports numerous cases of TBP-based uranium extraction from nitric acid solutions (Schulz *et al*., 1984; Schulz *et al*., 1987).

In certain conditions, the organic phase is separated in two layers, *i.e*., a „light" phase, which contains mainly the solvent, a small quantity of extracting agent and metal, and a „heavy" phase, which contains a large part of the extracting agent, metal and a low quantity of solvent. The occurrence of the third phase is caused mainly by the reduced solubility of the metal-ligand complex in the non-polar organic phase (Chiarizia *et al.,* 2003). The third phase formation in the extraction of Th (IV), U (IV) and Pu (IV) is well known and largely documented in literature (Jamal *et al*., 2005; Grenthe *et al*., 1992; Kolarik & Melin, 1982; Kotrly, 1985).

The formation of stable emulsions (the third phase) in the uranium purification process by liquid-liquid extraction exhibits to a series of disadvantages, such as:

- important uranium losses (both through physical entrainment and its presence in the structure of stable emulsions);
- important solvent losses (entrained into the stable emulsion mass);
- decrease in the uranium separation and purification efficiency/yield;
- decrease in the processing output of the extraction installation.

The formation of stable emulsions in the uranium extraction - re-extraction operations is caused by: impurities in the aqueous phase; impurities in the organic phase; temperatures below 20^oC in the operating environment, in cold weather when $UO_2(NO_3)_2$ crystallization occurs; decrease in the solution acidity, below 2.8N HNO_3.

The paper presents a statistical modeling of uranium purification by

liquid-liquid extraction in terms of achieving optimum process parameters. The general effect of the optimization consists in uranium decreasing technological losses (by avoiding the third phase formation) and, as a result, in increasing the efficiency of this processing operation by 5%.

In order to achieve the mathematical model, the following parameters were varied: the uranium contents in the aqueous phase, the acidity of the aqueous phase, the TBP concentration in kerosene, and the aqueous: organic phases ratio and that the number of extraction steps, using a factorial experiment 2^{5-2}. The mathematical model obtained by the processing of experimental data describes the dependence of yield on technically and economically significant operational parameters.

2. Experimental

Tri-n butyl phosphate used as an extractant was from FLUCKA with purity 99%. The diluent used was the kerosene Acros Organics (with purity 99%) which has a density of 790–800 kg/m^3 at 15°C, its boiling point range is 200 − 250°C, with aromatic content of max 0.2% (v/v) . Nitric acid was obtained from (MERCK, 65%).

The uranium aqueous solutions (impure uranyl nitrate - AUI) were prepared by dissolving the necessary amount of sodium diuranate – DUNa (obtained from pilot plant (with uranium content > *60* %) with the appropriate amount of concentrated nitric acid and distilled water. All other reagents were analytical grade and their respective solutions were prepared with distilled water. The uranyl nitrate solution used in the experiments had the following characteristics listed in Table 1.

Table 1

Chemical Composition of the Uranyl Nitrate Solution Used in Experiments

Uranium	300 g/L
Free acidity , HNO_3	3.2 N
Cl^-	3.45 g/L
Fe	2.42 g/ L
Mo	0.02 g/ L
Na^+	18.80 g/ L
SO_2^{-4}	0.84 g/ L
SiO_2	0.094 g/ L

The extraction was carried out in 250 ml separating funnel by stirring 2 min. different volumes (25 mL) of aqueous and organic phases (75 ml), corresponding a 1:3 aqueous – organic ratio. To make contact we use an IKA

HS 501 digital shaker. The mixtures were separated after 6 min. by decantation. It is very important to note that no third phase or any precipitation was observed during the extraction process.

Uranium was determined in the aqueous phase by HPG γ –spectral method using an ORTEC multi-channel analyser with Ge detector for γ radiations (0-3 MeV). The concentration of nitric acid in the aqueous phase solutions was calculated using a potentiometer titrator. The amount of uranium extracted by the TBP was determined from the difference between the initial and final concentrations of uranium in aqueous solutions.

3. Results and Discussions

To make modeling uranium purification by liquid-liquid extraction in terms of achieving optimum process parameters, it will be used the method of planning experiments (Panturu *et al*., 2008; Dobre & Marcano, 2007), which allows obtaining significant and sufficient information from a small number of experiments.

The studied variables that occur in the process of purifying uranium by extraction with TBP in kerosene are: uranium content in aqueous phase, aqueous – organic ratio, tri-n butyl phosphate concentration in kerosene, aqueous - organic ratio and number of extraction steps.

In this work we made a relatively large number of experiments that have studied the effects of three variables. Experimental conditions were reached in respect to the experimental matrix, presented in Table 2.

Table 2
The Factors Used in Extraction Factorial Model

Factors	UM	Factor code	Range $x_{jmin} \rightarrow x_{jmax}$	The experiment centre, X_{jo}	Δx_j	Level	
						inf. -	sup. +
Uranium content in aq. phase	g/L	x1	280→320	300	20	280	320
Aqueous: Organic ratio (A:O)	-	x2	1:2.8→1:3.2	1:3	0.2	1:2.8	1:3.2
Extraction steps	-	x3	6→10	8	2	6	10

The experiments were randomly performed in order to avoid a systematic error. Furthermore, it was performed 3 central reproductions (1°, 2°, 3°) for experimental error calculation, presented in Table 3.

Table 3
Value for Extraction Efficiency in the Central Point of the Domain

y_k0	$y_1°$	$y_2°$	$y_3°$
η(%)	98,75	97,63	99,54

The considered regression models for the selected factors are first order polynomial models that are obtained by variation analysis using Design Expert v.6 program.

The regression equation o *expressed depending on the codified terms (1/+1):*

$$Y = 101{,}028 + 7{,}299 \cdot x_1 - 1{,}162 \cdot x_2 - 2{,}476 \cdot x_3 - 5{,}686 \cdot x_1^2 - 0{,}174 \cdot x_2^2 - 4{,}164 \cdot x_3^2 + 1{,}376 \cdot x_1 \cdot x_2 + 3{,}164 \cdot x_1 \cdot x_3 - 0{,}491 \cdot x_2 \cdot x_3 + 0{,}205 \cdot x_1 \cdot x_2 \cdot x_3 \quad (1)$$

Hence, after the elimination of the insignificant interactions, the following regression equations were obtained:

$$Y = 101{,}028 + 7{,}299 \cdot x_1 - 1{,}162 \cdot x_2 - 2{,}476 \cdot x_3 - 5{,}686 \cdot x_1^2 - 4{,}164 \cdot x_3^2 + + 1{,}376 \cdot x_1 \cdot x_2 + 3{,}164 \cdot x_1 \cdot x_3 \quad (2)$$

The accuracy of mathematic model is tested through ANOVA variance of analysis and with Fisher's test. The value of the Fisher's test (F = 217) of the model emphasizes that this is adequate for the experimental data, existing a 4.32% probability that this value to be a simple occurrence.

The partial derivatives of first order were calculated in relation to each variable. The optimum is (0.84, 1.68, -0.02) in the a-dimensional coordinated. Note that the optimal values for x1, x2 and x3 are included in the scope of permissible limits (-1, 1) fixed, X_1 = 316.8 gU/L, X_2 = 1:3.33, X_3=8. The models will be obtained based plot of two parameters the other parameters remaining constant at 0 representing the scope of variation.For extraction yield (Y) will get three response surfaces characterized by the following mathematical models:

$$x_1 = 0 \quad Y = 101{,}028 - 1{,}162 \cdot x_2 - 2{,}476 \cdot x_3 - 4{,}164 \cdot x_3^2 \quad (3)$$

$$x_2 = 0 \quad Y = 101{,}028 + 7{,}299 \cdot x_1 - 2{,}476 \cdot x_3 - 5{,}686 \cdot x_1^2 - 4{,}164 \cdot x_3^2 + 3{,}164 \cdot x_1 \cdot x_3 \quad (4)$$

$$x_3 = 0 \quad Y = 101{,}028 + 7{,}299 \cdot x_1 - 1{,}162 \cdot x_2 - 5{,}686 \cdot x_1^2 + 1{,}376 \cdot x_1 \cdot x_2 \quad (5)$$

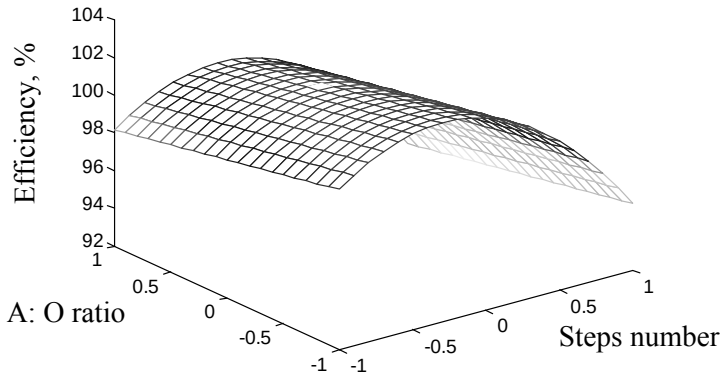

Fig. 1 – Effect of the aqueous – organic ratio and steps number on the efficiency of extraction, when the content of uranium in aqueous phase is maintained to zero value $Y = 101{,}028 - 1{,}162 \cdot x_2 - 2{,}476 \cdot x_3 - 4{,}164 \cdot x_3^2$.

The graphic representations of the mathematical models are presented in Figs. 1,…,3.

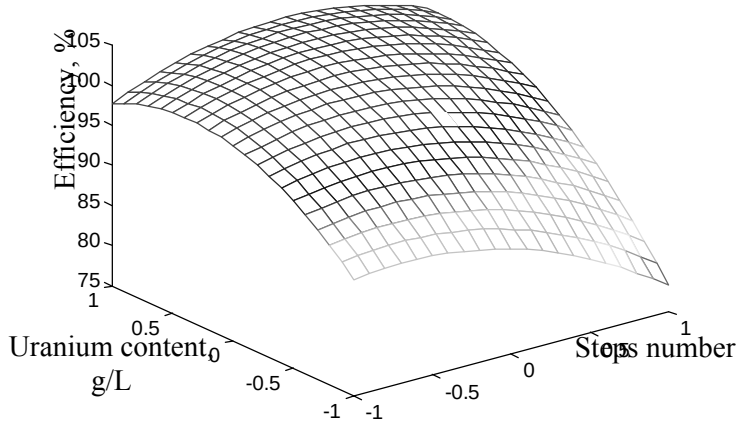

Fig. 2 – Effect of uranium content in aqueous phase and steps number on the efficiency of extraction when the A:O ratio is maintained to zero value $Y = 101{,}028 + 7{,}299 \cdot x_1 - 2{,}476 \cdot x_3 - 5{,}686 \cdot x_1^2 - 4{,}164 \cdot x_3^2 + 3{,}164 \cdot x_1 \cdot x_3$.

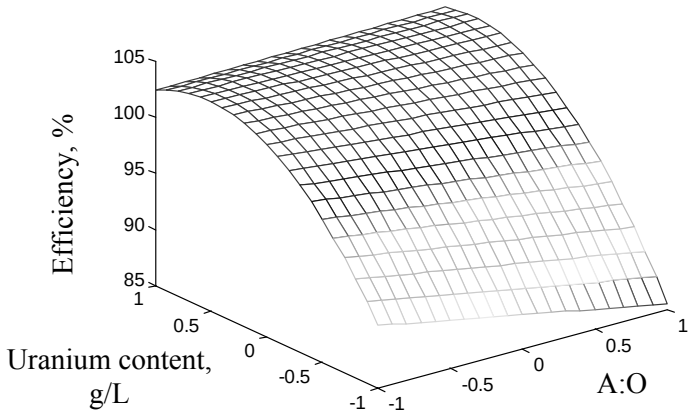

Fig. 3 – Effect of uranium content in aqueous phase and A:O ration on the efficiency of extraction when the steps number is maintained to zero value

$$Y = 101{,}028 + 7{,}299 \cdot x_1 - 1{,}162 \cdot x_2 - 5{,}686 \cdot x_1^2 + 1{,}376 \cdot x_1 \cdot x_2 .$$

4. Conclusion

The mathematical model obtained by the processing of experimental data describes the dependence of yield on technically and economically significant operational parameters.

The recommended optimal parameters necessary to obtain extraction efficiencies over 96 % are as follows: uranium content in aqueous phase - 310 - 315 g U/L; aqueous - organic ratio - 1:3 and steps number - 8.

The proposed mathematical model is able to calculate the extraction efficiencies for uranium for any value of considered parameters (uranium content, aqueous - organic ratio, steps number, free acidity) only in the range of studied experimental values with a precision of 95%.

This paper emphasizes the major factors that influence the uranium extraction efficiency, namely uranium content, aqueous - organic ratio and steps number in the studied experimental values range.

REFERENCES

Panturu E., Filip Ghe., Radulescu R., *Tehnologia recuperarii uraniului din minereuri.* Ed. EdyroPress, 12-15 (2008).

Constantin V., Georgescu P.D., Popa N., Nica L., Petrescu St., Filip Ghe., Radu M., *Procedeu de purificare a uraniului prin extracţie cu soluţie de tri-n-butil fosfat.* Brevet invenţie RO 120630.

Schulz W.W., Navratil J.D., Talbot A.E., *Science and Technology of Tributyl Phosphate, Synthesis. Properties, Reactions and Analysis.* **I**, Florida, 1984.

Schulz W.W., Navratil J.D., Talbot A.E. Bess T., *Science and Technology of Tributyl Phosphate. Selected Technical and Industrial uses*. **II**, *A*, Florida, 1987.

Chiarizia R., Thiyagarajan P., Jensen M.P., Borkowski M., Littrell K.C., *Third Phase Formation in TBP Solvent Extraction Systems as a Result of Interaction Between Reverse Micelles*. Hydrometallurgy, 917-920 (2003).

Jamal Stas, Ajaj Dahdouh, Habib Shlewit, *Extraction of Uranium (VI) from Nitric Acid and Nitrate Solutions by Tributylphosphate/Kerosene*. Periodica Polytechnica Ser. Chem. Eng., **49**, 1, 3–18 (2005).

Grenthe I., Fuger J., Konongs R.J.M., Lemire R.J., Muller A.B., Nguyen-Trung C., Wanner H., Edited by Wanner, H. – Forest, I., *Chemical Thermodynamics 1 (Chemical Thermodynamics of Uranium)*. North-Holland, 1992.

Kolarik Z., Melin G., *Handbook of Inorganic Chemistry UD2*. Edited by Keim, R., Marcus Y., Keller, C., *Springer-Verlag,* Berlin, ch2 - 4, 77 (1982).

Kotrly Š., *Handbook of Chemical Equilibria in Analytical Chemistry*. Ellis Horwood in *Analytical Chemistry*, 1985.

Panturu E., Radulescu, R, Filcenco-Olteanu A., *Statistics Model and Optimization of Uranium Extraction in Ultrasounds Field in Sulphuric Acid Medium*, CHEMPOR 2008, Book of Abstracts of the 10th International Chemical and Biological Engineering Conference, 465-466 (2008).

Dobre T., Marcano J.S., *Chemical Engeneering. Modelling, Simulation and Similitude.* Wiley VCH, 350 – 390 (2007).

MODELE NUMERICE PENTRU PURIFICAREA URANIULUI PRIN EXTRACŢIE LICHID – LICHID

(Rezumat)

În lucrarea de faţă se prezintă un studiu privind modelarea statistică a rezultatelor experimentale obţinute la purificarea uraniului prin extracţie lichid – lichid. Pentru realizarea modelului matematic au fost variaţi următorii parametrii: conţinutul de uraniu în fază apoasă, aciditatea fazei apoase, concentraţia TBP-ului în kerosen, raportul fazelor apoasă:organică şi respectiv numărul treptelor de extracţie, folosind un experiment factorial 2^{5-2}. Modelul matematic obţinut prin procesarea datelor experimentale descrie dependenţa randamentului de extracţie de parametrii operaţionali semnificativi din punct de vedere tehnic şi economic fiind capabil să calculeze eficienţa procesului de extracţie, în domeniul studiat, cu o precizie de 95%. Efectul general al optimizării constă în reducerea pierderilor tehnologice de uraniu prin evitarea formării fazei a treia. Formarea emulsiilor stabile în operaţiile de extracţie – reextracţie a uraniului se datorează: impurităţilor de fază apoasă, impurităţilor de fază organică şi condiţiilor de operare. Modelul matematic obţinut prin procesarea datelor experimentale este capabil să calculeze eficienţa extracţiei în plaja de valorilor experimentale, cu o precizie de 95%.

BULETINUL INSTITUTULUI POLITEHNIC DIN IAŞI
Publicat de
Universitatea Tehnică „Gheorghe Asachi" din Iaşi
Tomul LVII (LXI), Fasc. 4, 2011
Secţia
ŞTIINŢA ŞI INGINERIA MATERIALELOR

THE DETERMINATION OF A CONCEPTUAL MODEL OF THE TECHNOLOGICAL SYSTEM OF THERMAL ENERGY RECOVERY FROM WASTEWATERS

BY

TIMEA GABOR*, TIBERIU RUSU and VIOREL DAN

Universitatea Tehnică Cluj-Napoca,
Facultatea de Ingineria Materialelor şi a Mediului

Received: April 14, 2011
Accepted for publication: June 27, 2011

Abstract. Finding new sources of energy that can contribute to reduce energy consumption as well as reduce emissions of greenhouse gases, is a basic present and future concern of the mankind. This is the reason for which the heat of wastewaters is seeking to be recovered. Wastewaters have a relatively high temperature once they enter the sewage drainage pipes. Without being recovered, these heat leakages are dumped into the environment when the wastewaters enter the sewer pipes and treatment plants. The utilization of this thermal energy for domestic hot water preparation is an alternative to recover it.

The elements that define a system for heat recovery from wastewater are presented in this paper. The identification of the parameters that determine the heat transfer was the main objective of this paper. This study started from a conceptual model of the technological system, which involves the inputs and outputs characterized by technological and physic-chemical properties, measurable or imposed. These properties are the variables of the technological process. In conclusion, a theoretical system model was approached taking into account the disturbances that affect the technological system of heat recovery from wastewater.

Key words: wastewater, heat transfer, heat exchanger, heat balance.

* Corresponding author e-mail: Timea.Gabor@im.utcluj.ro

1. Introduction

The residual energetic sources are, nowadays, on focus. The rapid development of those processes for obtaining energy from wastes is a starting point. Wastewaters are considered liquid wastes resulted from domestic and industrial activities (Gabor *et al*., 2011). This residual thermal energy is possible to be recovered and recycled by using heat exchangers.

Waste heat is heat, which is generated in a process by way of fuel combustion or chemical reaction, and then „dumped" into the environment even though it could still be reused for some useful and economic purpose. The essential quality of heat is not the amount but rather its „value". The strategy of how to recover this heat depends in part on the temperature of the waste heat gases and the economics involved (Popa, 1971).

Large quantity of hot flue gases is generated from boilers, kilns, ovens and furnaces. If some of this waste heat could be recovered, a considerable amount of primary fuel could be saved. In any study of waste heat recovery, it is absolutely necessary that there should be some use for the recovered heat. Typical examples of use would be preheating of combustion air, space heating, or pre-heating boiler feed water or process water. The following Table 1 lists some heat sources in the low temperature range. Low temperature waste heat may be useful in a supplementary way for preheating purposes (B.E.E.).

Table 1

Waste Heat Temperature at Low Temperature Range from Various Sources

Nr.crt.	Source	Temperature [ºC]
1.	Process steam condensate	55 ÷ 88
Cooling waterfrom:		
2.	Furnaces doors	32 ÷ 55
3.	Bearings	32 ÷ 88
4.	Welding machines	32 ÷ 88
5.	Injection molding machines	32 ÷ 88
6.	Annealing furnaces	66 ÷ 230
7.	Forming dies	27 ÷ 88
8.	Air compressors	27 ÷ 50
9.	Pumps	27 ÷ 88
10.	Internal combustion engines	66 ÷ 120
11.	Air conditioning and refrigeration condensers	32 ÷ 43
12.	Liquid still condensers	32 ÷ 88
13.	Drying, baking and curing ovens	93 ÷ 230
14.	Hot ptocessed liquids	32 ÷ 232
15.	Hot ptocessed solids	93 ÷ 232

2. Defining Elements of the Waste Heat Recovery System

Heat transfer consists of a sequence of processes occurring in the heat exchanger. Setting the output temperature of the pre-heated fluid, and determining both the stages and the parameters of each stage, are representing the heat recovery process from wastewater.

From a phenomenological point of view, the process of heat recovery from wastewater can be analyzed at the level of components (micro process) or on the entire assembly of heat recovery unit (macro process).

The material and energy balances, for each phase in part or for the whole process, are necessary to be established for the quantitative description of the heat transfer process. The preparation of those balances requires good knowledge of the flow sheet (Leca *et al*., 1998).

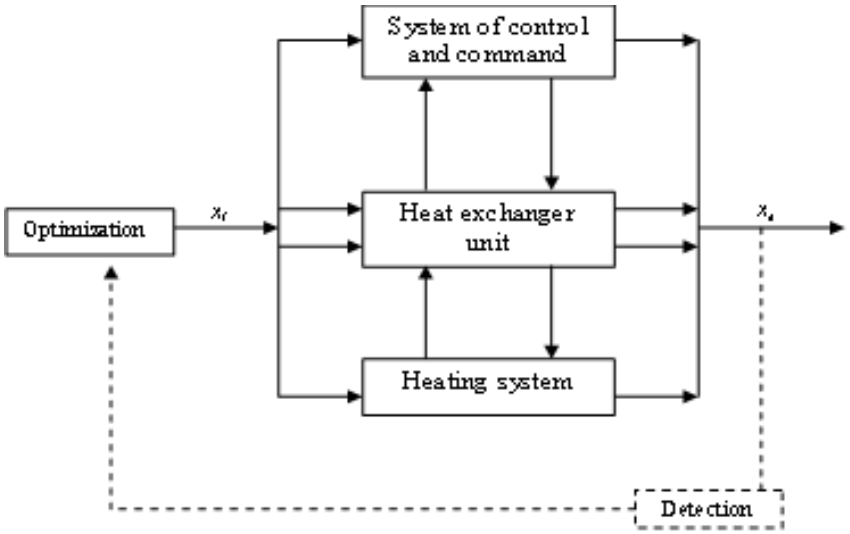

Fig. 1 – The block diagram technological system of the thermal energy recovery from wastewater.

The technological system of heat recovery from wastewater includes the process of heat transfer, unit and technological equipment and the connectors between them. The elements of the technological system are independent and form a single integer assembly.

This technological system, like any system is composed of inputs and outputs. The inputs consist of wastewater and cold water from the mains (fluids 1 and 2) and the outputs from cooled sewage water and from pre-heated water.

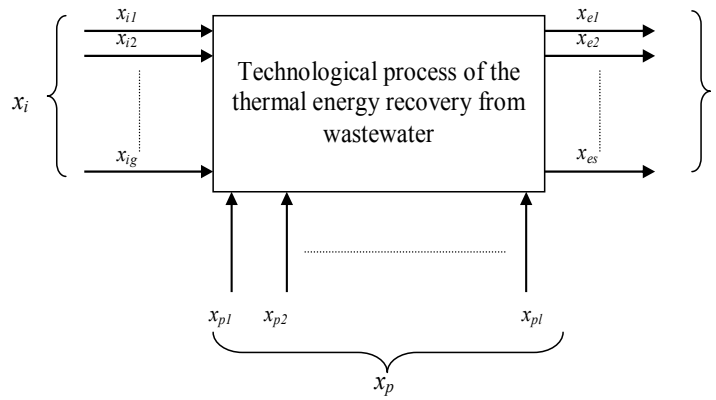

Fig. 2 – The proper variables of the technological process of heat recovery from wastewater.

Both inputs and outputs are characterized by physic-chemical properties as well as technological and economic properties, which can be measured or determined and vary quantitatively or qualitatively. The values of these properties are variables or inputs and outputs of the residual heat recovery process. Due to input variations, the process may be disrupted, which has implications for the output. The interferences can be compensated both by adjustment operations and control operations. The structure of the heat recovery technology can be presented as shown in Fig. 1 if the characteristics mentioned above are taken into account.

There are three fluxes, namely material, energetic and informational. The informational flux can be more or less obvious and evolved depending on the technological equipment, taking into account the human factor which has a primary role. This flux offers the possibility to optimize and direct the process with the help of computer, the information being the main part of the optimization (Leewongtanawit & Kim., 2009).

The analysis of the technological process of heat recovery from wastewater in terms of causality is also required. Thus knowing a series of initial information, other information can be determined by specifying certain conditions.

Process variables can be classified as follows:

- variables or inputs (x_i), which are independent of the process. Their values directly influence the process and can be modified as the process rolls on the desired direction;
- variables or outputs (x_e), which depend directly on the process;
- variables or disturbing values (x_p), which directly affect the process, but can not be changed at will.

The inputs and the disturbing values are also called variables of control because they affect the outputs, and the outputs are also called controlled variables. The variables used in the heat recovery process are shown in Fig. 2. The system is characterized by mutual links between these variables, represented by a set of performance functions such as:

$$y = f\left(x_1; x_2; ...; x_n\right) \tag{1}$$

The technological regime in which the performance function reaches an extreme value is considered the optimal condition. The optimization problem, in the case of the function presented in relation 1, consists of determining the values of variables x_1, x_2, ..., x_n for which the performance function y has a maximum (or minimum). Variabiles $x_1, x_2, ..., x_n$:

$$f_j\left(x_1, x_2, ..., x_n\right) = 0, \quad j = 1,2,...,k \quad k < n \tag{2}$$

are subjected to the following restrictions:

$$A_i \le x_i \le B_i; \;\; x_i \ge 0, \quad i = 1,2,...,n \tag{3}$$

The relation 2 usually represents the equation of heat or material balance of the technological process, and the inequalities (relation 3) represent the physical limitations or the nature of the technical requirements (Carabulea & Carabogdan 1982).

Many of the variables of the heat recovery process from wastewaters are of deterministic nature (vary continuously as well-defined laws, which allow the performances of the process to be defined by the causes of the process) and of stochastic nature (occur aleatory or randomly and often discreet, making the performances of the process do not directly track the causes that produce them).

3. Conceptual Aspects of an Optimal Heat Transfer

In the block diagram (shown in Fig. 1), the informational flux is marked in addition to material and energy fluxes.

A special attention should be given to the informational flux in the optimal control of the technological process. Finding a model of the process, based on which the optimal components should be determined, is much more convenient than carrying out a large number of practical tests, aimed at obtaining the optimal solution.

The informational flux is also a component of the control and command system of the technological activity. The informational system, associated with optimal control of the technological process of heat recovery from wastewaters, is composed of all information, sources and levels of consumption, channels of

circulation, procedures and means of handling information. The system should be structured such as to allow the application of methods in order to obtain the optimal decision by means of rules.

Two main ways to optimize the technological process of heat recovery from wastewaters are presented in Fig. 3:

- external optimization (open loop), where after determining the optimal decision, is applied in non-automatic way through the human element;
- internal optimization (closed loop), where the optimal decision is applied automatically, through an automatic element.

This two ways of optimizing heat transfer process are closely connected. The solution of the optimization problem emerges from the complete knowledge of the optimization criterion. Once known, the optimum solution should be seek.

Finding the optimum solution for the process of heat recovery from wastewaters requires the run through the following steps:

1. elaboration of the model that describes the process;
2. the developement of the optimization criterion;
3. setting the optimization algorithm;
4. solving the problem.

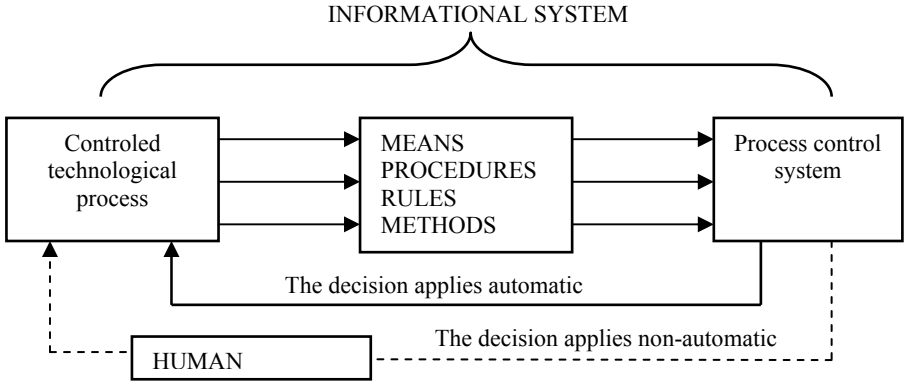

Fig. 3 – Informational system associated with optimal control of the technological process of heat recovery from wastewater.

The determination of the optimal solution is done by setting the values of independent variables in order to get the best value for the performance function (the optimized function). The essential step in solving the optimization problem is the selection of the performance function of analyzed process. The automatic control system is used to ensure the optimal regime of heat transfer and is represented schematically in Fig. 4. Setting the automatic system for mathematical modeling of thermal energy recovery process includes observation of the phenomena, elaboration of mathematical model, algorithm development for solving the model and the utilization of equipment designed to achieve optimal solution.

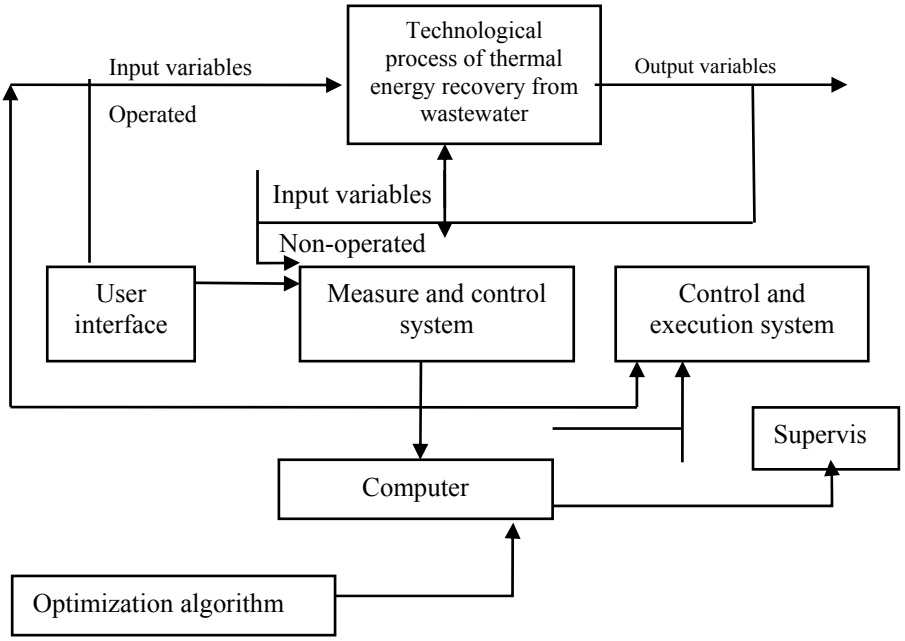

Fig. 4 – Automatic process control system of heat recovery from wastewater.

4. Identification of the Parameters of the Heat Recovery Process

The heat exchanger is composed of low-temperature heat pipes, because the temperature of wastewaters (heat source) is low (Tsai *et al*., 2010).

The heat exchanger pipes are positioned in a beam, being kept at middle by a central plate, which is also used to separates the unit into two parts. One part is for the primary fluid circulation (wastewater) which gives rise to heat that vaporizes the working fluid in the heat exchanger tubes. The working fluid condenses afterwards, the heat being succumbed to the cold water in the second part of the heat exchanger (Neaga & Mărunţelu, 2005).

The heat recovery process from wastewaters aims to reduce thermal pollution by stopping the discharge of warmer industrial wastewaters into drains, to reduce emissions of greenhouse gases and heat gain through the utilization of residual thermal energies.

The following parameters are involved in the case in which the heat of the warm industrial wastewater is transferred to the cold water circulating through the piping (Teberean, 2007).

- temperature, [°C];
- flow, [m^3/h];
- flow rate, [m/s];
- heat-transfer surface, [m^2];

- heat pipes properties: the convection coefficient of the working fluid in case of evaporation (α_{evap}) or condesation (α_{cond});
- pressure, [bar].

The transfer process is influenced by the properties of the technological system for waste energy recovery:

a) the thermic-physical proprerties of wastewater:

- thermal convection coefficient, $\alpha_{ext}^{1}\ \left[W/m^2 grad\right]$;
- specific heat, c_1 [J/kg·°C];
- temperature, t_1' [°C];
- input flow, V_1 [m^3/h];
- density, ρ_1 [kg/m^3];
- flow rate, w_1 [m/s];
- thermal diffusivity coefficient, a [m^2/s];

  $a = \dfrac{\lambda}{c \cdot \rho}$, characterizes wastewater capacity to conduct heat.

b) the physical properties of heat exchanger with heat pipes:

- outer length of heat exchanger, L [cm];
- outer width of heat exchanger, l [cm];
- outer height of heat exchanger, h [cm];
- wall thickness, d_p [cm];
- thickness of the separation wall, d_d [cm];
- height of the lower ”room”, h_i [cm];
- height of the uper ”room”, h_s [cm];
- outer radius of the heat pipes, R_e [cm];
- inner radius of the heat pipes, R_i [cm];
- distance between the tube and the lower wall, d_i [cm];
- distance between the tube and the uper wall, d_s [cm];
- fabrication material of: the wall, the separation wall and the tubes;
- working fluid circulating in heat pipes;
- overall heat-transfer coefficient of working fluid in case of evaporation;
- overall heat-transfer coefficient of working fluid in case of condensation.

c) the physic-chemical properties of cold water:

- inlet temperature, t_2' [°C];
- density, ρ_2 [kg/m^3];
- output flow, V_2 [m^3/h];
- flow rate, w_2 [m/s];
- specific heat, c_2 [J/kg·°C];

- thermal storage coeficient, b [$W \cdot s^{1/2}/m^2 \cdot °C$];
  $b = \sqrt{\lambda \cdot c \cdot \rho}$, it characterizes the water ability of storing the heat.

The values of these thermal and physical properties vary widely depending on the thermal conductivity of wastewaters and the properties of heat pipes, and depends on (Mostafa *et al*., 2007).

- the fluids flow;
- wastewaters composition;
- insulation of pipes and heat exchanger unit;
- heat balance of the heat exchanger unit;
- the efficiency of the heat exchanger unit;
- the overall heat-transfer coefficient;
- pressure losses in the heat exchanger unit.

Each of the parameters and their influencing factors, mentioned above, contributes in some degree to determine the thermal regime. Based on the analysis performed on the entire process of heat recovery from wastewaters, the following parameters can be mentioned as independent variables of the process: Physical parameters of the heat pipes; The thermal and physical properties of cold water; The thermal and physical properties of cold wastewaters; Heat-transfer surface; The number of heat pipes.

The following parameters are considered as dependent variables in the process of heat recovery from wastewaters: the inlet temperatures of cold water as well of wastewater, the discharges of wastewater and cold water, and the weight flows of the two fluids, the rate flow and the pressure of both fluids.

5. Conclusion

Optimal control of heat recovery process is a necessity for further developments in this area in oreder to achieve economic indicators at convenient values. This requires the computing of the process in the optimal regime, allowing the heat transfer without the degradation of the material, in the shortest time and with maximum economy.

This waste heat recovery technology from industrial wastewater must satisfy the physical, chemical, economic and environmental standards, but also this technology must present a low degree of pollution.

The energy security and the control of climate change must be subjected to an integrated approach. It is important to devise strategies in terms of cutting-edge technologies that are needed to be energy efficient and to use waste heat sources, such as to ensure a security of supply, for which the consumption should be controlled, at a reasonable price and, not least, to protect the environment.

Acknowledgement. This paper was suported by the project POSDRU 6/1.5/S/5, project co–founded from European Social Found through Sectorial Operational Program Human Resources 2007–2013.

REFERENCES

*** Bureau of Energy Efficiency (BEE), *Tips for Energy Conservation for Industrie,* New Delphi, source: http://www.bee-india.nic.in/miscellaneous/documents /useful_ownloads/TipsforEnergyConservationforIndustries.pdf;

Carabulea A., Carabogdan I.Gh., *Modele de bilanţuri energetice reale şi optime.* Editura Academiei Republicii Socialiste Române, Bucureşti, 73-93 (1982).

Gabor Timea, Rusu T., Dan V., *Heat Recovery from Wastewater Using Heat Exchangers and Heat Pumps.* II. Karpat-Medencei Kornyezettudomanyi Konferencia, **I**, Editura Abel, Cluj-Napoca, 160-164 (2011).

Leca A, Mladin, E.C., Stan, M., *Transferul de caldură şi masă.* Editura Tehnică, 1998.

Leewongtanawit., B., Kim., J.K., *Improving Energy Recovery for Water Minimisation*. Energy, **34**, 880-893 (2009).

Mostafa A. Abd El-Baky, Mousa M.Mohamed, *Heat Pipe Heat Exchanger for Heat Recovery in air Conditioning*. Applied Thermal Engineering, **27**, 795-801 (2007).

Neaga C., Mărunţelu S., *Procese tranzitorii în funcţionarea tuburilor termice gravitaţionale.* IV Conferinţă Naţională de Echipament Termomecanic clasic şi Nuclear şi Energetică Urbană*,* Universitatea Politehnică, Bucureşti, 127-130 (2005).

Popa B., *Recuperarea căldurii în industrie*. Editura Tehnică, Bucureşti, 1971.

Teberean I., *Termotehnică şi transmiterea căldurii*. Editura U.T. PRES, 2007.

Tsai T.E., Wu G.W., Chang C.C., Shih,W.P., Chen S.L., *Dynamic Test Method for Determining the Thermal Performances of Heat Pipes*. International Jurnal of Heat and Mass Transfer, **53**, 4567-4578 (2010).

STABILIREA MODELULUI CONCEPTUAL AL SISTEMULUI TEHNOLOGIC DE RECUPERARE A ENERGIEI TERMICE DIN APELE UZATE

(Rezumat)

Găsirea unor noi surse de energie care pot contribui la scăderea consumurilor energetice şi reducerea emisiilor de gaze cu efect de seră este o preocupare de bază a prezentului şi viitorului omenirii. Din acest motiv se caută soluţii pentru recuperea căldurii din apele uzate. Odată cu părăsirea conductei de drenaj apa uzată are o temperatură destul de ridicată. Această căldură este disipată în conductele de canalizare şi staţiile de epurare fără a fi recuperată. O alternativă pentru recuperarea acestei energii termice este utilizarea acesteia pentru prepararea apei menajere calde.

În această lucrare au fost studiate elementele care definesc un sistem de recuperare a energiei termice din apele uzate. Obiectivul principal a fost identificarea parametrilor care determină transferul de căldură. S-a plecat de la un model conceptual al sistemului tehnologic ce comportă intrări şi ieşiri caracterizate de proprietăţi tehnologice, fizico-chimice, măsurabile sau impuse. Aceste proprietăţi reprezintă variabilele procesului tehnologic. În concluzie s-a abordat un model din teoria sistemelor cu luarea în considerare a perturbaţiilor asupra sistemului tehnologic de recuperare a energiei termice din apele uzate.

BULETINUL INSTITUTULUI POLITEHNIC DIN IAŞI
Publicat de
Universitatea Tehnică „Gheorghe Asachi" din Iaşi
Tomul LVII (LXI), Fasc. 4, 2011
Secţia
ŞTIINŢA ŞI INGINERIA MATERIALELOR

STUDY ABOUT THE MAIN INFLUENCES ON MATERIALS FLOW IN FRICTION STIR WELDING PROCESS

BY

ANTONIA DIANA GHEORGHIU*, ROMEU CHELARIU and NICANOR CIMPOEŞU

"Gheorghe Asachi" Technical University of Iaşi

Received: April 27, 2011
Accepted for publication: June 27, 2011

Abstract. The paper deals with some aspects concerning the material flow during friction stir welding process. The experimental work conducted on different materials suggests that beside the recognized parameters – welding speed, rotational speed, pin geometry and so on, material properties must be considered. In this category one must take into account the kinetic coefficient of friction between tool and material as well as the internal friction coefficient. Both of them are part of the flow process and influence the microstructure into the weld. The work proves also that pin tilt angle has a substantial effect on the weld profile and soundness.

Key words: friction stir welding (FSW); material flow, coefficient of friction, internal friction.

1. Introduction

Currently, friction stir welding (FSW) process represents a new but tested method for welding aluminum and its alloys, especially high-strength

* Corresponding author e-mail: cutlutdig@yahoo.com

alloys. It is an environment friendly process that takes place in the solid state of the parts to be welded; no consumables are required.

The process is carried out by plunging a rotating tool into the interface of two clamped sheets. The rotating tool is composed from a primary cylindrical body ended with a concentric smaller tip, the pin. The free horizontal surface of the primary body is called shoulder. The pin is inserted into the pieces until the shoulder touches the surface of the materials to be welded, and then the tool moves along the weld line. The pin body shape design accepts different forms. As the tool moves, complex friction –especially on the shoulder-material surfaces– and deforming processes are simultaneously occurring, both heat generating ones. Heat sustains the plastic flow so bonding can occur between the surfaces.

It has been accepted that the FSW joint consists of four different regions. These are: the unaffected base metal; heat affected zone (HAZ); thermo-mechanically affected zone (TMAZ) and the friction stir processed zone, also called the nugget. The formation of above regions is affected by the material flow.

The finite weld exhibits a special kind of asymmetry, a consequence of the flow pattern. As the tool rotates into the material, on one side the rotational velocity and the travel speed has the same orientation, advancing side, while on the other side of the weld axis, the vectors are opposite, retreating side.

The flow of material during FSW is a complex process. Despite numerous investigations the metal flow into the weld is not completely understood. Some studies have compared material flow during FSW with wrought metal processes and supposed that weld nugget development is an extrusion process. It has been supposed that the nugget forms as a volume of material from the metal surface is extruded into the joint during each revolution of the tool (Hamilton *et al*., 2007). Also, a forge process occurs under the rotating shoulder. Most of the researchers agree that the main stress and, consequently, the strain into the weld is the shear one.

A more considerate study (Schmidt, *et al*., 2006) dedicated to the material flow divide the shear layer into specific zones, as follows. The shear layer closest to the pin is the rotation zone; a transition zone which consists of the material which is moved between the rotation zone and the parent material from the advancing side at the retreating. Between the transition zone and the unaffected material the authors propose a third zone, the deflection zone, a material layer characterized by low deformation level.

Another specific aspect of the FSW macrostructure is the so called “onion ring” structure, (Chen *et al*., 2007; Elangovan & Balasubramanian, 2007; Hamilton *et al*., 2007; Kumar & Kailas, 2007). The weld nugget is mainly characterized by this banded appearance but there are cases when it can not be quite evident, even if one of the accepted mechanisms involves thin layers of material that move toward the weld, (Hamilton *et al*., 2007; Kumar & Kailas,

2007; Schmidt, *et al*., 2006). It seems that there are few other conditions influencing the flow pattern into the FSW process.

The main process parameters are tool rotation speed, traverse speed or welding speed, tool (pin) geometry, and tool inclined angle. Tool angle is the angle between the tool axis and the normal to the surface of the sheets to be welded.

Traverse velocity and the rotational speed are the parameters controlling heat formed within process in deep connection with the shoulder/pin diameters ratio. Pin geometry is considered to influence above all the material flow and the nugget structure. Material properties are rarely mentioned in the dedicated literature.

The aim of this article is to explore the influence that an estimated coefficient of friction can undergo on the material flow during the process.

2. Experimental Conditions

First of all it must be emphasized that there are two kinds of friction, related to how the surfaces are moving relative to each other. In the FSW process the tool surfaces are simultaneously rotating and translating relative to the parts, and then it is obviously that a kinetic friction occurs. In this case the friction effect is smaller than in the static one.

Another aspect is the material internal friction that is the force resisting motion between material layers while it undergoes the deformation process. FSW deals with dry kinetic friction between surfaces and an intense internal friction. Both phenomena must be considered into a study.

In the present work different materials where used in order to compare the material flow. The chosen materials were: putty, plasticine, and lead.

Although putty and plasticine are amorphous materials, they are capable to simulate the material flow. Consider that plasticine has been used to model extrusion as well. Both materials offer some advantages: low price, little effort, different colors with almost the same properties, so a good color contrast that can improve macroscopic analysis. Between putty and plasticine there is a noticeable difference: when using putty it can be assumed that into the process lubricant friction occurs, so the coefficient of friction differs from that of the plasticine.

For the experiments putty and plasticine bars (different colors) of 10 x 20 x 150 mm were manually processed and kept two colors together in special designed boxes. The boxes were designed for the ease of manipulation of the amorphous samples during the process as well as before and after. Lead strips of 6 x 25 x 150 mm were prepared (cast and rolled to the desired dimensions).

Weld characteristics are highly dependent on operating parameters, such as tool profile, pin / shoulder diameter ratio, tool rotational velocity, tool traverse speed and tool tilt angle.

In this study tools with straight cylindrical pin with 6 mm diameter and 5mm length were used. In the experiments done on amorphous materials and lead the shoulder / pin ratio took the following values: 2, 3 and 4. Rotational speed of 215 and 350 rpm with transverse velocities of 60, 120 and 160 mm/min were used. The shoulder had no included angle. The tool inclined angle was of 0 and 3 degrees. The shoulder was inserted into the surface of the base material for 1mm.

As power source a classic milling machine was used.

3. Experimental Results

3.1. Influence of the Shoulder / Pin Diameter Ratio

Putty samples show little or no influence for the ratio value on the material flow. The main influence is exhibited on the flash form and volume in the retreating side, higher as the ratio increases, Fig. 1. The effect can be attributed to the higher peripherical velocity and to the increased quantity of displaced material. Plasticine samples are more sensitive to this factor. Better closure of the joint is obvious and also a better mixture of the parts into the section, Fig. 2.

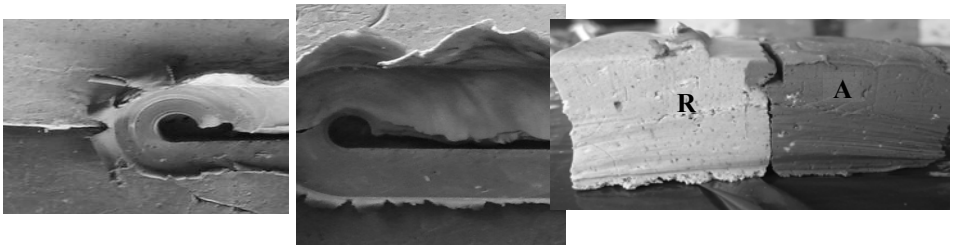

a *b* *c*

Fig. 1 – Plan view and section of FSW joints on putty – influence of the shoulder / pin ratio and typical material displacement. *a* – plan view for shoulder/diameter ratio equals 2; *b* – shoulder/diameter ratio equals 3; *c* – flow of material in section A-advancing side; R –retreating side.

On the putty samples one can assume that is a lubricate friction case, as the material has a great amount of mineral oil into its composition. By consequence, small layers are displaced in the top of the samples and in the middle of them too. As can be seen in Fig. 1*c*, material from the advancing side is carried out by the pin and left in the retreating side. Except the surface layer no displacement occurs from the retreating side to the advancing side. By consequence, no stir occurs and no mixing of the two materials takes palace. This is an extreme situation, but it suggests two aspects. The principal material displacement is from the advancing side. The shoulder has little effect on the

material displacement but contributes to the mixing effect by the banding effect of the displaced material, as can be seen in the same photo.

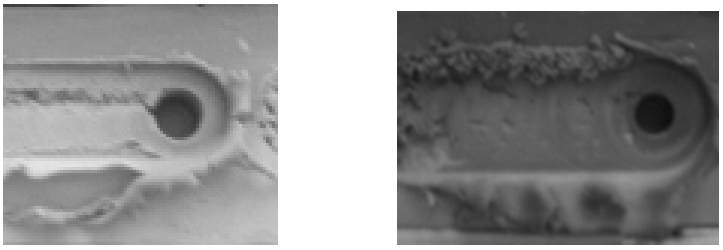

a *b*

Fig. 2 – Plan view of FSW joints on plasticine – influence of the shoulder / pin ratio.
a – plan view for shoulder/diameter ratio equals 2;
b– plan view for shoulder/diameter ratio equals 3.

Increasing the ratio has no effect in putty sample case. Plasticine samples are sensitive to the ratio value, as can be seen in Fig. 2. The effect is concentrated especially into the samples surfaces, Fig. 2, but some effect deep inside the joint can also be demonstrate, Fig. 3.

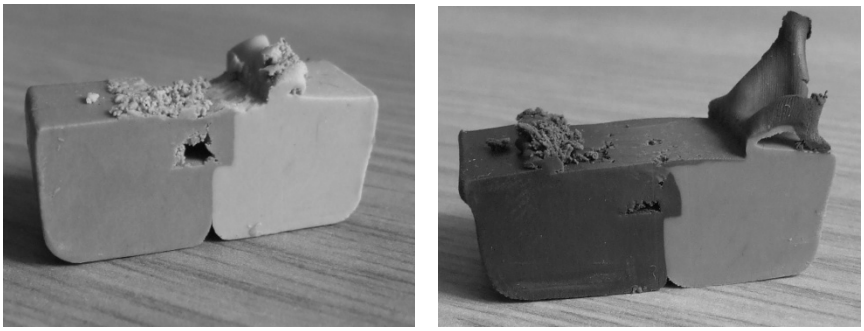

a *b*

Fig. 3 - Transverse sections of FSW joints on plasticine – influence of the shoulder / pin ratio. *a* – shoulder/diameter ratio equals 2; *b* – shoulder/diameter ratio equals 3.

As can be seen in the photos, increasing the surfaces ratio leads to a better filling of the space left behind by the pin. For ratio value 2, the transverse section exhibits the same profile as the putty ones, Fig. 3*a*. The forging effect is much better in this case and so the plan view has a better shape, thanks to the improved friction properties. Increasing the ratio value continuously improves the material flow, Fig. 3*b*. The empty space is almost fulfilled with material and a small discontinuity, a channel type defect, rests at the joint root. Material flow is more complex, the displaced material loses its rigid layer shape. It is difficult

to select between the possible effects of the ratio values: is about heat that forms in this space or just the forging effect. Rising supplementary the ratio value has no effect on the material flow.

3.2. Effect of the tilt Angle of the Tool

Using same welding parameters, i.e. welding speed, rotational speed and same tool, the inclination of the tool has been changed from 0 to 3 degrees.

For putty samples this change has little to no response. Plan view demonstrates a small improvement, the channel is almost closed, but transverse section proves no changes.

In case of plasticine samples, the inclination of the tool has spectacular effect, as can be seen in Fig. 4.

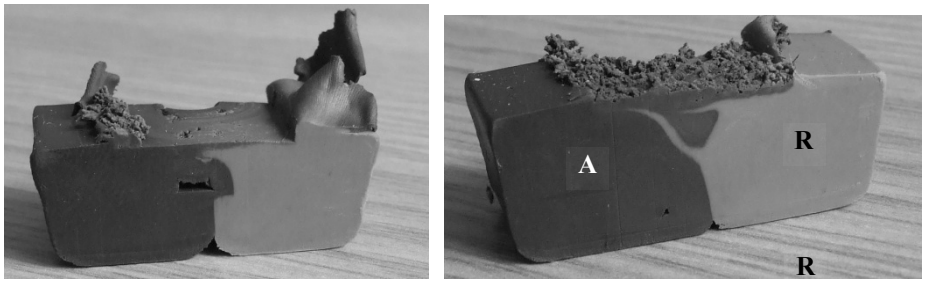

a *b*

Fig. 4 – Transverse sections of FSW joints on plasticine – influence of the tool inclined angle; *a* – tilt angle 00; *b* – tilt angle is 30.

One can notice that on the same experimental conditions, the use of an inclined tool has as consequence full closure of the channel. The most spectacular effect, especially for plasticine samples were different colors are used, is the complex material flow. Both materials are displaced from one side to the other. The forging effect changes dramatically the way material from the retreating side reacts. It doesn't just close the channel, but from the bottom of the channel some material from the retreating side is pushed through the surface. The tilt angle effect is rather inconvenient with respect to the surface quality.

3.3. Experiments on Lead

The purpose of this experimental step is to connect the data from the amorphous materials to the metallic, crystalline ones.

Sample in Fig. 5*a*, was obtained with a tool with shoulder/pin diameters ratio equal to two. It can be seen the lack of continuity, but the channel is displaced. The increased coefficient of friction helps the material displacement but the small shoulder diameter does not provide enough heat. Simply

increasing the ratio is not a complete solution, Fig. 5*b*. Shoulder rotational movement has as result "bridges" of materials that closes periodically the gap. Using tile angle the aspect of the surface for the lead samples has no longer discontinuities. It must be emphasized that in all the cases at the end of the joint surface flow of the material changes, even in the most effective case. In this peculiarity there are two hypotheses. First, as lead's melting temperature is not high, substantial heating develops and improves plasticity. Second, for lead properties the included angle of the tool is not a good choice. Lead from the beginning adheres to the pin and shoulder. The accumulation is of material later acts like a brow, tears out tiny fragments from the lead.

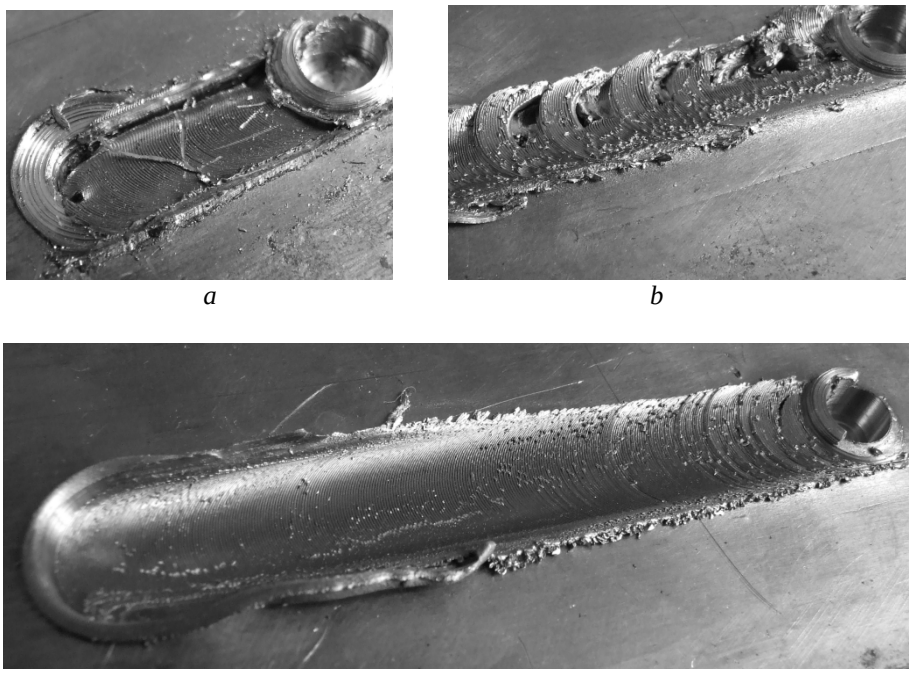

a *b*

c

Fig. 5 – Plan view of FSW processed material, lead. n=320rpm vs = 100mm/:
a – shoulder/pin diameter ratio = 2, tilt angle=0; *b* – shoulder/pin diameter ratio = 3, tilt angle=0; *c* – shoulder/pin diameter ratio = 3, tilt angle=3.

4. Conclusions

- the coefficient of friction between material and tool as well as the internal friction changes the flow of the base material;
- flow material pattern is sensitive at the tool' tilt angle and shoulder/pin ratio.

REFERENCES

Chen O.Z.W., Pasang T., Qi Y. - *Shear flow and Formation of Nugget Zone During Friction Stir Welding of Aluminium Alloy 5083*. Materials Science and Engineering, 2007. Available from: http://www.sciencedirect.com/

Elangovan K., Balasubramanian V., *Influences of Tool Pin Profile and Welding Speed on the Formation of Friction Stir Processing Zone in AA 2219 Aluminium Alloy*. Journal of Materials Processing Technology, 2007. Available from: http://www.sciencedirect.com/

Hamilton C., Dymek S., Blicharski M., *A Model of Material Flow During Friction Stir Welding, Materialscharacterization*, 2007. Available from: http://www.science direct. com/

Kumar K., Kailas Satish V., *The Role of Friction Stir Welding Tool on Material Flow and Weld Formation.* Materials Science and Engineering, 2007. Available from: http://www.sciencedirect.com/

Schmidt H.N.B., Dickerson H.N.B., Hattel J.H., *Material Flow in Butt Friction Stir Welds in AA2024-T*3. Acta Materialia, **54**, 1199–1209 (2006), Available from: http://www.sciencedirect.com/

STUDIU PRIVIND PRINCIPALELE INFLUENŢE ASUPRA CURGERII MATERIALELOR ÎN CADRUL SUDĂRII FSW

(Rezumat)

Lucrarea prezintă câteva aspecte legate de modul de curgere al materialelor pe durata sudării prin frecare cu element activ rotitor. Studiul experimental realizat pe diferite materiale sugerează că în afara parametrilor recunoscuţi – viteza de sudare, turaţia, geometria elementului rotitor, proprietăţile materialelor reprezintă un factor cu importanţă in proces. Dintre proprietăţi, coeficientul de frecare dintre material şi umărul elementului precum şi coeficientul de frecare internă prezintă o importanţă aparte. Ambii coeficienţi influenţează procesul de curgere şi implicit microstructura îmbinării. De asemenea se demonstrează că unghiul de atac al sculei modifică profilul îmbinării şi calitatea ei.

BULETINUL INSTITUTULUI POLITEHNIC DIN IAŞI
Publicat de
Universitatea Tehnică „Gheorghe Asachi" din Iaşi
Tomul LVII (LXI), Fasc. 4, 2011
Secţia
ŞTIINŢA ŞI INGINERIA MATERIALELOR

STEPS IN CONCEIVING AN EXPERT SYSTEM FOR CRYOGENIC TREATMENT OF STEELS

BY

DIANA ANTONIA GHEORGHIU*, VASILE BULANCEA and ŞTEFAN LUCIAN TOMA

"Gheorghe Asachi" Technical University of Iaşi

Received: April14, 2011
Accepted for publication: June 27, 2011

Abstract. The present paper has as purpose to highlight the main steps that a team must cover for a sustainable expert system design with appliance in cryogenic treatment of the steels. Comparing the stages that some consecrated expert systems did follow it seems very reasonable that an expert system must start making up the adequate data base. This should be open to as many as possible beneficiary so it can concentrate much more information. Another important step is selecting the parameters and especially the variables that will decide the expert system solutions. In order to achieve the task literature analysis and wide experimental work must be done. The main issues are the structure that results after quenching and the mechanism by which carbon clusters are formed at subzero temperatures.

Key words: system expert, data base, knowledge, residual austenite, carbon clusters

1. Introduction

Artificial intelligence is one the most active fields in the research world our days. The wide interest about it is stimulated by the complex domains of

* Corresponding author e-mail: cutlutdig@yahoo.com

applications, from natural language to robotics. But the widest application of the artificial intelligence is represented by the expert systems.

Expert system is a numerical structure that can order and control in an automatic mode, using an operation system and a programming environment (http://www.intechopen.com). Those are usually linked to a series of execution parts that fulfill the orders of the expert system.

The basic idea of the expert system is that expertise and knowledge can be stored to a computer. If knowledge implies not just information but also a number of well defined rules, then the human user, with little or no qualification in the specific area, can take an adequate solution from the expert system. The computer "thinks", makes inference, and gives its conclusion. Expert systems are remarkable flexible, so with an appropriate language for the necessary knowledge different issues in many fields can be solved. From archeology to commerce, from medicine to engineering systems, expert systems fulfill different tasks. Many industrial branches are more and more interested in developing their own expert systems. At the very limit of mathematics, computer science and engineering, new expert systems for industries need a complete team to work on it. The engineer brings in the team the expertise, or the specific information, the phenomena (rules) that take control under the intended process.

2. Expert Systems Classification and Structure

An expert system attempts a production/research/natural problem of which solutions can be determined in a logical manner by a deductive system (a system based on a series of solid knowledge) and that also includes a number of rules for a computer understanding.

A review article dated 2004 classifies the expert systems into eleven categories, with different specificities. The categories are: rule-based systems, knowledge-based systems, neural networks, fuzzy expert systems, object-oriented methodology, case-based reasoning, system architecture development, intelligent agent systems, modeling, ontology, and database methodology, (Liao, 2005).

As can be seen, expert system syntagm covers many categories of reasoning. For industrial appliance, the preferred categories are: rule-based systems, knowledge-based systems, case-based systems and the most new, powerful neural networks and fuzzy expert systems.

A rule-based system contains information and represents that information in the form of rules, as it is the rule IF–THEN. The respective rule can be used to perform operations on data in order to reach appropriate conclusion. A knowledge-based system can initiate human reasoning. It implies four components, at least: a knowledge base, an inference engine, a knowledge engineering tool, and a specific user interface. A database is a collection of data

organized to efficiently serve many applications by centralizing the data and minimizing redundant data. A case based systems works like a house keeper: in a similar case we did that way.

In any of the above specified cases, the system implies several components, similar to a base of facts, but adequate to the system purpose. In (Aldea *et al*., 2004) is presented a Concurrent Engineering Process Design System, composed of process design tools, process design teams, process design documents, and workflows. In order to ensure the proper work, the system requires the integration of the components to such an extent that they can operate synchronized and standardized procedure.

Another type of classification takes as criterion the way the computer is connected to the process. Related to this, the following cases can exist, (http://www.intechopen.com):

- expert system off-line type - the computer is not connected to the process. The data exchange between the computer and the process is established by the operator. An expert system of this type can be used in places where the delays do not affect the whole and dates handling is not expressive.
- expert system in-line type: in this kind of ES the operator introduces dates concerning the process directly in the computer. The results are manually applied by the operator.
- expert system on-line type is an expert system physically connected with the process. It gets information within the process, without human intervention and without delay. If the on-line process changes the information during the process, the system is named on line in real time.

About the system structure, it must include at the lowest level the knowledge as an adequate data base and the algorithm of thinking.

One can figure that an expert system can undergo many forms. On the other hand, a same expert system can evolve from a relatively simple form (rule based, data base) to more complicated and complex forms from those already mentioned. In any case, an expert system must evolve in time.

One of the most famous expert systems for heat processing metals, QuenchMiner System, (www.cs.wpi.edu) describes the stages that the system has suffered.

It started as a Web-based tool for analysis of quenching experimental data. Then the tool supported successive updates to QuenchPAD, the Quenchant Performance Analysis Database. It was then enhanced into an Expert System for Decision Support of Heat Treating processes. The system will still progress as two new facilities present a challenge for the research team.

3. Developing a New Expert System

For the development of new expert systems, one can understand that it must be fulfilled the following stages:

- Creating a complete but rational database: it must contain relevant information, history, statistics, components, coefficients, properties etc. Rational means that redundant data must be avoided.
- Knowledge accumulation, specific for the interest field (in the shape of links, rules and laws), gathered by an expert and associated with the problem.
- The analysis command, unit that analysis the rules, laws together with the actions of the user for the determination of the new conditions of identification of the possible solutions. The system will react in the field of the problem being based on the data base and using the input data from the final user.
- The user interface, that ensures the link between the previously described components, the expert system and user, designed in such a manner that it can offer explanations of the system actions.

The whole must be done by a team, that include at least a computer engineer and the technological expert, The first two steps need the expert, an engineer in the studied field, and the computer engineer, to express the knowledge in machine language. The two latter steps must be accomplished especially by the computer engineer.

4. Database and Knowledge Base for Cryogenic Treatment Expert System

The cryogenic treatment is a continuation of the quenching treatment: the part is cooled below the temperature of the quenching bath. The main effect is to complete the retained austenite transformation, which results both in the increase of hardness and the improvement of the geometrical stability of the treated part. A high hardness value is also associated to a good wear resistance. In fact, little residual austenite content, high values for hardness and a better dimensional stability are the main purposes for the cryogenic treatment. The user will ask the expert system what to do for one of these purposes.

In this case, the parameters for analysis are:

- Minimum temperature to be reached for the part: it can be a swallow subzero temperature (minimum temperature about -80°C, enough for residual austenite almost complete transformation) or a deep cryogenic temperature (under -180°C).
- Quality of cryogenic medium which is also a function on the minimum temperature to be reached (alcohol, carbonic snow, liquid nitrogen or liquid helium).
- Cooling rate, affected by a great number of factors;
- Hardness: a high value is associated with a good wear resistance. Also such a high value is associated with small residual austenite content.
- Cracking potential: It indicates if cracking is likely to occur in the batch.

- The imposed soaking time at the lowest temperature and/or time for different stages in the same cryogenic cycle.

From these parameters only a few must be included in the first stage of the expert system build-up.

Input variables depend upon the parameter(s) selected. Some of the variables are: composition of the parts to be treated; geometry of the parts; state of the cryogenic fluid and, if gaseous, its velocity. An important variable is the structure of the sample/part as it emerges from the quenching/tempering stage. This must be the most powerful parameter incriminated in the lack of repeatability of the properties, a specific aspect for the cryogenic treatment claimed especially in Europe. The as formed structure shall dictate the cryogenic treatment. This is the main challenge in the expert system, because two aspects are involved: the initial structure and the changes that occur during cryogenic treatment, still impossible to study in situ.

For a good perspective of the initiated expert system the data base should be written in an accessible language/program and then made available to persons or communities with interests in cryogenic treatment. The goal of this Expert System is predicting properties obtained under given quenching and cryogenic treatment conditions. So supporting decision can be made to improve performance.

The main objectives in the future for the expert system can be summarizing in the following ideas: to include as many experimental results (or literature data) as can be made/find and compare them to find a pattern; determine the effect of some parameters and the magnitude of their importance when present in combinations.

Acknowledgement. The study was supported by PNII Programme, research Project, No. 72217/2008.

REFERENCES

∗ ∗ ∗ Expert Systems, Edited by Petrica Vizureanu, Published by Intech, 2010, Available at http://www.intechopen.com/books/show/title/expert-systems

Aldea A., Banares-Alcantara R., Jimenez L., Moreno A., Martınez J., Riano D.,The *Scope* of *Application* of *Multi-Agent Systems* in the *Process Industry*: *Three Case Studies*. Expert Systems with Applications, *26*, 39–47, 2004, Available at www.elsevier.com/locate/eswa

Aparna S. Varde, Mohammed Maniruzzaman, Elke A. Rundensteiner and Richard D. Sisson Jr. *The QuenchMiner™ Expert System for Quenching and Distortion Control*. Available at www.cs.wpi.edu/~aparna/HTS03.pdf

Liao Shu-Hsien, *Expert System Methodologies and Applications—a Decade - Review* from 1995 to 2004, Expert Systems with Applications, *28*, 93–103 (2005), Available at www.elsevier.com/locate/eswa

PAŞI NECESAR A FI EFECTUAŢI ÎN CONCEPEREA UNUI SISTEM EXPERT DESTINAT TRATAMENTULUI CRIOGENIC AL OŢELURILOR

(Rezumat)

Articolul are ca scop stabilirea principalilor paşi pe care o echipă trebuie să-l parcurgă pentru realizarea unui sistem expert cu aplicaţie la tratamentul criogenic al oţelurilor. Comparând etapele parcurse de sisteme expert consacrate apare ca rezonabilă ideea că elaborarea unui sistem expert începe cu formarea bazei de date adecvate. Aceasta trebuie deschisă unui număr cât mai mare de posibili beneficiari, astfel încât să concentreze un volum mare de informaţii. Alt pas important este alegerea parametrilor de urmărit şi mai ales a variabilelor care vor decide soluţiile sistemului. Pentru rezolvarea sarcinii este necesară investigarea unui volum mare de literatură şi un material experimental bogat. Principalele probleme sunt structura rezultată după călire şi mecanismul specific prin care se formează clusterele de carbon la temperaturi sub zero.

BULETINUL INSTITUTULUI POLITEHNIC DIN IAŞI
Publicat de
Universitatea Tehnică „Gheorghe Asachi" din Iaşi
Tomul LVII (LXI), Fasc. 4, 2011
Secţia
ŞTIINŢA ŞI INGINERIA MATERIALELOR

STUDIES AND RESEARCHES OVER HEAT TREATMENTS APPLIED ON Nb-Ti ALLOY

BY

GABRIEL VALERIU GHICA* **and TRAIAN BUZATU**

University POLITEHNICA of Bucharest,
Department of Engineering and Management
of Metallic Materials Elaboration

Received: April 14, 2011
Accepted for publication: June 27, 2011

Abstract. The theme of this project is about heat treatment applied on Nb-Ti alloy exposed to heavy ions of oxygen (10^{13} ions/cm^2 – 7,6x10^{15} ions/cm^2). There have been applied heat treatments and cold plastic deformation in order to obtain structural modification, modification which has as a result an increase or decrease of supraconductibility critical parameters. The effects of heat treatments, radiation exposure and cold plastic deformation over the structure have been identified by electronic microscopy and R_X diffraction analyses. These analyses have showed the separation of phase α-Ti, concentrated at the limit of dislocations.

The analyses have been done with an electronic microscope type JEOL200CX (200keV) and a R_x difractometer type DRON.

Key words: alloy, heat treatment, microstructure.

1. Introduction

Great interest shown towards the action of radiation on various properties of superconductors can be explained only by the desire to know the fundamental point of view the formation mechanism of defects by irradiation, the nature of these defects and their influence on the material, but also through

* Corresponding author e-mail: gvghica@yahoo.com

the practical aspect of the problem, linked to the necessity of knowing the influence of radiation on the critical parameters of superconducting materials which are used in the construction of magnets for plasma confinement in accelerators, they are exposed to some powerful radioactive fields.

Of the various types of radiation (neutron, electrons, protons, X rays, etc.), a very special irradiation is the irradiation with ions and particularly with heavy ions, because of the advantages they present.

Indeed, using large effective ion charge on top, with a much greater mass than electrons, or neutrons, it is obtained maximum efficiency of displacements of atoms, this way succeeding to replace the long neutron irradiation by a shorter duration ion with 3-4 orders of magnitude.

In the case of superconducting materials, irradiation with ions is of a particular interest for at least two reasons beyond those stated above.

Thus, as we know, many theoretical and experimental work led to the common conclusion, that raising the critical temperature Tc of superconducting materials can be done by "softening of the phonon spectrum of materials", in other words by reducing the average frequency noise, which can be best achieved , in most cases, by ion irradiation.

On the other hand, superconducting ion irradiation, producing a variety of structural defects, leads at the same time to the creation of different "pinning" centers ultimately responsible for the high critical density observed in technique superconductors.

Also as a result of the creation of defects by irradiation, in the microstructure of superconductors has been a change in the value of penetration length, which directly modify Simzbourg-Landau parameter and value.

Besides these advantages, there is the one of the special order, the protection against radiation, the ions do not create radioactivity even at high energies. As study material was chosen Nb-Ti alloy with a composition weight ratio closer to the Nb-Ti = 1:1, which is used in case of technical alloys and which due to their high parameters and their affordable price they have a wide spread in the construction of superconducting magnets for detectors, accelerators Tokamak-type installations etc., and the construction of superconducting generators and motors.

The action of oxygen ion irradiation on Nb-Ti alloys was observed by considering variations that occurred as a result of irradiation on the main critical parameters: the critical temperature Tc and critical current density Ic.

As a helpful experience, the x rays have been used to clarify the changes that occurred in the internal structure of the irradiated material.

2. Experimental

Nb-Ti alloys of various compositions were studied in terms of microstructure, in order to observe the influence of heat and heavy oxygen ion

irradiation on the basic structural characteristics which determine the variation of superconductor critical parameters. One of the basic methods of investigation is the scanning microscopy.

Samples are prepared for study by electrochemical polishing in 20% perchloric acid in ethyl alcohol and then wash with alcohol in an ultrasonic bath. Electrochemical polishing is performed in dynamic conditions (electrolyte jet) for 10 s, at the following parameters: U = 30 V, I = 0.15 A.

Examination of samples is done by scanning microscopy on a JEOL 200CX microscope with scanning annex that is included in the INTEC SA Bucharest equipment.

Type detector photomultiplier was used for secondary electrons. Scanning beam electrons were accelerated to 40 kV and beam current of about 10^{-9}A, 30A resolution is reached. To match a good resolution with an acceptable depth of focus was used a 100 mm condenser aperture that allows a depth of focus in the „LOW-MAG" exceeding 0.5 mm, and in „SCANNING ULTRAHIGH RESOLUTION MODE" maximum 100 mm.

Information obtained in secondary electron image is complex, depending both surface topography and physico-chemical nature of microvolume emissive material.

Depth that can come from this information is not exceeding 0.5 mm.

2.1. Influence of Oxygen ion Irradiation on the Critical Parameters of Superconducting Nb-Ti Alloys

Of the various types of radiation (neutron, electrons, protons, X rays, etc.) a very special importance is the ion irradiation with heavy ions in general and in particular due to the advantages they present.

Using high effective ion charge and on top of a table with incomparably greater than that of electrons, or neutrons, to obtain maximum efficiency for the formation of primary recoil atoms and a large number of displacements of atoms, thus resulting in the replace long neutron irradiation of ions through a shorter duration by 3-4 orders of magnitude.

In the case of superconducting materials irradiation, irradiation with ions of particular interest for several reasons:

- raise the critical temperature T_C superconducting materials can be achieved by „soaking" phonon spectrum (decrease of phonon frequency);
- creation of various centers of „pinning" responsible by the high critical density observed in these materials;
- radiation protection - does not produce radioactive ions at high energies.

Action of oxygen ion irradiation on Nb-Ti aliajeior was pursued by considering the changes occurring after irradiation with fluxes between 10^{13} and 7.6 x10^{15} ioni/cm^2 the main critical parameters characterizing superconductors critical techniques, namely T_C and density temperature J_C critical current.

Taking into account that the influence of radiation on superconducting materials depends largely on their microstructure, the nature and concentration of initial defects, in the present work was carried out studies on materials which have undergone appropriate heat treatment, as well as cold-deformed materials, and their microstructure were analyzed by scanning electron microscopy.

It was found that, depending on alloy composition and thermo mechanical treatment which he suffered, applying an irradiation of a given flow can be obtained by structural changes such nature that cause increases or decreases the critical parameters of superconducting materials such Nb-Ti. In the critical current density value, if it is determined, the samples were not heat treated, the dislocations, the size and density depend on their effectiveness in pinning.

2.2. Characterization of Structures

Structures identified by electron microscopy samples to those samples showed an increase in the density of dislocations and a decrease in their size after irradiation, which increased the critical current density.

In the case of samples which have undergone heat treatment at 400°C, as both microphotographs and X-ray diffraction diagrams showed α-Ti phase separation, concentrated at the edges of dislocations, which led to a higher critical current density, but fell sharply after irradiation.

Following the microstructures of samples irradiated, could explain this decrease in critical current density by increasing the density of α-Ti precipitates are distributed evenly throughout the space, making it less effective in pinning.

Separation of large numbers of α-Ti precipitates after irradiation increased the critical temperature of the radiation flux due to solid solution enriched in Nb and Nb-βTi compositions thus moving towards higher critical temperature.

A conclusion J_C useful for obtaining high degrees of deformation is the need for large high density of dislocations leading to small and therefore more effective in pinning and further promote the distribution and α-Ti precipitates at their edges.

To study the influence of heavy ion irradiation on the microstructure of Nb-Ti alloy was used composition: Nb - 67% wt. Ti (sample I) was studied the influence of irradiation on the microstructure and heat-treated samples to those who have undergone a heat treatment before irradiation.

Synthesis of materials has been made from high purity elements in an arc furnace in argon atmosphere. For homogenization, the alloys were kept several hours at 1400 - 1500°C (mixing done in an induction furnace) in an inert atmosphere in Nb crucibles, after which they were hardened in water.

Samples were then subjected to mechanical treatment of cold rolling, achieving a 90% degree of deformation. Following heat treatment and recovery was conducted in vacuum (10 Torr) at temperatures of 400° C with the following

time: 2.5 hours for sample Nb - 67% wt Ti.

Irradiation was done with heavy ion accelerator at IFIN TANDEM assured that ion implantation of oxygen (^{16}O state 4 + ion) energy of 25 MeV and flows between 2.8 and 7.6 10^{15} 10^{13} ioni/cm^2.

To determine ion flow was developed based on the principle of high resolution gamma spectrometry of the Coulomb excitation lines emitted in heavy ion reaction with a film of metal (gold) deposited on the target. Microstructural characterization of samples by scanning electron microscopy in samples rich in titanium (67% wt Ti) are shown in Figs. 1, 2, (Unheat-treated samples) and in Figs. 4,…,7 (for samples that have suffered heat treatment).

Fig. 1 – Electron microscopy analysis (Scanning) x 20,000. Sample without heat treatment. Unirradiated sample. Field 1.

Fig. 2 – Electron microscopy analysis (Scanning) x 20,000. Sample without heat treatment. Unirradiated sample. Field 2.

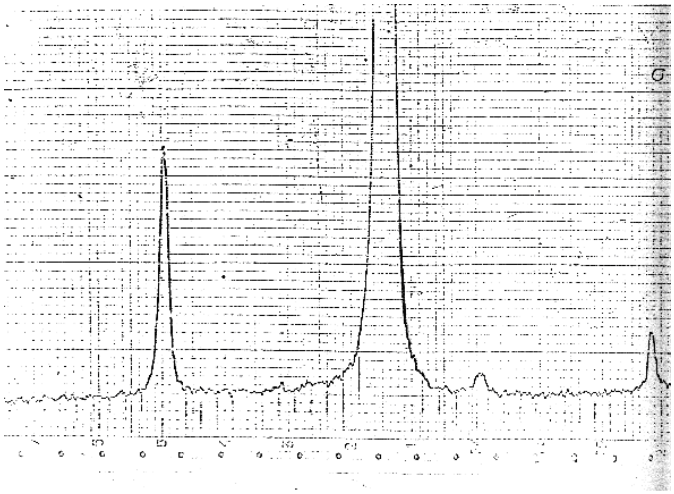

Fig. 3 - X-ray diffraction analysis of sample without heat-treated, unirradiated.

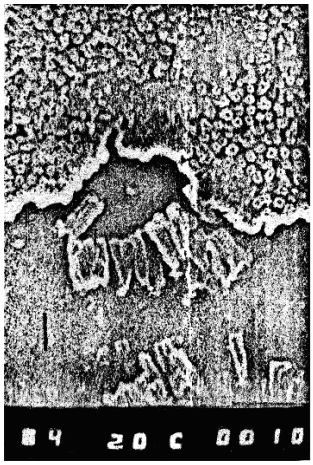

Fig. 4 - Electron microscopy analysis (Scanning) x 20,000. Sample after heat treatment. Unirradiated sample.Field 1.

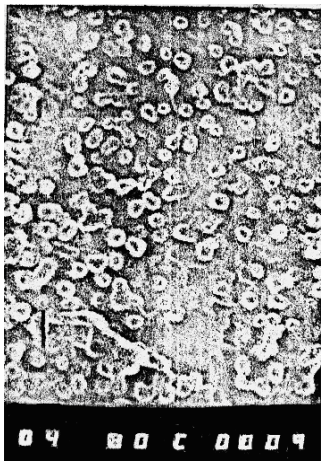

Fig. 5 - Electron microscopy analysis (Scanning) x 20,000. Sample after heat treatment. Unirradiated sample.Field 2.

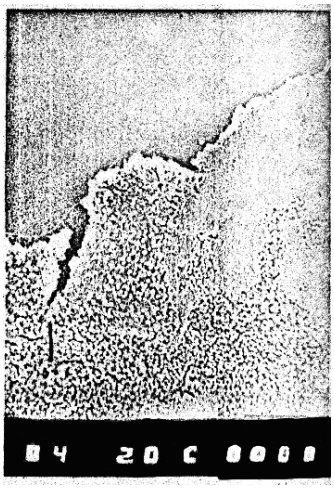

Fig. 6 – Electron microscopy analysis (Scanning) x 20,000. Sample after heat treatment. Irradiated sample. Phase α-Ti precipitates.

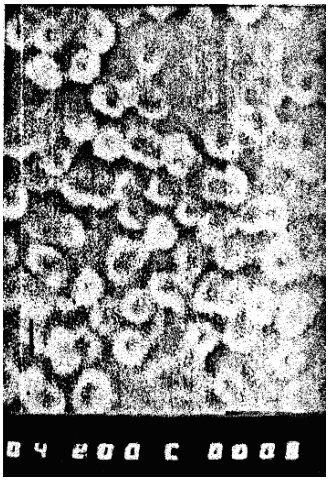

Fig. 7 – Electron microscopy analysis (Scanning) x 20,000. Sample after heat treatment. Irradiated sample. Phase α-Ti precipitates.

Samples heat-untreated. X-ray diffraction diagrams (Fig. 3.) Solid solution lines indicate only Nb-βTi, both before and after irradiation with oxygen ions.

Samples heat-treated. Samples that have undergone heat treatment as the main feature shows precipitation α - Ti phase. In the case of heat treated samples, irradiated X-ray diffraction diagram (Fig. 8.) Indicates phase α - Ti (2 θ angle corresponding line = 63.5 and 76.6). After irradiation of these samples

have undergone thermal treatment, observed a much higher density of precipitates α - Ti, about 4 10^9 / cm^2, evenly over the entire surface with a much smaller average size of about 50 μm occur so close together at a matrix of solid solution Nb-βTi (Fig. 9). X-ray diffraction diagram (Fig. 9). Indicates the appearance of α-Ti phase in solid solution matrix, relative intensity of α - Ti lines are more intense than the irradiated sample surface although the exposure was very small.

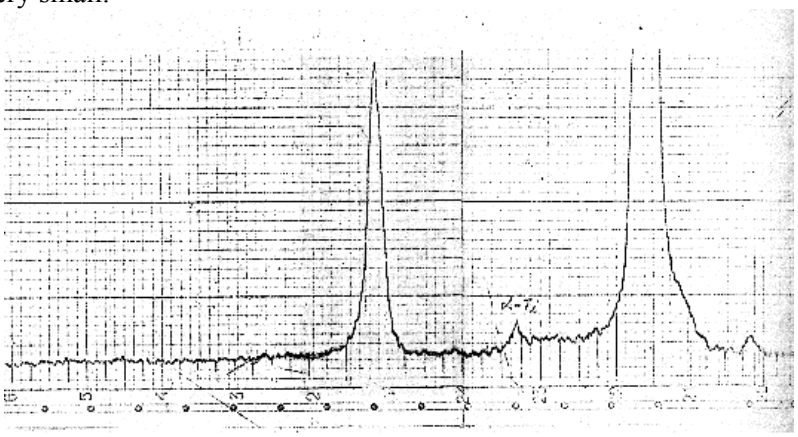

Fig. 8 – X-ray diffraction analysis of sample after heat-treated, unirradiated, (α -Ti).

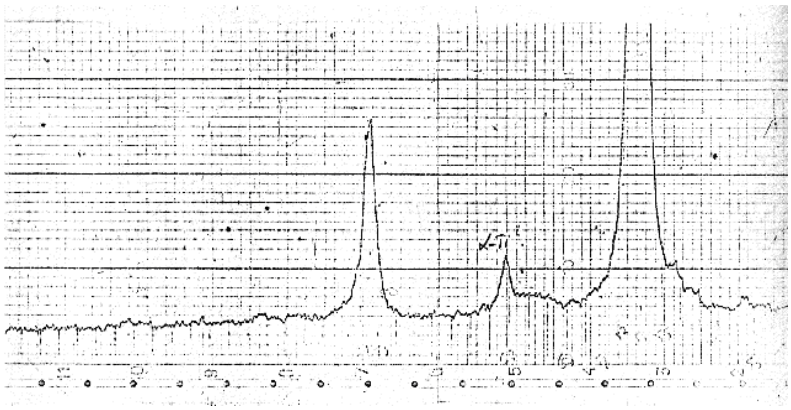

Fig. 9 – X-ray diffraction analysis of sample after heat-treated, irradiated, (α -Ti - strongly shaped).

2.3. Optimization of Heat Treatment and to Correlate Structural Properties with Critical Current Density Values

A second superconducting shoulders placed in a magnetic field is generally not too small value, enter the mixed state, magnetic flux penetrates in the form of an entity (fluxoizi Abrikosov) each containing one magnetic flux quantum.

When passing an electric current transmission through such material, the type fluxoizilor is a Lorentz force tending to move them. This force is opposed by a force due to rule on fixing fluxoizilor material inhomogeneity created by the application of thermo-mechanical treatment (dislocation cells, precipitates, etc.).

As long as the force density does not exceed the density of Lorentz force-type fasteners, power is transported without losses. Increasing the intensity of electric current through the material at a specific value of current density (critical density), the Lorentz force exceeds the strength of attachment is moved fluxoizi network and energy dissipation appears by default.

Fixation strength depends on the concentration and size than non-homogenous. Therefore there must be an optimum heat treatment influence on precipitation over the critical current density for several Nb-Ti system alloys. Fig. 10 is the critical current in zero fields according to treatment time of return to temperature of 400°C.

The appearance of peaks is due primarily to precipitation α - Ti. When heat treatment time is too long, secondary phase particles grow in size and become less effective in determining fluxoizilor.

Optimal Treatment moves towards higher values with decreasing Ti content because the rate of occurrence of secondary phases increases with increasing titanium content (Fig. 10, I sample deformed 90%, 60% Nb gr.Ti;) to Sample II - 90% Nb deformed 47% wt. Ti).

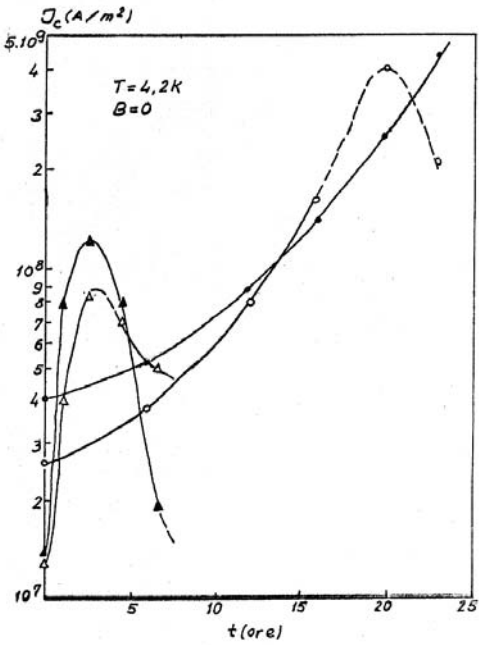

Fig. 10 - Zero field critical current depending on the time of treatment to return to temperature of 400°C. Legend: sample I - Nb-Ti alloy, Ti content ~ 60% wt., g_I = 90%; sample II - Nb-Ti alloy, Ti content ~ 47% wt. Ti, g_{II} = 90%; Nb-Ti alloy sample III, ~ 70% Ti content; g_{III} = 97%; Nb-Ti alloy sample IV, ~ 74% Ti content; g_{IV} = 93%.

Also a greater degree of deformation promotes the precipitation of α-Ti. Sample III has a higher degree of deformation than the sample 4 (g_{III}= 97% compared g_{IV} = 93%) and because of this the optimal time for sample III is smaller than sample IV, IV although the sample is richer in titanium (in sample III ~ 70% Ti content, Ti content in the sample IV ~ 74%).

This heat treatment also has another effect that becomes essential in alloys richer in Nb case, the α-Ti precipitate is weak or nonexistent.

Thus dislocations cells after cold deformation become net during heat treatment (and therefore more effective in determining fluxoizilor) by moving dislocations within cells to the wall. But a temperature too high or too long exposure time fade or even destroy the structure of cells. In a material subjected to a high degree of deformation (with a fine structure of cells of dislocations), after heat treatment discussed above, α -Ti particles are precipitated primarily on cell walls. Critical current density is so high.

3. Conclusion

To study the influence of heavy ion irradiation on microstructure of Nb-Ti alloy was used Nb-67% Ti alloy homogenized by maintaining the 1400-1500oC induction furnace in an inert atmosphere.

Alloy then suffered a mechanical treatment of cold rolling, achieving a 90% degree of deformation. There was a recovery (in vacuum) at 400^{o}C for 2.5 h.

Irradiation performed at IFIN Bucharest provided oxygen ion implantation energy of 25MeV and flows between 2.8 10^{13} and 7.6 10^{15} ions/cm^2.

Micrographs of samples heat treated α-Ti phase precipitation indicates the average size 100μm, density of 10^9/cm^2.

After irradiation, the density of α-Ti precipitates is approximately equal to 2,5 10^9 / cm^2, so two and a half times greater than the density before irradiation.

α-Ti precipitates are pinning criteria for these materials to determine the critical current density high.

Separation of a greater number of α-Ti after irradiation increases the critical temperature due to solid solution Nb- βTi enrichment in Nb and thus traveling compositions higher critical temperature.

In terms of optimizing thermal treatment and structural properties correlate with the critical current density values, we highlight the following:

When passing an electric current through a superconducting transmission of the second shoulders on fluxoizilor appears Lorentz force type and tend to move. This force is opposed by a force due to rule on fixing fluxoizilor material inhomogeneity created by the application of thermo-mechanical treatment (dislocation cells, precipitates, etc.).

As long as the force density does not exceed the density of Lorentz force-type fasteners, power is transported without losses. Increasing the

intensity of electric current through the material at a specific value of current density (critical density), the Lorentz force exceeds the strength of attachment is moved fluxoizi network and energy dissipation appears by default.

Fixation strength depends on the concentration and size than non-homogenous. Therefore there must be an optimum heat treatment influence on precipitation over the critical current density for several Nb-Ti system alloys. Figure 10 is the critical current in the field and analyzed according to time zero return to temperature treatment of 400°C.

The appearance of peaks is due primarily to precipitation α - Ti. When heat treatment time is too long, secondary phase particles grow in size and become less effective in determining fluxoizilor.

Optimal Treatment moves towards higher values with decreasing Ti content because the rate of occurrence of secondary phases increases with increasing titanium content (Fig. 5.10., I sample deformed 90%, 60% Nb gr.Ti;) to Sample II - 90% Nb deformed 47% wt. Ti).

Also a greater degree of deformation promotes the precipitation of α - Ti. Sample III has a higher degree of deformation than the sample IV (g_{III}= 97% compared g_{IV} = 93%) and because of this the optimal time for sample III is smaller than sample IV, IV although the sample is richer in titanium (in sample III ~ 70% Ti content, Ti content in the sample IV ~ 74%).

This heat treatment also has another effect that becomes essential in the case of alloys richer in Nb, the α-Ti precipitate is weak or nonexistent. Thus dislocations cells after cold deformation become net during heat treatment (and therefore more effective in determining fluxoizilor) by moving dislocations within cells to the wall. But a temperature too high or too long exposure time fade or even destroy the structure of cells.

In a material subjected to a high degree of deformation (with a fine structure of cells of dislocations), after heat treatment discussed above, α-Ti particles are precipitated primarily on cell walls. Critical current density is so high.

REFERENCES

[1]. Cherepanov G.P., *Practical Method of Determining the Fracture Energy of Metals*. Mat. Sci., **6**, 4, 2004.

[2]. Klueh R.J., *Alloys containing Titanium and Niobium*. Mat. Sci., **7**, *4*, 2004.

[3]. Shoesmith D.W., *Corrosion of Nuclear Fuel Waste Containers*. Proceedings of a Workshop, AECL – 10121, 1990.

[4]. Shoesmith D.W., Ikeda B.M., Quinn M.J., *Estimating the Lifetimes of Titanium Containers for Nuclear Fuel Waste*. A. Damage Function for the Crevice Corrosion of Grade-2, Titanium", AECL-11255, 1995.

[5]. James J.Noël, Grant Baitey M., *Hydrogen Absorption by Grade-2, Titanium*. AECL – 11608, 1996.
[6]. Shoesmith D.W., King F., Ikeda B.M., *An Assessment of the Feasibility of Indefinite Containment of Canadian Nuclear Fuel Wastes*. AECL – 10972 1995.
[7]. Rosenqvist T., *Principiile metalurgiei extractive -MeGrow-Hill*. Book Company, 1974.
[8]. ∗ ∗ ∗ *Manualul inginerului metalurg*. **I**, Editura Tehnică, Bucureşti, 1978.
[9]. lenciu M., Moldovan P., Panait N., Buzatu M., Marinescu D., Groza I., *Elaborarea şi turnarea aliajelor neferoase*. Edit. Didactică şi Pedacogică, Bucureşti, 1982.
[10]. ∗ ∗ ∗ Colecţia JOM –Extractive Metallurgy, 1990-2010.

STUDII ŞI CERCETĂRI ASUPRA TRATAMENTULUI TERMIC APLICAT ALIAJULUI Nb-Ti

(Rezumat)

Tema acestui proiect se referă la tratamentul termic aplicat aliajelor de Nb-Ti expuse în ioni grei de oxigen (10^{13} ions/cm^2 – $7{,}6\text{x}10^{15}$ ions/cm^2). S-au aplicat tratamente termice şi deformare plastică la rece cu scopul de a obţine modificări structurale, modificări care au ca rezultat creşterea sau descreşterea parametrilor critici de supraconductibilitate.

Efectele tratamentului termic, expunerea la radiaţii şi deformarea plastică la rece asupra structurii au fost identificate prin microscopie electronică şi analize prin difracţia cu raze X. Aceste analize au evidenţiat separarea fazei α-Ti, concentrată, la limita dislocaţiilor.

Analizele au fost realizate cu microscopul electronic tip JEOL200CX (200keV) şi difractometrul cu raze X de tip DRON.

BULETINUL INSTITUTULUI POLITEHNIC DIN IAŞI
Publicat de
Universitatea Tehnică „Gheorghe Asachi” din Iaşi
Tomul LVII (LXI), Fasc. 4, 2011
Secţia
ŞTIINŢA ŞI INGINERIA MATERIALELOR

STUDY CONCERNING THE BIOMECHANICAL BEHAVIOUR OF SOME AESTHETIC RESTORATIVE DENTAL MATERIALS

BY

IRINA GRĂDINARU[1]*, RALUCA – ELENA BACIU[1], DANIELA CALAMAZ[1] and MARIA BACIU[2]

[1] University of Medicine and Pharmacy of Iaşi,
Department of Dental Materials
[2]“Gheorghe Asachi” Technical University of Iaşi,
Faculty of Faculty of Materials Science and Engineering

Received: April 14, 2011
Accepted for publication: June 27, 2011

Abstract. The aim of the present work was to determine the biomechanical behavior of some aesthetic restorative dental materials frequently used in the dental office. Experimental researches related to the abrasive wear behavior were done for two light-cured composite resins: Progress Plus (K.B. Mutsumi) şi Rx Force (DLS UK).The specimens, with Ø=7 mm, were made in the Dental Material lab from the Faculty of Dental Medicine within “Gr. T. Popa” University of Medicine and Pharmacy of Iaşi. The wear tests were carried out with the help of Material Engineering and Industrial Security Department from the Faculty of Materials Science and Engineering, “Gheorghe Asachi” Technical University of Iaşi. The statistic analysis of data was made by means of SPSS software for Windows 12, using the “pair” t test. The conclusions we may draw after having studied the wear resistance of aesthetic restorative dental materials are the following: the substance loss increases linearly with the getting over of the friction layout and the intensity of the force applied. This aspect helps to choose the restorative dental material based on the size, location and design of the cavity.

Key words: composite resines, biomechanical behaviour, dental restorations**.**

* Corresponding author e-mail: maria_baciu2004@yahoo.co.uk

1. Introduction

Current possibilities for the restoration of the teeth lesions are diverse and include both aesthetic and non-aesthetic dental restorative materials.

The evolution of materials used in aesthetic dental restorations (from acrylic resins and silicate cements) was produced at the end of the XXth century, by the appearance of diacrylic composite resins.

These are aesthetic restorative materials, being composed of three phases: *an organic component* (represented by methacrylic monomers), *inorganic component* (which are minerals and represent the filling phase) and *binders* that are designed to unite the two phases, organic and inorganic.

The aim of the present work was to determine the biomechanical behaviors of some aesthetic restorative dental materials frequently used in the dental office.

2. Materials and Methods

Experimental researches related to the abrasive wear behavior were done for two light-cured composite resins: Progress Plus *(K.B. Mutsumi)* şi Rx Force *(DLS UK)*, presented in Table1.

Table 1
The light-Cured Composite Resins Under Study

Light-cured composite resins under study	Producer	Code of the specimens
Progress Plus	*K.B. Mutsumi*	PP
Rx Force	*DLS UK*	RF

The specimens, with Ø=7 mm, were made in the Dental Material lab from the Faculty of Dental Medicine within "Gr. T. Popa" University of Medicine and Pharmacy of Iaşi, according to the indications of the producers.

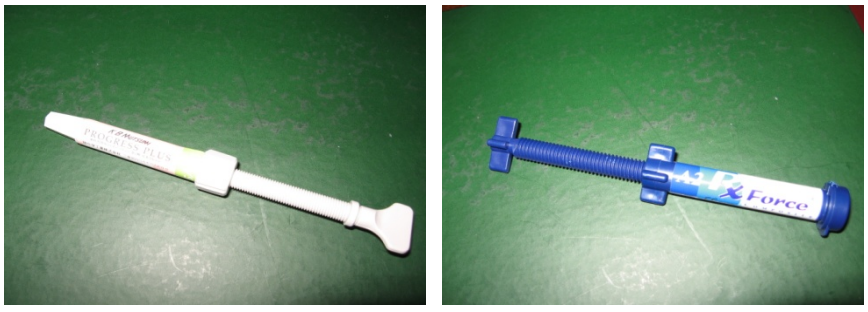

Fig. 1 – Presentation of the investigated composite resins.

Fig. 2 – Demetron LC light-curing unit from *Kerr*.

The composite resins (Fig.1) were condensed inside the glass test tubes, in successive 2 mm layers, each layer being light-cured for 40 seconds, with a Demetron LC light-curing unit from *Kerr* (Fig.2).

To obtain the precise diameter of specimens, we had to reduce their size by means of a facing device and a mill. The wear tests were carried out with the help of Material Engineering and Industrial Security Department from the Faculty of Materials Science and Engineering, "Gheorghe Asachi" Technical University of Iaşi.

The wear behavior of the investigated composite resins was studied in the conditions specific to dry friction at the level of frontal surface of specimens. The experimental assays were carried out during a continuous movement of rotation with sliding, the surfaces in contact being plane and having a cover coefficient of $0 < K_{ac} = 0.232 < 0.5$. The experimental researchers were made on a specialized wear testing machine.

Measurements aimed at determining the mass wear, namely the absolute variation (Δm_a) and relative variation (Δm_r) of specimens' mass, sizes that may be found in the calculation relations of the two indicators specific to the wear resistance. Determinations were made in 4 different time intervals to which certain friction lengths correspond (Table 2).

Table 2

Time – Length of the Friction Layout Run Correspondence

Test duration t, [min]	15	30	45	60
Friction length L_f, [m]	1500	3000	4500	6000

The abrasive wear behavior of the dental materials under analysis was highlighted by the determination of the mass wear, the intensity and speed of mass wear.

Fig. 3 – The analytical balance utilised in this study.

The mass wear was determined through the weighing of specimens by means of analytic scales before and after every determination and we evaluated the mass loss (Fig.3).

The statistic analysis of data was made by means of SPSS software for Windows 12, using the "pair" t test.

3. Results and Discussion

In the experimental assays regarding the abrasive wear behavior were determined by the evolution of the absolute mass losses (Δm_a) and relative mass losses (Δm_r), corresponding to the different values of the friction layout length and the 30 N pressure force.

Table 3

Mass Wear for Force F = 30 N

Friction layout length, [m]	SPECIMEN MASS, m [g] for F = 30 N	
	RF	PP
$L_0 = 0$	1.0144	0.6065
$L_1 = 1500$	0.8491	0.5733
$L_2 = 3000$	0.7424	0.5068
$L_3 = 4500$	0.6807	0.3776
$L_4 = 6000$	0.6588	0.2998

On the basis of these results, we calculated the absolute mass losses Δm_a (Fig. 4, Fig. 5).

The absolute mass losses were calculated with the regard:

$$\Delta m_a = \left(m_{L_0} - m_{Li}\right),\ i = \overline{0,4} \tag{1}$$

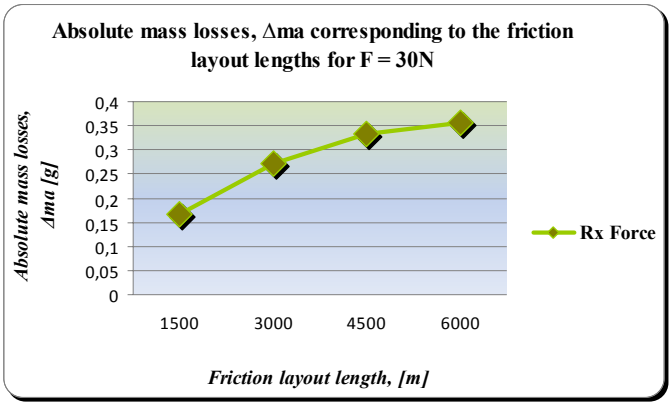

Fig. 4 – RxFORCE-Absolute mass losses, Δma corresponding to the friction layout lengths for F = 30N.

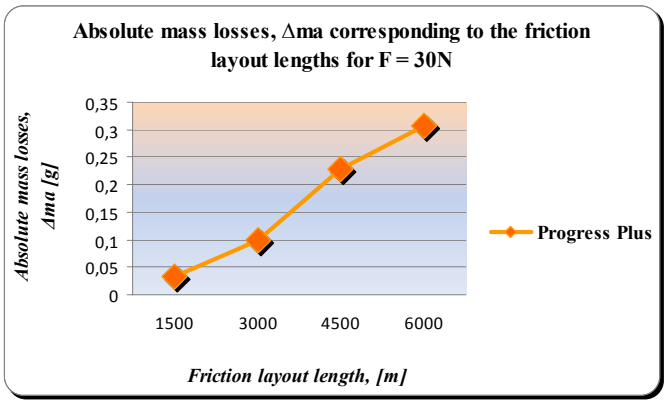

Fig. 5 – Progress Plus-Absolute mass losses, Δma corresponding to the friction layout lengths for F = 30N.

In Fig.6 are comparative presented for both materials, the absolute mass losses, Δma corresponding to the friction layout lengths for F = 30N

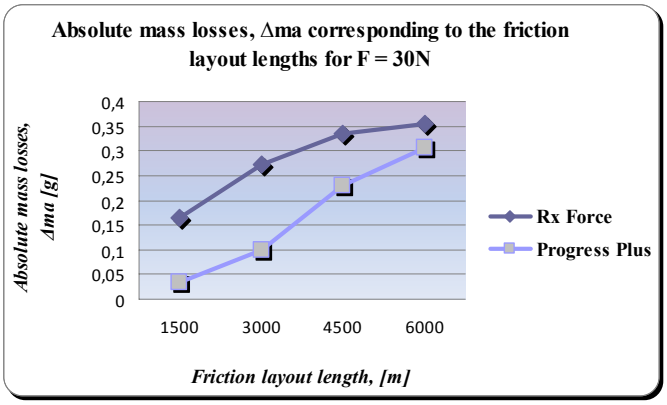

Fig. 6 – Comparative presentation for both materials of absolute mass losses, Δma corresponding to the friction layout lengths for F = 30N.

Were calculated the relative mass losses Δm_r (Figs.7, 8). The relative mass losses were calculated with the regard:

$$\Delta m_r = \frac{\Delta m}{m_{L0}} * 100\,,[\%] \qquad (2)$$

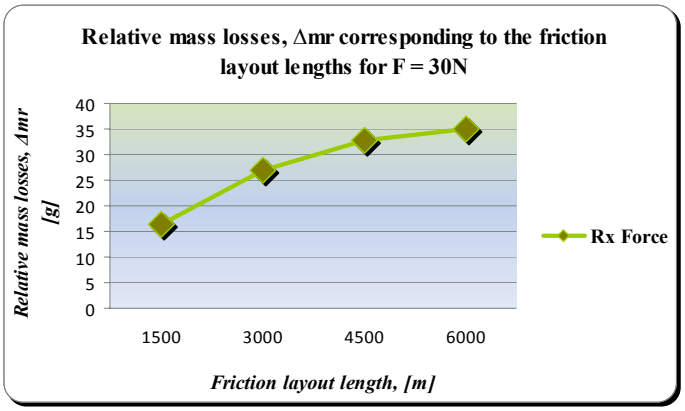

Fig. 7 – RxFORCE - Relative mass losses, Δmr corresponding to the friction layout lengths for F = 30N.

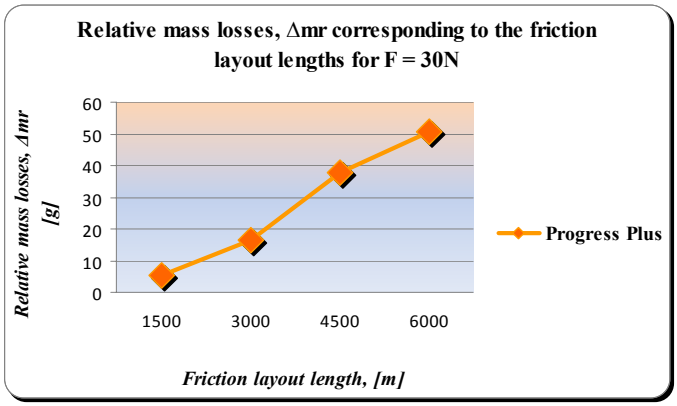

Fig. 8 – Progress Plus - Relative mass losses, Δmr corresponding to the friction layout lengths for F = 30N.

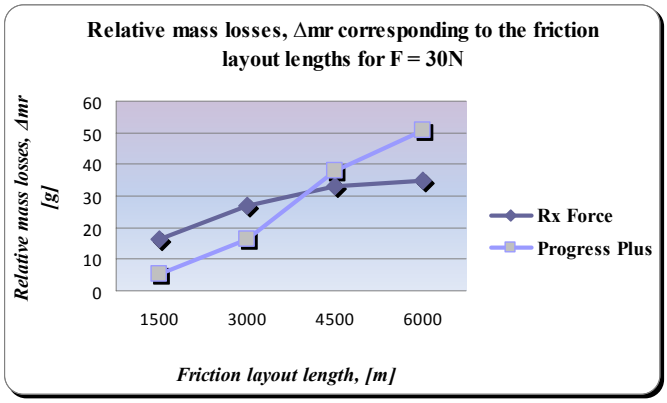

Fig. 9 – Comparative presentation for both materials of relative mass losses, Δmr corresponding to the friction layout lengths for F = 30N.

In Fig. 9 are comparative presented for both materials, the relative mass losses, Δmr corresponding to the friction layout lengths for F = 30N.

An indicator for the abrasive wear behaviour was represented by the mass wear intensity I_m.

The regard for this value is:

$$I_m = \frac{\Delta m}{A_f * L_f}, \ [g/m^3] \tag{3}$$

where: A_f represents the area of the friction surface; for the specimens with 7 mm diameter we obtained $A_f = 3{,}848 * 10^{-5}$, $[g/m^3]$.

Knowing the values of mass losses Δm and friction layout length L_f, was determined the evolution of mass wear intensity for every dental material considered in the study (Fig.10).

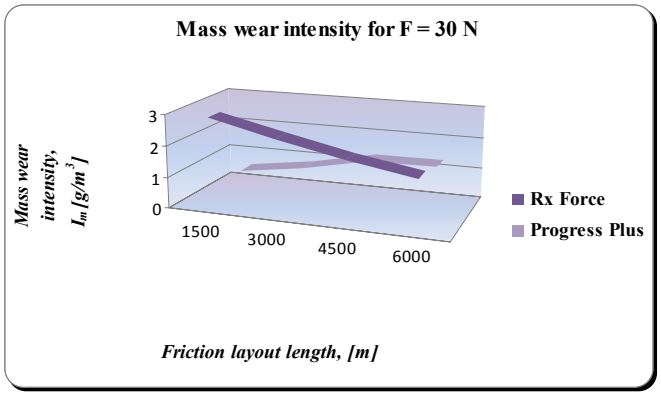

Fig. 10 – Comparative presentation of the mass wear intensity for F = 30 N.

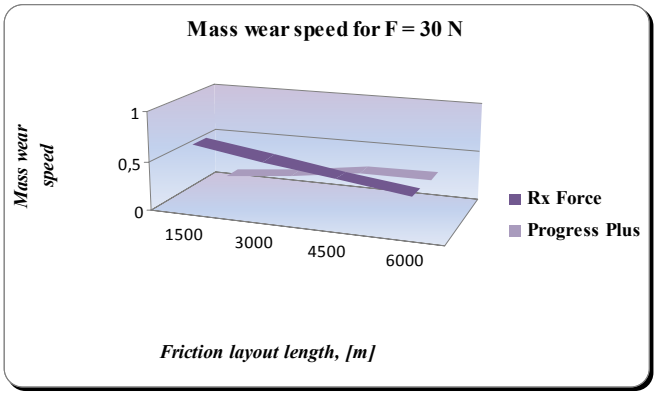

Fig. 11 – Comparative presentation of the mass wear speed for F = 30 N.

The mass wear speed, calculated by the formula: $V=\Delta_m/t$ (g/h), is comparative presented in Fig.11 for both materials included in the study.

4. Conclusion

The conclusions we may draw after having studied the wear resistance of aesthetic restorative dental materials are the following: the substance loss increases linearly with the getting over of the friction layout and the intensity of the force applied. This aspect helps to choose the restorative dental material based on the size, location and design of the cavity.

REFERENCES

[1]. Bratu D., *Materiale dentare în cabinetul stomatologic*. Editura Helicon, Timişoara, 1994.
[2]. Bratu D., *Materiale dentare: bazele fizico-chimice*. Editura Helicon, Timişoara, 1994.
[3]. Craig G.R., Powers M.J., *Restorative Dental Materials*. Ediţia a XIa, Editura Mosby, Inc, 2002.

STUDIU PRIVIND COMPORTAMENTUL BIOMECANIC AL UNOR MATERIALE RESTAURATIVE CORONARE FIZIONOMICE

(Rezumat)

Prezentul studiu a urmărit determinarea comportamentului biomecanic al unor materiale de restaurare coronară fizionomice frecvent utilizate în practica stomatologică. Material şi metodă. Cercetările experimentale au urmărit comportamentul la uzură abrazivă în cazul unor răşini compozite fotopolimerizabile: Progress Plus *(K.B. Mutsumi)* şi Rx Force *(DLS UK).* Epruvetele, cu Ø=7 mm, au fost elaborate în laboratorul de Materiale Dentare din cadrul Facultăţii de Medicină Dentară, UMF „Gr. T. Popa" Iaşi, în concordanţă cu indicaţiile producătorilor. Testele de încercare la uzare au fost efectuate în cadrul catedrei de Ingineria Materialelor şi Securitate Industrială din cadrul Facultăţii de Ştiinţă şi Inginerie a Materialelor, Universitatea Tehnică „Gheorghe Asachi" din Iaşi. Analiza statistică a datelor obţinute s-a realizat cu ajutorul programului SPSS for Windows 12, utilizând testul t "pereche". Concluzii. Testele efectuate au arătat faptul că volumul de material uzat creşte proporţional cu lungimea traseului de frecare şi cu forţa aplicată, fapt ce condiţionează alegerea materialului restaurativ în funcţie de mărimea, topografia şi design-ul cavităţii.

BULETINUL INSTITUTULUI POLITEHNIC DIN IAŞI
Publicat de
Universitatea Tehnică „Gheorghe Asachi" din Iaşi
Tomul LVII (LXI), Fasc. 4, 2011
Secţia
ŞTIINŢA ŞI INGINERIA MATERIALELOR

ADVANCED METHODS FOR ELECTROMAGNETIC EVALUATION USING METAMATERIALS

BY

RAIMOND GRIMBERG[1*], ADRIANA SAVIN[1], ROZINA STEIGMANN[1], NICOLETA IFTIMIE[1] and DAGMAR FAKTOROVÁ[2]

[1] National Institute of Research and Development for Technical Physics Iaşi
[2] University of Žilina, Slovakia

Received: April 15, 2011
Accepted for publication: June 27, 2011

Abstract. This paper presents a possibility to improve the spatial resolution of the electromagnetic nondestructive control systems that operate at frequencies of tens and hundreds of megahertz using metamaterials for evanescent waves focusing from the near neighbour of the controlled object. The transducer has been used for the effective visualization for delaminations produced by impacts on carbon fiber reinforced plastics (CFRP).

Key words: metamaterials, conical Swiss roll, electromagnetic evaluation, CFRP

1. Introduction

When the object to be examined has high electrical conductivity, under the action of the incident electromagnetic field, eddy currents will be induced in the material, as predicted by Faraday's law. The induced eddy

* Corresponding author e-mail: grimberg@phys-iasi.ro

current will generate a secondary electromagnetic field that will be in opposition to the incident electromagnetic field. If the incident electromagnetic field is created by a time varying current passing through an excitation coil, the interaction between the primary and secondary electromagnetic field causes modification of the electromotive force in the coil and therefore results in an apparent change in the impedance of the coil (Sophian *et al*., 2001). This change of the impedance depends on the distance between the coil and the object to be examined (lift-off), the electromagnetic properties of the material (electrical conductivity σ, magnetic permeability μ), the surface and subsurface geometry and the angular frequency ω. The penetration of eddy currents is limited, due to the skin effect (Balanis, 1989). The presence of material inhomogeneities (voids, inclusions, cracks, having lower electrical conductivity) will disturb or impede induced eddy current and in turn will also change the apparent impedance of the coil, which is measured as an indicator of the inhomogeneities (Tian *et al*., 1998). The material inhomogeneities will become a new current source inside the object to be examined (Dood & Deeds, 1968). As long as the frequencies used are not high (lower than 1GHz), the incident electromagnetic field is usually created by the coils circulated by alternative currents (Das *et al*., 2002) or current impulses (Mandache & Lefebvre, 2006). The detection of electromagnetic field created by the secondary current sources can be made either by coils of different shapes (Sophian *et al*., 2001).

In the case of low frequency incident electromagnetic field, the detection of the secondary electromagnetic field can be made also by sensors with Hall effect (Shull, 2002) or SQUID (Nagendran *et al*., 2010) and GMR sensors (Dogaru & Smith, 2001). In order to obtain a signal to noise ratio as larger as possible at detection, leading to the increase of detection probability for a higher reliability coefficient, it is necessary to use the smallest possible value of the lift - off (Shull, 2002) (distance between the electromagnetic transducer and the controlled piece). This leads to the necessity of working in near field due to the fact that the generated and respective the scattered electromagnetic waves are evanescent waves (waves that are rapidly attenuated with the distance and are difficult to be focalized using classical materials.

This paper presents a possibility to improve the spatial resolution of the electromagnetic nondestructive control systems that operates at frequencies of tens and hundreds of megahertz, using metamaterials (Pendry *et al*., 1999) for evanescent wave's focalization from the nearest neighbour of the controlled object. The optimal conditions for the metamaterials transducer (the conical Swiss rolls type) functioning, have been established, inverting data obtained from the measurement of network parameters. The transducer has been used for effective visualization of delamination of carbon fiber reinforced plastics (CFRP) created by impact.

2. Conical Swiss Roll as Metamaterials

Metamaterials can provide an engineered response to electromagnetic radiation that is not available from the class of naturally occurring materials. They consist of individual or arrays of elements for which all the geometrical dimensions are small compared to the wavelength of operation. Because the wavelength of the electromagnetic radiation is large (at 300MHz, the wavelength in air, λ_0=1m), the condition that the element should be much smaller than wavelength is accomplished.

A conical Swiss roll consists of a number of spiral-wound layers of an insulated conductor on a conical mandrel, Fig. 1. The insulated conductor is a copper foil with 18μm thickness and a layer of polyamide with 12μm thickness. The Copper and polyamide layers have been laminated without adhesive to decrease the losses at high frequencies. The insulated layer has a relative dielectric permittivity of 3.2 and loss tangent tanδ=0.0099. The conical Swiss rolls have 5 layers, 20mm base diameter, 3.2mm top diameter, the aperture angle 20^0 and height 55mm. A selection of few conical Swiss rolls with similar properties was made.

Pendry *et al*., (1999) proposed that Swiss roll made from thin conducting sheets have a macroscopic magnetic behaviour for a magnetic field applied along the rod. The radio frequency magnetic field will induce currents on the circumference of the cone and consequently a magnetization opposing the applied magnetic field.

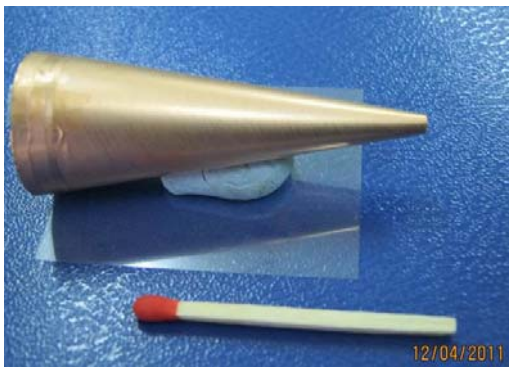

Fig. 1 – Conical Swiss roll.

The capacitive and conductive elements of the structure create a resonant RLC circuit whose induced currents are subject to, therefore a resonant μ with high positive and negative values for a range of frequencies is obtained.

Thus, a conical Swiss roll can act as radio frequency magnetic flux concentrator.

To determine the effective magnetic permeability of a conical Swiss roll, the S parameters have been measured using a Network/Spectrum/ Impedance Analyzer 4395A Agilent coupled with S Parameter Test Kit 87511A, Agilent, USA.

The measurement equipment is presented in Fig. 2.

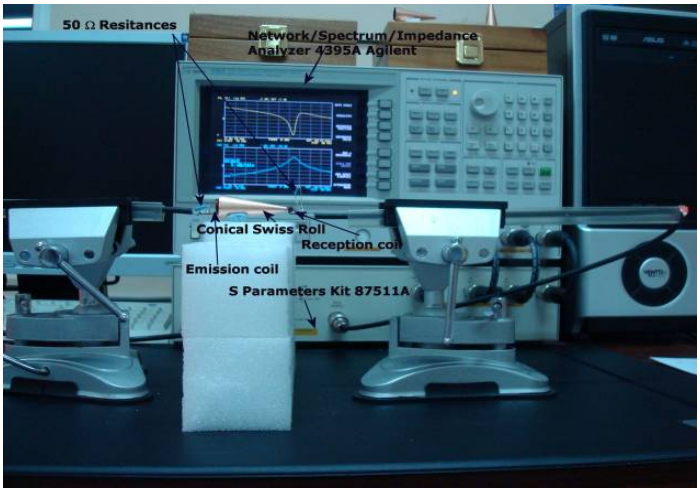

Fig. 2 – The equipment for measurement S parameters.

The electromagnetic field is generated by a coil with 2 turns having 16mm diameter, made of 1mm diameter copper wire. The response of conical Swiss roll metamaterial is detected with a reception coil having 2 turns of 3mm diameter.

The dependencies of real and imaginary components of S_{11} and S_{21} by the frequency are presented in Figs. 3, 4.

According to (Chen *et al*., 2004) the impedance of the metamaterial considered as a homogeneous slab excited by a plane wave is given by.

$$Z = \pm\sqrt{\frac{(1+S_{11})^2 - S_{21}^2}{(1-S_{11})^2 - S_{21}^2}} \tag{1}$$

The sign in front of the square root sign is chosen such that.

$$\mathrm{Re}(Z) \geq 0 \tag{2}$$

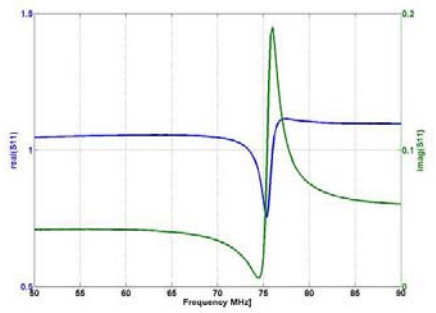

Fig. 3 - Dependency of S_{11} by frequency: real component and imaginary component.

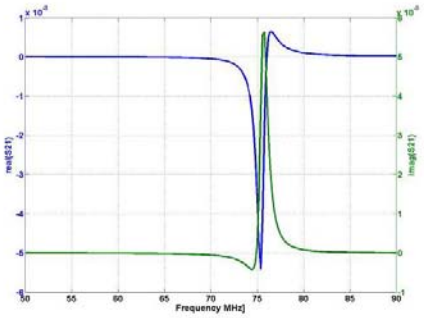

Fig. 4 - Dependency of S_{21} by frequency: real component and imaginary component.

The refraction index of metamaterial n, is obtained as a solution of transcendental equation.

$$e^{jnk_0 d} = \frac{1}{2S_{21}\left(1 - S_{11}^2 + S_{21}^2\right)} \pm j\sqrt{1 - \frac{1}{2S_{21}\left(1 - S_{11}^2 + S_{21}^2\right)}} \tag{3}$$

where $k_0 = \dfrac{2\pi f}{c}$ with frequency f, c is the speed of light in vacuum, $j = \sqrt{-1}$, and d is the height of the conical Swiss roll, the sign + or – is chosen such that.

$$\mathrm{Im}(n) \geq 0 \tag{4}$$

Thus, the effective magnetic permeability of conical Swiss roll is given by.

$$\mu_{eff} = nZ \tag{5}$$

In Fig. 5, the dependency of frequency for the effective magnetic permeability of a conical Swiss roll is presented.

It can be observed that the effective magnetic permeability becomes high for a certain frequency range, and for other frequencies it becomes negative. As applications in the domain of electromagnetic nondestructive

examination we are proposing an optimized work frequency of 72.5 MHz which assures a magnetic effective permeability of 22.

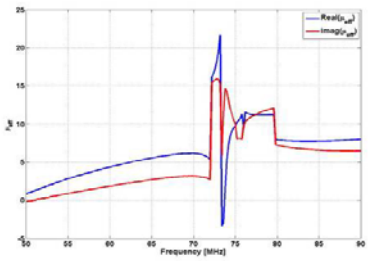

Fig. 5 – The frequency dependence of effective magnetic permeability of conical Swiss roll.

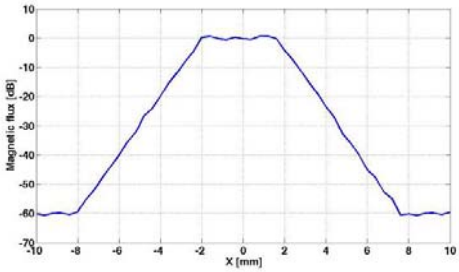

Fig. 6 – The frequency dependency of the induced emf amplitude in the reception coil at the scanning along the small base of the Swiss roll. Lift-off 0.2mm.

At this frequency, the property of a conical Swiss roll to act as an alternative magnetic flux concentrator has been verified. Using the Network/ Spectrum/Impedance Analyzer 4395A Agilent, the electromotive force (emf) induced in the detection coil that is displaced with a XY motorized stage Newmark type over the small basis of the conical Swiss roll at the distance of 1m it has been measured.

The dependency of the induced emf amplitude in the reception coil by the frequency is presented in Fig. 6. Examining data from Figure 6 it can be emphasized that, in the zone corresponding to the diameter of the small base of conical Swiss roll, for a frequency that assures a maximum of effective magnetic permeability of the investigated metamaterial, the concentration of the radio frequency magnetic flux is very high. Also, it must be mentioned that on this aperture the magnetic flux is almost constant, which suggests the existence of an electromagnetic plane wave.

3. Experimental Results

Plates from CFRP type having 6 layers of carbon fibers woven type 5 harness satin (Carbon T300 3K 5HS) with a layout that assures the quasi-isotropic properties of the plate were studied. The polymer matrix is made of Polyphenylene Sulphide (PPS). The thickness of the plate is 1.91mm with a 0.5 volume ratio. The plates are produced by TenCate Advanced Composites, Netherlands.

On these plates, delaminations due to impacts with different energies have been induced using a spherical impactor with 22mm diameter. The plates were examined by means the electromagnetic procedure presented above using the transducer (Grimberg & Savin, 2010; Grimberg *et al.*, 2011), (Fig. 7), which

contains a metamaterials lens for detection. For the generation of plane wave, a conical Swiss roll also has been used, acting as a flux concentrator. The lift-off was maintained constant at value of 0.25mm (the material to be examined can be considered) that is practically in the plane of the aperture; the reception coil is in the focal plane of the lens. The control frequency was 72.5 MHz.

In Fig. 8, we present (Akkerman, 2006) the schematic layout of the 5H satin carbon fibers woven and the picture of the layers.

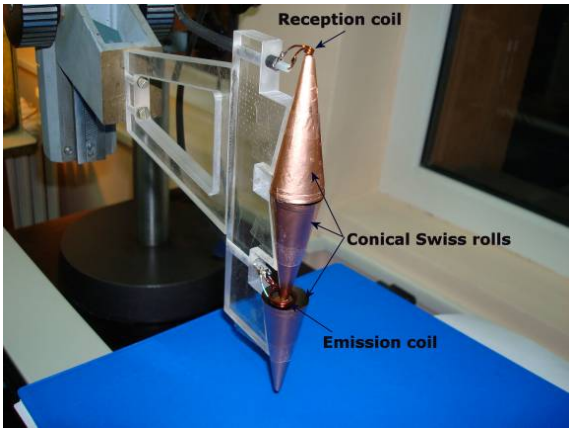

Fig. 7 – The electromagnetic transducer with metamaterials lens.

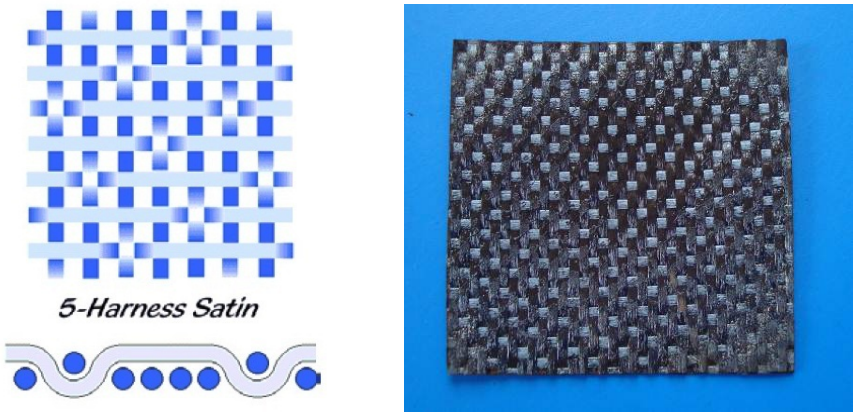

a *b*

Fig. 8 – *a*) 5H-biaxial woven fabric architectures; *b*) picture.

In Fig. 9 is presented the amplitude of the signal delivered by the electromagnetic transducer with metamaterials from the scanning of a region of composite without delamination. The structure of CFRP obtained with the

electromagnetic transducer with metamaterials respects with fidelity the image of the first layer of carbon woven 5H type.

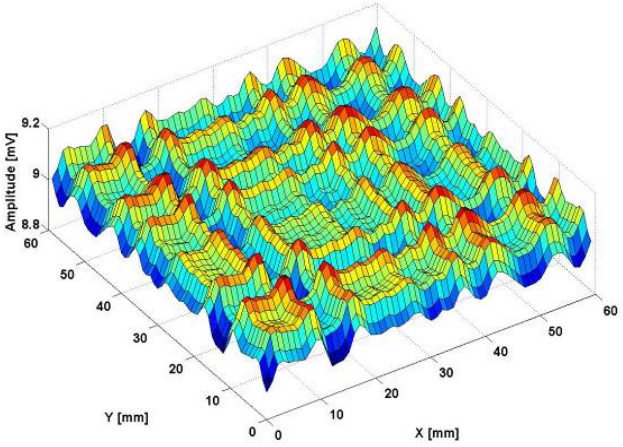

Fig. 9 – The measured amplitude of the signal delivered by the electromagnetic transducer with metamaterials from the scanning of a CFRP zone without delamination.

In Fig. 10 a is presented the picture of the plate impacted with 2.5J and in Fig. 10 b is presented the signal given by the same transducer at the scanning of a region of composite which contains the delamination. On the borders of the electromagnetic image, the structure of the woven can be observed; in the central zone, the delaminated region is emphasized.

This zone becomes electromagnetically detectable due to the modification of the electrical conductivity on the normal direction to the woven plane as a consequence of the impact.

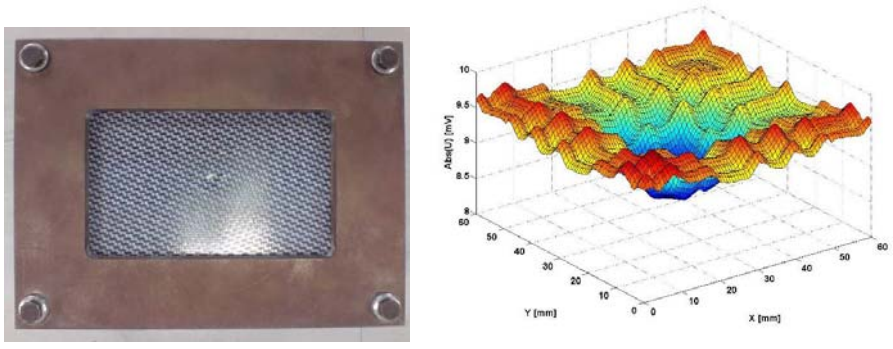

a *b*

Fig. 10 – *a*) The plate impacted; *b*) The measured amplitude of the signal

delivered by the electromagnetic transducer with metamaterials at the scanning of a CFRP zone with delamination.

4. Conclusion

The electromagnetic nondestructive evaluation was focused on the determination of inhomogeneities of electrically conductive objects which exhibit electrical conductivity lower than the host medium. In order to evaluate small dimensions conductive objects with lower conductivity, the use of evanescent electromagnetic waves that appear in the nearest vicinity of the scattering object - is proposed, in the case in which a high electromagnetic fields acts over the object to be examined. The evaluation will be more correct when the incident electromagnetic field is more focused on the region in which the scatter is placed. For the frequency range between tens and hundreds of MHz, the concentration of incident electromagnetic field can be made with a new type of metamaterials namely conical Swiss rolls. In order to concentrate the evanescent electromagnetic waves that appear at the surface of the scatter, the use of metamaterials lens made from two conical Swiss rolls is proposed. This method give good results at the examination of CFRP, including those with carbon fibers woven reinforcement, clearly emphasizing the delaminations due to low energy impact. The proposed method is limited by the fact that the evanescent waves are attenuated on small distances in common mediums, so that the scatters should be at small distances from the surface to be examined. Also, the roughness can affect the quality of the obtained electromagnetic image.

Acknowledgements. This paper is partially supported by the Romanian Ministry of Education, Research, Youth and Sports under Bilateral Projects ENDE Ro-Si 371/2010, MENDE Ro-Sk 468/2011 and Nucleus Contract No.09430104.

REFERENCES

Akkerman R., *Laminate Mechanics for Balanced Woven Fabrics*. Composites: Part **B**, *37*, 108-116 (2006).

Balanis C.A., *Advanced Engineering Electromagnetics*, Wilwey Eds., 1989.

Chen X., Grzegovczyk T., Wu B-I., Pocheco J., Kong J.A., *Robust Method to Retrieve the Constitutive Effective Parameters of Metamaterials*. Phys.Review E, *70*, 1-7(2004).

Das M., Shekhar H., Ciu X., Polikar R., Ramuhalli P., Udpa L., Udpa S.S., *A Generalized Likelihood Ratio Technique for Automated Analysis of Bobbin Coil Eddy Current Data*. NDT&E International, **35**, *5,* 329-336 (2002).

Dogaru T., Smith S. T., *Giant Magnetoresistance-Based Eddy-Current Sensor*. IEEE TRANSACTIONS ON MAGNETICS, **37**, *5*, 3831-3838 (2001).

Dood. C.V., Deeds W.E., *Analytical Solutions to Eddy Current Probe Coil Problems*. J. Appl. Phys., *39*, 2829-2838 (1968).

Grimberg R., Savin A., *Electromagnetic Transducer for Evaluation of the Structure and Integrity of Composite Materials with Polymer Matrix Reinforced with Carbon Fibers*. Romanian Patent, A/01062/08.11.2010.

Grimberg R., Savin A., Steigmann R., Serghiac B., Bruma A., *Electromagnetic Nondestructive Evaluation Using Metamaterials*. INSIGHT, **53**, *3*, 132-137 (2011).

Mandache C., Lefebvre J.H.V., *Transient and Harmonic Eddy Current: Lift-off Point of Intersection*. NDT&E International, **39**, *1*, 57-60 (2006).

Nagendran R., Thirumurugan N., Chinnasamy N., Janawadkar M.P., Baskaran R., Vaidhyanathan L.S., Sundar C.S., *Optimum Eddy Current Excitation Frequency for Subsurface Defect Detection in SQUID Based Nondestructive Evaluation*. NDT & E International, Available online, 19 August 2010.

Pendry J., Holden A.J., Robbins D.J., Stewart W.J., *Magnetism form Conductors and Enhanced Nonlinear Phenomena*. IEEE Trans.Microw.Theory Tech., *47*, 2075 (1999).

Shull P.J., *Nondestructive Evaluation: Theory, Techniques and Application*. Technology & Engineering, NY, 2002.

Sophian A., Tian G.Y., Taylor D., Rudlin J., *Electromagnetic and Eddy Current NDT: a Review*, INSIGHT, **43**, *3*, 302-306 (2001).

Tian G.Y., Zhao Z.X., Boires R.W., *The Research of Inhomogeneity in Eddy Current Sensors*. Sensors and Actuators **A**, *58*, 153-156 (1998).

METODE AVANSATE DE EVALUARE ELECTROMAGNETICĂ UTILIZÂND METAMATERIALE

(Rezumat)

Această lucrare prezintă posibilitatea de îmbunătăţire a rezoluţiei spaţiale a sistemului de control nedistructiv electromagnetic ce operează la frecvenţe de ordinul zecilor şi sutelor de MHz utilizând metamateriale pentru focalizarea undelor evanescente din apropierea obiectului de controlat. Traductorul a fost utilizat pentru vizualizarea efectivă a delaminărilor produse de impact a compozitelor de tip CFRP.

BULETINUL INSTITUTULUI POLITEHNIC DIN IAŞI
Publicat de
Universitatea Tehnică „Gheorghe Asachi" din Iaşi
Tomul LVII (LXI), Fasc. 4, 2011
Secţia
ŞTIINŢA ŞI INGINERIA MATERIALELOR

ADVANCED METHODS FOR ELECTROMAGNETIC EVALUATION USING METAMATERIALS

BY

RAIMOND GRIMBERG[1*], ADRIANA SAVIN[1], ROZINA STEIGMANN[1], NICOLETA IFTIMIE[1] and DAGMAR FAKTOROVÁ[2]

[1] National Institute of Research and Development for Technical Physics Iaşi
[2] University of Žilina, Slovakia

Received: April 15, 2011
Accepted for publication: June 27, 2011

Abstract. This paper presents a possibility to improve the spatial resolution of the electromagnetic nondestructive control systems that operate at frequencies of tens and hundreds of megahertz using metamaterials for evanescent waves focusing from the near neighbour of the controlled object. The transducer has been used for the effective visualization for delaminations produced by impacts on carbon fiber reinforced plastics (CFRP).

Key words: metamaterials, conical Swiss roll, electromagnetic evaluation, CFRP

1. Introduction

When the object to be examined has high electrical conductivity, under the action of the incident electromagnetic field, eddy currents will be induced in the material, as predicted by Faraday's law. The induced eddy

* Corresponding author e-mail: grimberg@phys-iasi.ro

current will generate a secondary electromagnetic field that will be in opposition to the incident electromagnetic field. If the incident electromagnetic field is created by a time varying current passing through an excitation coil, the interaction between the primary and secondary electromagnetic field causes modification of the electromotive force in the coil and therefore results in an apparent change in the impedance of the coil (Sophian *et al*., 2001). This change of the impedance depends on the distance between the coil and the object to be examined (lift-off), the electromagnetic properties of the material (electrical conductivity σ, magnetic permeability μ), the surface and subsurface geometry and the angular frequency ω. The penetration of eddy currents is limited, due to the skin effect (Balanis, 1989). The presence of material inhomogeneities (voids, inclusions, cracks, having lower electrical conductivity) will disturb or impede induced eddy current and in turn will also change the apparent impedance of the coil, which is measured as an indicator of the inhomogeneities (Tian *et al*., 1998). The material inhomogeneities will become a new current source inside the object to be examined (Dood & Deeds, 1968). As long as the frequencies used are not high (lower than 1GHz), the incident electromagnetic field is usually created by the coils circulated by alternative currents (Das *et al*., 2002) or current impulses (Mandache & Lefebvre, 2006). The detection of electromagnetic field created by the secondary current sources can be made either by coils of different shapes (Sophian *et al*., 2001).

In the case of low frequency incident electromagnetic field, the detection of the secondary electromagnetic field can be made also by sensors with Hall effect (Shull, 2002) or SQUID (Nagendran *et al*., 2010) and GMR sensors (Dogaru & Smith, 2001). In order to obtain a signal to noise ratio as larger as possible at detection, leading to the increase of detection probability for a higher reliability coefficient, it is necessary to use the smallest possible value of the lift - off (Shull, 2002) (distance between the electromagnetic transducer and the controlled piece). This leads to the necessity of working in near field due to the fact that the generated and respective the scattered electromagnetic waves are evanescent waves (waves that are rapidly attenuated with the distance and are difficult to be focalized using classical materials.

This paper presents a possibility to improve the spatial resolution of the electromagnetic nondestructive control systems that operates at frequencies of tens and hundreds of megahertz, using metamaterials (Pendry *et al*., 1999) for evanescent wave's focalization from the nearest neighbour of the controlled object. The optimal conditions for the metamaterials transducer (the conical Swiss rolls type) functioning, have been established, inverting data obtained from the measurement of network parameters. The transducer has been used for effective visualization of delamination of carbon fiber reinforced plastics (CFRP) created by impact.

2. Conical Swiss Roll as Metamaterials

Metamaterials can provide an engineered response to electromagnetic radiation that is not available from the class of naturally occurring materials. They consist of individual or arrays of elements for which all the geometrical dimensions are small compared to the wavelength of operation. Because the wavelength of the electromagnetic radiation is large (at 300MHz, the wavelength in air, λ_0=1m), the condition that the element should be much smaller than wavelength is accomplished.

A conical Swiss roll consists of a number of spiral-wound layers of an insulated conductor on a conical mandrel, Fig. 1. The insulated conductor is a copper foil with 18μm thickness and a layer of polyamide with 12μm thickness. The Copper and polyamide layers have been laminated without adhesive to decrease the losses at high frequencies. The insulated layer has a relative dielectric permittivity of 3.2 and loss tangent tanδ=0.0099. The conical Swiss rolls have 5 layers, 20mm base diameter, 3.2mm top diameter, the aperture angle 20^0 and height 55mm. A selection of few conical Swiss rolls with similar properties was made.

Pendry *et al*., (1999) proposed that Swiss roll made from thin conducting sheets have a macroscopic magnetic behaviour for a magnetic field applied along the rod. The radio frequency magnetic field will induce currents on the circumference of the cone and consequently a magnetization opposing the applied magnetic field.

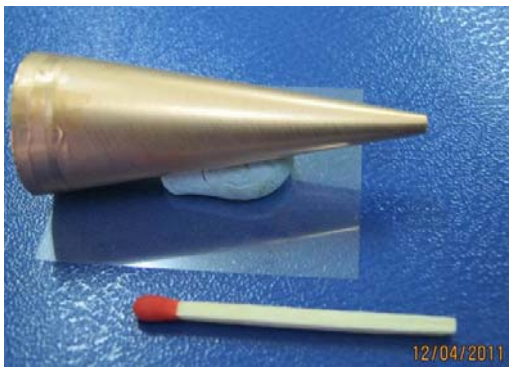

Fig. 1 – Conical Swiss roll.

The capacitive and conductive elements of the structure create a resonant RLC circuit whose induced currents are subject to, therefore a resonant μ with high positive and negative values for a range of frequencies is obtained.

Thus, a conical Swiss roll can act as radio frequency magnetic flux concentrator.

To determine the effective magnetic permeability of a conical Swiss roll, the S parameters have been measured using a Network/Spectrum/ Impedance Analyzer 4395A Agilent coupled with S Parameter Test Kit 87511A, Agilent, USA.

The measurement equipment is presented in Fig. 2.

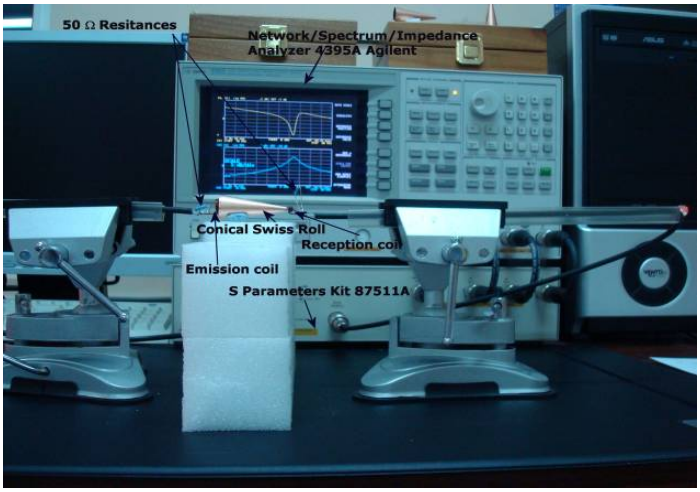

Fig. 2 – The equipment for measurement S parameters.

The electromagnetic field is generated by a coil with 2 turns having 16mm diameter, made of 1mm diameter copper wire. The response of conical Swiss roll metamaterial is detected with a reception coil having 2 turns of 3mm diameter.

The dependencies of real and imaginary components of S_{11} and S_{21} by the frequency are presented in Figs. 3, 4.

According to (Chen *et al*., 2004) the impedance of the metamaterial considered as a homogeneous slab excited by a plane wave is given by.

$$Z = \pm\sqrt{\frac{(1+S_{11})^2 - S_{21}^2}{(1-S_{11})^2 - S_{21}^2}} \tag{1}$$

The sign in front of the square root sign is chosen such that.

$$\mathrm{Re}(Z) \geq 0 \tag{2}$$

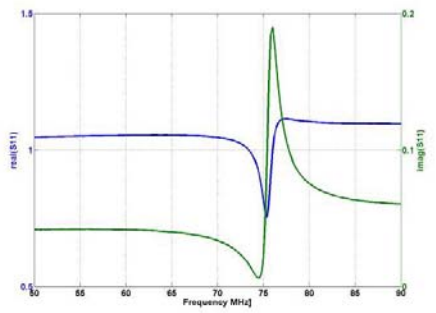

Fig. 3 - Dependency of S_{11} by frequency: real component and imaginary component.

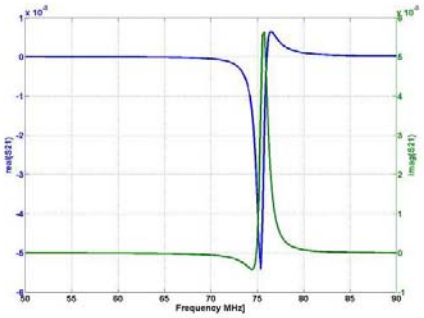

Fig. 4 - Dependency of S_{21} by frequency: real component and imaginary component.

The refraction index of metamaterial n, is obtained as a solution of transcendental equation.

$$e^{jnk_0 d} = \frac{1}{2S_{21}\left(1 - S_{11}^2 + S_{21}^2\right)} \pm j\sqrt{1 - \frac{1}{2S_{21}\left(1 - S_{11}^2 + S_{21}^2\right)}} \tag{3}$$

where $k_0 = \dfrac{2\pi f}{c}$ with frequency f, c is the speed of light in vacuum, $j = \sqrt{-1}$, and d is the height of the conical Swiss roll, the sign + or – is chosen such that.

$$\mathrm{Im}(n) \geq 0 \tag{4}$$

Thus, the effective magnetic permeability of conical Swiss roll is given by.

$$\mu_{eff} = nZ \tag{5}$$

In Fig. 5, the dependency of frequency for the effective magnetic permeability of a conical Swiss roll is presented.

It can be observed that the effective magnetic permeability becomes high for a certain frequency range, and for other frequencies it becomes negative. As applications in the domain of electromagnetic nondestructive

examination we are proposing an optimized work frequency of 72.5 MHz which assures a magnetic effective permeability of 22.

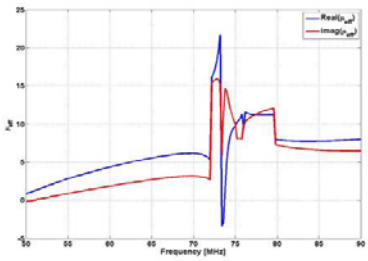

Fig. 5 – The frequency dependence of effective magnetic permeability of conical Swiss roll.

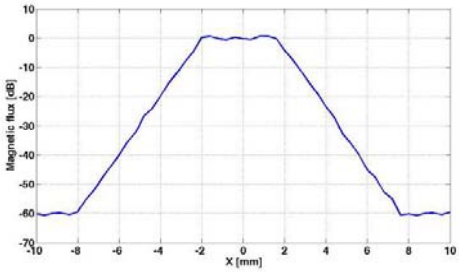

Fig. 6 – The frequency dependency of the induced emf amplitude in the reception coil at the scanning along the small base of the Swiss roll. Lift-off 0.2mm.

At this frequency, the property of a conical Swiss roll to act as an alternative magnetic flux concentrator has been verified. Using the Network/ Spectrum/Impedance Analyzer 4395A Agilent, the electromotive force (emf) induced in the detection coil that is displaced with a XY motorized stage Newmark type over the small basis of the conical Swiss roll at the distance of 1m it has been measured.

The dependency of the induced emf amplitude in the reception coil by the frequency is presented in Fig. 6. Examining data from Figure 6 it can be emphasized that, in the zone corresponding to the diameter of the small base of conical Swiss roll, for a frequency that assures a maximum of effective magnetic permeability of the investigated metamaterial, the concentration of the radio frequency magnetic flux is very high. Also, it must be mentioned that on this aperture the magnetic flux is almost constant, which suggests the existence of an electromagnetic plane wave.

3. Experimental Results

Plates from CFRP type having 6 layers of carbon fibers woven type 5 harness satin (Carbon T300 3K 5HS) with a layout that assures the quasi-isotropic properties of the plate were studied. The polymer matrix is made of Polyphenylene Sulphide (PPS). The thickness of the plate is 1.91mm with a 0.5 volume ratio. The plates are produced by TenCate Advanced Composites, Netherlands.

On these plates, delaminations due to impacts with different energies have been induced using a spherical impactor with 22mm diameter. The plates were examined by means the electromagnetic procedure presented above using the transducer (Grimberg & Savin, 2010; Grimberg *et al.*, 2011), (Fig. 7), which

contains a metamaterials lens for detection. For the generation of plane wave, a conical Swiss roll also has been used, acting as a flux concentrator. The lift-off was maintained constant at value of 0.25mm (the material to be examined can be considered) that is practically in the plane of the aperture; the reception coil is in the focal plane of the lens. The control frequency was 72.5 MHz.

In Fig. 8, we present (Akkerman, 2006) the schematic layout of the 5H satin carbon fibers woven and the picture of the layers.

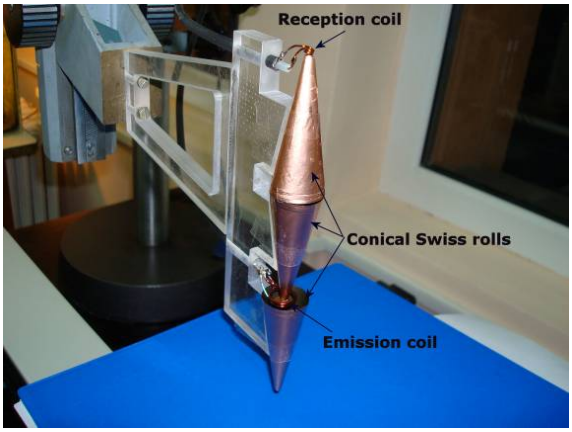

Fig. 7 – The electromagnetic transducer with metamaterials lens.

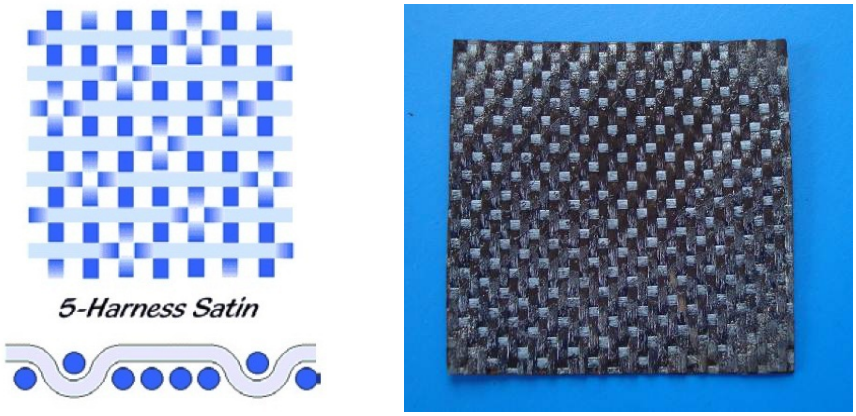

a *b*

Fig. 8 – *a*) 5H-biaxial woven fabric architectures; *b*) picture.

In Fig. 9 is presented the amplitude of the signal delivered by the electromagnetic transducer with metamaterials from the scanning of a region of composite without delamination. The structure of CFRP obtained with the

electromagnetic transducer with metamaterials respects with fidelity the image of the first layer of carbon woven 5H type.

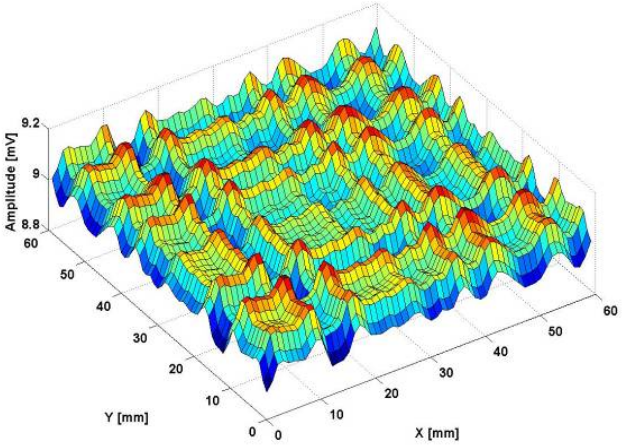

Fig. 9 – The measured amplitude of the signal delivered by the electromagnetic transducer with metamaterials from the scanning of a CFRP zone without delamination.

In Fig. 10 a is presented the picture of the plate impacted with 2.5J and in Fig. 10 b is presented the signal given by the same transducer at the scanning of a region of composite which contains the delamination. On the borders of the electromagnetic image, the structure of the woven can be observed; in the central zone, the delaminated region is emphasized.

This zone becomes electromagnetically detectable due to the modification of the electrical conductivity on the normal direction to the woven plane as a consequence of the impact.

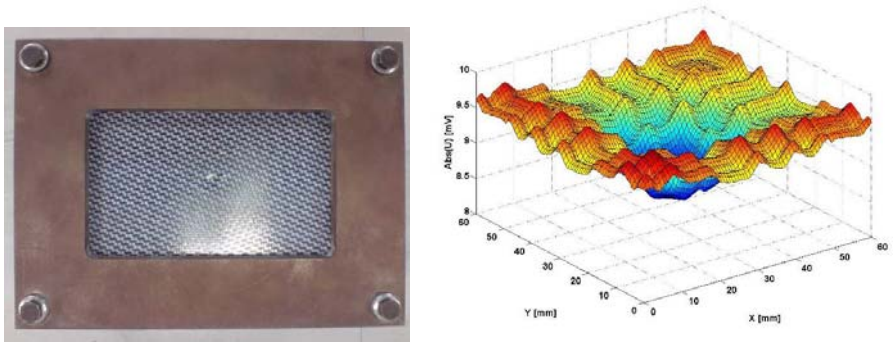

a *b*

Fig. 10 – *a*) The plate impacted; *b*) The measured amplitude of the signal

delivered by the electromagnetic transducer with metamaterials at the scanning of a CFRP zone with delamination.

4. Conclusion

The electromagnetic nondestructive evaluation was focused on the determination of inhomogeneities of electrically conductive objects which exhibit electrical conductivity lower than the host medium. In order to evaluate small dimensions conductive objects with lower conductivity, the use of evanescent electromagnetic waves that appear in the nearest vicinity of the scattering object - is proposed, in the case in which a high electromagnetic fields acts over the object to be examined. The evaluation will be more correct when the incident electromagnetic field is more focused on the region in which the scatter is placed. For the frequency range between tens and hundreds of MHz, the concentration of incident electromagnetic field can be made with a new type of metamaterials namely conical Swiss rolls. In order to concentrate the evanescent electromagnetic waves that appear at the surface of the scatter, the use of metamaterials lens made from two conical Swiss rolls is proposed. This method give good results at the examination of CFRP, including those with carbon fibers woven reinforcement, clearly emphasizing the delaminations due to low energy impact. The proposed method is limited by the fact that the evanescent waves are attenuated on small distances in common mediums, so that the scatters should be at small distances from the surface to be examined. Also, the roughness can affect the quality of the obtained electromagnetic image.

Acknowledgements. This paper is partially supported by the Romanian Ministry of Education, Research, Youth and Sports under Bilateral Projects ENDE Ro-Si 371/2010, MENDE Ro-Sk 468/2011 and Nucleus Contract No.09430104.

REFERENCES

Akkerman R., *Laminate Mechanics for Balanced Woven Fabrics*. Composites: Part **B**, *37*, 108-116 (2006).

Balanis C.A., *Advanced Engineering Electromagnetics*, Wilwey Eds., 1989.

Chen X., Grzegovczyk T., Wu B-I., Pocheco J., Kong J.A., *Robust Method to Retrieve the Constitutive Effective Parameters of Metamaterials*. Phys.Review E, *70*, 1-7(2004).

Das M., Shekhar H., Ciu X., Polikar R., Ramuhalli P., Udpa L., Udpa S.S., *A Generalized Likelihood Ratio Technique for Automated Analysis of Bobbin Coil Eddy Current Data*. NDT&E International, **35**, *5,* 329-336 (2002).

Dogaru T., Smith S. T., *Giant Magnetoresistance-Based Eddy-Current Sensor*. IEEE TRANSACTIONS ON MAGNETICS, **37**, *5*, 3831-3838 (2001).

Dood. C.V., Deeds W.E., *Analytical Solutions to Eddy Current Probe Coil Problems*. J. Appl. Phys., *39*, 2829-2838 (1968).

Grimberg R., Savin A., *Electromagnetic Transducer for Evaluation of the Structure and Integrity of Composite Materials with Polymer Matrix Reinforced with Carbon Fibers*. Romanian Patent, A/01062/08.11.2010.

Grimberg R., Savin A., Steigmann R., Serghiac B., Bruma A., *Electromagnetic Nondestructive Evaluation Using Metamaterials*. INSIGHT, **53**, *3*, 132-137 (2011).

Mandache C., Lefebvre J.H.V., *Transient and Harmonic Eddy Current: Lift-off Point of Intersection*. NDT&E International, **39**, *1*, 57-60 (2006).

Nagendran R., Thirumurugan N., Chinnasamy N., Janawadkar M.P., Baskaran R., Vaidhyanathan L.S., Sundar C.S., *Optimum Eddy Current Excitation Frequency for Subsurface Defect Detection in SQUID Based Nondestructive Evaluation*. NDT & E International, Available online, 19 August 2010.

Pendry J., Holden A.J., Robbins D.J., Stewart W.J., *Magnetism form Conductors and Enhanced Nonlinear Phenomena*. IEEE Trans.Microw.Theory Tech., *47*, 2075 (1999).

Shull P.J., *Nondestructive Evaluation: Theory, Techniques and Application*. Technology & Engineering, NY, 2002.

Sophian A., Tian G.Y., Taylor D., Rudlin J., *Electromagnetic and Eddy Current NDT: a Review*, INSIGHT, **43**, *3*, 302-306 (2001).

Tian G.Y., Zhao Z.X., Boires R.W., *The Research of Inhomogeneity in Eddy Current Sensors*. Sensors and Actuators **A**, *58*, 153-156 (1998).

METODE AVANSATE DE EVALUARE ELECTROMAGNETICĂ UTILIZÂND METAMATERIALE

(Rezumat)

Această lucrare prezintă posibilitatea de îmbunătăţire a rezoluţiei spaţiale a sistemului de control nedistructiv electromagnetic ce operează la frecvenţe de ordinul zecilor şi sutelor de MHz utilizând metamateriale pentru focalizarea undelor evanescente din apropierea obiectului de controlat. Traductorul a fost utilizat pentru vizualizarea efectivă a delaminărilor produse de impact a compozitelor de tip CFRP.

BULETINUL INSTITUTULUI POLITEHNIC DIN IAŞI
Publicat de
Universitatea Tehnică „Gheorghe Asachi" din Iaşi
Tomul LVII (LXI), Fasc. 4, 2011
Secţia
ŞTIINŢA ŞI INGINERIA MATERIALELOR

DETERMINATION OF ELASTIC TENSOR OF CFRP THROUGH ULTRASOUND PROCEDURES

BY

RAIMOND GRIMBERG*, ADRIANA SAVIN, ROZINA STEIGMANN, GABRIEL SILVIU DOBRESCU and NICOLETA IFTIMIE

National Institute of Research,
Development for Technical Physics Iaşi

Received: April 15, 2011
Accepted for publication: June 27, 2011

Abstract. This paper proposes the determination of elastic and shear modulus through measurements of longitudinal, transversal and Lamb wave propagation speed. The elastic and shear modulus in thickness direction are determined from the propagation speed of transversal and longitudinal waves generated by the US transducers with central frequency of 5MHz, respectively 4MHz and in-plane modulus are determined from the propagation speed of Lamb waves generated by air-coupled transducers with central frequency of 100 kHz.

Key words: ultrasound, CFRP, elastic properties, Lamb waves, compressional and shear waves, air coupled transducers.

1. Introduction

The use of composite materials in industrial applications has been increasing over the past years thanks to their very high specific strength, high

* Corresponding author e-mail: grimberg@phys-iasi.ro

specific stiffness, fatigue characteristics and moderate cost. Low electromagnetic reflectance and the ability to embed sensors and actuators have made fiber reinforced composites an attractive material for primary aircraft structures. In many other cases, FRPC (Fiber Reinforced Polymer Composites) materials are being developed and used to replace metal components, particularly those used in corrosive environments. Matrices used in polymer composites are typically epoxy, polyester Polyphenylene sulphide (PPS) while examples of reinforcements are carbon, glass or Kevlar (Kaw, 2006).

Typical aerospace applications for advanced composites are ultra-high-performance pressure vessels, rocket motor cases and launch tubes. Aeronautical applications include structural components as fuselages, helicopter rotor blades and external fuel tanks for combat aircraft. Commercial applications cover a wide range of uses including bike frames, tennis rackets, fuel containers used to store compressed natural gas for motor vehicles and high –performance tubular products used in the off-shore oil and gas industry (Morgan, 2002).

Because of their increasing utilization in structural applications, the nondestructive evaluation (NDE) of FRPC continues to receive considerable attention for research and development. Due to the heterogeneous nature of composites, the form of defects is often very different from those typically found in a metallic material and the fracture mechanisms are more complex.

Composite materials represent acoustically heterogeneous materials in which a variety of defects with different dimensions may be formed. Typical defects of FRPC include fiber breaks, micro cracks, delaminations, foreign objects or contaminants, impact damage and porosity or voids. Fiber/matrix distribution, fiber waviness, and fiber orientation are also important micro structural properties of composites. Many of these defects or microstructural variations cause change in the speed of ultrasound in composite materials, consequently, ultrasonic testing is currently one of the most frequently used methods for NDE of FRPC (Shull, 2002).

The propagation speed of ultrasound in solid materials depends by the elastic properties of these (Schmerr, 1998). In the case of composite materials, carbon fiber reinforces plastics (CFRP), it has been observed that the existence of some degradations as water adsorption or delamination due impacts with low energies leads to a significant modification of elastic properties (Grimberg *et al.,* 2010; 2006). From here results that, when the problem of global examination of CFRP structure is posed, we could detect both micro cracks, porosity or voids, as well as modifications that some degradations as delaminations, water adsorption, local superheating are brought to CFRP elastic properties.

In this paper we propose the determination of elastic properties of CFRP using ultrasound methods with normal transducers for longitudinal and

transversal waves that must be coupled with the examined material by means of classical coupling fluids as well as air-coupled ultrasonic transducers.

2. Air Coupled Ultrasound Transducers

Ultrasound transducers are used for generation and reception of ultrasound wave, their functioning being based on the piezoelectric phenomenon. Due high acoustic impedance of piezoelectric material, reported to the acoustic impedance of the air (the acoustic impedance is defined as the product between the propagation speed of the ultrasound and the medium density (Krautkramer & Krautkramer, 1990)), the transmission of ultrasound in air will be in a less degree, the majority of generated ultrasound beam being reflected by the interface piezoelectric material – air. From this reason, for an adequate coupling of the ultrasound transducer with the material, a coupling fluid is used.

To use the air as coupling fluid, special transducers have been developed, named air-coupled transducers, the most performing transducers use piezo-composites as active element (Newnham, 1980). Piezoelectric rods aligned in parallel along the thickness direction are embedded in a three-dimensional passive polymer matrix (1-3 configurations, Fig. 1*a*). The middle-to-middle distance between two rods must be smaller than half-wave length of the shear wave of the polymer matrix in order that the composite as a whole to vibrate (Fig. 1*b*). Both sides of rods are covered with Ni alloy electrodes and galvanization of Au layer. Afterwards, the transducers are focused by forming the composite into a spherical shape.

For a better acoustic impedance matching, a layer of silicon rubber containing air bubbles is deposed on the face of piezo-composite (Fig. 1*c*). The physical realization of the transducer is presented in Fig. 1*d*.

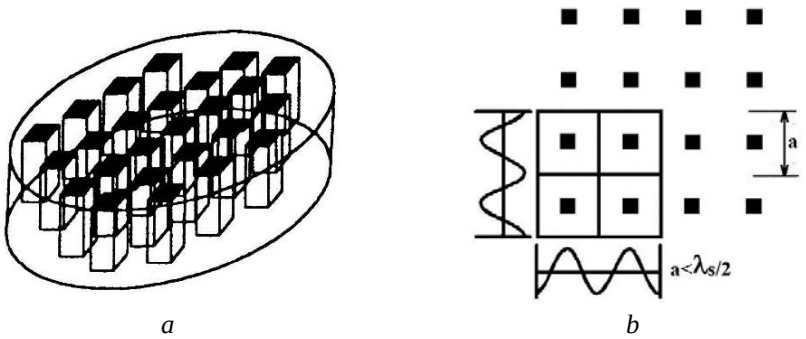

a *b*

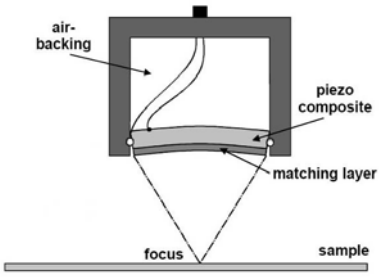

c

d

Fig. 1 – Air-coupled ultrasound transducers: *a*) 1-3 configuration; *b*) rods distribution; *c*) principle scheme; *d*) physical realization.

3. Studied Samples

Plates from composite having reinforcement from carbon fibers 5HS type and matrix from Polyphenylene sulphide (PPS) – a thermoplastic resin system have been taken into study. The studied samples have 1.91mm thickness containing 12 layers of carbon fibers woven, with quasi-isotropic global distribution (Fig. 2*a*), 0.5±0.03 volume ratio and 1460kg/m^3 density, produced by TenCate Cetex.

a

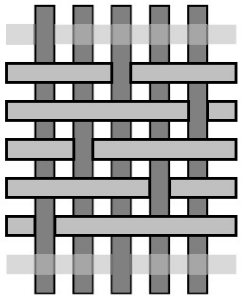

b

Fig. 2 – Studied samples: *a*) photo; *b*) scheme of 5HS carbon fiber woven.

The elastic modulus along the principal directions of the sample were determined using Dynamic Mechanical Analyzer DMA 242C-Netzsch Germany, 3 point bending fixture, on 5 samples. The principal directions are specified by the producer: X axis – direction 1, Y axis – direction 2 (X,Y are axis in the plane of composite) and Z axis - direction 3 is perpendicularly on the composite plane. For determination of elastic modulus E_1 and E_2, the samples were cropped at 50x10x1.191mm^3 and for 3rd direction 50x4x1.91mm^3.

4. Experimental SET-UP

The method impulse – echo was used for determination of compressional waves propagation velocity, with a transducer with 5MHz central frequency, A5518 Panametrics type, mounted on a delay block having 20mm thickness and 2700m/s velocity of compressional waves, using the gel ZG-F – GE as coupling fluid.

The method of transmission was used for determination of shear wave's propagation velocity, using two transducers for shear waves with 4MHz central frequency directly applied on the examined sample and honeybee, a very good non-Newtonian liquid.

The experimental equipment contains a Pulse Receiver 5073PR Pulser Receiver – Panametrics USA, the measurement of the times being made with a digital oscilloscope with memory, LeCroy Wave Runner 64Xi with 10GS/s sampling frequency, allowing a measurement precision of time of ±0.1ns.

For generation of surface waves, SH_0 type (shear waves horizontal, mode 0) as well as Lamb waves, the pitch-catch TR reflection method has been used with a pair of air coupled US transducers, type NCG100-D25-P76 –Ultran Group USA. The central frequency of the transducers is 100kHz, they are focused, having the focal distance of 76 mm.

The transducers were coupled to Pulse Receiver 5077PR – Panametrics USA, the signal delivered by the reception transducer being supplementary amplified with 40dB with ultrasonic preamplifier Panametrics USA. The time has been measured with the digital oscilloscope LeCroy Wave Runner 64Xi.

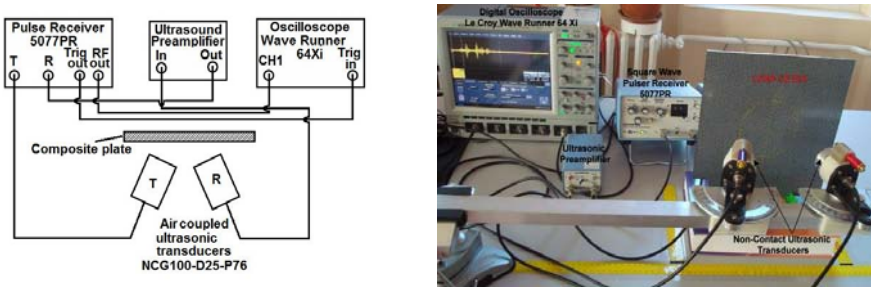

a *b*

Fig. 3 – Experimental set-up for generation of SH_0 and Lamb waves: *a*) block diagram; *b*) photo.

In Fig. 3 are presented the basic diagram (*a*) and the photo (*b*) of the experimental setup.

5. The Measurement Principle

Into an homogeneous and isotropic material, the compression wave and shear waves velocities depend on the elastic properties of material (Rose, 1999)

according the relation.

$$C_P = \sqrt{\frac{E}{\rho}\frac{1-\upsilon}{(1+\upsilon)(1-2\upsilon)}} \qquad (1)$$
$$C_S = \sqrt{\frac{G}{\rho}}$$

where E represents the elastic modulus, G – the shear modulus, υ - the Poisson coefficient and ρ the density.

Applying the compressional waves and respective the shear waves transducers on the surface of the composite plates, the propagation of the US beam will be made along the 3rd principal direction, so that , from the relation (1), E_3, $G_{13}=G_{23}$, and $\upsilon_{13}=\upsilon_{23}$ can be determined (Grimberg *et al.*, 2009).

For determination of elastic constants in the pane of composite, the procedures of generation of SH_0 and Lamb waves with air-coupled ultrasonic transducers were used.

The method starts from the observation that allows a critical incidence angle $i_{cr,}$ an incident ultrasound beam, compressive waves type, at the interface air-composite will have a change of mode, in material appearing both compressional as well as shear waves parallel with the interface, according to Fig. 4.

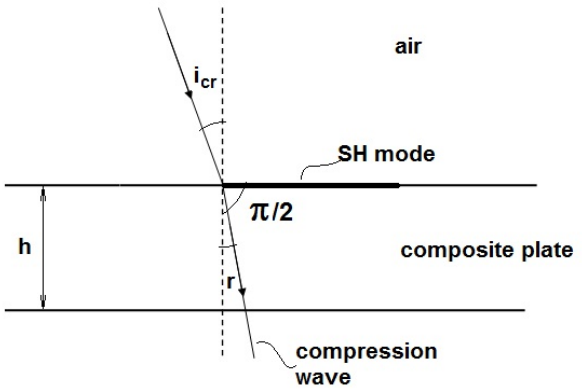

Fig. 4 – SH waves generation.

The dispersion equation for SH is given by the relation (Rose, 1999).

$$\left(\frac{\omega^2}{c_S^2} - k_m^2\right)^{1/2} h = \frac{m\pi}{2}, \qquad m - 0, 2, 4, ... \qquad (2)$$

where k_m is the wave's number of SH modes, c_S having the significance from above, with the observation that in this case it is referred to the propagation velocity of the shear waves along a direction in the composite's plane.

$$c_n = \frac{\omega}{\left[\frac{\omega^2}{c_s^2} - \left(\frac{m\pi}{2h}\right)^2\right]^{1/2}} \tag{3}$$

For SH_0 mode, m=0, so that (3) become.

$$c_0 = c_s \tag{4}$$

From the measurement of SH_0 mode propagation velocity, c_0, the propagation velocity of shear waves in the composite's plane can be determined along any direction.

In Fig. 5 are presented the signals delivered by the reception transducer (Fig.1*d*) when the incidence angle is equal to critical angle, determined with Snell's law.

$$\frac{c_{air}}{c_s} = \frac{\sin i_{cr}}{1} \tag{5}$$

c_{air}=340m/s
c_s=1970m/s.

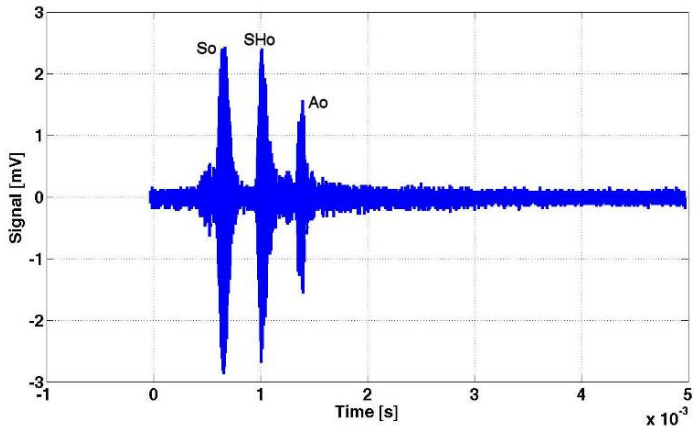

Fig. 5 – The propagation modes of US waves in studied composite plate for incident critical angle determined according to (5).

The Lamb waves are elastic waves guided between the faces of the composite plate, symmetric and anti-symmetric modes might appear, propagating into plate with different velocities.

The dispersion equations for Lamb waves are named Rayleigh-Lamb, at their mathematical form are.

$$\tan\left(\frac{pq}{ph}\right) = -\frac{4k^2 pq}{\left|q^2 - k^2\right|^2} \qquad for \text{ symmetrical modes}$$

$$\tan\left(\frac{qh}{ph}\right) = -\frac{\left|q^2 - k^2\right|^2}{4k^2 pq} \quad \text{for anti-symmetrical modes} \tag{6}$$

where

$$p^2 = \left(\frac{\omega}{C_s}\right)^2 - k^2; \qquad q^2 = \left(\frac{\omega}{C_p}\right)^2 - k^2; \qquad k = \frac{\omega}{c_{phase}}$$

C_{phase} being the phase velocity of Lamb waves.
The group velocity of Lamb wave is defined

$$c_{group} = \frac{d\omega}{dk} = c_{phase}^2 \left[c_{phase} - \omega \frac{dc_{phase}}{d\omega} \right]^{-1} \tag{7}$$

Relation available both for symmetrical as well as anti-symmetrical modes.

For relative small thickness of the plate and at relative low frequency, the velocity of the symmetric mode 0 (S_0) is constant so that $\frac{dc_{phase}S_0}{d\omega} \approx 0$ and $c_{group}S_0 \approx c_{phase}S_0$. In the same experimental conditions, also $c_{group}A_0 \approx c_{phase}A_0$, where A_0 represents 0 order anti-symmetric mode.

By the proposed experiments we can determine, with sufficient precision, the propagation group velocity of A_0 and S_0 modes, so that, solving the equations system (6), the propagation velocity of compressional waves in the composite plane can be determined. Knowing the propagation velocities of compressional and shear waves in the composite plane, the elastic and shear modulus as well as Poisson coefficients can be determined.

6. Results

The values of elastic modulus E_1, E_2, E_3 were determined using Dynamic mechanical Analyzer (DMA) with 3 points bending fixture as well as through ultrasound methods described above.

In Table 1 are presented the average of 5 measurements in the case of DMA using and 50 measurements for US procedures.

Table 1

The Elastic Modulus Along Principal Directions Measured on CFRP Studied Samples

Determination procedure	E_1 [GPa]	E_2 [GPa]	E_3 [GPa]
DMA	45.2 ± 0.7	44.3 ± 0.7	11.1 ± 0.3
US	45.8 ± 0.8	44.8 ± 0.9	11.4 ± 0.5

The shear modulus were determined only with ultrasound procedures previous described, the results being presented in Table 2.

Table 2

The Shear Modulus Measured on CFRP Studied Samples by Ultrasound Procedures

G_{12} [GPa]	G_{21} [GPa]	$G_{13} = G_{23}$ [GPa]
8.4 ± 0.2	8.4 ± 0.2	5.5 ± 0.1

Poisson's ratio have been determined also by ultrasound methods, the values obtained are presented in Table 3, as average of 50 measurements.

Table 3

Poisson's Ratio Determined by Ultrasound Procedures

υ_{12}	υ_{21}	$\upsilon_{13} = \upsilon_{23}$
0.32	0.32	0.03

Data from Table 1 show that the values of elastic modulus determined through the two procedures are closely enough, having, in addition, relative similarly dispersions. This fact shows that, using complex nondestructive procedures of US, described above, the elastic constants of composite materials reinforced with carbon fibers woven and matrix from PPS can be determined with good accuracy.

7. Conclusion

For determination of elastic and shear modulus, Poisson's ratio of the composite materials with reinforcement from carbon fiber woven, the using of combined ultrasound methods are proposed, namely impulse-echo for compressional waves, send-receive method for transversal waves as well as guided waves and surface waves using air-coupled US transducers with relatively low frequency. The obtained results are in good concordance with those obtained by destructive testing using Dynamic Mechanical Analysis.

Acknowledgement. This paper was partially supported by the Romanian Ministry of Education, Research, Youth and Sports under Nucleus Program –Contract

PN 09430104, and PN II Bilateral Cooperation Projects ENDE Ro-Si 371/2010 and MENDE Ro-Sk 468/2011.

REFERENCES

[1]. Kaw A.K., *Mechanics of Composite Materials*. 2nd Ed., Taylor and Francis, NY, 2006.
[2]. Morgan P., *Carbon fibers and their composites*. Taylor &Francis, NY, 2005.
[3]. Shull P.J., *Nondestructive Evaluation – Theory*. Techniques and Applications, Marcel Dekker, NY, 2002.
[4]. Schmerr Jr. L.W., *Fundamentals of Ultrasonic Nondestructive Evaluation*. A modeling approach, Plenum Press, NYLondon, 1998.
[5]. Grimberg R., Savin A., Steigmann R., Curtu I., Barsanescu P.D., Grum J., *Ultrasound and Eddy Current Nondestructive Evaluation of CFRP – Correlation with Mechanical Properties of the Composite*. ECNDT 2010 – the 10th European Conference on NDT, Moscow, Rusia, 7-11 June 2010.
[6]. Grimberg R., Savin A., Steigmann R., Bruma A., Barsanescu P., *Ultrasound and Eddy Current Data Fusion for Evaluation of Carbon Epoxy Composite Delaminations*. INSIGHT, **51**, *1*, 25-32 (2009).
[7]. Krautkramer J., Krautkramer H., *Ultrasonic Testing of Materials*. 4th Ed., Springer-Verlag, Berlin, 1990.
[8]. Newnham R.E., *Composite Piezoelectric Transducers*. Mater. Eng. 2, 93-106 (1980).
[9]. Rose J.L., *Ultrasonic Waves in Solid Media*. Cambridge University Press, Cambridge, 1999.
[10]. Grimberg R., Savin A., Steigmann R., Bruma A., Barsanescu P., Salavastru, *Determination of CFRP's Mechanical Properties Using Ultrasound Methods*. Proceeding D. of the 5th International Workshop NDT in Progress, Meeting of NDT experts, Prague, Czech Republic, 65-74, October 12 – 14, 2009.

DETERMINAREA TENSORULUI ELASTIC AL CFRP PRIN PROCEDURI DE ULTRASUNETE

(Rezumat)

Această lucrare propune determinarea modulului elastic şi de forfecare prin măsurători de unde longitudinale transversale şi unde Lamb. Modulul elastic şi de forfecare în direcţia grosimii sunt determinaţi din viteza de propagare a undelor transversale şi longitudinale generate de traductori de ultrasunete având frecvenţa centrală de 5MHz, respectiv 4MHz, iar modulul în plan este determinat din viteza de propagare a undelor Lamb generate de traductori de ultrasunete fără contact cu frecvenţa centrală de 100kHz.

BULETINUL INSTITUTULUI POLITEHNIC DIN IAŞI
Publicat de
Universitatea Tehnică „Gheorghe Asachi" din Iaşi
Tomul LVII (LXI), Fasc. 4, 2011
Secţia
ŞTIINŢA ŞI INGINERIA MATERIALELOR

ENVIRONMENTAL AND SAFETY LEGACIES OF A MINING INDUSTRY RESEARCH INSTITUTE

BY

LINN D. HAVELICK*

Colorado School of Mines Research Institute,

Received: April 14, 2011
Accepted for publication: June 27, 2011

Abstract. A metallurgical research institute that operated in Colorado for 75 years left a legacy of environmental and safety problems. Samples from ore bodies and mineral deposits from around the world were brought to the site for laboratory and pilot scale testing. After the completion of research projects the samples and wastes were typically disposed on the site. The contamination of buildings, soils and ground water by heavy metals and naturally occurring radionuclides required nearly 25 years of investigation and remediation, which is still ongoing. A 1992 water main break that flooded a settling pond into the adjacent stream helped to initiate federal government enforcement. The location of the site is at the edge of the Rocky Mountains on geologic strata that had been uplifted to the vertical, with several types of mineral bedrock underlying the site. This complicated determination of background concentrations of the naturally occurring contaminants. Risk modeling was used to develop site-specific cleanup standards for the contaminants of concern. The history of thousands of different materials deposited across the site complicated identification of the scope of contamination and led to the use of non-traditional investigative techniques. Cleanup is currently nearing completion with residual uranium contamination of ground water being monitored.

Key words: remediation; metals, radionuclides, mining, mines, Experimental Plant.

* Corresponding author; *e-mail:* Linn.Havelick@is.mines.edu

1. Introduction

In 1910 the State of Colorado appropriated funds for the construction of an Experimental Plant at the Colorado School of Mines in Golden, Colorado. The Experimental Plant rented equipment and facilities to the mining industry for the pilot-scale crushing, grinding, beneficiation and treatment of ores and minerals. Between 1912 and 1987 thousands of projects were performed on a wide variety of ore and minerals. Following projects the materials were disposed of in the adjacent Clear Creek, buried on site, or used as fill.

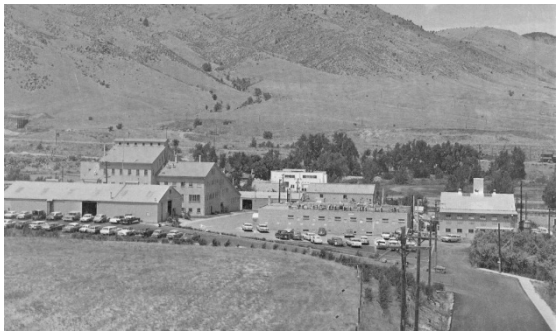

Fig. 1 – Colorado School of Mines Research Institute, ca. 1968, Golden, Colorado.

Investigation and remediation of contamination at the site began near the cessation of research activities in 1987.

2. Site History

The site is located at the eastern base of the Rocky Mountains in Golden, Colorado on the south bank of Clear Creek. During the second half of the 1800's the mountains above Golden were intensively mined for gold and silver using hard-rock underground mining techniques and placer mining techniques. During that period seven or eight ore smelters operated in the valley where the city of Golden is located to serve the mining industry. Coal and clay mines operated in the same valley during that time. Later mining operations were conducted in the Clear Creek watershed for lead, zinc, uranium, molybdenum, and other minerals.

A large portion of the research conducted at the site involved the handling and treatment of ores to concentrate the valuable minerals. The techniques used and developed for specific ore bodies and types dramatically increased the ability of the industry to use lower and lower grades of ore. Techniques such as gravity concentration, flotation, grinding, particle sizing, and leaching allowed the profitable recovery of minerals from low-grade ores that could not be economically processed with the mining and smelting processes used in the 19th century.

Research projects brought samples of ores and minerals to the site in quantities from analytical samples to drums and truck loads up to train car loads. Thousands of research projects were conducted involving ores and minerals that were of commercial interest during any given decade. Lead, tin, copper, molybdenum, gold, uranium, iron, tungsten, and many other ores, coals, and minerals were tested and evaluated. Exotic materials such as moon rocks or manganese nodules from the ocean floor were tested. The projects were conducted for thousands of clients from around the world.

The original Experimental Plant expanded operations until there were approximately seventeen buildings on the Site by the 1960's. Around 1950 a non-profit corporation, the Colorado School of Mines Research Foundation, was formed by the mining industry to operate the facilities. By the 1960's the corporation was renamed the Colorado School of Mines Research Institute (CSMRI).

By 1950 a one hectare area of the bed of Clear Creek adjacent to the Experimental Plant had received sufficient fill material to create an area now referred to as the lower terrace. The operational buildings were located above the bank of Clear Creek on a 2.5 hectare area now referred to as the upper terrace. Around 1950 a settling pond was constructed on the lower terrace.

3. Site Geology and Background Concentrations

The geologic setting of the site is complex. Situated at the eastern edge of the Rocky Mountains, the site is located on a geologic feature known as the Dakota Hogback. As the Rocky Mountains were formed, the uplifting tilted older, originally horizontal sedimentary strata, along the edges of the mountains to the vertical. The resulting Dakota Hogback formation has vertical layers of sandstone, clay, coal, and shale at the site. See Figure One. The clay and coal deposits were mined during the 1800's, leaving vertical fins of sandstone sticking out of the ground to the north and south of the site. The trenches between the sandstone fins were backfilled with soil, construction debris, trash, and other materials from across the area during the 1900's. At the site the bedrock is covered with alluvium from Clear Creek watershed.

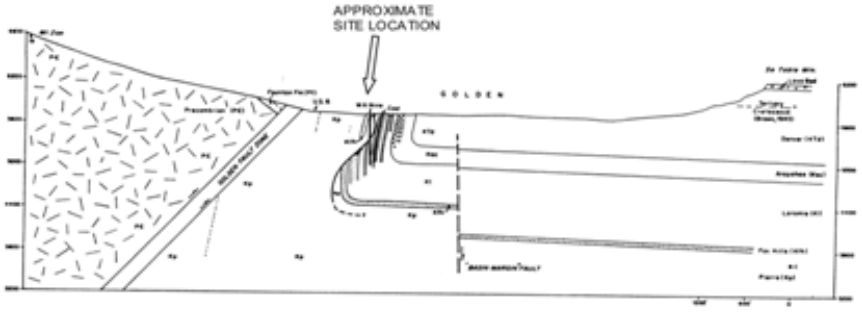

Fig. 2 – Cross Section of Site Geology.

Each of the geologic features present at the site contains naturally occurring concentrations of minerals specific to each feature. Thus the site is not atop a consistent geology with a single set of background values for the contaminants brought to the site. Multiple strata, alluvial deposits, man-made fill, historic mining activities, and effluent from earlier smelting operations all contributed to varying levels of metals and radionuclides that were present before research operations began.

Several investigations were performed to determine useful background levels for the contaminants of concern. The investigations included efforts to determine the typical levels of metals and radionuclides that were present in the Golden area whether or not the levels were naturally occurring or present in the area due to other activities such as mining or smelting, but not from site research operations.

4. Risk Assessment

The site contained contaminants regulated under different rules and regulations by the State of Colorado and the United States. Separate laws governed naturally occurring radionuclides, metals considered hazardous as wastes, soils with lower concentrations of metals that pose dangers to children, and numerous other rules and regulations. To determine the risks to humans and the environment associated with the various contaminants of concern several studies were performed.

Studies of risk associated with heavy metals in soils for occupants considered the potential for ingestion and inhalation of contaminated soils. Risks were examined for several potential land uses such as recreational, urban resident, and commercial use. Site-specific cleanup standards were developed based on accepted formulas that would demonstrate acceptable risk for the chosen land use.

Studies of risk associated with naturally occurring radionuclides brought to the site considered potential exposures from ingestion and inhalation as well as external radiation dose and indoor radon exposures resulting from uranium and radium decay.

For a given contaminant the site background concentration or activity was combined with the concentration or activity considered to present acceptable risks. This background plus contaminant level was used to generate tentative derived contaminant goal limits (tentative DCGL's). The DCGL's were used during investigation to determine the boundaries and expected volumes of soil expected to be excavated or controlled.

5. Settling Pond Flood and Clean Up

In December of 1992 a primary water main for the City of Golden

broke under the site. Several million liters of water flowed down from the upper terrace of the site to the settling pond. The banks of the settling pond overflowed and breached, with much of the water released in to Clear Creek.

The United States Environmental Protection Agency (EPA) mobilized to excavate the settling pond area, the dikes surrounding the pond, and portions of the stream bank above the pond. Approximately 17,000 cubic meters of contaminated soil was excavated and placed into a temporary stockpile adjacent to the site. To protect the soil below the stockpile a clay liner was installed prior to placement of the contaminated soil.

The EPA ordered the potentially responsible parties (PRP's) to evaluate the stockpile to determine options for remediation or disposition. Following a regulated process of public involvement and input, the option for disposal of the contaminated soil to an industrial waste landfill was selected and implemented.

6. Drum and Building Decontamination and Demolition

The site contained seventeen buildings, thousands of drums of materials, an industrial sewer system, and extensive laboratory and pilot facilities. Where possible, drum owners were identified and the drums returned to the owners. Additional drums required characterization and shipment for off-site disposal. The buildings were inspected for the presence of asbestos and identified materials removed under containment. Radionuclide contamination of concrete floors was identified and removed using bead-blasting machines equipped with HEPA filters. Buried industrial sewer lines were identified and flushed out to remove contamination.

Demolition debris from buildings was evaluated to determine disposal options. The decontamination activities performed prior to demolition resulted in a large majority of the demolition debris being acceptable for disposal at a local municipal waste landfill.

Following demolition of the buildings the remaining concrete floors and foundations and asphalt roadways were evaluated for contamination. Approximately half of the concrete and asphalt was considered appropriate for recycling and half for disposal in a municipal waste landfill. Less than one percent of the concrete and asphalt were required to be disposed at a hazardous waste landfill.

7. Investigation of the Nature and Extent of Soil Contamination

Sites are often investigated to determine the type of contaminants that exist and their physical distribution. This information is used to estimate the volume of material that needs to be addressed and to evaluate options for remediation. One method used for site investigation involves the collection and analysis of surface and subsurface samples through boreholes. Modeling techniques are used to

estimate the boundaries of contaminated zones, depth and shape of contaminant plumes or distribution, and volumes of material exceeding site contaminant limits.

This method of investigation was implemented at the site and the results were used to evaluate remedial alternative and costs. When excavation began based on those results it quickly became apparent that the complexities of the site had limited the usefulness of the traditional investigation methods. Unlike a typical industrial site with a limited number of material inputs and a likewise limited number of contaminant release methods, this site had thousands of different material inputs and an equally large variety of waste handling and disposal locations and distributions. The excavation was halted within six weeks of the start as it was clear that the extent and distribution of contaminants had not been adequately characterized.

One of the complexities that may have limited the success of contaminant modeling at the site lies in the nature of ores and of research operations. Modeling techniques typically rely on knowledge of contaminant distributions in the materials being deposited at the site. In the case of a typical milling operation, one or a few ore bodies of a specific ore type are used as feedstock to the operation. The target metal itself may be considered a contaminant in a later cleanup. Metals and minerals that are geologically deposited along with the target metal in ores can also be considered contaminants. For instance, a copper ore may have elevated levels of arsenic or a tin ore may have elevated levels of uranium, neither of which may be present in concentrations amenable to recovery. Many combinations of metals and contaminants are produced from ore bodies.

At this site thousands of projects with multiple ore types from different ore bodies resulted in the deposition of a complex mix of contaminants that included the target metals and associated minerals.

A revised investigation approach used the extensive collection of data that had been generated by the earlier investigation and excavation attempt. The excavation was re-initiated at each location where contamination was known to be located. Known contaminated soil was removed in 30 centimeter lifts. The base and sides of the excavation were then evaluated with field instrumentation to determine remaining contaminant levels and distribution. Additional lifts were removed sequentially until remaining soil met the tentative derived contaminant goal limits (DCGL's). Field instrumentation used included portable X-ray fluorescence analyzers, portable gamma spectrophotometers, and hand-held gamma scintillators. Excavated soils were placed into lined stockpiles on-site for further evaluation. Following evaluation of possible alternatives for disposition of the soil stockpiles, off-site disposal in appropriate landfills was selected as the preferred remedy.

8. Ground Water Evaluation

Numerous wells were placed to sample shallow ground water during

different phases of the project. The only contaminant consistently detected above regulatory limits was uranium. For most of the history of the site investigation and cleanup only one well was found to consistently have contamination above regulatory limits. That well appeared to be declining in concentration until the 2000's when the concentration of uranium was typically between one to two times the ground water regulatory limit of 30 parts per billion.

Following the completion of excavation work a well (Well 8) was added in a portion of the former pond area that was cleaned up by EPA in the 1990's. That well was found to have uranium concentrations ranging from 500 to 1800 ppb.

Additional investigation found that the EPA had not cleaned up the western portion of the lower terrace well enough during their efforts in the 1990's. Additional investigatory excavation was performed in 2010 in that portion of the site to identify contaminated soil contributing to the elevated uranium concentrations in ground water. Some of the existing wells were removed due to excavation in their locations. Excavations were backfilled with clean alluvial fill close to the nature of the original alluvium at the site.

Following that excavation wells that had been removed due to excavation were replaced and an additional well was placed to detect potential contamination in deep ground water. The deep ground water proved to be uncontaminated.

Monitoring of the shallow wells will continue for at least two years to determine uranium contamination levels and trends. Initial post-excavation results indicate that uranium levels dropped considerably in the vicinity of Well 8 but are still above ground water limits.

9. Conclusion

Several factors contributed to the complexity surrounding the investigation and clean up of the former Colorado School of Mines Research Institute site. These included the site geology with several different bedrock types each with unique background concentrations of minerals and historical mining activities that altered area concentrations of background minerals. Local mining and backfilling activities further altered the natural state of the site. The nature of a facility performing numerous research projects that brought a wide variety of ore types to the site complicated the identification of the distribution and extent of contaminants.

The site is now being brought back to beneficial use. The technical difficulties discussed here resulted in delays to progress on the site evaluation and cleanup, but financial, legal, political, and regulatory concerns also contributed.

REFERENCES

[1]. ⁎⁎ *Extensive documentation including investigation reports, work plans, analytical results, ground water monitoring reports, remediation reports, regulatory communications, maps, and drawings can be found at the website*: http://www.is.mines.edu/ehs/CSMRI/CSMRI2007.htm.

[2]. ⁎⁎ Weimer, 1976, Cretatious Stratigraphy, Tectonics and Energy Resources, Western Denver Basin.

[3]. ⁎⁎ Revised Remedial Investigation/Feasibility Study and Proposed Plan, New Horizons Environmental Consultants, January 21, 2004.

[4]. ⁎⁎ Revised Remedial Investigation/Feasibility Study and Proposed Plan, S.M. Stoller, May 2007.

[5]. ⁎⁎ Monitoring Report for CSMRI Site Fourth Quarter 2010, S.M. Stoller, February 2011.

[6]. ⁎⁎ Final Work Plan, Environmental Assessment and Characterization, Colorado School of Mines Research Institute Site, Flood Plain Area, Golden, Colorado, S.M. Stoller, August, 2010.

MOŞTENIREA UNUI INSTITUT DE CERCETARE ÎN INDUSTRIA MINIERĂ

(Rezumat)

Un institut de cercetare în domeniul metalurgiei, care a funcţionat în Colorado timp de 75 de ani, a lăsat în urmă o serie de probleme în domeniul protecţiei mediului şi securităţii muncii. Eşantioane de minereuri brute şi zăcăminte de minereuri din toată lumea au fost aduse în zonă pentru testări la nivel de laborator şi la nivel semiindustrial. După încheierea programelor de cercetare, eşantioanele şi reziduurile au fost lăsate pe teren. Contaminarea clădirilor, solului şi pânzelor freatice cu metale grele şi nuclizi radioactivi naturali a necesitat aproape 25 de ani de investigaţii şi încercări de rezolvare a problemelor, care sunt încă în desfăşurare. O avarie a sistemului de alimentare cu apă, care a cauzat inundarea unui bazin de decantare şi scurgerea apei într-un pârâu învecinat, a determinat guvernul federal să intervină pe cale legală. Locaţia terenului respectiv este la baza Munţilor Stâncoşi, pe formaţiuni geologice care s-au ridicat pe verticală, cu mai multe tipuri de roci la bază. Acest lucru făcut ca determinarea concentraţiilor contaminanţilor naturali să fie mai dificilă. Elaborarea standardelor necesare în vederea curăţirii zonei de contaminanţi s-a făcut prin programe de modelare a riscurilor. Datorită miilor de tipuri de materiale rămase în zonă, identificarea contaminanţilor a devenit foarte dificilă şi a fost necesară folosirea altor tehnici de investigare decât cele tradiţionale. Operaţiunea de curăţire a zonei este aproape de faza finală, contaminarea reziduală a solului cu uraniu fiind atent monitorizată.

BULETINUL INSTITUTULUI POLITEHNIC DIN IAŞI
Publicat de
Universitatea Tehnică „Gheorghe Asachi" din Iaşi
Tomul LVII (LXI), Fasc. 4, 2011
Secţia
ŞTIINŢA ŞI INGINERIA MATERIALELOR

HYDRAULIC PROPERTIES OF FERROALUMINO-BELITE CEMENT BASED ON ELECTRIC ARC FURNACE STEEL SLAG

BY

REMUS ION IACOBESCU[1]*, DIMITRA KOUMPOURI[2], RAMI SABAN[1] and GEORGE N. ANGELOPOULOS[2]

[1] PolitehnicaUniversity of Bucharest,
Department of Materials Science and Engineering
[2]University of Patras, Greece
Department of Chemical Engineering

Received: April 14, 2011
Accepted for publication: June 27, 2011

Abstract. Calcium ferroalumino-belite (FAB) cement was developed with addition, as raw material, of electric arc furnace steel slag (EAFS). Aimed to reduce the environmental impact of cement production, low lime saturation factor (LSF), in the range of 70% to 74%, and low firing temperature as 1320°C were applied. Three types of cements were examined, with different amount of EAFS: 10wt.%, 17wt.% and 27wt.% respectively. Raw materials were characterized by XRF and the obtained clinkers by XRD. Particles size distribution of the powdered clinkers was analyzed by laser analyzer. Compressive strength measurements were performed according to EN 196-1, whereas the hydration properties were investigated by SEM and TG-DTG measurements respectively. Relatively high compressive strength results have been registered on early days of hydration decreasing by increasing the EAFS addition. This has been attributed mainly to Klein compound reaction.

Key words: electric arc furnace steel slag valorization, ferroalumino - belite cement, hydration.

* Corresponding author e-mail: iacobescu.remus@hotmail.com

1. Introduction

In recent times, attention has been given to the development of modified cement clinkers, leading to energy saving. One of such promising low CO_2 emitting alternative cements contain as main mineralogical phases C_2S, $C_4A_3\hat{S}$, C_4AF and $C\hat{S}$. These compared to Ordinary Portland Cement (OPC) in which C_3S is the main compound, require lower clinkering temperatures. The hydration rate of $C_4A_3\hat{S}$, equation 1, is very fast, leading to the formation of trisulfoaluminate (AFt) (Kasselouri *et al.,* 1995). In the absence of adequate gypsum, $C_4A_3\hat{S}$ react only with water, equation 2, and forms AFm (monosulfoaluminate hydrate) (Dova *et al.,* 2005). In both cases crystalline $Al(OH)_3$ is formed also.

$$C_4A_3\hat{S} + 2C\hat{S}H_2 + 34H \rightarrow C_6A\hat{S}_3H_{32} + 2AH_3 \quad (1)$$

$$C_4A_3\hat{S} + 18H \rightarrow C_4A\hat{S}H_{12} + 2AH_3 \quad (2)$$

Ferrite phase in lack of anhydrite it hydrates to form hydrogarnet, according to equation 3 whereas if sufficient gypsum is available ettringite and AFm will be formed according to equation 4 and equation 5 (Meller *et al.,* 2004).

$$C_4AF + 10H \rightarrow (4/3)C_3(A_{0.75}F_{0.25})H_6 + (2/3)FH_3 \quad (3)$$

$$C_4AF + 3C\hat{S}H_2 + 30H \rightarrow C_6A\hat{S}_3H_{32} + FH_3 + CH \quad (4)$$

$$C_4AF + C\hat{S}H2 + (n + 2)H \rightarrow C_4A\hat{S}H_n + FH_3 + CH \quad (5)$$

From the hydration of ferrite phase, the formation of other calcium aluminate phases is also possible, however these are metastable with respect to hydrogarnet (Chrysochoou & Dermatas, 2006). On the other hand, ferroaluminate belite cements due to their low pH, their low porosity and the ability of ettringite and AFm phases to bind heavy metals, calcium sulfoaluminate cements are of interest in the field of hazardous waste encapsulation (Albino *et al.,* 1996; Peysson *et al.,* 2005; Zhou *et al.,* 2006). The main objective of this study was the characterization of the hydration products of the produced cements with addition of EAFS. Techniques as SEM and TG-DTG have been used.

2. Materials and Methods

Raw materials used for the preparation of the raw meals were: limestone, EAFS, bauxite and gypsum. Slag was used as received. Chemical analysis was performed by XRF (Philips PW 2400). Three types of clinkers

were produced using EAFS as raw material in 10wt.% (M1), 17wt.% (M2) and 27wt.% (M3) respectively. The mineralogical phases were estimated by adapting Bogue equations 6 to 10, to $CaO\text{-}SiO_2\text{-}Al_2O_3\text{-}Fe_2O_3\text{-}SO_3$ ($CSAF\hat{S}$) system (Chen & Juenger, 2010) as following:

$$\%C_4AF = 3.043(\%Fe_2O_3) \tag{6}$$

$$\%C_4A_3\hat{S} = 1.995(\%Al_2O_3) - 1.273(\%Fe_2O_3) \tag{7}$$

$$\%C_2S = 2.867(\%SiO_2) \tag{8}$$

$$\%C\hat{S} = 1.700(\%SO_3) - 0.445(\%Al_2O_3) + 0.284(\%Fe_2O_3) \tag{9}$$

$$\%C=1.000(\%CaO)-1.867(\%SiO_2)-1.054(\%Fe_2O_3)- -0.550(\%Al_2O_3)-0.700(\%SO_3) \tag{10}$$

The quality indexes, lime saturations factor (LSF), silica modulus (SM) and alumina modulus (AM) have been calculated using equations 11 to 13 (Bhatty *et al.,* 2004):

$$LSF = \%CaO / (2.8*\%SiO_2 + 1.2*\%Al_2O_3 + 0.65*\%Fe_2O_3) \tag{11}$$

$$SM = \%SiO_2 / (\%Al_2O_3 + \%Fe_2O_3) \tag{12}$$

$$AM = \%Al_2O_3 / \%Fe_2O_3 \tag{13}$$

For the preparation of the raw meals, it was attempted to maintain the above indexes in a close range. Due to the predetermined slag percentages the raw meal chemistry was attained by regulating the content of limestone, bauxite and gypsum, resulting in a small fluctuation of LSF and AM.

The mixtures proportions of limestone/bauxite/gypsum/EAFS are (in wt.%): 64.50/18.70/6.8/10.0 for M1, 62.5/14.5/6.0/17.0 for M2 and 60.0/10.0/3.0/27.0 for M3. The raw materials were milled in a planetary mill under 90μm particle sizes. After thorough mixing, a minimum quantity of water was added in order to form pellets by hand of 15mm to 20 mm diameter. Dehydration of the pellets was performed at 110°C for 24 hours in a muffle furnace. Preliminary firing tests showed that M1 meal has the lowest melting point, 1340°C. Following, all clinkers were fired in a Super Kanthal Nabertherm® furnace at 1320°C with 40 minutes soaking time. Pellets were loaded in magnesium-chromite crucible which was covered in order to minimize emissions during firing. Fast cooling was used by simultaneous hammer crushing and air blowing. Milling of the clinkers was performed in a planetary mill from 4000cm^2/g to 4100cm^2/g finesse. The particles size distribution was analyzed by a laser analyzer, CILAS 1064.

Powdered clinkers were characterized by XRD. In order to control the setting time they were mixed with 5wt.% flue gas desulfurization (FGD) gypsum.

Compressive strength measurements according to EN 196-1 were performed. For hydration studies, obtained cements were mixed with water at a 0.5 w/c ratio. After 1day, 3day, 7day and 28 days of hydration the process was halted by immersing the pastes in an acetone bath for 2 hours followed by drying at 70°C for 24 hours (Taylor, 1990). Following they were stored in a sealed vessel over silica gel until examination. The hydrated products were analyzed by thermogravimetry (TGA Q50, TA Instruments, heating rate of 10°C/min up to 980°C in static air (Taylor, 1990)) and SEM (gold coated samples, SEM type JSM 6300, Jeol LINK PentaFET 6699, Oxford Instruments) respectively.

3. Results and Discussions

The chemical composition of the raw materials is presented in Table 1. EAFS content in Cr_2O_3 is 1.38wt% and in P_2O_5, TiO_2 and SO_3 0.48wt%, 0.47wt% and 0.44wt% respectively. It also contains a small amount, 0.14wt% of BaO. The introduction of ions of the above elements as dopant into the crystal lattice of belite stabilize α'- and β- polymorphic forms; α'-form being more active than β-form (Lawrence, 2003).

Table 1

Chemical Composition (XRF) of the Raw Materials, %

Raw materials	EAFS	Limestone	Bauxite	Gypsum
CaO	32.5	48.90	3.62	24.73
Fe_2O_3	26.3*	1.00	23.00	0.04
SiO_2	18.1	9.00	14.30	12.76
Al_2O_3	13.3	1.36	49.20	0.18
MnO	3.94	n.d.	n.d.	n.d.
MgO	2.53	0.65	n.d.	1.85
Cr_2O_3	1.38	n.d.	n.d.	n.d.
P_2O_5	0.48	n.d.	n.d.	n.d.
TiO_2	0.47	n.d.	n.d.	n.d.
SO_3	0.44	n.d.	0.23	39.30
Cl	0.14	n.d.	n.d.	n.d.
BaO	0.14	n.d.	n.d.	n.d.
Na_2O	0.13	0.10	n.d.	n.d.
K_2O	n.d.	0.15	n.d.	n.d.
V_2O_5	0.06	n.d.	n.d.	n.d.
LOI	0.00	38.00	13.89	23.14
LOI: loss on ignitions, n.d.: not determined, * - FeO, Fe_2O_3				

The adapted Bogue equations and quality indexes results are presented in Table 2. The clinker with high ferrite content has the lower yeelimite content.

Table 2
Mineralogical Phases Predicted by Adapted Bogue Equations and Quality Indexes Results, wt.%

Targets	C_2S	C_4AF	$C_4A_3\hat{S}$	$C\hat{S}$	C	LSF	AM	SM
M1	45.7	32.88	18.65	2.6	0.21	70.45	1.51	0.59
M2	46.79	36.21	13.65	2.93	0.45	73.01	1.22	0.62
M3	48.25	42.25	8.10	1.36	0.08	74.31	0.93	0.63

The XRD patterns of M1, M2 and M3 clinkers are presented in Fig. 1. In all clinkers the characteristic peaks of brownmillerite (C_4AF), larnite (β-C_2S) and yeelimite ($C_4A_3\hat{S}$) are recognized. The peak intensity of the later is decreasing with increasing slag content in the raw meal as it was predicted by the adapted Bogue equations also. The estimated from Bogue equations $C\hat{S}$ it is not detected, probably due it's very low content as either its reacted or sulfurum was emitted.

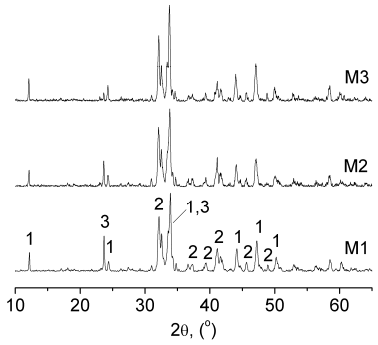

Fig. 1 – XRD patterns of M1, M2 and M3 clinkers. The main minerals are: 1 – brownmillerite (C_4AF), 2 – larnite (C_2S), 3 – yeelimite ($C_4A_3\hat{S}$).

Distribution of particle's size is presented in Fig. 2. In all clinkers the 90% of the particles' size is below 40μm. Given that the particles' size distribution is similar, differences in hydration rates due to particle size should be negligible.

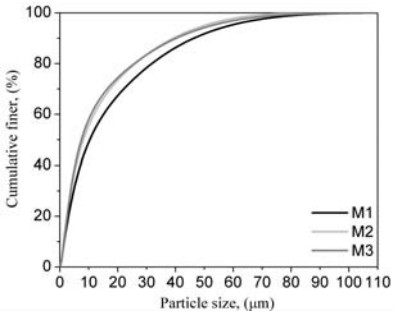

Fig. 2 – Particle size distribution of FAB powdered clinkers.

Compressive strength results are presented in Fig. 3. It is observed that increasing slag content in the raw meal, compressive strength is decreasing. For M1 and M2 compressive strength of 3 days is 13.1MPa, and 10.7MPa respectively as for M3 6.2MPa. The 28 days ones are 18.3MPa, 14.3MPa and 7.8 MPa for M1, M2 and M3 respectively. A rather slow increment of the strength with time is also observed. The higher early strength of M1 and M2 compared to M3 is attributed to the higher yeelimite content which react with gypsum and water to form ettringite (eq.1), AFm (eq.2) and poorly crystalline $Al(OH)_3$. The improvement of the mechanical properties by the reaction of C_4AF with gypsum to form etringite (eq. 4) was not possible due to the lack of gypsum.

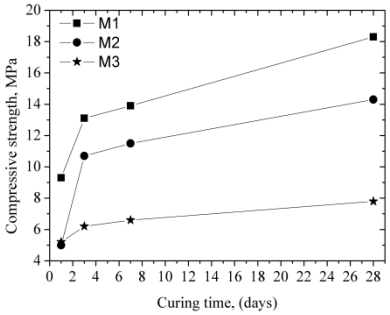

Fig. 3 – Compressive strength results of M1, M2 and M3 cement paste after different curing time.

SEM analysis of M1, M2 and M3 hydrated pastes at 1 day, 3 days, 7 days and 28 days are presented in Fig. 4.

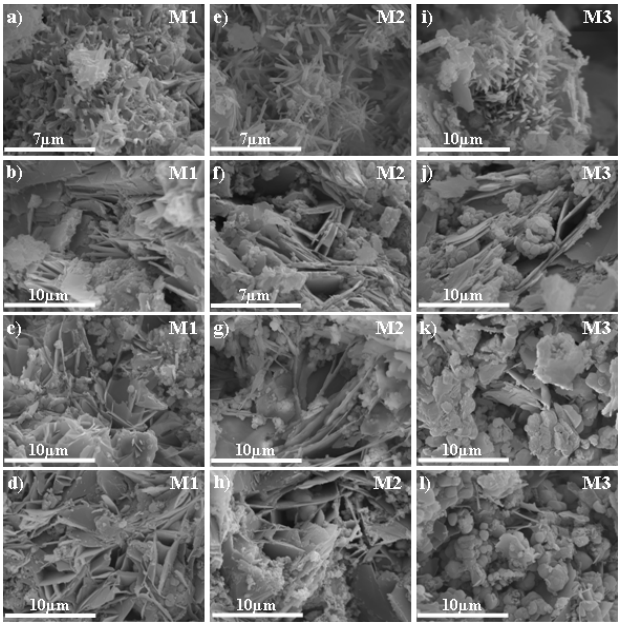

Fig. 4 – SEM micrographs of the hydrated pastes after different curing periods: M1 - 1 day (a), 3days (b), 7 days (c) and 28 days (d), M2 – 1 day (e), 3 days (f), 7 days (g) and 28 days (h), M3 – 1 day (i), 3 days (j), 7 days (k) and 28 days (l).

Due to very small particles size resulted on milling very fast reaction of yeelimite with water and gypsum occurs presenting ettringite like needles only at 1 day in all cement pastes. As the molar ratio $C\hat{S}/C_4A_3\hat{S}$ in M1 was lower and the reaction 1 require higher molar ratio (Kasselouri *et al.,* 1995) a part of $C_4A_3\hat{S}$ formed AFm flakes and hydrogarnet from 3 days and above. In the case of M2 and M3 the molar ratio $C\hat{S}/C_4A_3\hat{S}$ was higher and the remained $C\hat{S}$ reacts with C_4AF to form AFm. The hydrogarnet formed is visible as round smooth small particles (Fujita *et al.,* 2002). In M3 the formation of hydrogarnet was relatively more extended due to the increased slag content.

The thermogravimetric (TG) analyses as mass loss and derivative mass of the hydrated pastes after 1 day, 3 days, 7 days and 28 days are presented in Fig. 5*a*, …,*c*.

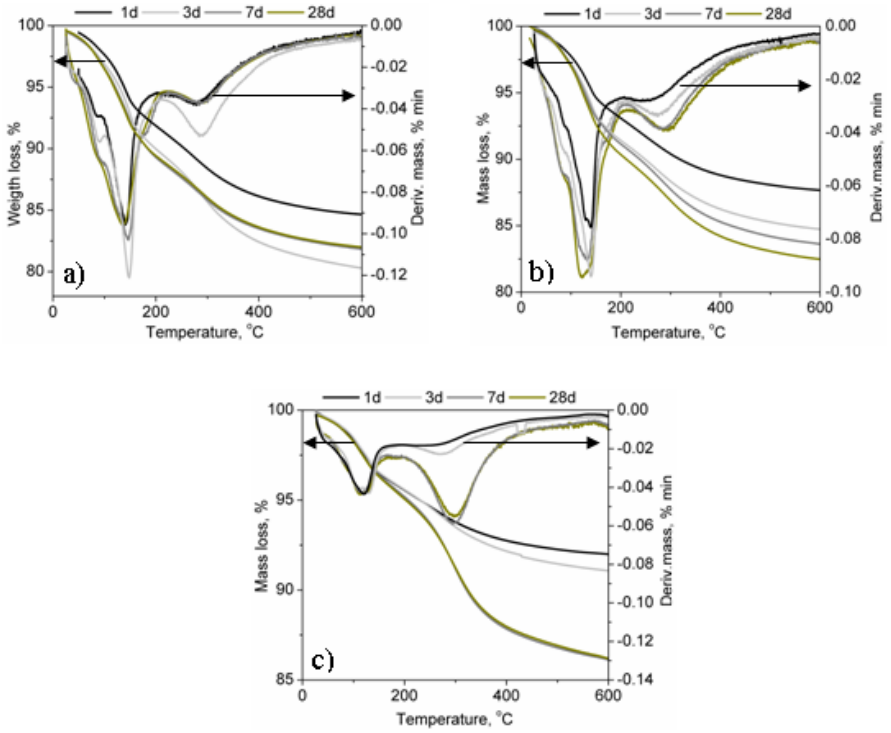

Fig. 5 – TG and DTG profiles of M1(a), M2(b) and M3(c) pastes after 1day, 3days, 7days and 28 days of hydration. The arrows indicate the TG (left) and DTG (right) scale.

At about 100°C the small shoulder like endothermic peak in the case of M1 and M2 is attributed to ettringite dehydration (Duvallet *et al.,* 2009), as in the case of M3 is not visible. This is because of the low ettringite formation caused by the lower yeelimite content and very fast reaction in the contact with

the water usually within 6 hours to 12 hours. The remained yeelimite caused by the molar ration of $C\hat{S}$/ $C_4A_3\hat{S}$ reacts with water (eq. 2) and forms AFm corresponding to the weight loss at about 150°C to 200°C (Duvallet *et al.,* 2009). The weight loss is increasing with curing time for M1 and M2, whereas for M3 reaches its maximum at 1 day. At about 300°C the weight loss is attributed to the dehydration of hydrogarnet, formed due to the high content of C_4AF reacted with water and lack of gypsum to form ettringite (eq. 4). Hydrogarnet has been speculated that can host Cr^{VI} being a benefit for high cements Cr^{VI} content for leaching reasons, now still under investigation (Hillier *et al.,* 2007). The obtained data are in agreement with the compressive strength results. The hydration studies shows that the hydration rate of β-C_2S was low even at the 28 days tested, probably due to the hydrogarnet formation or the small crystal sizes formed during clinkerization (Kasselouri *et al.,* 1995).

4. Conclusion

Ferroaluminate cements have been prepared by combining industrial raw materials and EAFS which were fired at 1320°C. Due to the lack of calcium sulfate phase in the clinker and low gypsum quantity added in order to control the setting time, the reaction of C_4AF to form ettringite was limited. Hydrogarnet was formed witch does not affect the mechanical properties.

Acknowledgements. R. I. Iacobescu and R. Saban acknowledge the support of the Sectoral Operational Programme Human Resources Development 2007-2013 of the Romanian Ministry of Labour, Family and Social Protection through the Financial Agreement POSDRU/6/1.5/S/16.

D. Koumpouri and G. N. Angelopoulos acknowledge the support of University of Patras through "Karatheodoris" 2011 research program.

TITAN Cement Company S.A. and SOVEL S.A. metallurgy industries are gratefully acknowledged for providing the raw materials as well as their technical assistance.

REFERENCES

Albino V., Cioffi R., Marroccoli M., Santoro L., *Potential Application of Ettringite Generating Systems for Hazardous Waste Stabilization*. Journal of Hazardous Materials, **51**, 241-252 (1996).

Bhatty J.I., F.M. Miller, S.H. Kosmatka, *Innovations in Portland Cement Manufacturing.* Portland Cement Association, 2004.

Chen I., Juenger M., *Synthesis and Hydration of Calcium Sulfoaluminate-Belite Cements with Varied Phase Compositions*, Journal of Materials Science, **46**, 2568-2577 (2010).

Chrysochoou M., Dermatas D., *Evaluation of Ettringite and Hydrocalumite Formation for Heavy Metal Immobilization: Literature Review and Experimental Study*. Journal of Hazardous Materials, *136*, 20-33 (2006).

Dova M., Palou M., Kovar L., *Heat Evolution and Mechanism of Hydration in CaO–Al2O3–SO3 System*. Ceramics − Silikáty, 104-108 (2005).

Duvallet Tristana, Rathbone Reobert F., Henke Kevin R., Jewell R.B., Low-Energy, *Low CO2-Emitting Cements Produced from Coal Combustion by-Products and Red Mud*. World of Coal Ash Conference, Lexington, KY, USA, 4-7 May 2009.

Fujita S., Suzuki K., Shibasaki Y., Mori T., *Synthesis of Hydrogarnet from molten Slag and its Hydrogen Chloride Fixation Performance at High Temperature*. Journal of Material Cycles and Waste Management, **4**, 70-76 (2002).

Gartner E., *Industrially Interesting Approaches to "low-CO2" Cements*. Cement and Concrete Research, *34*, 1489-1498 (2004).

Hillier S., Lumsdon D.G., Brydson R., Paterson E., *Hydrogarnet: A Host Phase for Cr(VI) in Chromite Ore Processing Residue (COPR) and Other High pH Wastes*. Environmental Science & Technology, *41*, 1921-1927 (2007).

Kasselouri V., Tsakiridis P., Malami C., Georgali B., Alexandridou, *A Study on the Hydration Products of a Non-Expansive Sulfoaluminate Cement*. Cement and Concrete Research, *25*, 1726-1736 (1995).

Lawrence C.D., *The Production of Low-Energy Cements*. Lea's Chemistry of Cement and Concrete (Fourth Edition), Butterworth-Heinemann, Oxford, 2003.

Meller N., Hall Christopher, Jupe A.C., Colston S.L., Jacques S.D.M, Barnesb P., Phipps J., *The Paste Hydration of Brownmillerite with and Without Gypsum: a Time Resolved Synchrotron Diffraction Study at 30, 70, 100 and 150C*. Journal of Materials Chemistry, **14**, 428-435 (2004).

Peysson S., Péra J., Chabannet M., *Immobilization of Heavy Metals by Calcium Sulfoaluminate Cement*. Cement and Concrete Research, *35*, 2261-2270 (2005).

Taylor H.F.W., *Cement Chemistry*. Academic Press, London, 1990.

Zhou Q., Milestone N.B., Hayes M., *An alternative to Portland Cement for Waste Encapsulation.The Calcium Sulfoaluminate Cement System*, Journal of Hazardous Materials, **136**, 120-129 (2006).

PROPRIETĂŢILE HIDRAULICE ALE CIMENTULUI FEROALUMINAT-BELITIC PRODUS CU ZGURĂ DE CUPTOR CU ARC ELECTRIC

(Rezumat)

Cimentul feroaluminat-belitic cu calciu (FAB) a fost produs cu adaugare de zgură de cuptor cu arc electric (EAFS) ca şi materie primă. Cu scopul de a reduce efectul asupra mediului înconjurător s-a trecut la producerea cimentului cu factor redus de saturaţie în var (LSF), în plaja de valori cuprinsă între 70%, 74% şi de asemenea s-au folosit temperaturi reduse 1320°C. Au fost analizate trei tipuri de ciment, cu procent

masic diferit de zgură (EAFS): 10%, 17% şi respectiv 27%. Materiile prime au fost analizate prin metoda XRF iar clincherele prin XRD. Distribuţia mărimii particulelor pulberii a fost analizată cu laser. Pentru determinarea rezistenţei la compresiune, s-a folosit starndardul EN 196-1. Proprietăţile de hidratare au fost investigate prin tehnicile SEM şi respectiv TG-DTG. Valori relativ ridicate ale rezistenţei la compresiune s-au înregistrat în primele zile de scădere a hidratării, prin creşterea zgurii (EAFS) adăugate. Acest fapt a fost atribuit în principal reactivităţii compusului Klein.

BULETINUL INSTITUTULUI POLITEHNIC DIN IAŞI
Publicat de
Universitatea Tehnică „Gheorghe Asachi" din Iaşi
Tomul LVII (LXI), Fasc. 4, 2011
Secţia
ŞTIINŢA ŞI INGINERIA MATERIALELOR

THERMO-SENSITIVE MAGNETIC PROPERTIES IN THE ALLOY SYSTEM Cr-Ni-Fe

BY

ALEXANDRU IORGA*, RAMI SABAN, LIVIU PALII , EROS A. PATROI and SORIN IORGA

POLITEHNICA University, Bucharest,
Faculty of Engineering and Materials Science

Received: April 14, 2011
Accepted for publication: June 27, 2011

Abstract. This work analysis on the basis of own researches and determinations, the influence of Cr in Fe-Ni alloys, upon the thermo-sensitive magnetic properties and the variation of the Curie point.

Key words: curie temperature, thermo sensitive materials, magnetic materials.

1. Introduction

This paper aims to study and experimental research the alloys used in construction of high voltage overhead conductors self-protection from frost and ice deposits. Thus, we aimed to obtain alloys with a Curie temperature (Tc) as close as frost forming temperature (-3°C) and avoid an additional thermal input of the conductor in the positive temperatures, in the specified application (Iorga *et al.,* 2011).

Modern technology allows adjustment of elementary composition to obtain preset values of Tc. Practical applications are currently only thermo-

* Corresponding author e-mail: iorga_alexandru@yahoo.com

reversible change with temperature compensation of magnetic induction of permanent magnets or magnetic circuits with permanent magnets, used especially in electrical measurement devices, high precision class. Thus, for these purposes, in actual practice has been imposed mainly Fe-Ni alloys and less Ni-Cu or Cr-Ni-Fe (Toshico, 2003; Tomiska, 2004).

There are also other alloying elements that controlled adversely affect the value of Curie temperatures in this area, the alloying with Ni, as would be Si, Al, Mn.

The analysis of known alloys which can achieve low values of Curie temperature (10°C - 70°C) by modeling the chemical composition, but also present opportunities while maximizing the magnetic and electrical properties of the alloy, and technological achievement to match practical applications, we opted for the Cr-Ni-Fe system alloys (Almasan *et al.,* 1989).

2. Experiments

Ferromagnetic materials display ferromagnetic properties but instead of parallel alignment of the dipoles, they have anti-parallel alignment of unequal spins. When these materials are subjected to increasing temperatures, there is an increase in thermal agitation. This increase in agitation means that there is a decrease in the effectiveness in the dipole alignment. When the temperature is great enough to completely break up the dipole alignment, the materials becomes paramagnetic. This temperature is referred to as the Curie temperature (Wasserman *et al.,* 1990).

In order to study the main physical and magneto-electric characteristics, and identifying areas of composition that present a Curie temperature as close to the formation point of frost (-3°C) and at the same time to provide sufficient heat input of frost formation, to prevent deposing, we established a number of 4 alloys compositions from the ternary system Cr-Ni-Fe (Table 1).

Table 1
Chemical Composition of Alloys

Sample	Chemical composition [wt. %]
S1	Cr11.5 Ni34 Fe54.5
S2	Cr10 Ni35 Fe55
S3	Cr11 Ni35 Fe54
S4	Cr12 Ni35 Fe53

Metals used had a purity of advanced technology, namely: Cr and Ni electrolytic (bulk resulting from electrolysis) and Fe is the type Armco. Melting was done in controlled atmosphere (Argon) Heraeus furnace with induction heating at 10 kHz. After casting, the alloys were annealed for stress relief and chemical homogeneity in the composition; the thermal conditions were 3 hours

at 700°C cooling with furnace. Treatment was carried out in controlled atmosphere (Argon) at atmospheric pressure. In the study of Cr - Ni - Fe alloys, with specific magnetic properties target, we also make researches on the chemical composition, metallographic research, X-ray diffraction and magnetic measurements. Structural condition, in which our material was analyzed, respectively cast and annealed, is the structure offering the lowest values of coercitive field Hc - the material is free of internal tensions, it has a minimum density of structural network defects (~ 107 defects / cm^3).

The magnetic measurements performed in this work, for the 5 alloys regarding the Curie temperature, were realized on two sample geometries, suitable for the methods and equipment used, namely:

- Spherical samples, weighing between 6-8 mg, for measurements of magnetization depending on temperature, M = f (T);
- Toroidal samples Ø30 x Ø25 x 5mm, for measurements of magnetic polarization depending on temperature, Js = f (T) both cast and annealed.

Ferromagnetic state of the solid is conditioned by some peculiarities of crystal structure, specific to each type of atom, combinations of atoms and their molar proportions. In essence, the Curie temperature TC is a 2nd order transformation (order - disorder), that occurs within a small range of temperature ΔT. Curie point measurements made on toroidal samples (cast and annealed) were done in closed magnetic circuit (Fig. 1), using a wattmeter and a climate chamber. Samples were wound with an equal number of turns, so we used 70 turns to 30 turns for primary and secondary.

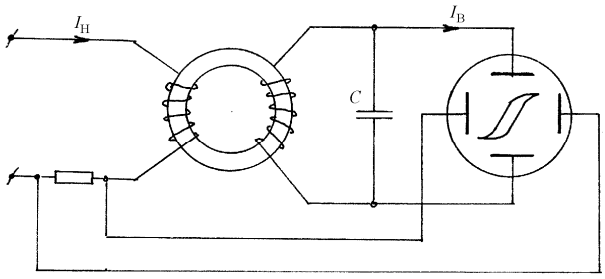

Fig. 1 – Scheme of the wattmeter.

Measurements on spherical samples were performed using MPMS (Magnetically Properties Measurement System) SQUID facility, in a magnetic field of 100 Öe. For both types of measurements, the temperature range at which we made measurements was - 40°C to +130°C.

3. Results and Discussions

Metallographic and XRD investigation reveals that all the alloys investigated are single phase on full scale of positive temperature, is solid

solution phase substitution, the crystal structure is γ / FCC type, the network parameter a ≈ 3.570 Å. The structure of these alloys confirms the possibility of technological operation by hot and cold plastic deformation with no problems. A way of determining the Curie temperature is plotting distinctive curves with a smooth, continuous appearance. The tangent to each curve at the inflexion points will be drawn. The values of the temperature will be obtained at their intersections with the abscise axis; their mean is the Curie temperature. For our measurements, we used the same principle as it shows the Figs. 2 and 3.

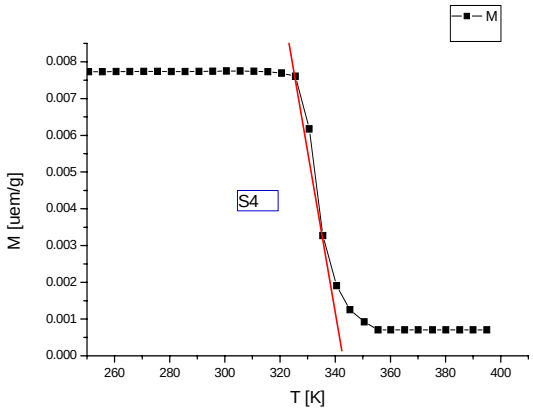

Fig. 2 – Graphical representation of M = f (T) for spherical sample S4.

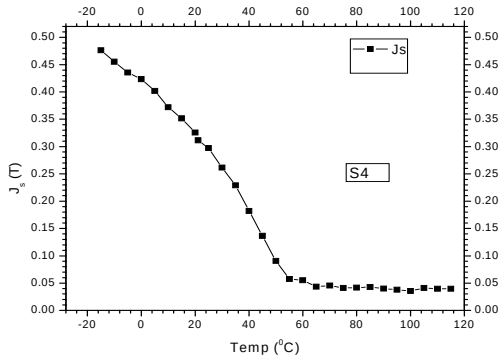

Fig. 3 – Graphical representation Js = f(T) for toroidal sample S4.

The thermo-magnetic alloy newly created for this purpose, was characterized through thermo sensitive magnetic predetermined and has reversible properties, without thermal hysterezis, and without transformations of the crystalline structure. The results are presented in Table 2.

Table 2
Measured Values of Curie Temperature Tc

Sample	Chemical composition [wt. %]	T_C spherical sample [°C]	T_C toroidal sample [°C]
S1	Cr11.5 Ni34 Fe54.5	+ 25	+ 24
S2	Cr10 Ni35 Fe55	+ 64	+ 60
S3	Cr11 Ni35 Fe54	+ 67	+ 65
S4	Cr12 Ni35 Fe53	+ 46	+ 45

After the magnetic measurements, the values of the coercitive field Hc show us that these alloys are very soft magnetic materials with values between 15 to 40 Öe. Also, the slope of the saturation curve magnetization at relatively small variations of temperature and sufficiently big values of magnetization in small magnetic fields, indicate properties of these alloys as magnetic field - temperature sensors. These characteristics have higher values than other similar materials uses in technical constructions.

An important aspect of magneto-thermal properties of these alloys is that hysteresis transition FM (ferromagnetic) to PM (paramagnetic) depending of temperature is small, $\Delta T = 3 - 5°C$, and there are no transformation of crystal structure in a large range of temperatures, shows that the alloys present a good magneto-thermal properties depending on temperature and time.

4. Conclusions

There have been realized four different alloys and measurements of the Curie point by two distinct methods. The results from the two measurement methods did not indicate significant differences between them. Alloys have Curie temperatures in the range +10 to +120°C.

Curie temperature Tc value depends essentially on the elemental chemical composition and practically does not depend on the structural state material. Also, the correlation composition - Tc has a linear trend, even within a solid single phase structure material, as in this case. Predictability parameter Tc is complicated because the material studied by us has three (Cr - Ni - Fe) magnetic active components.

Overall, magnetic measurements can be extended to other conditions and parameters. The two methods of determining the Curie temperature showed correct measurements performance, but also a verification method. There aren't notable differences on the values of the two measurements. Compositional area of interest for the intended use of these thermo-sensitive alloys, reveal interest at ~ 34-35% nickel concentrate containing ~ 11% Cr, rest Fe.

The alloys studied, because of the positive results, can be used in future researches regarding the manufacturing an electric overhead conductor with self-protection to deposits of frost/ice.

Acknowledgement. The work has been funded by the Sectoral Operational Programme Human Resources Development 2007-2013 of the Romanian Ministry of Labour, Family and Social Protection through the Financial Agreement POSDRU/6/1.5/S/16.

REFERENCES

Almasan C. *et al., Low-Temperature Phase and Magnetic Interactions in FCC Fe-Cr-Ni Alloys.* Journal of Magnetism and Magnetic Materials, **80**, Issues 2-3, 2 August 1989, 329-338

Iorga A. *et al*., *Electrical Overhead Conductor for Electric Energy Transports, Self-Protective at Frost and Ice Deposition*. Submitted at 2nd International Energy, Life Cycle Assessment, and Sustainability Workshop & Symposium, Nisyros Grece, 2011.

Tomiska Josef, *The System Fe–Ni–Cr: Revision of the Thermodynamic Description*. Journal of Alloys and Compounds, **379**, 176–187 (2004).

Toshico Kitamura, *Snow-Melting Magnetic Material Wire*. In Fujikura Technical Review, 23-25 (2003).

Wasserman E.F., Ferromagnetic Materials, ed. K.H.J. Buschow and E.P. Wohlfarth, North-Holland, **5**, 238-321 (1990).

PROPRIETĂŢI MAGNETICE TERMO-SENSIBILE ÎN ALIAJELE DIN SISTEMUL DE ALIAJE Cr-Ni-Fe

(Rezumat)

Prezenta lucrare analizează pe baza cercetărilor şi determinărilor proprii, influenţa Cr în aliajele Fe-Ni, asupra proprietăţilor magnetice termo-sensibile şi variaţia punctului Curie.

BULETINUL INSTITUTULUI POLITEHNIC DIN IAŞI
Publicat de
Universitatea Tehnică „Gheorghe Asachi" din Iaşi
Tomul LVII (LXI), Fasc. 4, 2011
Secţia
ŞTIINŢA ŞI INGINERIA MATERIALELOR

KINETICS OF THE LAYERS FORMATION IN IRON MATRICES THROUGH CARBOCROMIZATION

BY

SORIN IORGA*, MIHAI COJOCARU and ALEXANDRU IORGA

POLITEHNICA University, Bucharest,
Faculty of Engineering and Materials Science

Received: April 14, 2011
Accepted for publication: June 27, 2011

Abstract. The pores in the metal matrices obtained through powder metallurgy techniques, generate a range of features of the kinetics of the layers formation obtained in situ through thermochemical treatments. The purpose of this study is to determine and quantify the effect of the interaction between solid environments, providing carbon and chromium in active state, and the iron matrices: the results of experimental research on the kinetics of the layers formation through carbocromization in iron sintered matrices, are presented as a nonlinear mathematical model. The choice of thermal, temporal and chemical parameters of the two thermochemical treatments, the carburization and the chromization, was made based on a central compositional and orthogonal program of the second order.

Key words: kinetics, thermochemical treatments, powder metallurgy.

1. Introduction

Products made by powder metallurgy techniques, have become an increasingly viable alternative to those made by conventional techniques, namely classical metallurgy.

* Corresponding author e-mail: soriniorga1981@yahoo.com

These materials can be used in conditions similar to those obtained by conventional procedures, but taking into account their characteristics, particularly the presence of the pores in the material.

Such a material subjected to thermochemical treatments of carburization and chromization using the pack cementation method; significantly increase its level of mechanical characteristics and corrosion resistance, while preserving its core features unaltered.

2. Working Methods, Materials and Equipment Used in Research

The working methodology adopted for the research was the scheduled experiment. The advantages of using such methods are on one hand the reduction in the number of experiments and on the other hand the possibility of obtaining a maximum of concentrated information as the equations of the calculated mathematical model, and thus opening the way to optimize process parameters. The research used a variant of nonlinear programming - a central compositional and orthogonal program of the second order. The adoption of such a strategy was dictated by the fact that linear models in this case do not check the hypothesis of concordance.

Materials used in the research were iron powder obtained from Ductil Buzau DP200 (size fraction in the range of 160-200μm up to 15%, the rest being below 160μm), the carburization mixtures consisting of charcoal and carburizing activeness $BaCO_3$, the cromization mixtures consisting of chromium and ferrochromium with very low carbon content (max. 0,10%) powders, NH_4Cl and Al_2O_3.

Equipment/machinery used in the research were used to *characterize the powders* (standardized sets of sieves, optical microscope and stereomicroscope, 600KN hydraulic press), *forming* (600KN hydraulic press), *sintering* (oven with 150x450mm useful space dimensions and T_{max}=1100°C with purified nitrogen atmosphere), *thermochemical treatments* (oven controlled by program, with 150x450mm useful space dimensions and T_{max}=1100°C) and *estimation of the results* (Epytip type microscope and a Hanneman micro-hardness system: the estimation of the size of chromium carbides area was made using the information about the variation of the micro-hardness obtained in iron matrix after carbocromization, taking into account the fact that the carbides areas have micro-hardness values over 1000μHV and areas of solid solution of chromium in iron under 300μHV).

3. Result and Discussions

The experimental conditions were chosen in agreement with the programming adopted method, these and the results are listed in Table 1.

In later stages of statistical verification of the non-linear model coefficients and its compatibility, we reached at the particular form of the model equation (ec.1) and its graphic expressions (Figs.1, 2).

$$\tilde{Y} = 24{,}985+2{,}237X_1+2{,}58X_2+4{,}273X_3-2{,}386X_5-3{,}028X_1X_2+6{,}58X_1X_3- \\ -2{,}9X_2X_4+4{,}18X_3X_4+6{,}166X_3X_5 \quad (1)$$

where: X_1, X_2, X_3, X_4, and X_5 are the coded values of independent parameters under consideration, and $\tilde{Y}$ is the natural value of the size of the areas of chromium carbides.

Table 1

The Orthogonal Central Compositional Programming Matrix of the Second Order for k=5 Independent Parameters

Factors	Z_o	Carb. temp. °C, Z_1	Carb. period hours, Z_2	Cromiz. temp °C, Z_3	Cromiz. period hours, Z_4	Mixture comp., Z_5	Y Chromium carbides layer, μm (No.div. x 0,285, μm)
Cod	X_0	X_1	X_2	X_3	X_4	X_5	-
Base level, Z_{io}		930	8	1000	9	14/1	
Variation interval ΔZi		50	4	50	3	7/1	
Upper level, $Z_{io}+\Delta Zi$		980	12	1050	12	21/1	
Lower level, $Z_{io}-\Delta Zi$		880	4	950	6	7/1	
Exp.1	+1	+1	+1	+1	+1	+1	***42,75***
Exp.2	+1	+1	+1	+1	+1	-1	***45,45***
Exp.3	+1	+1	+1	+1	-1	+1	***28,5***
Exp.4	+1	+1	+1	-1	+1	+1	***9,4***
Exp.5	+1	+1	-1	+1	+1	+1	***29,64***
Exp.6	+1	-1	+1	+1	+1	+1	***37,33***
Exp.7	+1	+1	+1	+1	-1	-1	***41,04***
Exp.8	+1	+1	+1	-1	-1	+1	***7,98***
Exp.9	+1	+1	-1	-1	+1	+1	***9,52***
Exp.10	+1	-1	-1	+1	+1	+1	***23,94***
Exp.11	+1	-1	+1	+1	+1	-1	***11,97***
Exp.12	+1	+1	-1	+1	-1	+1	***28,5***

Continuation Table 1

Factors	Z_o	Carb. temp. ^oC, Z_1	Carb. period hours, Z_2	Cromiz. temp ^oC, Z_3	Cromiz. period hours, Z_4	Mixture comp., Z_5	Y Chromium carbides layer, μm (No.div. x 0,285, μm)
Exp.13	+1	-1	+1	-1	+1	+1	***10,83***
Exp.14	+1	+1	+1	-1	+1	-1	***14,53***
Exp.15	+1	-1	+1	+1	-1	+1	***24,22***
Exp.16	+1	+1	-1	+1	+1	-1	***39,9***
Exp.17	+1	-1	-1	-1	+1	+1	***8,26***
Exp.18	+1	-1	-1	+1	+1	-1	***16,8***
Exp.19	+1	-1	+1	+1	-1	-1	***0***
Exp.20	+1	+1	+1	-1	-1	-1	***13,96***
Exp.21	+1	+1	-1	-1	-1	+1	***17,67***
Exp.22	+1	-1	+1	-1	+1	-1	***16,24***
Exp.23	+1	+1	-1	+1	-1	-1	***32,77***
Exp.24	+1	-1	-1	+1	-1	+1	***34,42***
Exp.25	+1	+1	-1	-1	+1	-1	***42***
Exp.26	+1	-1	+1	-1	-1	+1	***31,92***
Exp.27	+1	-1	-1	-1	-1	+1	***9,12***
Exp.28	+1	-1	-1	-1	+1	-1	***35***
Exp.29	+1	-1	-1	+1	-1	-1	***0***
Exp.30	+1	-1	+1	-1	-1	-1	***45***
Exp.31	+1	+1	-1	-1	-1	-1	***22,23***
Exp.32	+1	-1	-1	-1	-1	-1	***11,68***
Exp.33	+1	+α	0	0	0	0	***31,06***
Exp.34	+1	-α	0	0	0	0	***22,51***
Exp.35	+1	0	+α	0	0	0	***34,48***
Exp.36	+1	0	-α	0	0	0	***11,68***
Exp.37	+1	0	0	+α	0	0	***33,91***
Exp.38	+1	0	0	-α	0	0	***14,53***
Exp.39	+1	0	0	0	+α	0	***26,5***
Exp.40	+1	0	0	0	-α	0	***19,38***
Exp.41	+1	0	0	0	0	+α	***31,92***
Exp.42	+1	0	0	0	0	-α	***40,47***
Exp.43	+1	0	0	0	0	0	***23,65***

*Obs. *The samples used were realized in identical conditions: 735 MPa pressure, that ensures a density of 7,04g/cm^3 and a calculated porosity of ~10%, followed by sintering at 1050^{o}C/4hours in purified nitrogen environment.*

***The composition of the mixture used for cromization was made of different proportions of components that contain chromium (chromium and ferrochromium powder in 1:4 ratio), ammonium chloride and alumina. In the research program the proportion of the active components from the mixture was varied discrete (chromium and ferrochromium powder, within 21÷63%), their share in a given experiment, being given by the difference 100% - the sum of alumina and chloride ammonium ratios in the mixture under consideration. The significance of the fractions shown in table 1 are: the ratio between the components not containing chromium found in the mixture used for cromization, %Al_2O_3:%NH_4Cl, the latter being always 3% for an Al_2O_3-NH_4Cl mixture.*

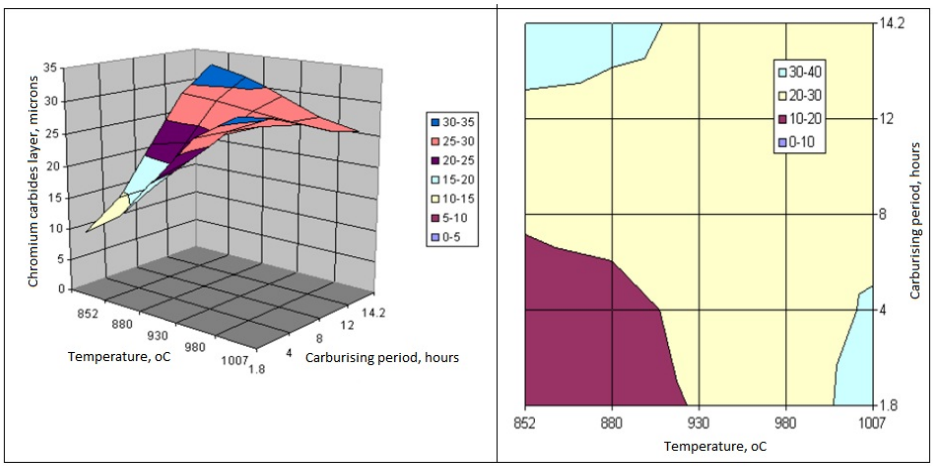

Fig. 1 – The calculated response surface of the model and the proprieties areas determined in the particular conditions of cromization occurred at values of the process parameters at appropriate based levels (X_3=0, X_4=0, X_5=0).

The regression equation in its codified form (ec.1) and its graphic expressions (Figs. 1, 2) provides useful information on how the independent variables must be modified to increase or decrease the size of the chromium carbides layer generated by applying the sequence of carburization and cromization operations to the iron matrices:

- the discrete increase of any of the process parameters, the carburization temperature, the maintaining isothermal time of the carburization, or the cromization temperature ensure an increase in the size of the carbide area;

- reducing the ratio of the proportions of the components that don't contain chromium causes an increases of the activity of the cromization

environment and thereby increase the area size of chromium carbides;

- increasing or on the contrary decreasing simultaneously any of the couples of parameters: the carburization temperature - the isothermal maintaining time at carburization (X_1X_2), the carburization temperature - the cromization temperature (X_1X_3), the periods of isothermal retention for the two temperatures at which the thermochemical processes take place (X_2X_4), implies a reduction in the size of chromium carbide layer.

- increasing any of the couples of parameters: the maintaining temperature of the cromization - the isothermal maintenance time of the cromization (X_3X_4), or the maintaining temperature of the cromization - the ratio of the proportions of the components that don't contain chromium (X_3X_5), implies an increase in size of the layer.

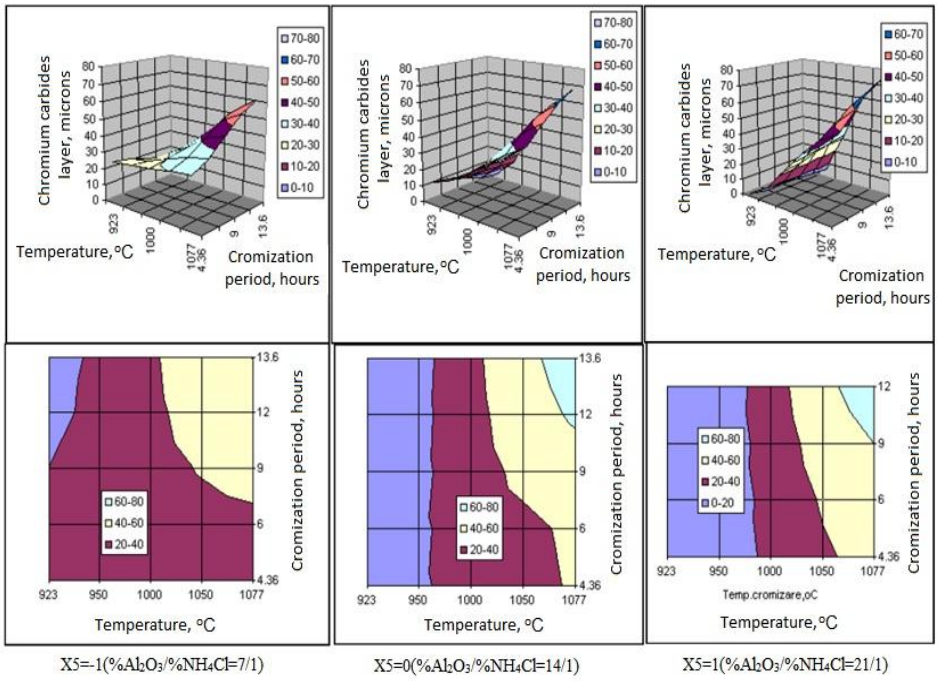

Fig. 2 – The influence of the cromization conditions on the carbides layer dimensions (optimal conditions chosen for carburization: $T_{carb}=T_{max}=1007°C$; $t_{carb}= t_{min}=4h$).

Metallographic analysis performed on samples that were subjected to thermochemical treatments (Figs. 3, 4), revealed the presence of the surface area were the reactive diffusion of the two elements occurred, carbon and chromium.

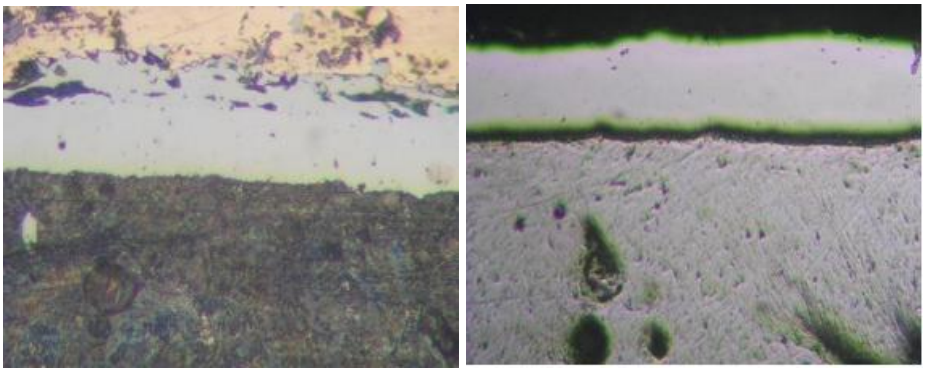

a *b*

Fig. 3 – The layer's microstructure on an iron matrix, Reagents: Nital 2% (*a*) and Murakami (*b*) Magnification: 375:1 x 3,6.

Obs. Realization conditions: carburization: 980°C/12hours in charcoal mixed with 30% $BaCO_3$, followed by cromization at 1050°C/12hours in environment with 25% components containing chromium.

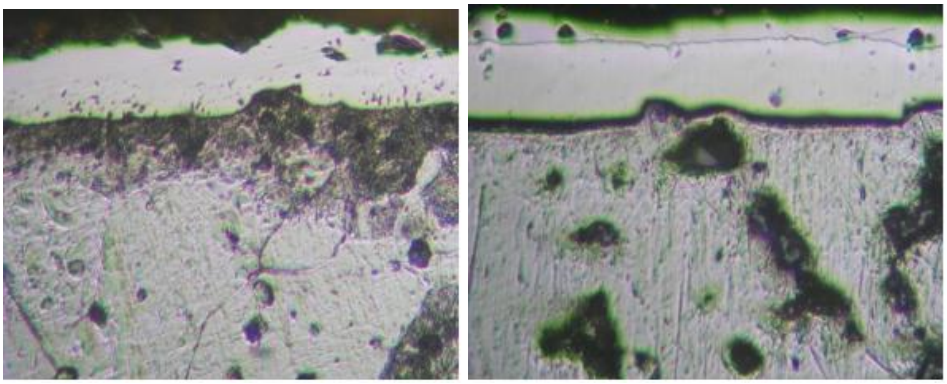

a *b*

Fig. 4 – The layer's microstructure on an iron matrix, Reagents: Nital 2% (*a*) and Murakami (*b*) Magnification: 375:1 x 3,6.

Obs. Realization conditions: carburization: 980°C/4hours in charcoal mixed with 30% $BaCO_3$, followed by cromization at 1050°C/12hours in environment with 75% components containing chromium.

Note that in the research to identify the chromium carbides area we used the information provided by the superficial layers micro-hardness and took into account the net difference between the micro-hardness of these phases and that of the solid solutions of chromium in iron (μHV_{50} $Cr_{23}C_6$=1650; μHV_{50} Cr_7C_3=1336; μHV_{50} Cr_3C_2=1350, for comparison μHV_{50} SS Cr-Fe<300,

depending on the concentration of chromium). The results of these measurements are very close to that obtained by direct measurement of the carbide area after using the Murakami reagent.

Starting from the micro-hardness values of the carbide areas we can make assumptions about their type: $Cr_{23}C_6$ to the outside area of carbides, it occurs in the presence of very active environments, and towards the interior of the carbides area Cr_7C_3 frequently occurs (Fig. 4*b*).

Obs. Obviously when referring to a type of chromium carbide we should consider the fact that often in reality, they are double carbides of iron and chromium.

4. Conclusions

The experimental investigations aimed at the kinetics of the layers formation in iron matrices through carbocromization revealed that:

- the forming of the double carbides layers of iron and chromium is conditioned by the corresponding chosen parameters of the two processes, carburization and cromization;

- the parameters of the two processes, the carburization and the cromization, determine a certain phase composition of the carbide layer, the layer being composed of carbides with high chromium content $(Cr, Fe)_{23}C_6$, average chromium content $(Cr, Fe)_7C_3$, or low chromium content $(Cr, Fe)_3C_2$, thereby having a different behavior in service and therefore different destinations.

Acknowledgement. The work has been funded by the Sectoral Operational Programme Human Resources Development 2007-2013 of the Romanian Ministry of Labour, Family and Social Protection through the Financial Agreement POSDRU/88/1.5/S/60203.

REFERENCES

[1]. Lahtin Iu.M., Arzamasov B.N., *Himico-termicescaia obrabotka metallo.* Metallurghia, Moskva, 1985.

[2]. Cojocaru M., *Pulberi metalice. Producere & Procesare*. Edit. Fair Partners, Bucureşti, 2009.

[3]. Samsonov G.V., *Tugoplavkie soedinenie*. Moskva, 1963.

[4]. Storms E., *The Refractory Carbides*. Acad. Press, New York and London, 1967.

[5]. Taloi D., *at al*., *Optimizarea proceselor metalurgice*. Edit. Didactică şi Pedagogocă, Bucureşti,1983.

CINETICA FORMĂRII STRATURILOR CARBOCROMIZATE ÎN MATRICI METALOCERAMICE DE FIER

(Rezumat)

Prezenţa porilor în matricile metalice realizate prin tehnici specifice metalurgiei pulberilor generează o serie de particularităţi cineticii formării straturilor obţinute „in situ" prin tratamente termochimice. Scopul prezentei lucrări este de a determina şi cuantifica efectul interacţiunii mediilor solide, furnizoare de carbon şi respectiv crom în stare activă, cu matricile de fier metaloceramice: sunt prezentate rezultatele cercetărilor experimentale privind cinetica formării straturilor carbocromizate în matrici metaloceramice de fier, sinterizate, sub forma unui model matematic neliniar. Alegerea parametrilor termici, temporali şi chimici ai celor două tratamente termochimice de carburare şi respectiv cromizare s-a realizat în baza unui program compoziţional central ortogonal de ordinul II.

BULETINUL INSTITUTULUI POLITEHNIC DIN IAŞI
Publicat de
Universitatea Tehnică „Gheorghe Asachi" din Iaşi
Tomul LVII (LXI), Fasc. 4, 2011
Secţia
ŞTIINŢA ŞI INGINERIA MATERIALELOR

UTILIZATION OF A NATURAL ION EXCHANGER FOR HEAVY METALS REMOVAL FROM ACID MINE DRAINAGE

BY

AGNES ALEXANDRA KERI[1*], NICOLAE HAR[2], MONICA URSU[3], CLAUDIU TĂNĂSELIA[3], ANDRADA MĂICĂNEANU[4] and TIBERIU RUSU[1]

[1]Technical University Cluj-Napoca,
Faculty of Materials Science & Engineering
[2]University Babeş-Bolyai Cluj-Napoca,
Faculty of Biology and Geology
[3]Research Institute for Analytical Instrumentation,
[4]University Babeş-Bolyai Cluj-Napoca,
Faculty of Chemistry and Chemical Engineering

Received: April 14, 2011
Accepted for publication: June 27, 2011

Abstract. The interest for volcanic tuffs in wastewater treatment processes is due to their adsorptive and ionic exchange properties caused by the presence of the natural zeolites which are their main mineralogical component. The volcanic tuff from Mirşid (Salaj County, Romania) has an aleuritic-psammitic texture and consists mainly of zeolites, volcanic glass, quartz, feldspars, micas and clay minerals. Clinoptilolite and heulandite are the main zeolites identified in the volcanic tuff from Mirşid. The high quantities of zeolites give the volcanic the quality of a natural ion exchanger. By a complex process that involves both adsorption and ionic exchange, zeolites removes heavy metals from wastewaters.

Acid mine drainage (AMD) has a high loading of heavy metals, especially Fe, Zn, Cd, Cu, Pb etc. For this reason before AMD are discharged into the natural receptors, the elimination of heavy metals is necessary. Using the zeolitic

* Corresponding author e-mail: agneskeri@yahoo.com

volcanic tuff from Mirşid, different experiments were performed in order to remove the heavy metal ions from AMD of Larga Mine (Alba County).

Key words: zeolitic volcanic tuff, clinoptilolite, Mirşid, AMD Larga Mine.

1. Introduction

The most common materials used as ion exchangers are resins, natural and synthetic zeolites, clay minerals and humic soils. These materials have preferential selectivity to certain ions or classes of ions (Gaikwad, 2010).

Both, natural and synthetic zeolites have special properties and behaviour in processes as catalyse, adsorption and ion exchange. Thus, zeolites are successfully used in removal and retention of metal ions from the wastewaters (Gaikwad, 2010).

Volcanic tuffs are rocks formed by the consolidation and diagenesis of volcanic ashes. They consist of volcanic glass, and different types of minerals and lithic clasts. The diagenetic as well as the alteration processes caused by the circulation of hydrothermal or aqueous solutions, on the system of cracks and pores, of the tuffs led to the crystallization of the volcanic glass with formation of zeolites, clay minerals, carbonates etc. The natural ion exchanger character of the volcanic tuffs is due to their high content of zeolites (Gaikwad, 2010).

The zeolites utilization to remove and retain metals from wastewaters has been used since the early '60s. Different methods and materials (synthetic or natural) for wastewater treatment are known:

- Ion exchange resins: for retention of cations and anions (Bejan *et al*., 2007; Gaikwad, 2010; Gaikwad *et al*., 2009);
- Natural unmodified zeolites or in modified form to improve the capacity of adsorption and ion exchange: the elimination of Cu^{2+}, Pb^{2+}, Zn^{2+}, Cr^{3+}, Fe^{3+}, Co^{2+}, Mn^{2+} (Ali – Sewailem, 2007; Gaikwad, 2010; Erdem *et al*., 2004; Inglezakis *et al*., 2002). The zeolitic volcanic tuffs from Romania were used in the removal of Pb^{2+}, Zn^{2+}, Fe^{2+}, Cu^{2+} from synthetic solutions (Burtică *et al*., 2003; Măicăneanu *et al*., 2008; Stanca *et al*., 2003);
- The mixture of zeolite (secondary product resulted from tuff grading operation) and Portland cement to reduce Pb^{2+}, Cu^{2+}, Cd^{2+}, Zn^{2+} from wastewater (Ok *et al*., 2007).

Acid mine drainage (AMD) represents polluted water formed by the interaction between natural waters and metallic minerals from the ore deposits. The metals and sulphur of the sulphides (pyrite, chalcopyrite, galena, etc.) are released in the water. AMD acidity is due to the pyrite dissociation in water under aerobic conditions. Innovative methods for AMD treatment applicable to industrial scale are difficult to be found due to their acid pH and complex

chemical compositions. The successful application of zeolitic volcanic tuff in the removal of metals from wastewaters is due by their capacity of metals retention. The acid form of a natural clinoptilolite was used to remove Al^{3+}, Cu^{2+}, Zn^{2+} and Fe^{2+} from an acid rock drainage from Britannia Mine (Canada) (Li *et al*., 2008). The retention of Cu^{2+}, Ni^{2+}, Pb^{2+}, Zn^{2+} and Cd^{2+} from AMD from the Larga de Sus Mine (Alba County) using zeolitic volcanic tuff from Mirşid (Sălaj County) is investigated in the present paper.

2. Materials and Methods

Two samples of AMD were collected directly from the drainage pipe which gets out from the Larga de Sus Mine (Zlatna, Alba County). Larga de Sus Mine was opened in 1962 − 1963, and mining activity was discontinued in 2006. The first sample was collected in April 2010 after a rainy period and the second one in June 2010 after a droughty period. The wastewater used in the experiment were resulted from mixing the two samples and then analyzed by ICP-MS for the content of the following cations: Cu^{2+}, Ni^{2+}, Pb^{2+}, Zn^{2+} and Cd^{2+}. The pH and the electrical conductivity of the AMD sample were determined by Consort C861 device.

Fig. 1 – AMD drainage pipe - sampling point.

The zeolitic volcanic tuff was crushed and sieved. The sort 0.2 – 2.0 mm were used in the experiment of wastewater treatment in order to study the retention of the above mentioned cations. Mineralogical and petrographic features of the zeolitic volcanic tuff from Mirşid were presented in a previous study (Keri *et al*., 2010). From the mineralogical point of view, the zeolitic volcanic tuff consists of zeolites (clinoptilolite and heulandite), quartz, feldspars, micas, iron oxy-hydroxides, clay minerals and calcite. The content of Cu^{2+}, Ni^{2+}, Pb^{2+}, Zn^{2+}, Cd^{2+} from tuff samples were determined by ICP-MS, based on a method developed by The Research Institute for Analytical

Instrumentation Cluj Napoca (INCDO INOE 2000 ICIA). The inductive coupled plasma mass spectrometer used was a Perkin Elmer Elan DRC II model (Toronto, Canada), which has a quadrupol and a Dynamic Reaction Cell to eliminate interferences. First, a semi-quantitative method (TotalQuant) was used to determine the concentrations ranges of Cu, Ni, Pb, Zn and Cd ions. After preliminary tests, dilutions were made being necessary for a quantitative method by using a 6-point calibration curve in the range of 10-100 mg/L. Hereby, the final content of cations were obtained.

3. Experimental

The experiment was conducted using batch technique with immobile phases, at constant temperature of 20°C. The method consists in putting into static contact of the zeolitic volcanic tuff (ZVT) and the acid mine drainage (AMD). The interaction time was set at 0.5 hours, 2 hours, 24 hours and 48 hours. The dimensions of ZVT grains used in the experiment ranged between 0.2 and 2.0 mm. When the experiment was completed, the two media were separated by filtration. The ZVT: AMD ratio was 1: 25 (40 g of tuff and 1000 mL AMD).

4. Results

4.1. Physical and Chemical Features of AMD

The pH and electrical conductivity are the physical parameters determined for AMD. The AMD has an acid pH equal to 2.44. Before the experiment, the AMD sample do not underwent any changes of the acidity. The value of electrical conductivity, 2.79 mS/cm, indicates high amounts of dissolved salts in the water. The content of the Cu, Zn, Pb, Cd and Ni cations in acid mine drainage determined by ICP-MS − inductively coupled plasma mass spectrometry, are presented in Table 1.

Tabel 1

The Content of Cu, Zn, Pb, Cd and Ni Cations in AMD

Metal / Sample	Cu (mg/L)	Zn (mg/L)	Pb (mg/L)	Ni (mg/L)	Cd (mg/L)
AMD	1.198	11.080	0.034	0.254	0.500

4.2. Chemical Features of Mirşid Volcanic Tuff

The same cations were analyzed also in the volcanic tuff from Mirşid. The ICP-MS analysis results are shown in Table 2.

Tabel 2
The Content of Cu, Zn, Pb, Cd and Ni Cations in ZVT

Metal / Sample	Cu (mg/kg)	Zn (mg/kg)	Pb (mg/kg)	Ni (mg/kg)	Cd (mg/kg)
ZVT	5.900	46.500	11.900	6.280	0.070

4.3. Batch Experiment Results

After the experiment (0.5 h, 2 h, 24h and 48 h) the zeolitic volcanic tuff grains were analyzed. All analyzed samples are enriched in the Cu, Zn, Pb, Ni and Cd cations. The enrichment was calculated using the formula:

$$\Gamma = \frac{C_f - C_i}{C_f} 100 \text{ , (\%)} \quad (1)$$

where: Γ − Enrichment (%); C_f − The metal concentration of the ZVT sample at the end of time interaction (mg/kg); C_i − The initial concentration of metal in ZVT sample (mg/kg).

There is an increasing of the copper content of the ZVT samples (Fig. 2). The highest content was achieved after 48 hours of static contact. The retention of copper from AMD is achieved very rapidly in the first 2 hours of the interaction (Fig. 3). The highest enrichment of ZVT in copper was after 48 hours, 60 % higher as compared with the initial content of the copper in natural ZVT sample.

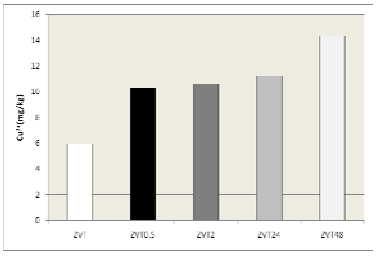

Fig. 2 – The content of Cu^{2+} in natural ZVT and after 0.5 h, 2 h, 24h and 48 of static interaction with AMD.

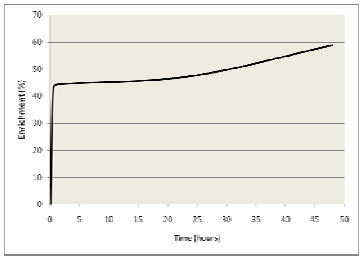

Fig. 3 – The evolution of the Cu^{2+} in ZVT, during the experiment.

The highest content of nickel in the ZVT was achieved for the sample measured at 2 hours after the beginning of the interaction (Fig. 4). The nickel content recorded at 48 hours is 6 % lower as compared with the content at 2 hours. The enrichment of the ZVT samples in nickel is an extremely fast process in the first 2 hours of the interaction, when the highest content of nickel

in the ZVT can be noticed. The observed enrichment exceeds with maximum 10 % the initial content of nickel in natural ZVT sample (Fig. 5).

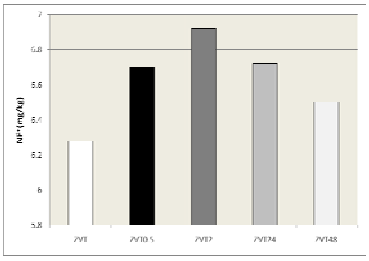

Fig. 4 – The content of Ni^{2+} in natural ZVT and after 0.5 h, 2 h, 24h and 48 of static interaction with AMD.

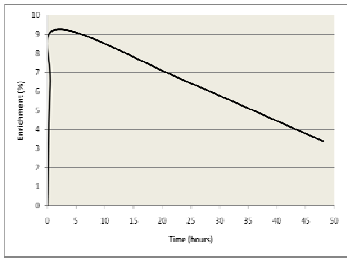

Fig. 5 – The evolution of the Ni^{2+} in ZVT, during the experiment.

After the first two hours of experiments, the nickel content of the ZVT is decreasing until 48 hours, but compared with the initial content of volcanic tuff grains have higher amounts of nickel. Such a release of nickel in the water during the experiment could be explain by a continuously ion exchange process.

The highest lead content of ZVT samples is determined at 0.5 hours and 24 hours respectively, having similar values (Fig. 6). The content at 0.5 hours is 14.3 mg/kg while at 24 hours the lead content is 14.4 mg/kg respectively. During the experiment there are two different trends in variation of the ZVT lead content (Fig. 6):

I. Between 0 and 0.5 hours, 2 and 24 hours respectively, there is an enrichment of the lead content in ZVT;

II. Between 0.5 and 2 hours, 24 and 48 hours respectively, there is a depletion of the lead content in ZVT.

The increasing and decreasing of the lead content in the ZVT during the experiment could be explain, as in the case of nickel, by the continuously ion exchange process between the two media.

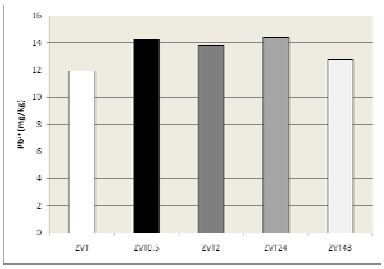

Fig. 6 – The content of Pb^{2+} in natural ZVT and after 0.5 h, 2 h, 24h and 48 of static interaction with AMD.

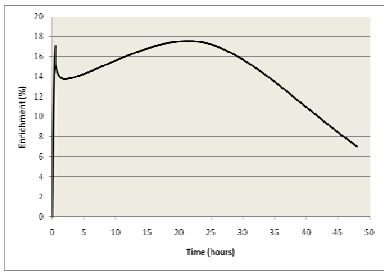

Fig. 7 – The evolution of the Pb^{2+} in ZVT, during the experiment.

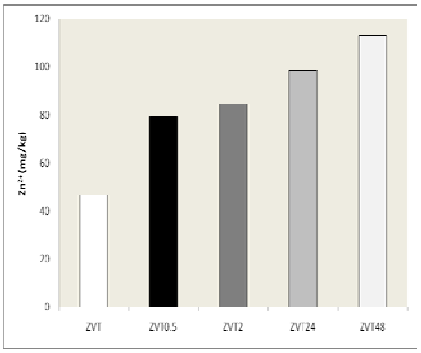

Fig. 8 – The content of Zn^{2+} in natural ZVT and after 0.5 h, 2 h, 24h and 48 of static interaction with AMD.

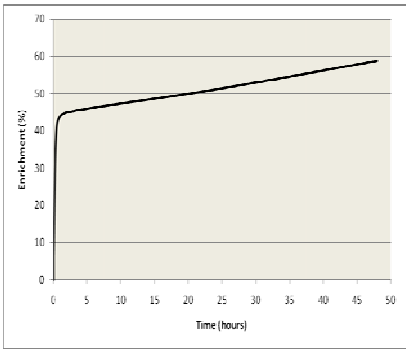

Fig. 9 – The evolution of the Zn^{2+} in ZVT, during the experiment.

The zinc content of tuff samples subjected to the experiment showed a continuous increasing in time (Fig. 8). In the first 2 hours of the interaction, the enrichment increased rapidly (Fig. 9). The enrichment in zinc of the ZVT sample is maxim at 48 hours, being about 59 % higher as compared with the natural sample of volcanic tuff.

Of the five metals investigated, the highest enrichment of ZVT samples was obtained for cadmium. Even if the cadmium content of tuff sample determined at 48 hours is decreasing (Fig. 10), there is an obviously enrichment trend of Cd between 2 and 48 hours (Fig. 11). The maximum enrichment is about 90 %.

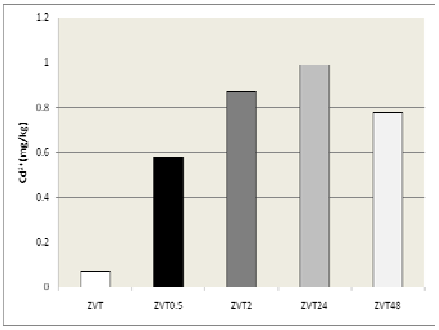

Fig. 10 – The content of Cd^{2+} in natural ZVT and after 0.5 h, 2 h, 24h and 48 of static interaction with AMD.

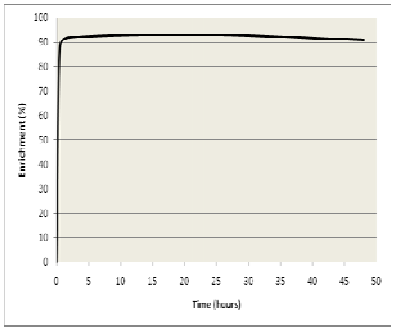

Fig. 11 – The evolution of the Cd^{2+} in ZVT, during the experiment.

There is an important vriation of the pH during the experiment. In the first two hours, there is a migration of the metallic cations and H^+ from water to the volcanic tuff grains.

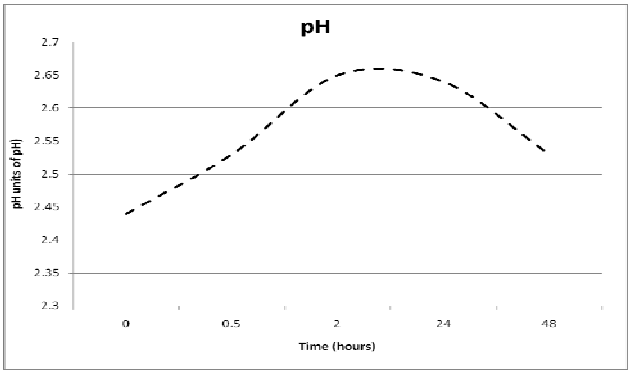

Fig. 12 – The AMD pH during the experiment.

During the experiment the acid features of the water is still preserved. Therefore, some of the metallic cations and H^+ held in the ZVT during the first part of the experiment are released again into the water. The releasing of the metallic cations in the water is correlated with the pH decreasing.

5. Conclusion

Zeolite volcanic tuff from Mirşid (Sălaj) was used as natural ion exchanger in order to retain Cu^{2+}, Ni^{2+}, Pb^{2+}, Zn^{2+} and Cd^{2+} ions dissolved in AMD sampled from the Larga de Sus Mine (Alba County). The experiment was carried out by batch method and the following observations were made:

- A pronounced enrichment of ZVT samples was identified in the first 0,5 hours for lead or in the first 2 hours for the other metals;
- The enrichment of tuff samples in Cu^{2+}, Zn^{2+} and Cd^{2+} is carried out more slowly after 2 hours of the interaction;
- Of the five investigated metals, increasing and decreasing of the lead and nickel contents in the ZVT during the experiment can be noticed.

Based on the geochemical behaviour of the five metallic cations investigated during the experiment, a selectivity series were determined (Table 3).

Table 3

Selectivity Series Set for the Zeolitic Volcanic Tuff from Mirşid According to the Time of Interaction

Time of interaction	Selectivity series
30 minutes	Cd > Cu > Zn > Pb > Ni
2 hours	Cd > Zn > Cu > Ni ≈ Pb
24 hours	Cd > Zn > Cu > Pb ≈ Ni
48 hours	Cd > Cu > Zn ≈ Pb > Ni

The results of the experiments point out that the ideal period of interaction is of two hours even if the content of metallic cations at 48 hours is higher.

Acknowledgement. This research was conducted within PRODOC, Contract POSDRU/6/1.5/S/5 ID7676, with the support of Research Institute for Analytical Instrumentation, Cluj-Napoca.

REFERENCES

Ali – Sewailem M.S. *Characteristics of Lead Sorption by Zeolite Minerals*. Journal of Applied Sciences, **7**, *13*, 1718 – 1725 (2007).

Bejan M., Rusu T., Avram S., *Metode performante de recuperare a metalelor grele din apele de mină*. Buletin AGIR, *1*, 7 – 12 (2007).

Burtică G.Gh., Pode R., Pop Al., Likarec M.T., Iovi A., Negrea P., *Utilizarea unor materiale compozite pe bază de tufuri vulcanice, dopate cu săruri, pentru eliminarea unor poluanţi din apă*. Environment & Progress, 83 – 86 (2003).

Calvo B., Canoira L., Morante F., Martínez-Bedia J.M., Vinagre C., García-González J.-E., Elsen J., Alcantara R., *Continuous Elimination of Pb^{2+}, Cu^{2+}, Zn^{2+}, H^{+} and NH_4^{+} From Acidic Waters by Ionic Exchange on Natural Zeolites*. Journal of Hazardous Materials, **166**, 2-3, 619 – 627 (2009).

Erdem E., Karapinar N., Donat R., *The Removal of Heavy Metal Cations by Natural Zeolites*. Journal of Colloid and Interface Science, **280**, *2*, 309 – 314 (2004).

Gaikwad R.W., Misal S.A., Irendra D.H., Gupta D.V., *Removal of Copper Ions from Acid Mine Drainage (AMD) by Ion Exchange Resins: INDION 820 and INDION 850*. Journal of Applied Scinces in Environmental Sanitation – Electronic Eddition, 91 – 97 (2009).

Gaikwad R.W., *Review and Research Needs of Active Treatment of Acid Mine Drainage by Ion Exchamge*. Electronic Journal of Environmental, Agricultural and Chemistry, **9**, *8*, 1343 – 1350 (2010).

Inglezakis V.J., Loizidou M.D., Grigoropoulou H.P., *Equilibrium and Kinetic Ion Exchange Studies of Pb^{2+}, Cr^{3+}, Fe^{3+} and Cu^{2+} on Natural Clinoptilolite*. Water Research, **36**, 2784 – 2792 (2002).

Keri A.A., Măicăneanu A., Har N., Avram S., Rusu T., *Considerations on Acid Mine Drainage Treatment With Zeolitic Volcanic Tuff*. International Conference „Mineral Resources and Environment", Baia Mare – Romania, 28–30 October, 2010.

Li L.Y., Tazaki K., Lai R., Shiraki K., Asada R., Watanabe H., Chen M., *Treatment of Acid Rock Drainage by Clinoptilolite – Adsorptivity and Structural Stability for Different pH Environments*. Applied Clay Science, **39**, 1 – 9 (2008).

Măicăneanu A., Bedelean H., Stanca M., *Zeoliţii naturali – Caracterizare şi aplicaţii în protecţia mediului*, Presa Universitară Clujeană, 325 (2008).

Ok Y.S., Yang J.E., Zhang Y.S., Kim S.J., Chung D.-Y., *Heavy Metal Adsorption by a Formulated Zeolite-Portland Cement Mixture*. Journal of Hazardous Materials, **147**, 91 – 96 (2007).

Stanca M., Dulămiţă N., Burcă S., Ghiţulescu R.E., *Recuperarea zincului din ape reziduale*. Environment & Progress, Cluj Napoca, 491 – 493 (2003).

UTILIZAREA UNOR SCHIMBĂTORI DE IONI NATURALI ÎN ELIMINAREA METALELOR GRELE DIN DRENAJELE ACIDE MINIERE

(Rezumat)

Interesul manifestat pentru cercetarea depozitelor de tufuri vulcanice se datorează proprietăţilor adsorptive şi de schimb ionic ale zeoliţilor naturali, caracteristici care determină utilizarea acestora la depoluarea apelor. Tuful de Mirşid, prezintă structură aleurito-psamitică, fiind constituit în principal din sticlă vulcanică zeolitizată şi cristaloclaste (cuarţ, feldspat, biotit, minerale argiloase). Zeolitul principal identificat este clinoptilolitul însoţit de heulandit. Prezenţa zeoliţilor în cantităţi ridicate imprimă tufului calitatea de schimbător de ioni naturali. Printr-un proces complex ce implică atât adsorbţie cât şi schimb ionic, zeoliţii elimină metalele grele din apele uzate.

Drenajele acide miniere (DAM) prezintă o încărcătură ridicată cu metale grele, în special Fe, Zn, Cd, Cu, Pb, etc. Din acest motiv se impune diminuarea concentraţiei de metale înainte de deversare în receptori naturali. În acest articol se propune utilizarea tufului vulcanic zeolitic de la Mirşid pentru eliminarea unor ioni de metale grele din DAM.

BULETINUL INSTITUTULUI POLITEHNIC DIN IAŞI
Publicat de
Universitatea Tehnică „Gheorghe Asachi" din Iaşi
Tomul LVII (LXI), Fasc. 4, 2011
Secţia
ŞTIINŢA ŞI INGINERIA MATERIALELOR

OPTIMIZATION OF SnO_2-BASED GAS SENSORS VIA BULK DOPING: DO WE HAVE ANY LIMITATIONS?

BY

G. KOROTCENKOV*, B.K. CHO

Gwangju Institute of Science and Technology, of Korea,
Department of Material Science and Engineering

Received: April 14, 2011
Accepted for publication: June 27, 2011

Abstract. The doping influence on electrophysical, structural and gas sensing properties of the SnO_2 was considered. It was concluded that changes observed in gas sensing properties of Fe-, Co-, Ni-, and Cu-doped SnO_2-based thin films deposited by spray pyrolysis were connected with both the appearance of fine dispersed phase formed in the SnO_2 matrix, and structural disordering of heavy doped based oxide.

Key words: SnO_2, spray pyrolysis, doping, transition metals, gas sensors, parameters, analysis.

1. Introduction

Current research has shown that simple metal oxides are not ideal materials for gas sensor application satisfying all requirements to gas sensing matrix. To overcome present imperfection of sensing material, in many works it was suggested to turn from simple binary gas sensitive metal oxides, such as TiO_2, SnO_2, ZnO, In_2O_3, or WO_3, to complex multi-component materials

* Coprresponding author e-mail: ghkoro@yahoo.com

(Yamazoe *et al.,* 1983; Meixner & Lampe 1996; Williams, 1999 ; Korotcenkov, 2005), which in addition to the base oxide matrix could contain various additives introduced in metal oxides during their deposition or synthesis.

2. The Role of Additives in Multi-Component Oxides

A conception of multi-component approach is based on a statement that the appearance of additional components in gas sensing matrix could improve parameters of metal oxides important for gas sensor applications. Research has shown that for these purposes both catalytic active additives (noble metals and transition metal oxides), and inert impurities may be used. According to numerous studies the incorporation of additives into base metal oxides can change their parameters such as concentration of charge carriers; chemical and physical properties of the metal oxide matrix; electronic and physical–chemical properties of the surface (energetic spectra of surface states, energy of adsorption and desorption, sticking coefficients, etc.); surface potential and intercrystallite barriers; phase composition; and so on (Yamazoe *et al.,* 1983; Gopel & Scherbaum 1995) ; Korotcenkov *et al.,*2005; Kawamura *et al.,*2001; Madou &, Morrison 1989). The doping can also be accompanied by decrease of the grain size. For example, the SnO_2 doping by In, Sn, and Nb (0.1–4 mol%) caused the decrease of crystallite size from 220 nm for pure SnO_2 to about 30 nm for Nb (0.1 mol%) doped samples (temperature of calcination was equal to 900°C), (Szezuka *et al.,* 2001). It was established that the thermal stability of nanocomposites might be significantly higher than that of the individual homogeneous oxide components as well. For example, in (Yang *et al.,* 2000) it was shown that NiO, MoO_3, CuO, Cr_2O_3 oxides dispersed on the surface of SnO_2 can retard the decrease in the specific surface area of the samples and the increase in the crystallite size of SnO_2 during calcinations at T_{an} = 500°C.

The mentioned above effects have real nature, because additives incorporated in metal oxides even in small quantity can modify catalytic activity of based oxide, stabilize a particular valence state of metal, favor formation of active phases, stabilize the catalyst against reduction, increase the electron exchange rate and change the conditions of base oxide growth. For example, in (Kawamura *et al.,* 2001) it was established that the presence of Cr^{3+} accelerates the SnO_2 growth rate in the (Yang *et al.,* 2000) direction and suppresses that in the (Szezuka *et al.,* 2001) direction. Estimations made in (Kawamura *et al.,* 2001) have shown that when trivalent cations are adsorbed on the site of Sn^{4+}, the oxygen in the neighborhood of the Sn^{4+} site is destabilized, which results in desorption of oxygen from the matrix so as to maintain electrically neutrality. Desorption of oxygen on the S (stepped) face is identical to transformation of an S-face to a rough K (kinked) face. Research of such a two-phase systems, in which the concentration of the second oxide phase is much less than based oxide concentration, has shown that the second phase, as a rule, is fine disperse

one, and it is being formed on the surface of the based oxide's grains (Varela *et al.,* 1999; Szezuka *et al.,* 2001; Carreno *et al.,* 2002; Pagnier *et al.,* 2001). Just the appearance of additional inter-grain boundaries between adjacent grains of Me(1)O and Me(2)O inhibit the cation inter-diffusion and crystallite growth during synthesis and following annealing.

In addition, the using of volatile impurities as additives can cause a process, which could improve the porosity of gas sensing matrix. Additives such as alkali and alkaline earth metals are known as electron exchange promoters, presumably because of the higher partial charge on the neighboring oxygen, whereas transition metals incorporated in metal oxide matrix are promoters favorable to the formation of active sites (Madou &, Morrison 1989). The later is connected with possibility for cation in transition metal oxides to be in several valencies. So, phase modification opens up exciting additional possibilities for varying the structure, electro-physical and catalytic properties of metal oxide materials.

3. Doping Influence on Operating Characteristics of the SnO_2-Based Gas Sensors

It is necessary to note, that experimental facts related to influence of bulk doping on gas sensing properties of different metal oxides may be found in various reviews [(Yamazoe *et al.,* 1983; Meixner & Lampe 1996; Williams, 1999; Korotcenkov, 2005; Madou &, Morrison 1989 ; McAleer *et al.,* 1988; Gopel & Scherbaum 1995). However, research carried out has shown that bulk doping is the most unpredictable method of structural engineering, saying about results. At first, it was established that the mechanism of gas impact on the electrical properties of nano-composites Me(1)O–Me(2)O is much more complicated as compared with sensing mechanism of homogeneous oxides and has special features (Gaskov & Rumyantseva, 2001). When Me(2) is a transition element (*d*-element), these reactions can change the Me(2) oxidation state, coordination number, and cation distribution between the surface and lattice positions. The reversible variations of Me(2) oxidation state and position in the presence of specific gas molecules could result in a sharp change of the electronic state of the grain boundaries and the transport properties of nanocrystalline materials. So, the grain boundary state, responsible for the electrical properties of nano-composites, is self-adjusted depending on the reduction–oxidation (redox) properties of the atmosphere as well as the crystal-chemical properties of Me(2) cations such as their electronic configuration and ionic radius. Secondly, the influence of doping elements on gas sensing properties of metal oxide gas sensors does not always coincide with catalytic activity of these additives. This regularity has been shown especially clear for a group of transition metals (Cr, Mn, Fe, Ni, Co, Cu, Zn, and Ga), which is widely used in catalysis. Such situation is quite appropriate. It is known that

both gas sensitivity and catalytic activity despite of surface nature of these processes have essential differences in the mechanisms. If the result of the surface catalysis is the final product of reactions taking place on the surface of metal oxide, the sensor response is a change of resistance of an oxide matrix being a consequence of surface reaction. The surface catalysis can flow without electronic exchange with a conduction band of an oxide matrix, but for appearance of gas sensitivity such electronic exchange is obligatory. That is why high catalytic activity of additives is not always accompanied by high sensor response. Thirdly, as we described before, depending on both the concentrations of additives and crystallization modes, it can take place a simultaneous modification of structure, accompanied by the grain size change and appearance of second phase in base oxide, and electro-physical and surface properties of metal oxides (Cabot *et al.,* 2001). Therefore, trying to determine a mechanism of doping influence on gas sensing characteristics of metal oxides, one should take into account that all parameters of doped films are being changed. Only in the framework of such approach, false conclusions can be prevented. In particular, in this case it would be possible to understand that observed often modifications of gas sensing characteristics are not connected with appearance of additional active catalytic centers, but are a consequence of ether the change of the grain size (t), or concentration of free charge carriers (N_d) (Fliegel *et al.,* 1994). For example, according to (Szezuka *et al.,* 2001), the SnO_2 doping by Nb and Sb in the range 0.01–1.0 mol% during sol–gel preparation with following annealing at T = 900°C leaded to a drop of film resistance in 10^2 and 10^4 times correspondingly, while the doping by In was accompanied by a rise of film resistance approximately by a factor of 10^2. Such situation was analyzed in (Yamazoe *et al.,* 1983; Korotcenkov, 2005; Brynzari *et al.,* 2000) using the results of both theoretical simulations and experimental study. It was shown that at certain conditions the influence of indicated above factors (t and N_d) may be much stronger than the influence of catalyst particles.

During ceramic and thick film gas sensors fabrication, the problem of additives influence on the grain size and bulk concentration of free charge carriers can be resolved through the compounding of components, for example such as the SnO_2 and Al_2O_3 powders, at the final stage of both ceramics and pastes preparation (Ihokura & Watson, 1994). In this case there is small probability that the properties of SnO_2 would be determined by the doping impurities (Al^{3+}) incorporated into the tin dioxide lattice. In such system Al_2O_3 added to tin dioxide matrix plays the role of filler, which only separates SnO_2 crystallites, decreasing the area of intercrystallites contacts and preventing their sintering. As a result, both stability and sensitivity of sensors may be increased.

In thin film technology it is impossible to exclude mutual influence of additives and the base oxide during the nanocomposite deposition. No doubts it

creates some troubles while selecting an optimal composition of gas sensing matrix. Our experiments have shown that small concentrations of dopants practically did not influence morphology of the SnO_2 films deposited by spray pyrolysis. The main distinctive feature of doped films was a drop of X-ray Diffraction (XRD) peaks intensity (see Fig. 1*a*). It became stronger with the growth of the concentration of introduced additives, as well as small XRD peaks' broadening, indicating on the decrease of the grain size in doped films. However, the decrease of the grain size was much smaller than it was observed while using ceramics technologies (Szezuka *et al.,* 2001). Even at maximum concentrations of dopants the decrease of the average grain size in the SnO_2 films determined by XRD method was ~40%. While using a ceramics technology, the grain size in doped material decreased in times.

The absence at XRD patterns of peaks corresponding to the second oxide phase and the drop of XRD peaks' intensity allowed us making two important conclusions: (1) the second oxide in the oxide matrix presents in the form of crystallites with size smaller than 1 – 3 nm; and (2) doping is being accompanied by the growth of the contents of fine dispersed amorphous-like SnO_2 phase. Scanning electron microscopy (SEM) and atomic force microscopy (AFM) measurements have shown that the fine dispersed phase, formed at the surface of the big grains of the main oxide, fills inter-crystallite space. Assumed structure of doped films is shown in Fig. 1b. We believe that the growth of the fine dispersed phase's contents in doped films is conditioned by the appearance of the additional nucleation centers for the SnO_2 growth, formed by the second oxide phase (Korotcenkov, 2008).

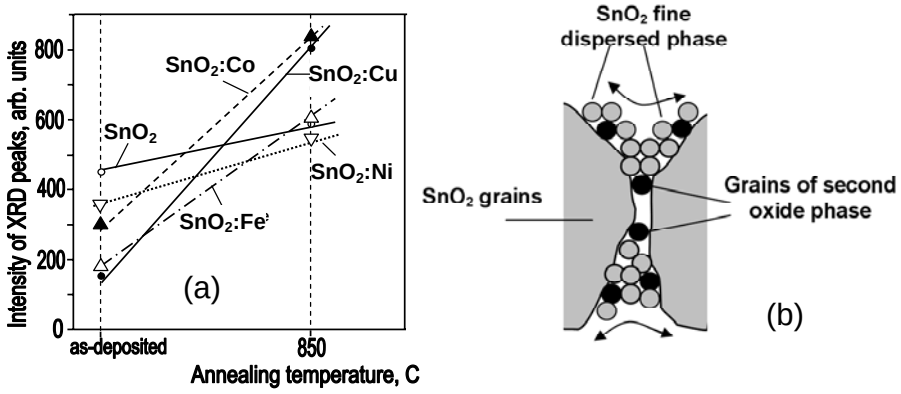

Fig. 1 – Influence of doping on (a) the intensity of (110) XRD peaks of doped SnO_2 films (16 at.%), and (b) the structure of deposited films: T_{pyr}=450°C; d~120 nm.

A morphology analysis of the SnO_2 films grown at various temperatures has shown that consequences of doping also depend on deposition temperature.

For example, while deposition temperature is being increased, the influence of doping on aggregation of growing crystallites strongly increases. In case of the film deposited at low temperatures (T~350°C), agglomerates have the shape of spherulites. At higher temperatures (T_{pyr} >450°C), agglomerates obtain faceting, characteristic for tetragonal system. At that detailed study of SEM and AFM images of the SnO_2 films deposited at T >450°C allowed establishing that the doping by transition metals leads to a sharp increase of probability of the SnO_2 crystallites' twinning. Tendency to twinning was mostly shown in the films, doped by Cu and Co. According to the results of high resolution transmission electron microscopy (HRTEM) analysis, the plane of twinning is one from the (101) crystallographic planes' family. Agglomerate's size also depends on dopant and attains the biggest values at doping by Cu. It is known that mentioned above effects, due to the increase of the area of intergrain contacts, do not promote the improvement of gas sensing properties.

Regarding the influence of the nature of doping additives on the thermal stability of the SnO_2 films, one can say that obtained data testify that the doping during film deposition practically did not have a positive effect on thermal stability, characteristic for ceramics technology. At best, the doping did not worsen strongly thermal stability of material. Such situation was observed for SnO_2, doped by Ni and Fe. However, after doping by Cu, sharp worsening of structure's thermal stability took place. As one can see in Fig. 1a, maximum change of XRD peaks' intensity we observed just for SnO_2:Cu. Similar effect was observed earlier for the SnO_2 powders during their sintering. In particular, it was established that additives with low melting temperature, such as CuO, at high temperature treatments (T_{an} > 800°C) could stimulate the growth of the SnO_2 grains (Panchapakesan, 2001). We believe that the main mechanism responsible for observed thermal instability is the growth of the SnO_2 crystallites due to their coalescence with the fine dispersed phase, which forming was being observed during doping process. AFM study confirmed this conclusion. After annealing at T_{an}=850°C all AFM images even for the SnO_2 films doped by cooper had clearly defined contours of the grains, confirming the absence in the SnO_2 matrix of grains with sizes, smaller than the limit of resolution of used measurement instruments.

Some results connected with study of gas sensing properties of doped SnO_2 films deposited by spray pyrolysis are presented in Fig. 2. SnO_2 sensors were fabricated as standard thin film gas sensors and tested using methodology described in (Brinzari, 2001). (Brinzari, 2001; Korotcenkov, 2001; Korotchenkov, 1999). It is seen that the doping of the SnO_2 films can significantly improve both sensitivity and selectivity of gas sensors. However, this improvement takes place in very limited range of doping concentrations. Optimal concentration of catalytic active additives providing achievement of the SnO_2 sensor response maximum lies in the range <1–3 wt.%. It is important that ultimate solubility of transition metals in SnO_2 corresponds to just these

concentrations. Results presented, as well as the results of numerous research discussed in (Xingqin, 1993), testify that superfluous concentration of additives does not contribute to the improvement of operating characteristics of gas sensors.

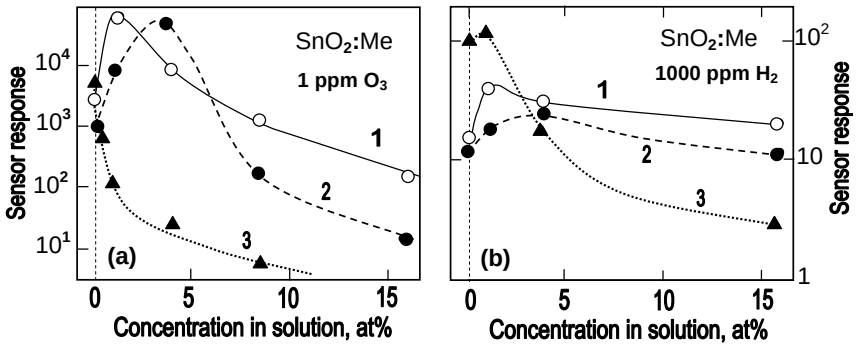

Fig. 2 – Influence of SnO_2 doping by Co, Ni, Cu and Fe during film deposition by spray pyrolysis on gas response to (a) ozone and (b) H_2: T_{pyr} = 410–420°C; *d*~45–55 nm; 1: SnO_2:Fe; 2: SnO_2:Co; 3: SnO_2:Cu.

According to the results of our research, the worsening of gas sensing characteristics of sensors with high concentration of doping additives can be connected with the *appearance of the second oxide phase.* At certain concentration, exceeding limited mutual solubility, the second phase with less gas sensitivity could start determining electro-conductivity of the gas sensing matrix. Changes, which might take place in two-phase metal oxide matrix while a concentration of the second phase is being increased, are demonstrated in Fig. 3.

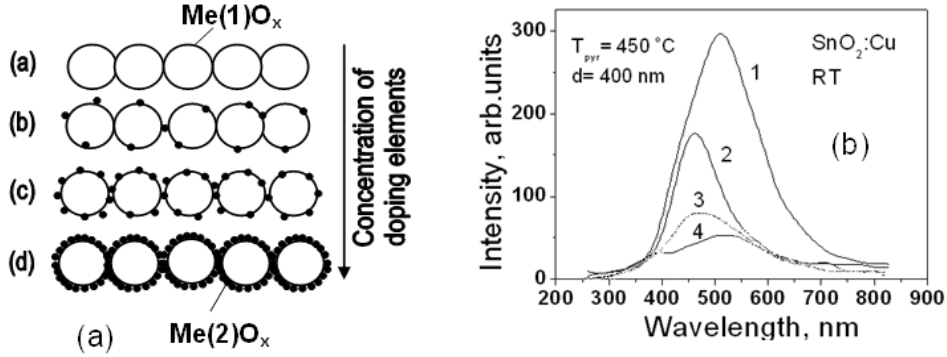

Fig. 3 – Diagrams showing the influence of doping on the change of (a) film structure, and (b) cathodoluminescence spectra of Cu-doped SnO_2 films (T_{pyr}=450 °C; d~250 nm: 1 – undoped SnO_2; 2- Cu 1 at.%; 3- Cu 4 at.%; and 4- Cu 16 at.%.

One can see that if at low concentration of additives the second phase just modifies the properties of based oxide. At the following stages it can contribute to the limitation of electro-conductivity of the metal oxide matrix. At that at final stage at certain correlation of electro-conductivity and gas sensitivity of indicated oxide phases, either full blockage of based oxide for interaction with surrounding atmosphere, or shunting of matrix of based oxide through more conductive second metal oxide phase, could take place. All mentioned above will certainly lead to fundamental change of both electrophysical and gas sensing properties of the metal oxide matrix.

Observed strong decrease of sensor response could be also explained by high catalytic activity of the transition metal oxides, *i.e*. by high rate of both ozone dissociation and catalytic oxidation of reducing gases (CO or H_2). Because of the fact that these reactions take place on the surface of the second oxides, they are probably not accompanied by a change of concentration of chemisorbed oxygen on the surface of basic oxide, responsible for conductivity. A transition metal oxide, presenting as separate phase, can act as surface catalytically active filter, converting detecting gas in other products, which do not influence a charge state of the SnO_2 surface. Indicated behavior confirms once again that sensor response is determined not by the catalytic surface activity by itself, but by the surface reactions, which are being completed by chemisorption on the surface of gas sensing material.

Considerable structural disordering of heavy doped based oxide is other factor which can control operating characteristics of the SnO_2-doped gas sensors. As it is known, in heavy doped metal oxides the density of surface states should sharply increase. According to theoretical estimations (Brynzari *et al.,* 2000) the increase of surface state density may lead to pinning of surface Fermi level position, and, therefore, to a decrease of sensor response. Results of both transmission and luminescence spectra analysis are direct experimental confirmation of this statement. At doping concentration, exceeding the level 1–4 wt.%, at which the maximum sensor response is being attained, we observed both the diffusion of absorption edge, connected with appearance of tails of density states distribution inside the SnO_2 band gap, and a drop of intensity of photo- and cathode- luminescence (Fig. 3*b*). These effects were especially strong for the SnO_2 films doped by Cu and Fe (Korotcenkov, 2010).

The worsening of gas sensing characteristics may be conditioned by *forming of additional p–n hetero-junctions* in gas sensing matrix as well. Above-mentioned conclusion was made on the base of the following considerations: (a) Metal oxides formed by a transition metals from the end of IV period in the lower oxidation state, *i.e.* deficiency of oxygen, exhibit usually *p*-type conductivity; (b) The adsorption of oxygen with formation of acceptor like species on *p*-type semiconductors is difficult due to the lack of conduction electrons; (c) Charge transfer in transition of metal oxides, while the number of *d*-electrons exceeds 3 is not described by zone model. In this case we have to

take into account the Geitler–London model of localized electrons; and (d) The direction of conductivity response to oxidizing and reducing gases for *p*-type oxides is different in comparison with *n*-type oxides (SnO_2), *i.e.* such changes may compensate each other. Some of these remarks were made earlier in (Williams, 1999). Such situation allows us being skeptical in evaluation of perspectives of wide use of mixed *p*-, *n*-type oxide matrix for standard solid state chemisorption-type sensor design.

4. Conclusion

Additional element in metal oxides can play an important role in the forming of their electrophysical, structural and gas sensing characteristics. However, while selecting both the type and the concentration of these additives, one should be very careful because we need to take into account many factors such as ability to form oxides of different oxidation states, catalytic activity, volatility, value and type of conductivity, and limited mutual solubility with base metal oxide. The last one is especially important for structural engineering of gas sensing materials, because this very parameter controls both the phase state of additives in based metal oxide, and structural disordering of the surface layer of the metal oxide grains. The concentration of transition metal oxides in SnO_2 used for gas sensor design should not be higher than 1-3 wt.%. At higher concentration a strong decrease of sensor response takes place.

Acknowledgements. This work was supported by the project through a grant funded by Ministry of Education, Science and Technology (MEST) of Korea (No. 2009-0078928) and by the World Class University program at GIST through a grant provided by MEST of Korea (No. R31-20008-000-10026-0).

REFERENCES

Brinzari V., Korotcenkov G., Golovanov V., Thin Solid Films, **391**, *2*, 167-175(2001).
Brynzari V., Korotchenkov G., Dmitriev S., J., Electron Technol., **33**, 225-235 (2000).
Cabot A., Dieguez A., *et al.,* Sens. Actuators **B 79**, 98-106 (2001).
Carreno N.L.V., *et al.,* Sens. Actuators **B 86**, 185-192 (2002).
Fliegel W., Behr G., Werner J., Krabbes G., Sensors Actuators **B 18-19**, 474-477 (1994).
Gaskov A.M., Rumyantseva M.N., Rus. J. Appl. Chem., 74, 3, 440-444 (2001).
Gopel W., Scherbaum K.D., Sens. Actuators **B 26-27**, 1-12 (1995).
Ihokura K., Watson J., *The Stannic Oxide Gas Sensor, Principle and Applications*, CRC Press, 1994.
Kawamura F., Takahashi T., Yasui I., Sunagawa I., J. Cryst., Growth, *233*, 259-268 (2001).
Kawamura F., Yasui I., Kamei M., Sunagawa I., J. Am. Ceram. Soc., *84*, 1134 (2001).
Korotcenkov G., Brinzari V., Boris I., J. Mater. Sci., **43**, *8*, 2761-2770 (2008).

Korotcenkov G., *et al*., Thin Solid Films, **471**, *1-2*, 310-319 (2005).
Korotcenkov G., *et al*., Curr. Appl. Phys., **10**, 1123-1131 (2010).
Korotcenkov G., *et al.,* Sens. Actuators, **B 77**, 1-2, 244-252 (2001).
Korotcenkov G., Sens. Actuators, **B 107**, 209-232 (2005).
Korotchenkov G., Brynzari V., Dmitriev S., Sens. Actuators, **B 54**, 202-209 (1999).
Madou M.J., Morrison S.R., *Chemical Sensing with Solid State Devices*. Academic Press, Inc. San Diego and London, 1989.
McAleer J.F., *et al*., J. Chem. Soc., Faraday Trans.,**1**, *84*(*2*),441-457 (1988).
Meixner H., Lampe U., Sens. Actuators, **B 37**, 198-202 (1996).
Pagnier T., *et al*., Sens. Actuators, **B 71**, 134-139 (2001).
Panchapakesan B*., et al*., Nanotechnology, **12**, 336-349 (2001).
Szezuka D., *et al.,* Appl. Surf. Sci. *179*, 301-306 (2001).
Varela J.A., *et al.,* Ceramics Intern. **25**, 253-256 (1999).
Williams D.E., Sens. Actuators, **B 57**, 1–16 (1999).
Xingqin L., *et al*., Sens. Actuators, **B 17**, 1-5 (1993).
Yamazoe N., Kurokawa Y., Seiyama T., Sens. Actuators, **4**, 283-289 (1983).
Yang G., Haibo Z., Biying Z., J. Mater. Sci., **35**, 917-923 (2000).

OPTIMIZAREA SENZORILOR PE BAZĂ DE SnO_2 PRIN DOPARE. EXISTĂ VREO LIMITĂ?

(Rezumat)

S-a studiat influenţa dopării asupra proprietăţilor electrofizice, structurale şi a sensibilităţii la gaze a SnO_2. S-a ajuns la concluzia că modificările observate în sensibilitatea la gaz a stratelor subţiri de SnO_2 dopate cu Fe-, Co-, Ni-, şi Cu-, depuse prin piroliza spray sunt legate de apariţia unei faze fin dispersată formată în matricea de SnO_2, şi cu dezordinea structurală a stratului pe bază de oxizi puternic dopat.

BULETINUL INSTITUTULUI POLITEHNIC DIN IAŞI
Publicat de
Universitatea Tehnică „Gheorghe Asachi" din Iaşi
Tomul LVII (LXI), Fasc. 4, 2011
Secţia
ŞTIINŢA ŞI INGINERIA MATERIALELOR

ENERGY-SAVING MECHATRONIC DRIVE OF THE MANIPULATOR

BY

L. KOZLOV*

Vinnitsa National Technical University

Received: April 27, 2011
Accepted for publication: June 27, 2011

Abstract. The paper presents a circuit of the two-flow drive for the manipulator that can be used in industry, transport and construction. The circuit comprises variable hydraulic pumps with regulators, proportional directional control valves, pressure and position pickups, and a free-programmable controller. The circuit provides automatic connection of the pump to the two simultaneously-operated hydraulic engines. Under changing value and direction of the load at the hydraulic engines the stability of the pre-set value of the actuator motion speed is ensured. Presence of the throttling directional control valves enables quick adjustment of the pre-set value of the actuator motion speed. A non-linear mathematical model of the manipulator drive is elaborated. The equations of the mathematical model are solved using Matlab software package. Relationships between the value of the flow rate to hydraulic engines and the input pressure are calculated. Stabilization error in the pressure range from 0,1 to 1,0 pmax does not exceed 8% under counter load and 13,2% under tail load conditions. It was determined that losses in the pump control system do not exceed 0.062 from the maximal pump flow rate value. Hydraulic efficiency varies in the range from 41% to 89%. With the increased value of the useful power consumed by the hydraulic engine the hydraulic efficiency is increased.

Key words: manipulator, two-flow drive, free-programmable controller, proportional directional control valve, mathematical model, stabilization error, hydraulic efficiency.

* Corresponding author e-mail: vadikkov@ukr.net

1. Introduction

At present manipulators are extensively used in industry, transport and construction engineering. In manipulators hydraulic drives regulated from free-programmable controllers are widely used, which makes it possible to provide various functional possibilities, convenience of control and high productivity in operation. However, a search for such circuit solutions has been going on, that will enable higher positioning accuracy and economic efficiency of manipulator operation during simultaneous motion of several engines (Pedersen & Munzer Marc, 2001; Andersen Torben, 2001; Song Liu & Bin Yao, 2002).

In Vinnytsia National Technical University a circuit of the manipulator mechatronic drive is developed that provides simultaneous operation of any two hydraulic engines with high economic efficiency and the possibility of the actuator motion speed control independent from the load direction and value.

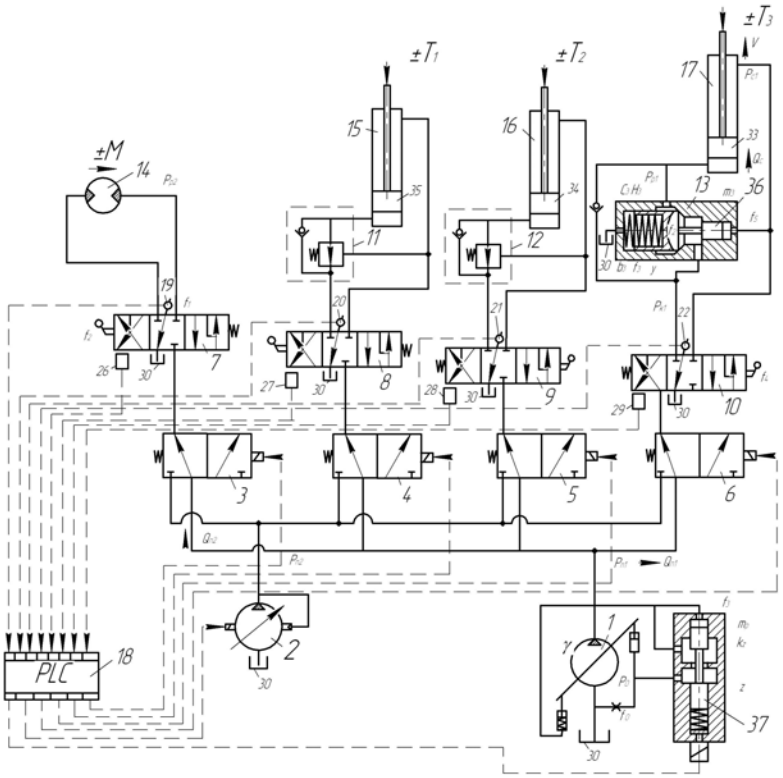

Fig. 1 – Hydraulic circuit of the manipulator two-flow drive.

Fig. 1 presents a hydraulic circuit of the manipulator two-flow drive. The drive includes two regulated pumps *1* and *2*, each of them connected to

directional control valves *3*, *4*, *5*, *6* which, in their turh, are communicated with throttling directional valves *7*, *8*, *9*, *10*. Through throttling directional valves *7*, *8*, *9*, *10* hydraulic motor *14* and hydraulic cylinders *15*, *16*, *17* are connected correspondingly. To piston chambers of hydraulic cylinders *15*, *16*, *17* backpressure valves *11*, *12*, *13* are correspondingly connected. Position of throttling directional control valves *7*, *8*, *9*, *10* are determined by position pickups *26*, *27*, *28*, *29*. Pickup signals are supplied to controller *18* that controls directional control valves *3*, *4*, *5*, *6* and variable pumps *1*, *2*.

The drive operates in the following way. When one of the proportional directional control valves (*e.g.* 10) is switched on, pickup *29* will supply signal to controller *18* that through directional control valve *6* and proportional directional control valve *10* connects pump *1* to hydraulic cylinder *17*, its rod being under the influence of the counter load or tail load.

Under the influence of counter load T_3 working fluid is supplied to the piston chamber of hydraulic cylinder *17* and actuates piston *33*. The rod of hydraulic cylinder *17* is under the action of force T_3, which will cause the action of pressures pp1 and p_{k1}, the values of which will be proportional to value of force T_3.

Working fluid from hydraulic cylinder *17* will be discharged to tank *30* through proportional directional control valve *30*. At the same time, the signal from pressure pickup *22* that through controller *18* will be supplied to the regulator of pump *1* will maintain constant value of the pressure drop p_1 = pn1 – p_{k1} at the hydraulic drive section including working port of the proportional directional hydraulic valve *10* with the area f_4. Varying the value of area f_4, the value of flow rate Q_{n1} supplied to hydraulic cylinder *17* by pump *1* can be regulated. When load T_3 on the rod of hydraulic cylinder *17* increases (decreases), the value of pressures pp1, pk1 and pn1 will also increase (decrease). However, interaction between pickup *22,* controller *18* and the regulator of pump *1* will ensure keeping constant values of pressure drop P1, which will determine the unchanged value of flow rate Q_{n1} and, therefore, stable motion speed of piston *33*. If the direction of piston *33* motion changes under the influence of counter load T_3, piston *33* will move from top to bottom.

Working fluid from pump *1* will flow to hydraulic cylinder *17* through directional control valve *6* and proportional directional control valve *10* and will be discharged to tank *30* through backpressure valve *13*, that is fully opened under the influence of pressure *pc1*, and proportional valve *10*. At the same time the possibility to control the value of flow rate Q_{n1} of pump *1* will be also provided by varying the working port area f4 as well as stabilization of piston *33* motion speed value.

When the counter load force T_3 changes its direction while piston *33* moves from top to bottom, pressure P_{C1} is reduced, working port of backpressure valve *13* is partially closed providing regulation of the flow rate from the piston chamber of hydraulic cylinder *17*. Simultaneous operation of

pickup *22*, controller *18* and regulator of pump *1* ensures maintaining constant value of pressure drop p_1 in the section from proportional valve *10* that includes the working port with the area f_4.

Varying the value of area f_4, the value of flow rate Q_{n1} from pump *1* to hydraulic cylinder *17* could be proportionally changed and in this way the motion speed of piston *33* is regulated. If the value of tail load T_3 increases (decreases) backpressure valve *13* will increase (decrease) its working port area compensating for the change of tail load valve so that piston *33* motion speed stabilization will be provided independent from the value of tail load T_3.

In the process of pump *1* and hydraulic cylinder *17* operation one of the three other hydraulic engines could be connected (hydraulic cylinders *15*, *16* or hydraulic motor *14*). Switching of the corresponding throttling directional control hydraulic valve (*e.g. 7*) will lead to pressure pickup *26* operation, the signal of which is supplied to controller *18* and will provide switching of directional control valve *3* so that working fluid from pump *2* through directional control valve *1* and through directional valve *7* will flow to hydraulic motor *14* actuating its shaft. Discharge of the working fluid from hydraulic motor *14* will be provided through throttling directional control valve *7* to tank *30*, pickup *19*, controller *18* and the regulator of pump *2* will maintain constant pressure drop *p2* in the section from pump *2* to the output of the throttling directional control valve *7* with the working port area f_2. Varying the value of area f_2, the change of flow rate value Q_{n2} supplied to hydraulic motor *14* by pump *2*, can be provided. In this way the rotation speed of the shaft is regulated. Moment Mc at the shaft of hydraulic motor *14* determines the value of pressure p_{p2} at the hydraulic motor input while pickup *2* provides the value of pressure p_{n2} so that pressure drop $p_2 = p_{n2} - p_{p2}$ will remain unchanged.

When moment Mc at the shaft of hydraulic motor *14* increases (decreases), the value of pressure p_{n2} will increase (decrease) correspondingly while flow rate Q_{n2} from the pump to the hydraulic motor and speed of the hydraulic motor rotation will also remain unchanged.

In order to study working processes in the hydraulic drive, non-linear mathematical model was elaborated with the following assumptions: lump parameters of the drive are considered, working fluid temperature is assumed to be constant, wave processes in the drive are not taken into account, flow coefficients are non-cavitational, pressure losses in hydraulic lines were not taken into account, compliance coefficient of the fluid was taken into account as an average valve for the pressure range under consideration, leakage flows of the working fluid in the slots of the pump, hydraulic cylinders and values were not taken into account.

The controller was considered as a proportional member, pressure losses at the working port of directional control valve *6* were not taken into account (Козлов, 2000).

Mathematical model of the drive operation under counter load conditions has the form of

$$\frac{\pi \cdot d_7^2}{4} \cdot d_8 \cdot k \cdot n \cdot tg\gamma = \tag{1}$$

$$= \mu \cdot f_4 \cdot \sqrt{\frac{2 \cdot (p_{n1} - p_{\kappa 1})}{\rho}} + \mu \cdot k_z \cdot z \cdot \sqrt{\frac{2 \cdot (p_{n1} - p_o)}{\rho}} + \beta \cdot W_{n1} \cdot \frac{dp_{n1}}{dt}$$

$$\mu \cdot f_4 \cdot \sqrt{\frac{2 \cdot (p_{n1} - p_{\kappa 1})}{\rho}} = \mu \cdot \pi \cdot D_1 \cdot y \cdot \cos\alpha \cdot \sqrt{\frac{2 \cdot (p_{\kappa 1} - p_{p1})}{\rho}}; \tag{2}$$

$$\mu \cdot k_z \cdot z \cdot \sqrt{\frac{2 \cdot (p_{n1} - p_o)}{\rho}} = \mu \cdot f_o \cdot \sqrt{\frac{2 \cdot p_o}{\rho}} + \beta \cdot W_o \cdot \frac{dp_o}{dt}; \tag{3}$$

$$\mu \cdot \pi \cdot D_1 \cdot y \cdot \cos\alpha \cdot \sqrt{\frac{2 \cdot (p_{\kappa 1} - p_{p1})}{\rho}} = F_{c1} \cdot V + \beta \cdot W_c \frac{dp_1}{dt}; \tag{4}$$

$$J \cdot \frac{d^2\gamma}{dt^2} = p_{n1} \cdot F_5 \cdot \ell - p_o \cdot F_4 \cdot \ell - b_\gamma \cdot \frac{d\gamma}{dt} - M_c \tag{5}$$

$$m_c \frac{dV}{dt} = p_{p1} \cdot F_{p1} + N - b_c \cdot V - T_c \cdot signV; \tag{6}$$

$$m_3 \frac{d^2y}{dt^2} = p_{\kappa 1} \cdot (f_5 - f_3) - b_3 \frac{dy}{dt} - c_3(H_3 + y) - T_3 \cdot sign\frac{dy}{dt}; \tag{7}$$

$$m_p \frac{d^2z}{dt^2} = p_{n1} \cdot f_p - b_p \frac{dz}{dt} - T_p \cdot sign\frac{dz}{dt} - K_M \cdot i; \tag{8}$$

$$P_{p1} \cdot K_\kappa = L\frac{di}{dt} + R \cdot i + K_n \frac{dz}{dt} \tag{9}$$

$$M_c = 26{,}41 - 3{,}17 \cdot \left(\frac{p_{n1} - 9 \cdot 10^6}{7 \cdot 10^6}\right) - 9{,}86 \cdot \left(\frac{Q_{n1} - 0{,}67 \cdot 10^{-3}}{0{,}5 \cdot 10^{-3}}\right). \tag{10}$$

In the mathematical model the following designations are adopted:
Q_{n1} – flow rate of the pump *1*; M_c – moment of resistance on the pump faceplate; μ – coefficient of flow through throttling and spool elements; p – density of the working fluid; β – fluid compression ratio, d_7 – diameter of the pump piston; d_8 – diameter of the circle of pump pistons contact with the faceplate; b_k – the number of pistons in the pump; n – rotational speed of the pump shaft; f_4, f_2 – port areas of

the throttling directional control valves; W_n, W_c, W_p, W_0 – volumes of hydraulic lines; m_c, m_3, m_p – masses of piston *33*, spools *36* and *37*; C_p, C_3 – strengths of the springs; Z_p, H_3 – pre-compession of the springs; b_y, b_c, b_3, b_p – damping coefficients of the pump faceplate, plunger of the pump faceplate control, spools *36* and *37*; N – hydraulic cylinder load value; k_2 – gain factor of the working port of the pump regulator; F_{c1}, F_{p1} – areas of the pump *33*; F_4, F_5 – areas of the pump control plungers; J – inertia moment of the pump faceplate; T_C, T_3, T_p – friction forces of piston *33*, spools *36* and *37*; f_3, f_p, f_5 – areas of the spools *36* and *37*; z, y – positional coordinates of spools *36* and *37*; V – motion speed of spool *33*; p_{n1}, p_{c1}, p_{p1}, p_0 – values of pressure in hydraulic lines; γ – rotation angle of the pump *2* faceplate; K_k – transfer coefficient of the controller; L – inductive resistance of the solenoid wire; R – active resistance of the solenoid wire; K_n – coefficient of the counteraction to the electromotive force; K_m – solenoid gain factor; D_1 – diameter of the backpressure valve; α – inclination angle of the backpressure valve seat.

Investigations were performed with the following initial values of the hydraulic drive state variables: $z(0)$ = 0,1·10-3 m, $y(0)$ = 4·10-3 m, $V(0)$ = 0; $p_{n1}(0)$ = 17·105 H/m^2; $p_{p1}(0)$ = 1·105 H/m^2; $p_0(0)$ = 17·105 H/m^2; $\gamma(0)$ = 0,03 rad; $p_{k1}(0)$ = 4·105 H/m^2; i = 0,01 mA.

Main parameters of the hydraulic drive have the following values: μ = 0,6; ρ = 900 kg/m^3; β = 10-10 m^2/H; W_{n1} = 3·10-3 m^3; W_{p1} = 2·10-3 m^3; W_0 = 0,05·10-3 m^3; m_c = 1600 kg; m_3 = 0,05 kg; m_p = 0,02 kg; C_p = 1·104 H/m; C_3 = 1·104 H/m; Z_p = 6·10-3 m; H_3 = 48·10-3 m; b_c = 3000 H·s/m; F_{p1} = 30·10-4 m^2; F_4 = 4,2·10-4 m^2; F_5 = 2·10-4 m^2; J = 0,2 kg·m^2; T_c = 350 H; T_3 = 8 H; T_p = 3 H; f_3 = 3,2·10-4 m^2; f_p = 3,2·10-4 m^2.

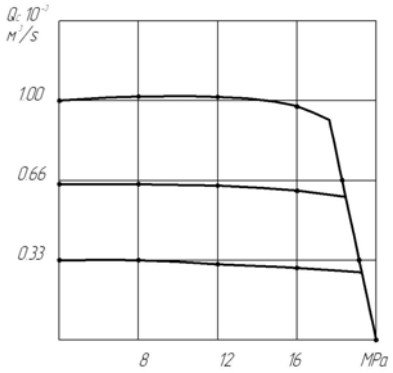

Fig. 2 – The dependences of the flow rate supplied to the input of hydraulic cylinder on pressure pp1.

Nonlinear equations of the mathematical model were solved using Simulink module of the MATLAB software package. In the process of calculation values of the variables were found that describe the hydraulic drive state when counter load or tail load at the hydraulic cylinder were changed (Черных, 2003).

Fig. 2 presents the dependences of the flow rate supplied to the input of hydraulic cylinder *33* on pressure pp1 in the piston chamber of this hydraulic

cylinder. In the pressure range $p_{p1} = (0,1…1,0)p_{max}$ stabilization of the flow rate Q_{n1} is ensured under counter load at the hydraulic cylinder. Adjustment of the flow rate Q_c to the hydraulic cylinder was changed in the range of $Q_c = (0,1…1,0)Qmax$ stabilization error of the flow rate value did not exceed 8% in the entire range of p_{p1} and Q_{n1} variations. Under counter load conditions independence of the flow rate value Q_{n1} from the load is also observed in all ranges of the flow rate and load variations. Stabilization error of Q_{n1} did not exceed 12%. Maximal values of the flow rate and pressure were $Q_{max} = 1,33 \cdot 10\text{-}6$ m^3/s, $P_{max} = 20\ M_{Pa}$. During hydraulic motor operation maximal stabilization error was 13,2% in the same range of moments and flow rate variation.

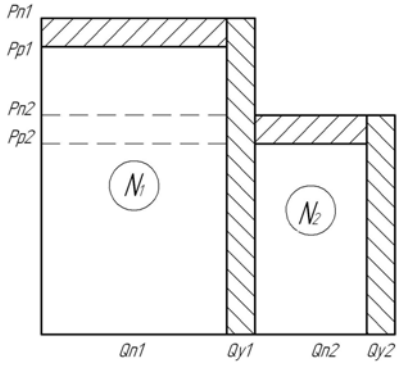

Fig. 3 – Shows the diagram of power distribution in a two-flow drive during simultaneous operation of two hydraulic engines.

Fig. 3 shows the diagram of power distribution in a two-flow drive during simultaneous operation of two hydraulic engines. In the process of each hydraulic engine operation the pump output pressure constantly exceeds the pressure at the hydraulic engine input - $\Delta p = (0,9...1,0)\ M_{Pa}$, determined by the setting of the controller. Flow rate losses in the pump control system did not exceed the value $Q_c \leq 0,062Q_{max}$. As the value of the useful power consumed by the hydraulic engine is reduced, the share of losses is somewhat increased and hydraulic efficient decreases. In the variation ranges of $p_{p1} = (0,1…1,0)p_{max}$ and $Q_{n1} = (0,1…1,0)Q_{max}$ the range of hydraulic efficiency varies from 41% to 89%. Higher values of efficiency correspond to the increased values of flow rate Q_{n1} and pressure p_{p1}.

3. Conclusion

1. Mechatronic drive provides simultaneous motion of any two hydraulic engines, which creates the possibility to achieve higher productivity of the manipulator operation.

2. The drive creates the possibility to stabilize the motion speed of the hydraulic engines, which makes it possible to improve the conditions of the operator's work while he is guiding the manipulator towards the object.

3. Unproductive power losses in the drive are minimized by the usage of pressure pickups, a controller and regulated pumps with electromagnetic control in the control system.

REFERENCES

Pedersen P., Munzer Marc E., *Strategies for Stabilization of Flow Control System with Counter Balance Valves* // Proceedings of 2001 Drives and Controls and Power Electronics Conference, Session 7: Fluid Power. – London, 32-39 (2001).

Andersen Torben O, *Hansen Michael R. Evaluation pf Velocity Control Concepts Involving Counter Balance Valves in Mobile Cranes* // Conference of Fluid Power Transmission and Control. – Hangzhou (China), 2001.

Song Liu, Bin Yao., *Energy-Saving Control of Single-Rod Hydraulic Cylinders with Programmable Valves and Improved Working Mode Selection* //National Fluid Power Association and Society of Automobile Engineers, NCFP J02-2.4 / SAE OH 2002-01-1343-P.81-91.

Козлов Л.Г. Вдосконалення системи керування гідроприводів з LC-регулюванням [Текст]: дис. на здобуття наук. ступ. канд. наук: 26.04.2000 / Козлов Леонід Геннадійович. – Вінниця, 2000 – 320 с.

Черных И.В. Simulink: среда создания инженерных приложений / И.В. Черных. – М.: Диалог, 2003. – 236 с.

ECONOMISIREA ENERGIEI LA UN MANIPULATOR MECATRONIC

(Rezumat)

Lucrarea prezintă un circuit cu două fluxuri pentru manipulatoare care pot fi utilizate în industrie, transport şi construcţie. Circuitul este compus din pompe hidraulice cu regulatoare, supape de control direcţional, senzori de presiune şi poziţie, şi un controler programabil. Circuitul este prevăzut cu conexiune automată a pompei la două motoare hidraulice operate simultan. La schimbarea direcţiei şi valorii sarcinii la motoarele hidraulice este asigurată stabilitatea vitezei presetate a mişcării actuatorului. Prezenţa supapelor de control direcţionale face posibilă ajustarea rapidă a valorii presetate a vitezei. A fost alcătuit un model matematic non-linear pentru manipulator. Ecuaţia modelului matematic a fost rezolvată folosind pachetul de programe Matlab. Relaţia dintre valorile debitului către motorul hidraulic şi presiunea de intrare este calculată. Eroarea stabilizării presiunii în plaja de valori 0,1 - 1,0 nu depăşeşte 8% în sarcină şi 13,2 în condiţii normale. S-a determinat că pierderile de presiune la sistemul de control nu depăşesc 0.062 din debitul maxim al pompei. Eficienţa hidraulică variază în intervalul de la 41% la 89%. Cu creşterea valorii puterii utile consumate de motorul hidraulic eficienţa hidraulică creşte.

BULETINUL INSTITUTULUI POLITEHNIC DIN IAŞI
Publicat de
Universitatea Tehnică „Gheorghe Asachi” din Iaşi
Tomul LVII (LXI), Fasc. 4, 2011
Secţia
ŞTIINŢA ŞI INGINERIA MATERIALELOR

DYNAMIC CHARACTERISTICS OF THE HYDRAULIC DRIVE WITH PROPORTIONAL FLOW RATE CONTROL

BY

L. KOZLOV*, S. LOZOVSKIY, V. KOVALCHUK and V. TSIMBAL

Vinnitsa National Technical University

Received: April 27, 2011
Accepted for publication: June 27, 2011

Abstract. The paper presents research results on the influence of a regulator design parameters on the dynamic characteristics and stability of the hydraulic drive operation. Hydraulic drives with proportional control of the working fluid flow rate are used in manipulators that operate in wide ranges of speeds of the actuators motion. Operation modes of such hydraulic drives are characterized by frequent switching on and switching off the directional control valves, variable values of motion speed and load at the actuators. These circumstances, taking into account hydraulic drive automatic response to the changes of flow to working organs and changing loads at the hydraulic engines, determine the necessity of dynamic behavior investigation.

Key words: hydraulic drive, non-linear mathematical model, proportional control.

1. Introduction

Fig. 1 shows a hydraulic drive circuit developed in Vinnytsia National Technical University. The circuit includes pump *1*, throttles *1* and *3*, hydraulic

* Corresponding author e-mail: vadikkov@ukr.net

cylinder *4*, hydraulic motor *5*, regulators *6* and *7*, spools *8* and *9* with springs *14* and *15*, hydraulic lines *10-13*.

The presented hydraulic drive circuit operates in the following way. Flow rate Q_p from pump *1* is supplied to pressure hydraulic line *10* and is divided into two parts (Q_1 and Q_2) proportional to areas f_1 and f_2 of throttles *2* and *3*. Flow rate Q_1 trough the working port F_3 of regulator 6 flows to hydraulic cylinder 4 and determines speed V_1 of its piston motion.

At the input of hydraulic cylinder *4* and hydraulic motor *5* pressures p_c and p_m are established proportional to the load T_R and moment M_R.

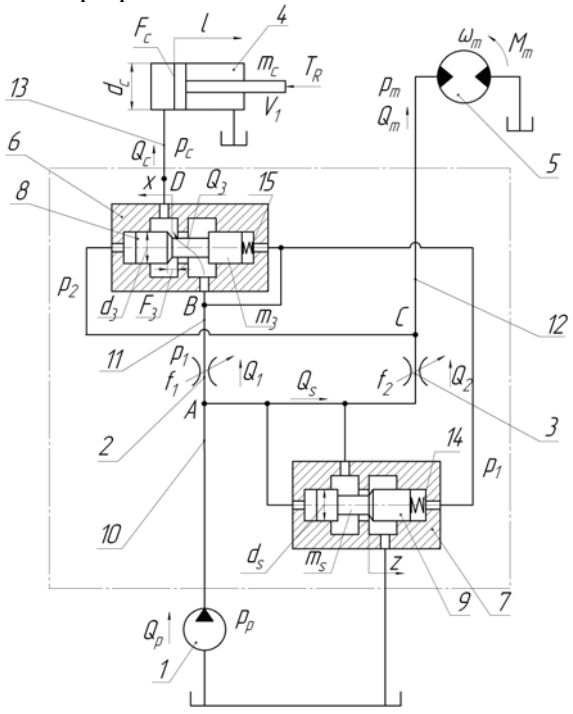

Fig. 1 – The hydraulic drive design circuit.

At the same time working fluid with pressure p_1 flows to regulator *7*, the spool of which is also under the action of working fluid pressure p_2 that is supplied from pump *1*, spool *8* of the regulator *6* and spool *9* of the regulator *7* that stay under the influence of pressures p_1, p_2, p_p and spring *13* and *14* correspondingly will maintain pressure drops $\Delta p_{thr.1} = p_p - p_1$ and $\Delta p_{thr.2} = p_p - p_2$, which do not depend on the values of load T_R and moment M_R and, correspondingly, flow rate values $Q_1 = Q_c$ and $Q_2 = Q_m$ that are supplied to hydraulic cylinder *4* and hydraulic motor 5 will not depend on the

values of load T_R and moment M_R. By changing the values of areas f_1 and f_2 of throttles *2* and *3* the values of flow rates Q_1 and Q_2 could be proportionally changed. In the case when $Q_1 + Q_2 = Q_p$ the regulator closes and the entire flow rate Q_p of pump *1* will be supplied into pressure line *10* and further trough throttles *2*, *3* and regulator *6* – to hydraulic cylinder *4* and hydraulic motor *5*. The orifice F_3 of regulator *6*, through which the less loaded hydraulic cylinder *4* is fed, will be partially closed. So such conditions are created under which flow rates Q_1 and Q_2 flowing to hydraulic cylinder *4* and hydraulic motor *5* depend only on the values f_1 and f_2 of the areas of throttles *2* and *3*.

The main advantage of such hydraulic drive consists in providing control and maintenance of constant load-independent values of the working fluid flow to hydraulic engines through the usage of regulators *6* and *7*. As a result, simultaneous motion of the actuators, supplied from one pump, is provided.

Dynamic characteristics of the hydraulic drive can be determined using a mathematical model.

The mathematical model of the hydraulic drive comprises flow continuity equations for points *A*, *B*, *C* and *D* as well as the equation of forces acting on spools *8*, *9* and a piston of hydraulic cylinder *4* and the equation of moments acting on the shaft of hydraulic motor *5*.

The mathematical model equations are composed with the following assumptions: the temperature of working fluid is constant; wave processes are not taken into account; operation modes are non-cavitational; working fluid leakage in the slots of the pump, hydraulic cylinder and regulators are ignored (Абрамов, *et al.,* 1977; Свешников & Усов, 1982).

Mathematical model in the form of Cauchy is given by:

$$b_S \frac{dz}{dt} = p_p \cdot \frac{\pi \cdot d_S^2}{4} - p_1 \cdot \frac{\pi \cdot d_S^2}{4} - C_S(H_S + z) - T_S \cdot sign\frac{dz}{dt}, \tag{1}$$

$$b_3 \frac{dx}{dt} = p_1 \cdot \frac{\pi \cdot d_3^2}{4} - p_2 \cdot \frac{\pi \cdot d_3^2}{4} + C_3(H_3 - x) - T_3 \cdot sign\frac{dx}{dt}, \tag{2}$$

$$m_C \frac{d^2 l}{dt^2} = p_C \cdot F_C - b_C \frac{dl}{dt} - T_R - T_C \cdot sign\frac{dl}{dt}, \tag{3}$$

$$J_m \frac{d\omega_m}{dt} = \frac{p_m \cdot q_m}{2\pi} - M_R - b_m \omega_m - M_{fr} \cdot sign\ \omega_m, \tag{4}$$

$$Q_p = \mu \cdot \pi \cdot d_S \cdot \sin\delta \cdot \sqrt{\frac{2p_p}{\rho}} + \mu \cdot f_1 \cdot \sqrt{\frac{2 \cdot |p_p - p_1|}{\rho}} \cdot sign(p_p - p_1) + \\ + \mu \cdot f_2 \cdot \sqrt{\frac{2 \cdot |p_p - p_2|}{\rho}} \cdot sign(p_p - p_2) + W_A \cdot \beta \frac{dp_p}{dt} \quad (5)$$

$$\mu \cdot f_1 \cdot \sqrt{\frac{2 \cdot |p_p - p_1|}{\rho}} \cdot sign(p_p - p_1) = \mu \cdot \pi \cdot d_3 \cdot \sin\alpha_3 \cdot \sqrt{\frac{2 \cdot |p_1 - p_C|}{\rho}} \times \\ \times sign(p_1 - p_C) + W_B \cdot \beta \frac{dp_1}{dt} \quad (6)$$

$$\mu \cdot f_2 \cdot \sqrt{\frac{2 \cdot |p_p - p_2|}{\rho}} \cdot sign(p_p - p_2) = W_C \cdot \beta \frac{dp_2}{dt} + q_m \cdot \omega_m , \quad (7)$$

$$\mu \cdot \pi \cdot d_3 \cdot \sin\alpha_3 \cdot \sqrt{\frac{2 \cdot |p_p - p_C|}{\rho}} \cdot sign(p_p - p_C) = \frac{dl}{dt} \cdot F_C + W_D \cdot \beta \frac{dp_C}{dt} \quad (8)$$

where Q_p – pump flow rate value, Q_1 – value of the flow rate through throttle *2*, Q_2 – value of the flow rate through throttle *3*, Q_3 – value of the flow rate through regulator *6*, p_p – pressure in the pump line, p_c – pressure in hydraulic cylinder *4*, p_m – pressure at the input of hydraulic motor *5*, p_1 – pressure at the output of throttle *2*, p_2 – pressure at the output of throttle *3*, W_A, W_B, W_C, W_D – volume of the working fluid in hydraulic lines *10*, *11*, *12* and *13*, d_s – diameter of the spool of regulator *7*, d_3 – diameter of the spool of regulator *6*, m_c – mass of the piston of hydraulic cylinder *4*, F_c – area of the piston-free chamber of hydraulic cylinder *4*, f_1 – opening area of the working port of throttle *3*, F_3 – opening area of the working port of regulator *6*, z – motion coordinate of regulator *7* spool, x – motion coordinate of regulator *6* spool, l – motion coordinate of the piston of hydraulic cylinder *4*, ρ – working fluid density, μ – flow rate coefficient, C_s – strength of the spring of regulator *7*, C_3 – strength of the spring of regulator *6*, δ – inclination angle of the working edge of spool *9*, α_3 – inclination angle of the working edge of spool *8*; β – coefficient that takes into account total deformation of the gas-liquid mixture and steel-rubber sleeves, H_s – initial compression of spring *14*, H_3 – initial compression of spring *15*, T_R – load at the rod of hydraulic cylinder *4*, M_R – loading moment at the shaft of hydraulic motor *5*, b_s – viscous damping coefficient of the spool of regulator *7*, b_3 – viscous damping coefficient of the spool of regulator *6*, b_c – viscous damping coefficient of rod of hydraulic cylinder *4*, b_m – viscous damping coefficient of the shaft of hydraulic motor *5*, q_m – working volume of hydraulic motor *5*, ω_m – angle velocity of hydraulic motor *5*, J_m – inertia

moment of hydraulic motor *5*, T_s, T_3, T_c – dry friction forces acting on the spool of regulator *7*, the spool of regulator 6 and on the rod of hydraulic cylinder *4*, M_{fr} – moment of the contact friction forces of hydraulic motor *5*.

Mathematical model equations are solved under the following initial conditions: $p_p(0) = 28 \cdot 10^5$ N/m^2; $p_1(0) = 12 \cdot 10^5$ N/m^2; $p_2(0) = 10 \cdot 10^5$ N/m^2; $p_c(0) = 10 \cdot 10^5$ N/m^2; $x(0) = 0.3 \cdot 10^{-3}$ m; $z(0) = 0$ m; $l(0) = 0$ m.

Values of the main design parameters of the hydraulic drive: $Q_p = 2 \cdot 10^{-3}$ m^3/s; $d_3 = 20 \cdot 10^{-3}$ m; $d_S = 27 \cdot 10^{-3}$ m; $d_c = 50 \cdot 10^{-3}$ m; $C_S = 30 \cdot 10^{-3}$ N/m; $C_3 = 30 \cdot 10^2$ N/m; $H_3 = 15 \cdot 10^{-3}$ m; $H_S = 19 \cdot 10^{-3}$ m; $f_1 = 15 \cdot 10^{-6}$ m^2; $m_C = 50$ kg; $\rho = 900$ kg/m^3; $\beta = 10^{-9}$ m^2/N; $\omega = 62.8$ s^{-1}; $q_M = 65 \cdot 10^{-6}$ m^3; $T_R = 500$ kN; $M_R = 50$ kNm.

Transient process was simulated by instantaneous change of the value of f_1 – opening area of the working port of throttle *2*.

Mathematical model processing was performed using MATLAB Simulink software package. Simulink is an interactive tool for modeling, simulation and analysis of dynamic systems, an application of MATLAB package, fully integrated with it (Черных, 2003). In the process of the mathematical model processing the dependence of the hydraulic drive state variables is determined. Principal block-diagram of the equation set solution is shown in Fig. 2.

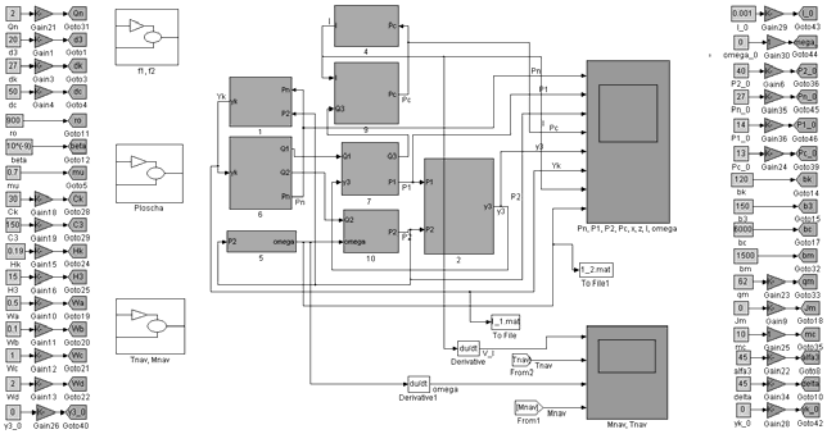

Fig. 2 – Block-diagram of the equation set solution.

The dependencies of the hydraulic drive state variables have been found that enable its stability evaluation for steady-state mode and make it possible to determine the dynamic characteristics (Бурєнніков *et al.,* 2005).

The variation ranges of the design parameters were as follows: the nominal flow of the hydraulic pump *Qp* = 0.8…2.5·10-3 m3/s, diameter of the spool of regulator *7 dS* = 10...30·10-3 m, the working edge inclination angle of the spool of regulator *7* δ = 30…90º.

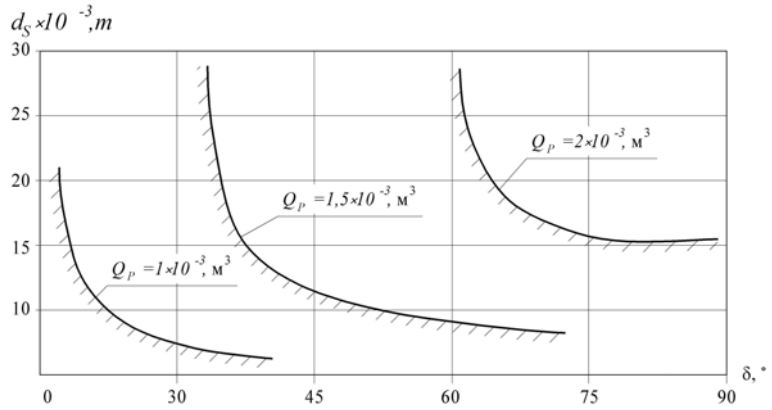

Fig. 3 – Hydraulic drive stability limits.

Fig. 3 presents the dependence of the hydraulic drive stability limit on the values of *dS* and δ that characterize the hydraulic system operation modes.

Analyzing location of the stability limit, a conclusion could be drawn that the worst conditions of the hydraulic drive operation are those that emerge under maximal value of the spool diameter ds of the regulator *7* and maximal value of the spool edge inclination angle δ. As it is shown in Fig. 4, the best zone of the hydraulic drive stable operation is provided by the pump with nominal flow *Qp* = 2.0⊙10-3 m3/c. Fig 4 shows the influence of the flow rate of hydraulic pump *1* and parameters ds and δ of regulator *7* on the transient process time, along the abscissa axis the values of non-dimensional parameters A_0/A_{max} are plotted, where A_0 – current value of the parameters, A_{max} – maximal value of the parameters.

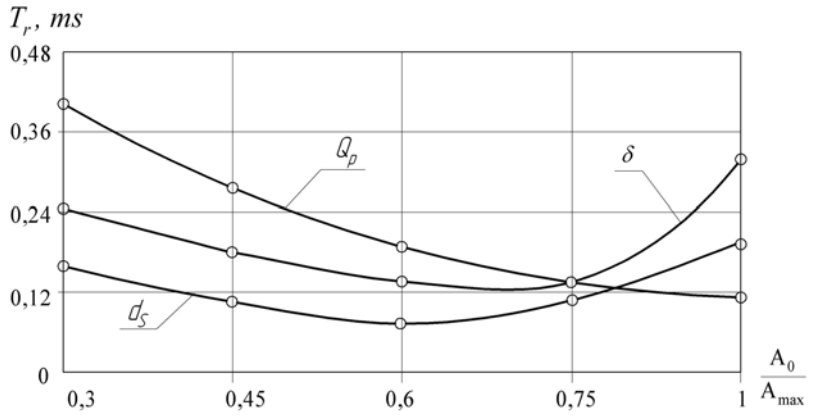

Fig. 4 –The influence of the hydraulic drive parameters on the transient process time.

The calculated dependences make it possible to draw conclusions about the influence of the design parameters of regulator *7* on the hydraulic drive dynamic characteristics. Increase of the spool diameter of regulator *7* to ds=0.6dmax leads to the regulation time reduction, and then the value of the transient process time is gradually increased. The increase of the spool inclination angle in regulator *7* from δ=0.3δ_{max} to δ=0.75δ_{max} causes reduction of the transient process time, while increase of the inclination angle from δ=0.7δ_{max} to δ=1.0δ_{max} leads to sharp increase of the transient process value. If the nominal flow *Qp* of the hydraulic pump is increased, the transient process time is reduced.

Proceeding from the analysis of the obtained dependences, at the design stage of regulator *7* it could be recommended to choose the following values of the design parameters for the hydraulic drive with load-independent flow distribution: the value of the hydraulic drive flow Qp = (0.75...1.0) *Qp max*, the inclination angle of the spool edge for regulator 7 δ = 0.75δmax, diameter value for the spool of regulator *7 ds*=(0.5…0.65)*dmax.*

2. Conclusion

The developed hydraulic drive circuit provides proportional control and maintenance of the constant load-independent values of the working fluid flows to hydraulic engines trough the usage of regulators.

Analysis of the influence of the regulator *7* design parameters (diameter of the spool *ds*, inclination angle of the spool edge δ) and the value of the hydraulic pump flow *Qp* on the transient process time has made it possible to determine design parameters of regulator 7 (*ds*=18…23⊙10-3m, δ=75°) and flow rate of hydraulic pump *1* (*Qp* = 2.0⊙10-3 m^3/s) that ensure stable hydraulic drive operation and regulation time not exceeding 0.5 s.

REFERENCES

[1]. Beitrag E., *Load-Sensing Steuerung: Anwendungen und Ausbaustufen.* Der Konstrukteur, *5*, 60-64 (1988).

[2]. Козлов Л.Г., *Вдосконалення систем керування гідроприводів з LS-регулюванням.* Дис. … канд. техн. наук: 05.02.03. – Вінниця, 2000.

[3]. Буренников Ю.А., Козлов Л.Г. *Пропорциональный распределитель для гидросистемы, чувствительной к нагрузке.* Весник НТУУ „КПИ": Машиностроение, Київ, Вып. **42**, *Т.2*, 37–39 (2002).

[4]. Принципы L.S., *LUDV в гидросистемах открытого контура.* В.А. Бондар, Ред. журн. – Суммы,–. Рус. – Деп. в ГНТБ Украины 16.02.95; Ук95, *362*, 5 (2003).

[5]. HE Qing-hua, HAO Peng, ZHANG Da-qing, *Modeling and Parameter Estimation for Hydraulic System of Excavator's Arm.* J. Cent. South Univ. Technol – China, *15*, 382-386 (2008).
[6]. Абрамов Е.И., Колесниченко К.А., Маслов В.Т., *Элементы гидропривода (Справочник).* Киев, «Техніка», 320 (1977).
[7]. Свешников В.К., Усов А.А., *Станочные гидроприводы: Справочник*. М.: Машиностроение, 464с (1982).
[8]. Черных И.В. , *Simulink: среда создания инженерных приложений*. Диалог-МИФИ, 2003.
[9]. Бурєнніков Ю.А., Козлов Л.Г., Лозінський Д.О., *Оптимізація системи управління гідророзподільником з електрогідравлічним регулюванням*. Вісник ВПІ, *6*, 225–229 (2005).

CARACTERISTICILE DINAMICE ALE ACŢIONĂRILOR HIDRAULICE CU REGULATOR DE DEBIT PROPORŢIONAL

(Rezumat)

Lucrarea prezintă rezultatele cercetărilor experimentale a influenţei parametrilor de proiectare a regulatorului asupra caracteristicilor dinamice şi de stabilitate a funcţionării acţionării hidraulice. Acţionarea hidraulică cu controlul proporţional al regulatorului de debit este utilizată în manipulatoare ce operează într-o gamă largă de viteze, la funcţionarea elementelor de acţionare. Modul de operare a acestor transmisii hidraulice sunt caracterizate prin frecventa pornire şi oprire a supapelor de control direcţional, viteze şi sarcini variabile de mişcare. În aceste circumstanţe, luând în calcul răspunsul automat al acţionării hidraulice la schimbarea de debit şi a sarcinii asupra motoarelor hidraulice, determină necesitatea de investigare a comportamentului dinamic.

BULETINUL INSTITUTULUI POLITEHNIC DIN IAŞI
Publicat de
Universitatea Tehnică „Gheorghe Asachi" din Iaşi
Tomul LVII (LXI), Fasc. 4, 2011
Secţia
ŞTIINŢA ŞI INGINERIA MATERIALELOR

PREVENTIVE MAINTENANCE - HIGH SECURITY FOR WORKERS

BY

DRAGOŞ – ALIN LĂPUŞNEANU*

"Gheorghe Asachi" Technical University of Iaşi

Received: April 15, 2011

Abstract. This paper concerns the impact of preventive maintenance work on safety and health for electronic computing equipment.

Key words: preventive maintenance, safety, health, computing equipment.

1. Introduction

1.1. General Things About Maintenance

Maintenance is a set of technical, administrative and management undertaken during the life cycle of equipment, for maintaining or restoring it to a condition that can meet the required function, protecting it against damage or defects.

Maintenance work include inspection, testing, replacing parts or subassemblies; adjustment, repair, fault detection, technical assistance.

There are two main types of maintenance:

- Preventive maintenance (proactive) - performed to ensure operational status of equipment, usually it is planned and scheduled in accordance with the manufacturer's instructions;

* Corresponding author e-mail: dragosh8@yahoo.com

- Corrective maintenance (reactive) - repair of equipment for its re-use; an unscheduled duty, unplanned, usually associated, risks and dangers greater than preventive maintenance.

1.2. The Necessity of Performing Maintenance

Since 1989, they adopted a series of European directives which establish the general requirements for the protection of workers. These directives apply to maintenance activities. First, among these is the Framework Directive which requires employers to conduct a risk assessment in the workplace.

Moreover, employers have a moral obligation to protect the safety and health of the personnel in every aspect of business. Employers should not be limited to legal compliance, but should show by example a real commitment to safety and health.

From a financial standpoint, a misunderstanding of maintenance activities is extremely costly, and may involve loss of income, fines, costs associated with judicial processes, reduced productivity and loss of business reputation. Maintenance, from the safety point of view, is the interest of employers. Proper management of occupational health and safety is good business, being a characteristic of effective organizations. In the case of maintenance, there is a link between the appropriate management of safe and healthy work and quality assurance procedures. A properly maintained equipment will produce products of superior quality.

2. Applicable law

2.1. Directives

- Directive 89/391/EEC (Framework Directive), establishes general principles for the protection of workers against occupational accidents and diseases.
- Directive 89/654/EEC laying down minimum requirements for workplace safety.
- Directive 89/655/EEC lays down minimum safety and health in the use of work equipment.
- Directive 89/656/EEC lays down minimum safety and health in the use of personal protective equipment at work.
- Directive 92/57/EEC concerning minimum safety and health requirements at temporary or mobile worksites.
- Directive 98/24/EC concerning the protection of workers from risks related to chemical agents.

- Directive 83/477/EEC concerns the protection of workers from risks related to exposure to asbestos.
- Directive 2006/42/EC provides essential health and safety requirements for the design and construction machinery (Annex I, "Essential health and safety of design and construction machinery).

2.2. Reference Documents

- ISO 9001:2001 Quality management systems. Requirements.
- ISO 14001:2005, Environmental management systems. Requirements with guidance for use.
- Specification OHSAS 18001:1999 - Occupational health and safety management systems - Specification (security management systems and health - Specification).

3. Repairs and Transportation Equipment

3.1. Definitions and Acronyms

Maintenance work - preparation, testing and maintaining the cleanliness of equipment during use.

Remedial work - checking operations and / or adjusting various parts of the equipment without replacing the parts or components.

Repair work - operations, with a high degree of complexity, involving and replacement of components or subassemblies.

3.2. Planning

Maintenance should start with proper planning. Employers should conduct a risk assessment in relation to maintenance activities that they are proposing, and should involve employees in this process.

Among the issues they should consider:

- the scope of the task - what to do and how they have affected other workers and other workplace activities;
- appropriate risk assessment: the potential hazards must be identified and measures should be developed to eliminate or minimize the risks associated;
- elements of business processes: the people involved, roles and responsibilities of each, the equipment they will use personal protective equipment required;
- time and resources involved in the activities;
- communication between staff responsible for carrying out maintenance and staff responsible for all other parties concerned.

3.3. Training Workers

Formation of the maintenance workers involved in a task (and those who work around them) is a very important aspect of planning phase. Competence of persons performing maintenance, including inspection and verification is vital to ensure safety and, although most workers are involved in some aspects of maintenance, accidents may occur if workers try to perform tasks when you do not have competence or experience. Employers must ensure that workers have the necessary skills required for these tasks, are informed of procedures for working safely and know what to do if their capabilities are exceeded in a given situation.

Employers should carefully consider the "ladder of persons" engaged in maintenance work and any procedures that will be used during the activity, including reporting procedures if a problem arises. Continuous consultation and informing workers are vital throughout the planning phase. Employees who perform maintenance work should not only be informed of the results of the initial assessment of risk, but also involved in its making. Due to the knowledge of the workplace, they are often in the best position to identify hazards and most effective ways to deal with them. Employee participation in the planning procedure enhances not only safety for our maintenance activity, but also its quality.

3.4. Responsibilities

Head of Commercial - Approves annual maintenance program for computer equipment and ensures the establishment of consumption electronic components, parts and manual labor. Ensures preparation of estimates and work schedules.

Chief of Diagnostics - Completes Notes Minutes finding and fact-finding and maintenance work planning, ensures the electronic computing equipment, and develops annual maintenance program and its aims to achieve the deadlines.

Head of Maintenance Center - Participates in equipment authorization and persons covered by the technical requirements of ISCIR, coordinates maintenance activities, ensures the supply of components, parts and materials required maintenance works, using the necessary Minutes and Bills, Notes and Minutes of finding the revisions. Answers for the collection of components, subassemblies and materials for maintenance work, resulting from maintenance activities and teaches them to stop collecting.

Answers for organizing and carrying out safe maintenance work for the persons that he leads, and he is also responsible for the application of security and health regulations at the workplace.

3.5. The Purchase of Equipment

Procurement procedures should be adopted to ensure that the necessary tools and personal protective equipment (together with the necessary training and retention of the equipment) are available for the safe execution of maintenance. It may be necessary to provide appropriate personal protective equipment (*e.g.,* respiratory protection is used when cleaning the filters).

During the acquisition of new equipment for carrying out maintenance, it must be taken into account the ease of reaching them to carry out maintenance work: risks during maintenance work can be minimized or even eliminated through proper design work equipment, availability of relevant tools and information from the supplier or manufacturer.

3.6. Assuring Work Zone Safety

At this stage, the procedures developed in the planning phase must be implemented. Work area should be secure (restrict access to employees that are not allowed in the work zone, for example, using barriers and signs). Also, the area must be kept clean and safe, mobile equipment components should be blocked, temporary ventilation systems should be installed, safe access routes should be established for entry and exit of workers from the work area. Warning plates should be placed on every equipment, and these plates should include the date and time freezes, and the name of the person authorized to remove the lock - in this way, the safety of the worker who is performing the maintenance of the equipment will not be jeopardized by another worker who would accidentally put the equipment in operation mode. If possible, protection should be provided in order to carry out minor maintenance work of electronic computing equipment without removing the safety devices. If the safety devices must be removed or disabled, the procedures for restricting access will be applied. Operators and workers responsible for maintenance activities are being trained on how and under what conditions the safety devices can be removed.

3.7. Mode of Work

On the basis of electronic computing equipment list is drawn up annual maintenance program (maintenance, repair and servicing).

For planning, the current directives/regulations are used, which should be in accordance with the manufacturer's instructions.

In the case of planned maintenance of electronic computing equipment the following work should be performed:

- clean the natural ways that the air circulates from inside to the outside of the computer;

- clean power source (grease the cooler's gears);
- check CPU's cooling system which consists of the radiator and cooler (fan), cleansing and replacing it where necessary, ensuring silicone heat transfer paste between the processor and heatsink;
- remove dust from cooler;
- remove and clean the dust from RAM memory;
- cleaned with special substances the reading / writing mechanism of optical equipment;
- clean the monitor, keyboard and mouse;
- check (visually) the physical integrity of ports;

In the case of repairing electronic computing equipment the following work should be performed:

- identifying and replacing defective components with similar components;
- before starting to work within central units and LCD monitors or LED type, these must be grounded and the work equipment that is used must be antistatic to avoid the appearance electrostatic voltages that can affect various parts of the computer;
- replacement of components is done according to their attachment system on the CPU cover, by unscrewing the screw fasteners or fastening components, extracting the defect components and assemble the good ones;
- when working on CRT monitors the first to do is to discharge the capacitors from the power supply and the CRT tube to prevent accidental electrocution by touching;
- after the interventions, verifications must be made to ensure that all components are properly positioned and secured;
- verify that the equipment operates at nominal parameters.

3.8. Verifications

Maintenance process must be completed with checks to ensure that the task has been completed, the status of the equipment or the mode of transportation subject to maintenance is safe and that all waste materials arised during the maintenance process have been eliminated. After everything has been checked and declared safe, the task can be terminated, and supervisors and other workers notified. The last step is compiling a report outlining the work and comment on any difficulties encountered, together with recommendations for improvement. Ideally, this should be discussed at a meeting of staff involved in the process, where workers and those working around them can make comments on the maintenance activity and can come up with appropriate suggestions for improvement process.

4. Conclusion

- "Health and safety above all", and maintenance helps maintain this motto.
- A proper maintenance programme will save time, money and a lot of headache for any employer.
- The best way to plan maintenance activities is with the workers who deal first hand with the equipment.

Maintenance should be made by authorized workers and with proper equipment.

REFERENCES

[1]. ∗∗∗ *Legea securităţii şi sănătăţi în muncă*. *319*, 2006.
[2]. ∗∗∗ http://osha.europa.eu/topics/maintenance
[3]. ∗∗∗ http://inspectiamuncii.ro.

MENTENANŢA PREVENTIVĂ - SECURITATE RIDICATĂ A LUCRĂTORILOR

(Rezumat)

Lucrarea se referă la impactul lucrărilor de mentenanţă preventivă asupra securităţii şi sănătăţii în muncă în cazul echipamentelor de calcul electronic.

BULETINUL INSTITUTULUI POLITEHNIC DIN IAŞI
Publicat de
Universitatea Tehnică „Gheorghe Asachi" din Iaşi
Tomul LVII (LXI), Fasc. 4, 2011
Secţia
ŞTIINŢA ŞI INGINERIA MATERIALELOR

CONSIDERATION REGARDING Ti-Mo ALLOYS USED AS BIOMATERIALS IN ORTHOPEDIC IMPLANTS

BY

ANDREEA MAGHERU*, BRÂNDUŞA GHIBAN, NICOLAE GHIBAN and MIHAI MARIN

Politehnica University from Bucharest,
Faculty of Materials Science and Engineering

Received: April 14, 2011
Accepted for publication: June 27, 2011

Abstract. Titanium alloys are more often use as biomaterials because their excellent specific characteristics.

Therefore this paper focuses its attention mainly on titanium-molybdenum alloys used as biomaterials for medical applications especially for hip implants. The paper presents an overview of various aspects of titanium-molybdenum alloys that make this material an ideal choice for bio-applications.

Key words: biomaterials, biocompatibility, Ti-Mo alloys, orthopedic implants.

1. Generalities

Biomaterials are materials used for making devices that can interact with biological systems to coexist in the human body for a longer time with minimal failure. Williams (1981) defined biomaterials as "nonviable materials used in medical devices, intended to interact with the biological systems". Biomaterials are widely used in repair, replacement, or augmentation of diseased or damaged parts of the musculoskeletal system such as bones, joints and teeth. These devices when are placed inside the body like implants are intended to remain there for a

* Corresponding author e-mail: dianadumitru1986@yahoo.com

substantial period of time, and when are use like prosthesis they are permanently fixed in the body for long-term application until the end of lifetime (Kamachi *et al.*).

Another complementary definition essential for understanding the biomaterials science is the "biocompatibility''. The same Williams (1987) said that the biocompatibility is ''the ability of a material to perform with an appropriate host response in a specific application'' (Ratner, 2004).

Recently, alloys applied as biomaterials have been intensively studied with emphasis on their electrochemical behavior, surface properties and biocompatibility in implants. Materials of low elasticity modulus can better simulate a natural bone, so there is an interest in alloys of such characteristics in order to obtain new materials for implants.

Orthopedic implants have improved the quality of life for millions of people over the last century. Therefore the clinical objectives of the implants are to relieve pain and increase the ease of movement in the joint; the engineering objective is to provide minimal physiological stress to the remaining bone system so that the integrity and functionality of the bone and prosthetic materials will be maintain over a long service life. Thus, materials suitable for implantation are those that are well-tolerated by the body and can withstand cyclic loading in the aggressive environment of the body. The materials used in orthopedics are ceramics, polymers and metals and alloys (Kamachi *et al.*).

Titanium alloys are preferred for orthopedic applications due to their low elasticity modulus, excellent biocompatibility, corrosion resistance, appropriated mechanical properties (Satendra Kumar & Sankara Narayanan), high-strength/density ratios, strong adhesion to bone tissue (Kawahara, 1983), formability and no potential toxic elements in most cases (Oliveira & Guastaldi).

2. Titanium and Alloying Elements

Titanium exists in two allotropic forms. At low temperatures it has a closed packed hexagonal crystal structure (cph), which is commonly known as α, whereas above 883°C it has a body centered cubic structure (bcc) termed β. The α to β transformation temperature of pure titanium either increases or decreases based on the nature of the alloying elements.

The alloying elements such as (Al, O, N etc.) that tend to stabilize the α phase are called alpha stabilizers and the addition of these elements increase the beta transus temperature, while elements that stabilize β phase are known as beta stabilizers (V, Mo, Nb, Fe, Cr etc.) and addition of these elements depress the β transus temperature. Some of the elements that do not have marked effect on the stability of either of the phase but form solid solutions with titanium are termed as neutral elements (Zr and Sn). Alloys having only α stabilizers and consisting entirely of α phase are known as α alloys. Alloys containing 1–2% of β stabilizers and about 5–10% of β phase are termed as near α alloys. Alloys containing higher

amounts of β stabilizers which results in 10–30% of β phase in the microstructure are known as α+β alloys. Alloys with still higher β stabilizers where β phase can be retained by fast cooling are known as metastable β alloys. These alloys decompose to α+β on aging. Most of the biomedical titanium alloys belong to α+β or metastable β class. In all conventional titanium alloys, α to β transus temperature (known as β transus) plays a central role in evolution of microstructure and is of great technological importance in determining heat treatment and processing schedule. The alloys processed/heat treated above the β transus temperature result in acicular or lamellar structure and are typically known as β treated structure. When these alloys are mechanically processed below the β transus (α+β phase field) and heat treated in α+β phase region, the microstructure consists of a mixture of equiaxed α and β phases. Depending upon the alloy chemistry, heat treatment temperatures and cooling rate, volume fraction of equiaxed α and nature of β phases may change. In faster cooled structure, transformed β phase may constitute martensite or α lath along with the retained β, while on slow cooling the transformed β phase may entirely be retained β. In metastable β alloys, the β phase is usually retained on quenching from the β phase field and very fines α precipitates on aging at lower temperatures, which leads to extremely high strength in these alloys (Geetha *et al.*). In Fig. 1 is given the influence of the thermomechanical processing on the development of various microstructures in alpha- beta titanium alloys.

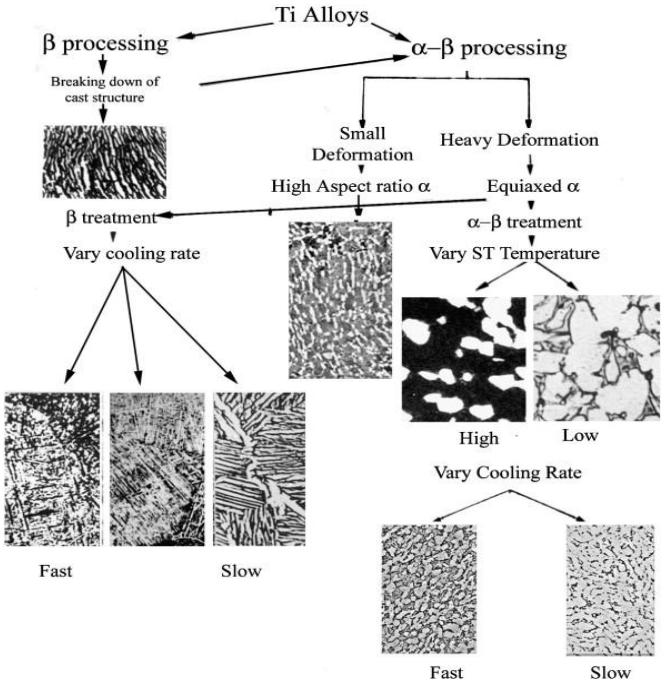

Fig. 1 – The influence of the thermomechanical processing on the development of various microstructure in alpha- beta titanium alloys.

In the mid of 1980s, the $\alpha+\beta$ phase of Ti–6Al–4V was commonly regarded as an ideal material for medical implants due to its appropriate mechanical properties and corrosion resistance. However, more recent research has revealed that Ti–6Al–4V debris contains Vanadium, which is harmful to human health (Woei-Shyan Lee *et al.*) and the leaching of V and Al exceeds a threshold level may cause peripheral neuropathy, osteomalacia and Alzheimer diseases. (Rao *et al.,* 1996; Walker *et al.,* 1990; Yumoto *et al.,* 1992) and can lead to mechanical failure of the device (Wen-Fu Ho *et al.*). The toxicity of vanadium and can be also aggravated when an implant is fractured and subsequently undergoes fretting. Release of titanium ions into the tissues adjacent to the implants results in discoloration of the tissues. This may also be detrimental to the bone attachment and further bone growth on the implant surface (Kamachi *et al.*).

To improve the mechanical properties or corrosion resistance of pure metals or alloys, new alloys are being developed through the addition of different elements to a given metal. For instance, when Nb, Ta, Zr, Mo, Sn are added to titanium its corrosion resistance is improved (Oliveira & Guastaldi).

A new material was developed with these characteristics, which are appropriate on the human body. Ti with different concentration of molybdenum was analyzed by many authors in their attempt to make it an ideal choice of material for bio-applications. Therefore they study the morphology, the various surface modification techniques, the mechanical properties, the electrochemical behavior, the corrosion resistance and the biocompatibility of this new biomaterial in hope that will discover a better one for orthopedic implants.

3. Development of Ti-Mo Alloys for Medical Applications

Ho et al. observe the new α″ phase Ti–7.5Mo alloy with a lower elastic modulus that had been developed for biomedical applications. This Ti–7.5Mo alloy also exhibits an even better strength/modulus combination and excellent corrosion resistance. Titanium alloys doesn't bond directly to living bone (Yan & Davies, 1998; Nishiguchi *et al.,* 1999) and therefore the (Wen-Fu Ho *et al.*) study the bioactive coatings on commercially pure titanium (c.p. Ti) and Ti–7.5Mo.

C.p. Ti and Ti–7.5Mo were initially immersed in a 5, 10 or 15M NaOH solution at 60°C for 24 h, resulting in the formation of a porous network structure composed of sodium titanate ($Na_2Ti_5O_{11}$). The X-ray diffraction (XRD) results indicated that the intensity of the sodium titanate peak increased with an increasing NaOH concentration.

The specimens were then immersed in simulated body fluid (SBF) at 37°C for 3, 7 and respectively 28 days. It is known that an essential requirement for an artificial material to bond to living bone is the formation of a bonelike apatite layer on its surface in the body environment (Kokubo, 1991) and

(Hench, 1991). The apatite-forming ability of alkali-treated Ti–7.5Mo was higher than that of alkali-treated c.p. Ti on exposure to 5, 10 or 15M NaOH aqueous solutions. The XRD results also indicated that the deposited amounts of calcium phosphate were much greater for alkali-treated Ti–7.5Mo than for alkali-treated c.p. Ti. The average thickness of calcium phosphate layer of 15M NaOH-treated Ti–7.5Mo after immersion in SBF for 28 days was about 15 μm.

The alkali treatment of Ti–7.5Mo by NaOH aqueous solutions can be anticipated to be promising artificial bone substitutes or other hard tissue replacement materials for heavy load-bearing applications due to their wonderful combination of bioactivity, low elastic modulus and low processing costs.

The same material (Ti–7.5Mo) also was used by the Escada et.al. in (Escada *et al.*) and their purpose was to modify the surface but this time by a different method (biomimetic). The work was to evaluate the growth of calcium phosphates at the surface of the experimental alloy Ti–7.5Mo. These ingots was treated at 1100°C for one hour, cooled the samples in water, and cold-worked the cooled material by swaging and machining. After that the samples was prepared with a specific roughness (Ra) of (1.3 and 2.6 μm) and cut discs with (13 mm in diameter and 4 mm in thickness) from each group. The samples were treated by biomimetic methods for 7 or 14 days to form an apatite coating on the surface. The samples treated in a 5.0-M NaOH aqueous solution at 80°C for three days and heat-treated at 600°C for 1 h could form apatite after soaking in SBF. Therefore, alkaline and heat treatments are effective pre-treatment methods for apatite formation on Ti–7.5Mo alloys. Regarding the different surface roughness values (Ronold *et al.,* 2003), we obtained the best results for samples with a roughness of Ra=2.6 μm subjected to an alkaline treatment (NaOH) and a heat treatment (600°C), with subsequent immersion in SBF for seven days. These samples exhibited a greater growth of apatite, resulting in the formation of a continuous film. The samples also exhibited an increased wettability. Therefore, in this study we can conclude that increasing the roughness of the substrate allowed decreasing the time of formation of apatite from fourteen to seven days (Escada *et al.*).

Lin D.J et al. introduce into the metallic matrix of titanium different contents of iron. Experimental results indicated that α″ phase-dominated binary Ti–7.5Mo alloy (Ho *et al.,* 1999) exhibited a fine, acicular martensitic structure. When 1 wt% or more iron was added, the entire alloy became equi-axed β phase structure with a grain size decreasing with increasing iron content (Lin *et al.,* 1999). The thermal ω phase was formed in the alloys containing iron of roughly between 0.5 and 3 wt% (Sikka *et al.,* 1982; Bur' ík & Weatherly 1999). A largest quantity of ω phase and highest microhardness were found in Ti–7.5Mo–1Fe alloy (Collings *et al.,* 1972). The binary Ti–7.5Mo alloy had a lower microhardness, bending strength and modulus than all iron-containing alloys. The alloys with iron contents closer to 1 wt% exhibited the highest

microhardness level. Despite the strong hardening effect of ω phase, the bending strength of Ti–7.5Mo–1Fe alloy was relatively low due to its premature, brittle fracture. The highest bending strength was found in Ti–7.5Mo–2Fe alloy (Lin *et al.*). They said that the present alloys with iron contents of about 2–5 wt% seem to have a great potential to be use as an implant material.

For structure and properties of a series of binary Ti–Mo alloys with molybdenum contents ranging from 6 to 20 wt% have been investigated in (Ho *et al.*). Experimental results indicated that crystal structure and morphology of the cast alloy were sensitive to their molybdenum contents. The hexagonal α′ phase c.p. Ti (Bania, 1993) exhibited a feather-like morphology. When Mo content was 6 wt%, a fine, acicular martensitic structure of orthorhombic α″ phase was observed. But when Mo content was 7.5 wt%, the entire alloy was dominated by the martensitic α″ structure. When Mo content was increased to 10 wt% or higher, the retained β phase became the only dominant phase (Bagariaskii *et al.,* 1959; Davis & Flower 1979). Among all Ti–Mo alloys, the α″ phase Ti–7.5Mo alloy had the lowest hardness. The bending strength of Ti–7.5Mo was similar to that of Ti–15Mo and Ti–13Nb–13Zr, and higher than c.p. Ti by nearly 60%. The bending modulus of the α″-dominated Ti–7.5Mo alloy was lower than that of Ti–15Mo by 22%, of Ti–6Al–4V by 47%, of Ti–13Nb–13Zr by 17%, and of c.p. Ti by 40%.

The (Gordin *et al*.) have synthesized a new alloy that combines Ti with the non-toxic elements like Ta and Mo. The alloy was annealed at 950°C for one hour under high vacuum and quenched in water at room temperature. The alloy was characterized by X-ray diffraction, observed by microscopy and found to have a body-centered-cubic structure (β-type). Measuring the Young's modulus of Ti-12Mo-5Ta by ultrasonic technique it was observed a lower value (about 74 GPa) than the classical α+β Ti-6Al-4V alloy (120 GPa), which is much better in order to use it as hip prostheses and to avoid stress shielding and thus prevent bone reabsorbtion (Schutz, 1993). As long-term stability in biological environment is required, they evaluated the electrochemical behavior of both alloys. Experiments, i.e. measurements of open-circuit potential (OCP) versus time and the observation of linear and cyclic potentiodynamic polarization curves, were carried out in simulated body fluid (Ringer's solution) for two immersion times. Under these conditions both titanium alloys exhibit spontaneous passivity and high corrosion resistance (Schenk, 2001). The excellent electrochemical properties combined with low elastic modulus make the new beta-type Ti-12Mo-5Ta alloy suitable for use as a bone substitute.

Satendra Kumar *et. al.* study the corrosion behavior of Ti–15Mo alloy in Ringer's solution evaluated by potentiodynamic polarization, cyclic polarization and chronoamperometric/current–time transient (CTT) studies. The corrosion protective ability of Ti–15Mo alloy was compared with that of commercially pure (CP) titanium (grade-2) and Ti–6Al–4V alloy under similar

experimental conditions. The study reveals that Ti–15Mo alloy (Nag *et al.,* 2005) possesses a β-phase microstructure and moderate hardness. The open circuit potential of Ti–15Mo alloys is relatively nobler than CP–Ti and Ti–6Al–4V alloy. The average passive current density of all the three Ti materials studied lies in the range of 32×10^{-6} A/cm^2. The passivation range of Ti–15Mo alloy is relatively large when compared to that of Ti–6Al–4V alloy and CP–Ti. The loop area of the cyclic polarization curve of Ti–15Mo alloy is quite similar to that of Ti–6Al–4V alloy but relatively smaller than that of CP–Ti. There is no appreciable variation in the steady state current density of all the three Ti materials measured at +0.5 V vs. SCE whereas a significant variation is observed at +1.25 V vs. SCE (Kumar Satendra & Sankara). The β-phase structure, moderate hardness and the ability to offer a better corrosion resistance in Ringer's solution make the Ti–15Mo alloy an excellent alternative candidate material for orthopedic implant applications.

Electrochemical behavior of pure Ti and Ti–Mo alloys (6–20 wt.% Mo) was investigated as a function of immersion time in electrolyte simulating physiological media by (Oliveira & Guastaldi). Open-circuit potential values indicated that all Ti–Mo alloys studied and pure Ti undergo spontaneous passivation due to spontaneously formed oxide film passivating the metallic surface, in the chloride-containing solution. It also indicated that the addition of Mo to pure Ti up to 15 wt.% seems to improve the protection characteristics of its spontaneous oxides. Electrochemical impedance spectroscopy (EIS) (Shukla & Balasubramaniam, 2006) studies showed high impedance values for all samples, increasing with immersion time, indicating an improvement in corrosion resistance of the spontaneous oxide film (Oliveira *et al.,* 2007).

The fit obtained suggests a single passive film present on the metals' surface, improving their resistance with immersion time, presenting the highest values to Ti–15Mo alloy (Oliveira & Guastaldi, 2008). Potentiodynamic polarization showed a typical valve-metal behavior, with anodic formation of barrier-type oxide films, without pitting corrosion, even in chloride-containing solution. In all cases, the passive current values were quite small, and decrease after 360 h of immersion. All these electrochemical results suggest that the Ti–15Mo alloy is a promising material for orthopedic devices, since electrochemical stability is directly associated with biocompatibility and is a necessary condition for applying a material as biomaterial.

Electrochemical investigation on the as-cast Ti–Mo alloys (4–20 Mo wt.%) applied as biomaterials in Na_2SO_4 and Ringer physiological solutions is reported in (Oliveira & Guastaldi). Analyses of the open-circuit potential indicated that all alloys present spontaneous passivation. SEM and cyclic voltammograms obtained in the Ringer solution showed that the samples studied do not present pitting corrosion at potentials up to 8 V (SCE), indicating high corrosion resistance (Oliveira *et al.,* 2005). Open-circuit potential profiles of the anodic oxides growth in both solutions show that the presence of chloride

ions during the anodization does not influence the oxides' chemical stability, and also clearly indicate that adding Mo to pure Ti improves the stability of the anodic oxides. All these results suggest Ti–Mo alloys promissory to be applied as biomaterials, mostly in the orthopedic field.

4. Conclusion

The new develop material Ti-Mo alloys is the ideal choice for medical application, specially in orthopedic field because can be anticipated to be promising artificial bone substitutes or other hard tissue replacement materials for heavy load-bearing applications due to their wonderful combination of bioactivity, corrosion resistance, low elastic modulus and low processing costs.

Acknowledgements. The work has been funded by the Sectoral Operational Programme Human Resources Development 2007-2013 of the Romanian Ministry of Labour, Family and Social Protection through the Financial Agreement POSDRU/88/1.5/S/60203.

REFERENCES

Bagariaskii I.A., Nosova G.I., Tagunova T.V., *Factors in the Formation of Metastable Phases in Titanium-Base Alloys.* Sov Phys Dokl (Engl Transl), 3 (1959).

Bania P.J., *Beta Titanium Alloys and Their Role in the Titanium Industry*. In: D Eylon, R Boyer and D Koss Editors, Beta Titanium Alloys in the 1990's TMS. Warrendale, PA (1993).

Bur' ík J., Weatherly G.C., *Transformation of the β-(Ti, V) Phase in Ti–V–C Alloys.* Scripta Mater. 40 (1999).

Collings E.W., Ho J.C., Jaffee R.I., *Superconducting Transition Temperature, Lattice Instability and Electron-To-Atom Ratio in Transition-Metal Binary Solid Solutions*. Phys. Rev. B. 5 (1972).

Davis R., Flower H.M., West D.R.F., *Martensitic Transformations in Ti–Mo Alloys.* J. Mater. Sci. 14 (1979).

Escada A.L.A., Rodrigues Jr. D., Machadoand J.P.B., Alves Claro A.P.R., *Surface Characterization of Ti–7.5Mo Alloy Modified by Biomimetic Method.*

Geetha M., Singh A.K., Asokamani R., Gogia A.K., Ti Based Biomaterials, the Ultimate Choice for Orthopaedic Implants–A Review.

Gordin D.M., Gloriant T., Nemtoi Gh., Chelariu R., Aelenei N., Guillou A., Ansel D., Synthesis, *Structure and Electrochemical Behavior of a Beta Ti-12Mo-5Ta Alloy as New Biomaterial.*

Hench L.L., *J. Am. Ceram. Soc.,* 74 (1991).

Ho W.F., Ju C.P., Chern lin J.H., *Structure and Properties of Cast Binary Ti–Mo Alloys.* Biomaterials, 20 (1999).

Ho W.F., Ju C.P., Chern Lin L.H., *Structure and Properties of Cast Binary Ti–Mo Alloys.*

Kamachi Mudali U., Sridhar T. M., Baldev RAJ- Corrosion of bio implants.

Kawahara H., *Cellular Responses to Implant Materials: Biological, Physical and Chemical Factors*. Int. Dent. J., *33,* 1983.

Kokubo T., *Biomaterials* 12 (1991).

Kumar Satendra, Sankara Narayanan T.S.N., *Electrochemical Characterization of β-Ti Alloy in Ringer's Solution for Implant Application.*

Lin D.J., Chern Lin J.H., Ju C.P., *Structure and Properties of Ti–7.5Mo–xFe Alloys.*

Lin D.J., Ju C.P., Chern lin J.H., *Structure and Properties of Cast Ti–Fe Alloys*. AFS Trans*,* 216 (1999).

Nag S., Banerjee R., Fraser H.L., Mater. Sci. Eng. C 25 (2005).

Nishiguchi S., Nakamura T., Kobayashi M., Kim H.M., Miyaji F., Kokubo T., *Biomaterials,* 20 (1999).

Oliveira N.T.C., Aleixo G., Caram R., Guastaldi A.C., *Electrochemical Behavior of Ti–Mo Alloys Applied as Biomaterials*. J. Mater. Sci. Eng. A, 452–453 (2007).

Oliveira N.T.C., Biaggio S.R., Rocha-Filho R.C., Bocchi N., J. Biomed. Mater. Res. A 74A (3) (2005).

Oliveira N.T.C., Guastaldi A.C., *Electrochemical Behavior of Ti–Mo Alloys Applied as Biomaterial*.

Oliveira N.T.C., Guastaldi A.C., *Electrochemical Behavior of Ti–Mo Alloys Applied as Biomaterial*. Corros. Sci. 50 (4) (2008).

Oliveira N.T.C., Guastaldi A.C., *Electrochemical Behavior of Ti–Mo Alloys Applied as Biomaterial*.

Oliveira N.T.C., Guastaldi A.C., *Electrochemical Stability and Corrosion Resistance of Ti–Mo Alloys for Biomedical Applications.*

Rao S., Ushida T., Tateishi T., Okazaki Y., Asao S., *Effect of Ti, Al, and V Ions on the Relative Growth Rate of Fibroblasts (L929) and Osteoblasts (MC3T3-E1) Cells*. Bio-Medical Materials Engineering, 6 (1996).

Ratner Buddy D., Hoffman Allan S., Schoen Frederick J., Lemons Jack E., *Biomaterials Science - An Introduction to Materials in Medicine* . 2nd Edition, 2004.

Ronold H.J., Lyngstadaas S.P., Ellingsen J.E., *Biomaterials,* 24 (2003).

Satendra Kumar, T.S.N. Sankara Narayanan, *Corrosion Behaviour of Ti–15Mo Alloy for Dental Implant Applications.*

Schenk R., *The Corrosion Properties of Titanium and Titanium Alloys*. In: D.M. Brunette, P. Tengvall, M. Textor and P. Thomsen, Editors, Titanium in Medicine, Springer, New York, 2001.

Schutz R.W. In: D. Eylon, R.R. Boyer, Koss D.A., *The Mineral, Metals & Materials Society*. Editors, Titanium Alloys in the 1990's, P.A., Warrendale (1993).

Shukla A.K., Balasubramaniam R., *Effect of Surface Treatment on Electrochemical Behavior of CP Ti, Ti–6Al–4V and Ti–13Nb–13Zr Alloys in Simulated Human Body Fluid*. Corros. Sci., 48 (2006).

Sikka S.K., Vohra Y.K., Chidambaram R., *Omega Phase in Material*. Progr Mater Sci. **27,** 1982.

Walker P.R., Leblanc J., Sikorska M., *Effects of Aluminium and Other Cations on the Structure of Brain and Liver Chromatin*. Biochemistry, 28 (1990).

Wen-Fu Ho, *A Comparison of Tensile Properties and Corrosion Behavior of Cast Ti–7.5Mo with c.p. Ti, Ti–15Mo and Ti–6Al–4V Alloys*.

Wen-Fu Ho, Chien-Hung Lai, Hsueh-Chuan Hsu, Shih-Ching Wu, *Surface Modification of a Low-Modulus Ti–7.5Mo Alloy Treated with Aqueous NaOH*.

Woei-Shyan Lee , Chi-Feng Lin, Tao-Hsing Chen, Hsin-Hwa Hwang - Effects of Strain Rate and Temperature on Mechanical Behaviour of Ti–15Mo–5Zr–3Al Alloy.

Yan W.Q., Davies J.E., *Bioceramics*,11 (1998).

Yumoto S., Ohashi H., Nagai H., Kakimi S., Ogawa Y., Iwata Y., *Aluminum Neurotoxicity in the Rat Brain*. International Journal of PIXE, 2 (1992).

ALIAJELE DE Ti-Mo FOLOSITE CA BIOMATERIALE ÎN IMPLANTURILE ORTOPEDICE

(Rezumat)

Aliajele de titan sunt folosite în special ca şi biomateriale datorită calităţilor specifice excelente.

Din această cauză această lucrare se axează pe aliajele titan-molibden folosite ca biomateriale pentru aplicaţii medicale, în special pentru implaturile de şold. Lucrarea prezintă o privire de ansamblu asupra diferitelor aspecte ale aliajelor de titan-molibden care fac ca aceste materiale să reprezinte alegerea ideală pentru bioaplicaţii.

BULETINUL INSTITUTULUI POLITEHNIC DIN IAŞI
Publicat de
Universitatea Tehnică „Gheorghe Asachi” din Iaşi
Tomul LVII (LXI), Fasc. 4, 2011
Secţia
ŞTIINŢA ŞI INGINERIA MATERIALELOR

NUMERICAL INVESTIGATION ON HEAT CONDUCTION IN SEMINFINITE WORK-PIECES IRRADIATED BY A MOVING HEAT SOURCE

BY

O. MANCA[1*], A. MINEA[2*], S. NARDINI[1], D. RICCI[1] and S. TAMBURRINO[1]

[1]Seconda Università degli studi di Napoli,Italia
[2] “Gheorghe Asachi” Technical University of Iaşi

Received: April 14, 2011
Accepted for publication: June 27, 2011

Abstract. Moving and stationary heat sources are frequently employed in many manufacturing processes and contact surfaces. In recent years applications of localized heat sources have been related to the development of laser and electron beams in material processing, such as welding, cutting, heat treatment of metals and manufacturing of electronic components. This is mainly due to the possibility to concentrate, with high accuracy, a large heat flux density over small localized areas and to the necessity to predict the way localized heat sources perform in the process. Typical parameters involved in the processes for any particular application should be evaluated, in order to optimize the material processing and forecast the behaviour of the solid. A three dimensional conductive field is analyzed and solved by means of the COMSOL Multiphysics code. The investigated work-pieces are irradiated by a laser source with Gaussian distributions; the heat source is considered moving with a constant velocity along motion direction. The solid dimension (x) along the motion direction is assumed to be semi-infinite as well as in the orthogonal direction z, while finite width (2ly) is considered. Thermal properties are considered temperature dependent and the materials are considered isotropic. Surface heat losses toward the

* Corresponding authors e-mail: oronzio.manca@unina2.it; aminea@tuiasi.ro

ambient are take into account. In fact, several convective heat transfer coefficients on the upper surface, with corresponding Biot numbers and Peclet numbers, are considered with negligible radiative heat losses. Results in terms of temperature profiles and thermal fields are given for some Peclet and Biot number values.

Key words: Heat Conduction, Moving Sources, Manufacturing.

1. Introduction

The use of new materials and innovative processes require the employment of lasers and electron beams, such as welding, cutting, heat treatment of metals and manufacturing of electronic components (Viskanta & Bergman, 1998; Kannatey-Asibu, 2009).

Problems, connected to aforementioned cases, can be solved by means of analytical and numerical models (Kannatey-Asibu, 2009). The analysis of thermal conductive and optical fields induced in the work-pieces as well as the control of the main process parameters is of paramount importance. Therefore, computational investigations are carried out in order to optimize the manufacturing process and predict the behaviour of the material. In some laser beam applications, such as surface heat treatments, the contribution of convective heat transfer by a gaseous impinging jet must also be taken into account (Shuja *et al.,* 1998). Quasi-steady state thermal fields induced by moving localized heat sources have been widely investigated (Shuja *et al.,* 1998) (Shuja *et al.,* 1998; Bianco & Manca, 2000; Bianco *et al.,* 200; Li *et al.,* 2004), as well as the analysis of temperature distribution in transient heat conduction has been carried out, as recently given in (Modest & Abakians, 1986; Bianco *et al.,* 2004; Rozzi *et al.,* 2000; Rozzi *et al.,* 2000; Hou & Komanduri, 2000 ; Yilbas *et al.,* 2003; Gutierrez & Araya, 2003; Bianco *et al.,* 2004). Modest and Abakians (1986) analyzed the one-dimensional unsteady temperature distribution in a moving semi-infinite solid subject to a pulsed Gaussian laser irradiation. A finite difference numerical solution to the three-dimensional transient heat conduction for a moving elliptical Gaussian heat source on a finite dimension solid was obtained in (Bianco *et al.,* 2004). They took into account the variation of thermo-physical properties. Rozzi *et al*. (2000, 2004) deepened the effect of rotation and translational speed, as well as the laser beam diameter and power on the thermal behaviour of the work-piece. They analyzed a laser assisted machining of a rotating silicon nitride work-piece heated by a translating CO_2 laser and material removing by a cutting tool. The Jaeger's heat source method to evaluate the transient and steady state analytical solutions for the temperature rise at any point in a solid due to both stationary and moving plane heat sources of different shapes was used in (Hou &

Komanduri, 2000). A numerical study for the transient heating of a titanium work-piece irradiated by a pulsed laser beam, with an impinging turbulent nitrogen jet was presented in (Yilbas *et al.,* 2003). A remarkable temperature rise in the solid was found in the onset of laser pulse. The numerical simulation of the temperature distribution generated by a moving laser heat source was carried out in (Gutierrez & Araya, 2003). Radiation and convection effects were accounted into. A numerical analysis of transient conduction in a solid irradiated by a moving Gaussian laser source was studied in (Bianco *et al.,* 2004) where radiation and convection effects were considered. In some cases a parametric analysis of the problem allows to employ two-dimensional models in thermal field evaluations inside the irradiated solids (Leung, 2001; Couëdel *et al.,* 2003). An analytical solution for a quasi-steady phase-change heat transfer problem in a plate heated by a moving Gaussian rectangular heat sources was developed in (Leung, 2001). The heat source moved at a constant speed over the upper surface of the solid and the physical model was set up to simulate a laser transformation hardening process. A two-dimensional analytical solution using vibrated or non-vibrated Gaussian source models were presented in (Couëdel *et al.,* 2003). The proposed solutions were applied to an infinite longitudinal half-plane and to a limited width semi-infinite longitudinal half-plane. The sensitivity of the thermal fields to both the source size and the boundary was studied. In some cases the analysis of the problem allows to employ three-dimensional models in thermal fields evaluation inside solids irradiated (Bianco *et al.,* 2010; Minea *et al.,* 2010). A laser source with combined donut-Gaussian distributions was considered moving with a constant velocity. The solid dimension along the motion direction was assumed to be infinite or semi-infinite, while finite width and thickness were considered. Thermal properties were considered temperature dependent and surface heat losses toward the ambient were taken into account.

In this paper a numerical analysis of a transient three-dimensional thermal conductive field induced in a metallic finite solid by a Gaussian and donut moving laser beam is carried out using a finite volume numerical technique. Several convective heat flux values on the upper surface have been considered .This approach is suitable for a work-piece with a width much lower than the laser beam radius along the normal to the motion direction.

2. Mathematical Description and Numerical Model

The mathematical formulation for the proposed model is reported in this section. A brick-type solid irradiated by a moving heat source was considered. The solid dimension along the motion direction was assumed to be semi-infinite, while finite thickness and width were assumed. A three-dimensional model was

developed and convective heat losses were taken into account. The thermo-physical properties of the material were assumed to be temperature dependent, except the density. The transient conductive regime was considered. A sketch of the investigated configuration is reported in Fig. 1. If a coordinate system fixed to the heat source is chosen, according to the moving heat source theory (*Metals Handbook*, 1981), a mathematical statement of the three dimensional transient thermal conductive problem is:

$$\frac{\partial}{\partial x}\left(k(T)\frac{\partial T}{\partial x}\right)+\frac{\partial}{\partial y}\left(k(T)\frac{\partial T}{\partial y}\right)+\frac{\partial}{\partial z}\left(k(T)\frac{\partial T}{\partial z}\right)=\rho c\left(\frac{\partial T}{\partial \theta}-v\frac{\partial T}{\partial x}\right) \quad (1)$$

$$\text{for } 0 \le x,\ 0 \le |y| \le l_y/2,\ 0 \le z < +\infty,\ \theta > 0$$

The boundary and initial conditions are:

$$T(x \to +\infty, y, z, \theta) = T_{in} \quad (1\text{ a})$$

$$\text{for } 0 \le |y| \le l_y/2;\ 0 \le z < +\infty;\ \theta > 0$$

$$\frac{\partial T(x, 0, z, \theta)}{\partial y} = 0 \quad (1\text{ b})$$

$$\text{for } 0 \le x;\ 0 \le z < +\infty;\ \theta > 0$$

$$-k\frac{\partial T(x, \pm l_y/2, z, \theta)}{\partial y} = h_l(x, y, \theta) \times \left[T(x, \pm l_y/2, z, \theta) - T_f\right] \quad (1\text{ c})$$

$$\text{for } 0 \le x;\ 0 \le z < +\infty;\ \theta > 0$$

$$-k\frac{\partial T(x, y, 0, \theta)}{\partial z} = q(x, y) - h_u(x, y, \theta)\left[T(x, y, 0, \theta) - T_f\right] \quad (1\text{ d})$$

$$\text{for } 0 \le x;\ 0 \le |y| \le l_y/2;\ \theta > 0$$

$$T(x, y, z \to +\infty, \theta) = T_{in} \quad (1\text{ e})$$

$$\text{for } 0 \le x;\ 0 \le |y| \le l_y/2;\ \theta > 0$$

$$T(x, y, z, 0) = T_{in} \quad (1\text{ f})$$

$$\text{for } 0 \le x;\ 0 \le |y| \le l_y/2;\ 0 \le z < +\infty$$

where the absorbed heat flux q(x,y) is:

$$q = q_0 \left[exp\left(\frac{x^2 + y^2}{r^2_g} \right) \right] \tag{2}$$

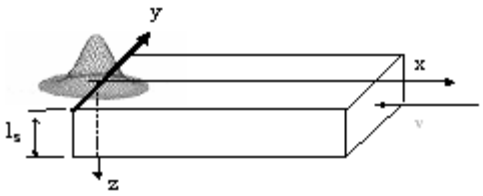

Fig. 1 – Sketch of the model.

Problems were solved by means of the COMSOL Multiphysics 3.5 code. Several different unstructured grid distributions were tested to ensure that the calculated results were grid independent. Maximum temperature differences of the fields were less than 0.1 percent by doubling the mesh nodes.

3. Results and Discussion

Results are presented in terms of temperature profiles of the work-piece surface, such as at y = z = 0, along the motion direction axis, x, at several times in order to analyze the transient behaviour. Two laser beam profiles were assumed: Gaussian, ζ=1. The spot radius r_g, and the width of the work-piece were equal to 0.0125 while the solid dimension (*x*) along the motion direction is assumed to be semi-infinite as well as in the orthogonal direction *z*. Furthermore, some convective heat transfer coefficient values on the upper surface were considered. They correspond to Biot numbers equal to 0.0, 0.025, 0.1 and 1.0 with the Biot number defined as $Bi=hL_y/\lambda$. Temperature dependent thermo-physical properties were taken from [19] for a 10-18 steel material: k = 53.7-0.03714(T-273.15) [W/(mK)], ρ=7806 [kg/m^3] and c_p = 500.0 + 0.40(T-273.15) [J/(kg K)]. The absorbed laser heat flux was set to 120 W/cm^2. The work-piece velocity is 2.0 10^{-4} and, consequently, the Peclet number is equal to 1.0. The ambient temperature is assumed to be 290 K.

Fig. 2 depicts the temperature profiles for a Gaussian laser beam profile. It clearly shows the thermal development along the work-piece upper surface. For Bi = 0.0 and r_g/s_{met} = 2, temperature increases as time increases, as reported in Fig. 2*a*. The quasi-steady state condition is achieved at about θ= 60s. The maximum surface temperature is detected close to x = 0 m (x > 0 m) and its values is 518 K. In Figs. 2*b* and 2*c*, it is observed, that the maximum surface temperature decreases increasing the thickness as well as the asymptotic

values and, consequently, the curve slopes increase at increasing of solid thickness. It is interesting to observe for $L_z \rightarrow \infty$ ($r_g/s_{met} \rightarrow \infty$) the maximum surface temperature is slightly lower than the one for configuration with the ratio r_g/s_{met} equal to 10, while the curve slope is the same of previous configuration.

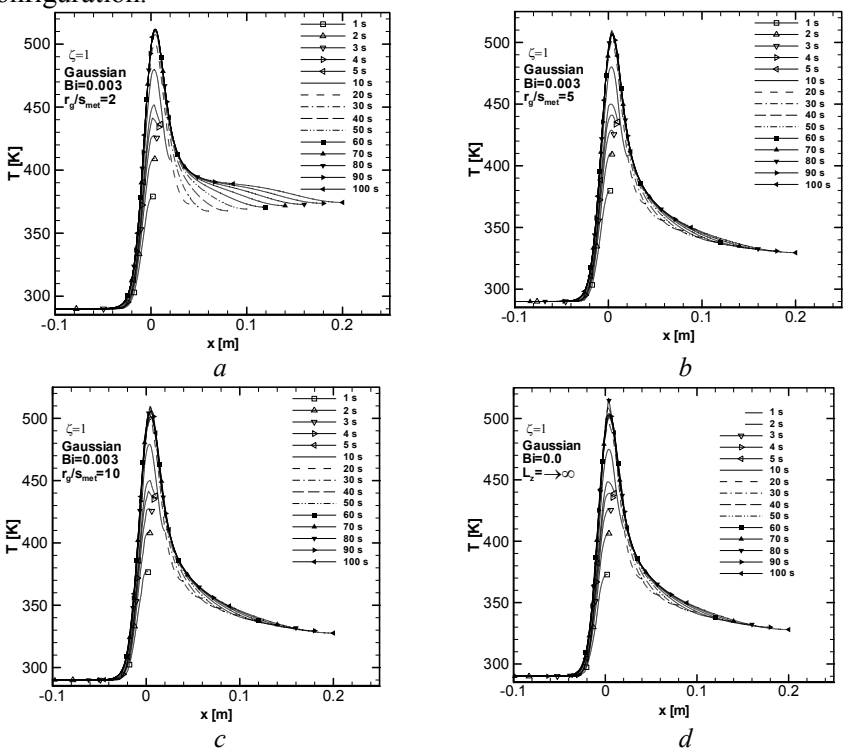

Fig. 2 – Temperature profiles for Gaussian distribution and Bi=0.0, *a*) r_g/s_{met}=2; *b*) r_g/s_{met}=5; *c*) r_g/s_{met}=10; *d*) $l_z \rightarrow +\infty$.

Fig. 3 show temperature profile for Biot number equal to 1.0. It is observed that the two configuration have the same behaviour, but for $L_z \rightarrow \infty$, the maximum surface temperature is slightly lower than the one for the configuration with the ratio r_g/s_{met} equal to 2. Moreover, the surface temperature, at large x values ($x > 0.18$), tends toward T_{in}.

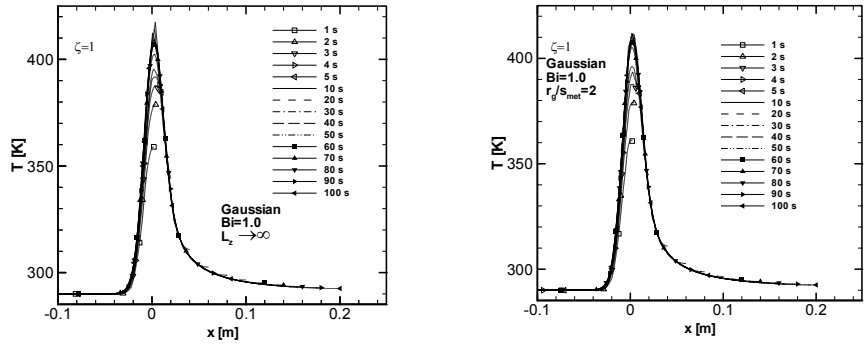

a *b*

Fig. 3 – Temperature profiles for Gaussian distribution for Bi=1.0; *a*) r_g/s_{met}=2, *b*) $l_z \rightarrow +\infty$.

In Fig. 4, it is observed that at the Biot number increasing the maximum surface temperature decreases whereas the curve slope increases and, after θ= 10 s, the edge temperature values decrease, as it is possible to detect in the downstream region at x value increasing. In Fig. 4*c* it is observed that the achieved temperature values decrease at increasing the Biot number, but the attained maximum temperature value is lower than the one in the previous analyzed configuration. Also, in this case, the slope of the curve increases as well as the Biot Number increase. Moreover, in Fig. 4 it is noted that the quasi steady state condition is reached at lower time value at increase the Bi value.

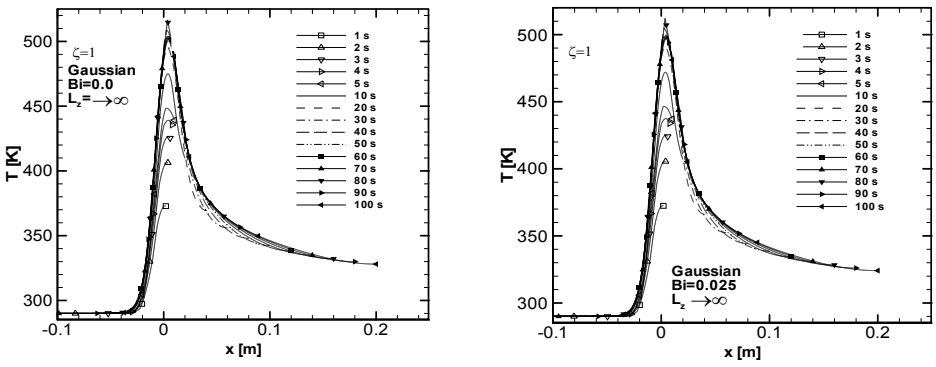

a *b*

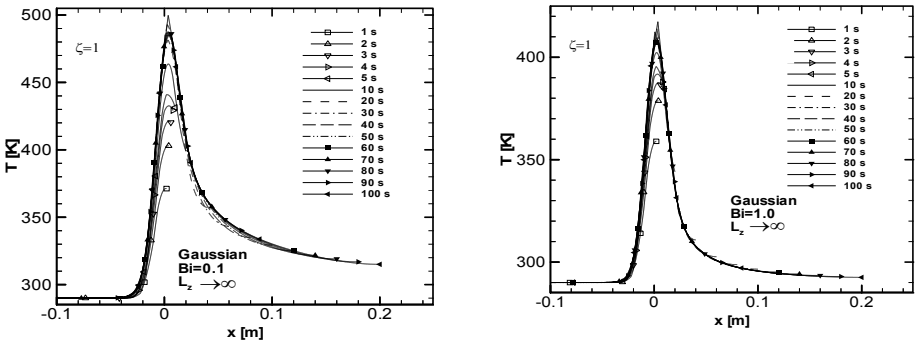

c *d*

Fig. 4 – Temperature profiles for Gaussian distribution; for $L_z \to +\infty$; *a*) Bi=0.0, *b*) Bi=0.025; *c*) Bi=0.1; *d*) Bi=1.0.

The surface temperature distributions (z=0 m) for different time values are shown in Fig. 5. The Biot number is equal to 0.1. At first considered instant, θ=1 s, the surface temperature presents the lowest maximum value respect to the other considered instants. It is noted the temperature increase up to θ=50 s, as detected by means of the differences among the hot spot on the surface at different times. After this value the hot spot presents a constant distribution and this indicates that the quasi-steady state is reached, according also with the surface temperature profiles reported in Fig. 4*c*.

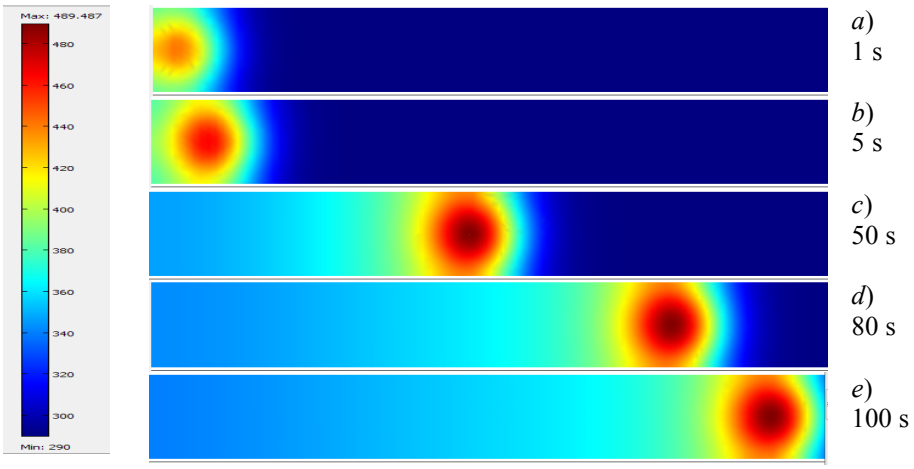

Fig. 5 – Temperature fields for Gaussian distribution and Bi=0.1, *a*) 1s, *b*) 5s, *c*) 50s, *d*) 80s; *e*) 100s.

4. Conclusion

The present numerical investigation allowed estimating three-dimensional transient heat conductive fields in semi-infinite metallic solids due

to a moving laser source, characterized by a Gaussian beam profile. The numerical analysis has been carried out by the means of the Comsol Multiphysics 3.5 code. The numerical model took into account convective heat losses whereas the radiative heat transfer was neglected. It was pointed out that surface temperature profiles decreased for increasing solid thicknesses and Biot number values while the constant slope of the temperature curves increased.

Nomenclature

c = specific heat (J kg^{-1} K^{-1})	Greek symbols
h = convective heat transfer coefficient (W m^{-2} K^{-1})	α = thermal diffusivity (m^2 s^{-1})
k = thermal conductivity (W m^{-1} K^{-1})	θ = time (s)
l = length (m)	ρ = density (kg m^{-3})
Pe = Peclet number ($vr_G/(2\square)$)	Subscripts
Bi = Bi=hL_y/λ	a = ambient
Q = absorbed heat flux (W m^{-2})	b = bottom surface
r = radius (m)	f = fluid
T = temperature (K)	G = Gaussian beam
v = velocity of the work-piece (m s^{-1})	in = initial for $x \rightarrow +\infty$
x,y,z Cartesian coordinates (m)	u = upper surface
	x,y,z = along axes

REFERENCES

* * * *Metals Handbook*, 9th Ed. ASM, Metal Park, OH, (1981).

Bianco N., Manca O., *A Parametric Study of the Quasi-Steady State Temperature Field by a Moving Heat Source for Surface Treating*. ASME HTD, **366-3**, 285-294 (2000).

Bianco N., Manca O., Nardini S., *Comparison Between Thermal Conductive Models for Moving Heat Sources in Material Processing*. ASME HTD, **369-6**, 11-22 (2001).

Bianco N., Manca O., Nardini S., Tamburrino S., *Effect of Solids Thickness on Transient Heat Conduction in Workpieces Irradiated by a Moving Heat Source*. Defect and Diffusion Forum, *297-301*, 1445-1450 (2010).

Bianco N., Manca O., Nardini S., *Two Dimensional Transient Analysis of Temperature Distribution in a Solid Irradiated by a Gaussian Laser Source*. Proceedings of ESDA04, paper n. ESDA2004-58286 7TH Biennial Conference on Engineering Systems Design and Analysis, July 19–22, 2004, Manchester, United Kingdom., 2004.

Bianco N., Manca O., Naso V., *Numerical Analysis of Transient Temperature Fields in Solids by a Moving Heat Source*. Proc. 3rd Int. Conf. Heat Transfer, Fluid Mechanics Thermodynamics, n. BN2, Cape Town, South Africa, 21–24 June 2004.

Couëdel D., Rogeon P., LemassonV, Carin M., Parpillon J. C., Bertet R., *2D-Heat Transfer Modelling Within Limited Regions Using Moving Sources:*

Application to Electron Bean Welding. Int. J. Heat Mass Transfer, **46**, 4553-4559 (2003).

Gutierrez G., Araya J.G., *Temperature Distribution in a Finite Solid Due to a Moving Laser Beam*. Proc. ASME - IMECE 2003, paper IMECE 2003-42545 (2003).

Hou Z.B., Komanduri R., *General Solutions for Stationary/moving Plane Heat Source Problems in Manufacturing and Tribology*. Int. J. Heat. Mass. Transfer, **43**, 1679-1698 (2000).

Kannatey-Asibu E. Jr., *Principles of Laser Materials Processing*. Wiley., 2009.

Leung M., *Phase-Change Heat Transfer in Laser Transformation Hardening by Moving Gaussian Rectangular heat Source*. J. Phys. D: Appl. Phys. **34**, 3434-3441 (2001).

Li J.F., Li L., Stott F.H., *Comparison of Volumetric and Surface Heating Sources in the Modeling of Laser Melting of Ceramic Materials*. Int. J. Heat Mass Transfer, **47**, 1159-1174 (2004).

Minea A.A., Manca O., Nardini S., Tamburrino S., *Transient Heat Conduction in Solids Irradiated by a Moving Heat Source with Combined Donut and Gaussian Distributions*. Internat. Review of Mechanical Egng., **4**, *2*, 123-127 (2010).

Modest M.F., Abakians H., *Heat Conduction in a Moving Semi-Infinite Solid Subjected to Pulsed Laser Beam*. J. Heat Transfer, **108**, 597-601 (1986)

Rozzi J.C., Incropera F.P., Shin Y.C., *Transient Three-Dimensional Heat Transfer Model for the Laser Assisted Machining of Silicon Nitride: II: Assessment of Parametric Effects*. Int. J. Heat. Mass. Transfer, **43**, 1425-1437 (2000).

Rozzi J.C., Pfefferkon F.E., Incropera F.P., Shin Y.C., *Transient, Three-Dimensional Heat Transfer Model for the Laser Assisted Machining of Silicon Nitride: I. Comparison of Predictions with Measured Surface Temperature Histories*. Int. J. Heat. Mass. Transfer, **43**, 1409-1424 (2000).

Shuja S.Z., Yilbas B.S., Budair M.O., *Modeling of Laser Heating of Solid Substance Including Assisting Gas Impingement*. Numeric. Heat Transfer, Part. A, **33**, 315-339 (1998).

Viskanta R., Bergman T. L., *Heat Transfer in Material Processing*, *in Handbook of Heat Transfer*. Chap. 18, McGraw-Hill., 1998.

Yilbas B.S., Shuja S.Z., Hashmi M.S.J., *A Numerical Solution for Laser Heating of Titanium and Nitrogen Diffusion in Solid*. J. Mat. Proc. Tech., **136**, 12-23 (2003).

ANALIZA NUMERICĂ A CONDUCŢIEI ÎN PIESE SEMIINFINITE IRADIATE DE O SURSĂ LASER ÎN MIŞCARE

(Rezumat)

Sursele de căldură staţionare sau în mişcare sunt folosite deseori în procesele de încălzire industriale ce implică încălziri superficiale sau în întreg volumul. În ultimii ani, sursele locale de căldură uzuale se referă la încălzirile cu laser pentru sudură, debitare, tratament termic şi realizarea componentelor electronice. Acest lucru se datorează, în principal, posibilităţilor de concentrare a fluxului termic într-un punct sau pe o suprafaţă foarte mică. În această lucrare s-au studiat parametrii specifici unui astfel

de proces utilizând simularea şi optimizarea cu ajutorul programului comercial CFD Comsol Multiphysics. Astfel, în lucrare s-a pornit de la un model 3D a câmpului conductiv pe suprafţa considerată de studiu şi s-a urmărit comportarea solidului la iradierea cu laser cu distribuţie Gaussiană. S-au realizat şi unele presupuneri: dimensiunea x a solidului în lungul direcţiei de mişcare este semi-infinită; la fel şi dimensiunea în planul z, în timp ce grosimea este considerată finită. Proprietăţile termice ale materialului sunt constante în toate direcţiile(material isotropic). Transferul termic prin radiaţie este neglijat, dar s-a ţinut cont de transferul de căldură către mediul exterior. Rezultatele au fost oferite ca profile de temperatură şi câmp termic pentru diferite valori ale numerelor lui Peclet şi Biot.

BULETINUL INSTITUTULUI POLITEHNIC DIN IAŞI
Publicat de
Universitatea Tehnică „Gheorghe Asachi" din Iaşi
Tomul LVII (LXI), Fasc. 4, 2011
Secţia
ŞTIINŢA ŞI INGINERIA MATERIALELOR

NUMERICAL ANALYSIS OF AN IMPINGING JET ON HEAT CONDUCTION IN WORK PIECES IRRADIATED BY MOVING HEAT SOURCE

BY

O. MANCA[1*], A. MINEA[2*], S. NARDINI[1], D. RICCI[1], S. TAMBURRINO[1]

[1] Seconda Università degli studi di Napoli,Italia,
[2] "Gheorghe Asachi" Technical University of Iaşi

Received: April 14, 2011
Accepted for publication: June 27, 2011

Abstract. A three-dimensional heat transfer model for laser material processing with a moving Gaussian and Donut heat source is developed using the commercial code Comsol Multhiphysics. Laser beam, having a defined power distribution, strikes the surface of an opaque substrate of semi-infinite length but finite width and depth moving with an uniform velocity in the positive x direction. A gas jet on the upper surface allows the enhancement of the convective heat transfer coefficient, as well used for shielding in welding and surface treatment. Quasi-steady state thermal fields induced by moving localized heat sources have been widely investigated whereas further attention seems to be devoted to the analysis of temperature distribution in transient heat conduction. The solid dimension along the motion direction is assumed to be infinite or semi-infinite, while finite width (2ly) and thickness (s) are considered. Thermal properties are considered temperature dependent and the materials are considered isotropic. Surface heat losses toward the ambient are taken into account. Several convective heat flux values on the upper surface, with corresponding Reynolds jet, and Peclet numbers are considered with negligible radiative heat losses. Results in terms of temperature profiles and thermal fields are given for some Reynolds jet number values. They are presented in terms of temperature profiles to evaluate the effect of solid thickness and surface heat transfer coefficient.

* Corresponding author e-mail: oronzio.manca@unina2.it; aminea@tuiasi.ro

Key words: Heat Conduction, Laser Source, Moving Sources.

1. Introduction

In recent years applications of moving localized heat sources have been related to the development of laser and electron beams in material processing, such as welding, cutting, heat treatment of metals and manufacturing of electronic components [1, 2]. This is mainly due to the possibility to concentrate, with high accuracy, a large heat flux density over small localized areas. In particular, many studies have been carried out to predict temperature fields in such processes. The aforementioned problems can be solved by means of analytical and numerical models [1, 2]. In each application the significant process parameters should be evaluated, in order to optimize the manufacturing process and to predict the behaviour of the material. In some laser beam applications, such as surface heat treatment, the contribution of convective heat transfer by a gaseous impinging jet must also be taken into account [3, 4].

Quasi-steady state thermal fields induced by moving localized heat sources have been widely investigated [3-7], whereas further attention seems to be devoted to the analysis of temperature distribution in transient heat conduction, as recently given in [8-15].

One of the first solution for a moving laser Gaussian heat source on a material was determined, analytically, in [16]. Modest and Abakians [17] analyzed the one-dimensional unsteady temperature distribution in a moving semi-infinite solid subject to a pulsed Gaussian laser irradiation. A finite difference numerical solution to the three-dimensional transient heat conduction for a moving elliptical Gaussian heat source on a finite dimension solid was obtained in [18]. They took into account the variation of thermophysical properties. The experimental validation of a transient three-dimensional numerical model of the process by which a rotating silicon nitride work-piece is heated with a translating CO_2 laser beam, without material removal was carried out in [8]. The effect of rotation and translational speed, as well as the laser beam diameter and power, on thermal conditions was analyzed by means of surface temperature history measurements. In another paper Rozzi et al. [9] used the afore-mentioned transient three-dimensional numerical model to elucidate the effect of operating parameters on thermal conditions within the work-piece and to assess the applicability of an approximate analysis. The above referred numerical and experimental investigation was extended to the transient three-dimensional heat transfer in a laser assisted machining of a rotating silicon nitride work-piece heated by a translating CO_2 laser and material removing by a cutting tool [10, 11]. The Jaeger's heat source method to

evaluate the transient and steady state analytical solutions for the temperature rise at any point in a solid due to both stationary and moving plane heat sources of different shapes was used in [12]. A numerical study for the transient heating of a titanium work-piece irradiated by a pulsed laser beam, with an impinging turbulent nitrogen jet was presented in [13]. The nitrogen diffusion coefficient into the solid substrate was also evaluated. A remarkable temperature rise in the solid was found in the onset of laser pulse. The numerical simulation of the temperature distribution generated by a moving laser heat source was carried out in [14]. Radiation and convection effects were accounted for. A numerical analysis of transient conduction in a solid irradiated by a moving Gaussian laser source was studied in [15]. In the numerical model radiation and convection from the work-piece surfaces were considered. In some cases parameters analysis of the problem allows to employ two-dimensional models in thermal fields evaluation inside solids irradiated by moving Gaussian thermal sources [20-22]. An analytical solution for a quasi-steady phase-change heat transfer problem in a plate heated by a moving Gaussian rectangular heat sources was developed in [20]. A temperature field in a thin moving sheet heated by a Gaussian laser beam was calculated in [21]. In the analysis, surface cooling in ambient was considered and the problem became two dimensional by averaging the temperature field over the sheet thickness. A two-dimensional analytical solutions using vibrated or non-vibrated Gaussian cylindrical or line source models were presented in [22]. The proposed solutions were applied to an infinite longitudinal half-plane and to a limited width semi-infinite longitudinal half-plane. In some cases the analysis of the problem allows to employ three-dimensional models in thermal fields evaluation inside solids irradiated by moving by combined donut and Gaussian thermal sources [28-29]. A laser source with combined donut-Gaussian distributions is considered moving with a constant velocity along motion direction. The solid dimension along the motion direction is assumed to be infinite or semi-infinite, while finite width and thickness are considered. Thermal properties are considered temperature dependent and the materials are considered isotropic. Surface heat losses toward the ambient are taken into account.

In this paper a numerical analysis of a transient three-dimensional thermal conductive field induced in a metallic finite solid by a Gaussian and donut moving laser beam is carried out using a finite volume numerical technique. This approach is suitable for a workpiece with a width lower than the laser beam radius along the normal to the motion direction.

2. Mathematical Description and Numerical Model

The mathematical formulation for the proposed model is reported in the following. A brick-type solid irradiated by a moving heat source is considered. The solid dimension along the motion direction is assumed to be semi-infinite,

while finite thickness and width are assumed. A 3-D model is presented, convective heat losses are taken into account. The thermophysical properties of the material are assumed to be temperature dependent, except the density. The transient conductive regime is considered.

A sketch of the investigated configuration is reported in Fig.1. If a coordinate system fixed to the heat source is chosen, according to the moving heat source theory [20], a mathematical statement of the three dimensional transient thermal conductive problem is:

$$\frac{\partial}{\partial x}\left(k(T)\frac{\partial T}{\partial x}\right)+\frac{\partial}{\partial y}\left(k(T)\frac{\partial T}{\partial y}\right)+\frac{\partial}{\partial z}\left(k(T)\frac{\partial T}{\partial z}\right)=\rho c\left(\frac{\partial T}{\partial \theta}-v\frac{\partial T}{\partial x}\right) \tag{1}$$

$$\text{for } 0\le x,\ 0\le |y|\le l_y/2,\ 0\le z\le l_z,\ \theta>0$$

The boundary and initial conditions are:

$$T(x\to+\infty, y, z, \theta)=T_{in} \tag{1 a}$$

$$\text{for } 0\le |y|\le l_y/2;\ 0\le z\le l_z;\ \theta>0$$

$$\frac{\partial T(x, 0, z, \theta)}{\partial y}=0 \tag{1 b}$$

$$\text{for } 0\le x;\ 0\le z\le l_z;\ \theta>0$$

$$-k\frac{\partial T(x, \pm l_y/2, z, \theta)}{\partial y}=h_l(x, y, \theta)\times\left[T(x, \pm l_y/2, z, \theta)-T_f\right] \tag{1 c}$$

$$\text{for } 0\le x;\ 0\le z\le l_z;\ \theta>0$$

$$-k\frac{\partial T(x, y, 0, \theta)}{\partial z}=q(x, y)-h_u(x, y, \theta)\left[T(x, y, 0, \theta)-T_f\right] \tag{1 d}$$

$$\text{for } 0\le x;\ 0\le |y|\le l_y/2;\ \theta>0$$

$$-k\frac{\partial T(x, y, l_z, \theta)}{\partial z}=h_b(x, y)\times\left[T(x, y, l_z, \theta)-T_f\right] \tag{1 e}$$

$$\text{for } 0\le x;\ 0\le |y|\le l_y/2;\ \theta>0$$

$$T(x, y, z, 0)=T_{in} \tag{1 f}$$

$$\text{for } 0\le x;\ 0\le |y|\le l_y/2;\ 0\le z\le l_z$$

where the absorbed heat flux q(x,y) is:

$$q = q_0 \left[\zeta \, exp\left(\frac{x^2 + y^2}{r_G^2} \right) + (1 - \zeta) \left(\frac{x^2 + y^2}{r_D^2} \right) * exp\left(\frac{x^2 + y^2}{r_D^2} \right) \right] \quad (2)$$

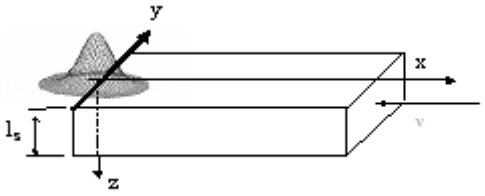

Fig. 1 – Sketch of the semi-infinite work-piece.

The 3-D conductive models are solved by means of the COMSOL Multiphysics 3.4 code. Several different grid distributions have been tested to ensure that the calculated results are grid independent. Maximum temperature differences of the fields are lower than 0.1 percent by doubling the mesh nodes. The grid mesh is unstructured.

3. Results and Discussion

Results are presented for two cases: a) Gaussian, ζ=1; b) donut, ζ=0. Several Reynolds jet numbers on upper surface are studied: 20000, 40000, 60000, 80000, and 120000. The spot radius r_G, and the width of the workpiece are equal to 0.0125 m.

Several convective heat transfer coefficient values on the upper surface, with corresponding Biot numbers, are considered with negligible radiative heat losses. The Biot is defined as $Bi=hL_y/\lambda$. Temperature dependent thermophysical properties are taken from the Metals Handbook [30] for a 10-18 steel material: k=53.7-0.03714(T-273.15) in W/(mK), ρ=7806 in kg/m^3 and c_p=500.0 + 0.40(T-273.15) in J/(kg K). The absorbed laser heat flux is equal to 120 W/cm^2. The workpiece velocity is 2.0 10^{-4} m/s and the Peclet number is equal to 1. The ambient temperature is assumed equal to 290 K. In Fig. 2*a*, temperature profiles at y=z=0 m, along the motion direction, x, for several times, from 1 s to 100 s are given for the Gaussian case, Pe=1.0 and ζ=1.0, temperature profiles, along the motion direction, x, for several times, for Re_{jet} number equal to 40000, are given and they show the thermal development along the heated surface.

In Fig. 2*b* it is observed that when the solid thickness increases the maximum temperature value attained decreases, the curve slope increases and the temperature values increase only in downstream region for increasing x value.

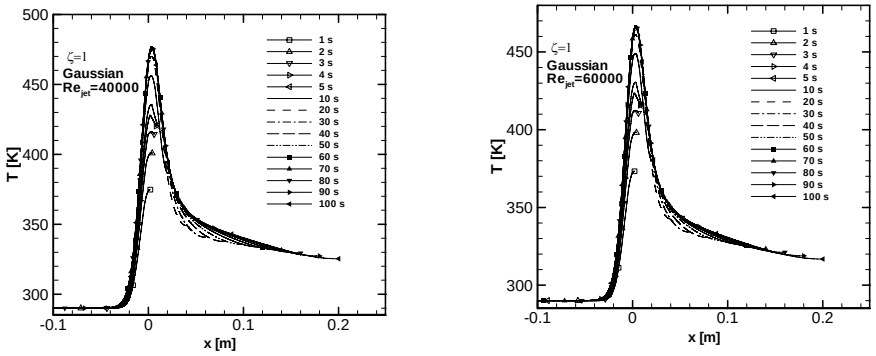

a *b*

Fig. 2 – Temperature profiles for Gaussian distribution:
a) Re_{jet} equal to 40000, *b*) Re_{jet} equal to 60000.

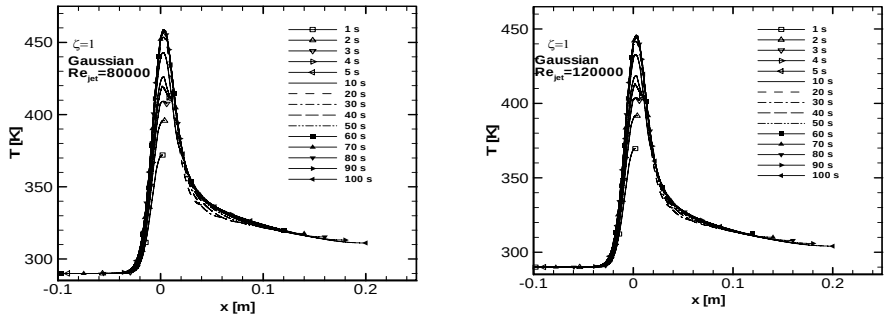

a *b*

Fig. 3 – Temperature profiles for Gaussian distribution:
a) Re_{jet} equal to 80000, *b*) Re_{jet} equal to 120000.

For Re_{jet} = 80000 the profiles are more similar than for Re_{jet} = 60000 but the temperature values are lower than the previous run. In Fig. 3*b* it is observed that temperature values achieved decrease at increasing the Reynolds jet number, but the maximum temperature value attained is lower than the previous analyzed configuration. Moreover, the slope of the curve increases at increasing the Re_{jet} member.

For the donut distribution and Pe=1.0 with Re_{jet} = 40000 and 60000, when the convective heat losses are present, the quasi-steady state is reached for t>60 s, in Fig. 4. It is observed that the temperature values, along x, increase at increasing the time. This is due to the heat transfer coefficient imposed on the upper surface. It is worth observing that the slope of this curve is constant. The slope increases as the Re_{jet} number values increase. Moreover, the temperature values reached decreasing when the heat transfer coefficients increase.

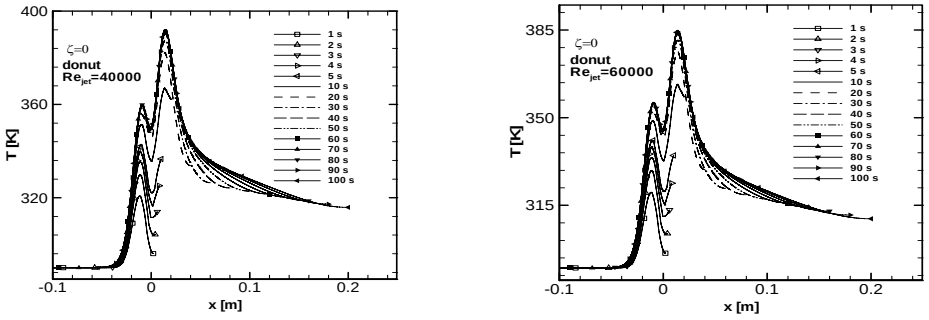

a) b)

Fig. 4 - Temperature profiles for Donut distribution:
a) Re_{jet} equal to 40000, b) Re_{jet} equal to 60000.

For the donut case, it can be observed that the temperature profiles are nearly symmetrical with reference to x=0 at the beginning of the heating. It is observed, that at the increasing of solid thickness, the slope of the curves at the semi-infinite workpiece boundary surface, x=vt, increases due to the surface heat transfer.

The temperature behaviour for Re_{jet} = 120000 is the same for Re_{jet} = 80000. The temperature reached is lower than the previous case studied as shown in Fig. 4. At the increasing of Reynolds jet number, the slope of the curves increases. in Fig. 5*b*, the effect of the convective heat transfer is very strong and it determines a large decrease in the temperature profile.

4. Conclusion

A three dimensional numerical model on conductive field in a semi-infinite solid with finite thickness and width irradiated by a laser source was investigated.

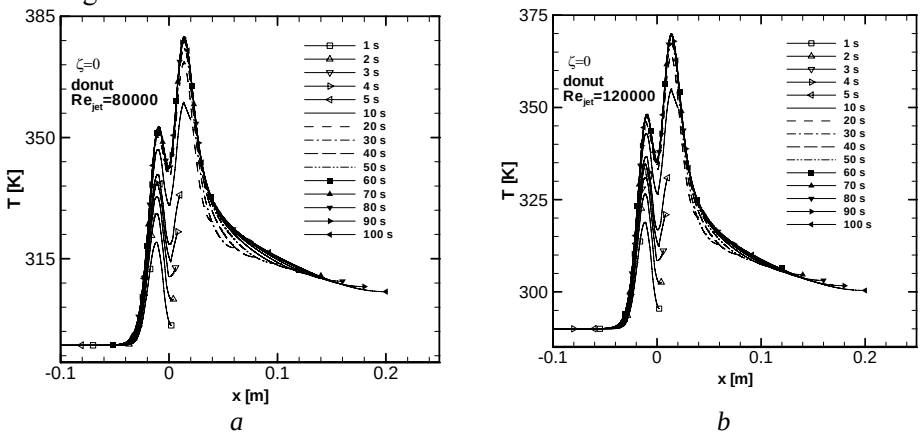

a *b*

Fig. 5 – Temperature profiles for Donut distribution:

a) Re_{jet} equal to 80000, *b*) Re_{jet} equal to 120000.

The numerical model took into account convective heat losses through the surface whereas the radiative heat transfer was neglected. The numerical simulations were carried out by means the COMSOL Multiphysics code and thermal properties were considered temperature dependent. The considered laser source distribution was a linear combination of Gaussian and donut function and the velocity along motion direction was assumed constant. Two heat source distributions were examined Gaussian and donut. Different behaviours were detected between the Gaussian and donut distributions. At the increasing of Re_{jet} the temperature decreases and the slope of the temperature profiles increases.

Nomenclature

c = specific heat (J kg^{-1} K^{-1})	Greek symbols
h = convective heat transfer coefficient (W m^{-2} K^{-1})	α = thermal diffusivity (m^2 s^{-1})
	θ = time (s)
k = thermal conductivity (W m^{-1} K^{-1})	ρ = density (kg m^{-3})
l = length (m)	Subscripts
Pe = Peclet number (= $vr_G/(2\alpha)$)	a = ambient
Bi = Biot number (=hL_y/λ)	b = bottom surface
Q = absorbed heat flux (W m^{-2})	D = Donut beam
r = radius (m)	f = fluid
Re_{jet} = Reynolds jet number	G = Gaussian beam
T = temperature (K)	in = initial for $x \rightarrow +\infty$
v = velocity of the work-piece (m s^{-1})	u = upper surface
x,y,z= Cartesian coordinates (m)	x,y,z = along axes

REFERENCES

[1]. Viskanta R., Bergman T. L., *Heat Transfer in Material Processing*, *in Handbook of Heat Transfer*. Chap. 18, McGraw-Hill., 1998.

[2]. Steen W.M., Mazumder J., Watkins K. G., *Laser Material Processing*, 4th ed., Springer.. 2010.

[3]. Shuja S.Z., Yilbas B.S., Budair M.O., *Modeling of Laser Heating of Solid Substance Including Assisting Gas Impingement*. Numeric. Heat Transfer, Part. A, **33**, 315-339 (1998).

[4]. Shuja S.Z., Yilbas B.S., 3-Dimensional conjugate laser heating of moving slab, *Appl. Surface Science*. **167**, 134-148 (1999).

[5]. Bianco N., Manca O., *A Parametric Study of the Quasi-Steady State Temperature Field by a Moving Heat Source for Surface Treating*. ASME HTD, **366-3**, 285-294 (2000).

[6]. Bianco N., Manca O., Nardini S., *Comparison Between Thermal Conductive Models for Moving Heat Sources in Material Processing*. ASME HTD, **369-6**, 11-22 (2001).

[7]. Li J.F., Li L., Stott F.H., *Comparison of Volumetric and Surface Heating Sources in the Modeling of Laser Melting of Ceramic Materials*. Int. J. Heat Mass Transfer, **47**, 1159-1174 (2004).

[8]. Rozzi J.C., Pfefferkon F.E., Incropera F.P., Shin Y.C., *Transient Thermal Response of a Rotating Cylindrical Silicon Nitride Workpiece Subjected to a Translating Laser Heat Source*, *Part I: Comparison of Surface Temperature Measurements with Theoretical Results.* J. Heat Transfer, **120**, 899-906 (1998).

[9]. Rozzi J.C., Incropera F.P., Shin Y.C., *Transient Thermal Response of a Rotating Cylindrical Silicon Nitride Workpiece Subjected to a Translating Laser Heat Source*, *Part II: Parametric Effects and Assessment of a Simplified Model.* J Heat Transfer, **120**, 907-915 (1998).

[10]. Rozzi J.C., Pfefferkon F.E., Incropera F.P., Shin Y.C., *Transient, Three-Dimensional Heat Transfer Model for the Laser Assisted Machining of Silicon Nitride: I. Comparison of Predictions with Measured Surface Temperature Histories*. Int. J. Heat. Mass. Transfer, **43**, 1409-1424 (2000).

[11]. Rozzi J.C., Incropera F.P., Shin Y.C. *Transient, Three-Dimensional Heat Transfer Model for the Laser Assisted Machining of Silicon Nitride*: II: *Assessment of Parametric Effects*. Int. J. Heat Mass Transfer, **43**, 1425-1437 (2000).

[12]. Hou Z.B., Komanduri R., *General Solutions for Stationary/moving Plane Heat Source Problems in Manufacturing and Tribology.* Int. J. Heat. Mass. Transfer, **43**, 1679-1698 (2000).

[13]. Yilbas B.S., Shuja S.Z., Hashmi M.S.J., *A Numerical Solution for Laser Heating of Titanium and Nitrogen Diffusion in Solid.* J. Mat. Proc. Tech., **136**, 12-23 (2003).

[14]. Gutierrez G., Araya J.G., *Temperature Distribution in a Finite Solid Due to a Moving Laser Beam*. Proc. ASME - IMECE 2003, paper IMECE 2003-42545 (2003).

[15]. Bianco N., Manca O., Naso V., *Numerical Analysis of Transient Temperature Fields in Solids by a Moving Heat Source*. 3rd Int. Conf. Heat Transfer, Fluid Mechanics Thermodynamics, Cape Town, South Africa, in press. 2004.

[16]. Cline H.E., Anthony T.R., Heat Treating and Melting Material With a Scanning Laser or Electron Beam. *J*. Appl. Physics, **48**, *9*, 3895-3900 (1977).

[17]. Modest M.F., Abakians, H., *Heat Conduction in a Moving Semi-Infinite Solid Subjected to Pulsed Laser Beam*, J. Heat Transfer, **108**, 597-601 (1986).

[18]. Bianco N., Manca O., Nardini S., *Two Dimensional Transient Analysis of Temperature Distribution in a Solid Irradiated by a Gaussian Laser Source.* Proceedings of ESDA04, paper n. ESDA2004-58286 7TH Biennial Conference on Engineering Systems Design and Analysis July 19–22, 2004, Manchester, United Kingdom., 2004.

[19]. Shankar V., Gnamamuthu D., *Computational Simulation of Laser Heat Processing of Materials*. J. Thermophysics Heat Transfer, **1**, 182-183 (1987).

[20]. Leung M., *Phase-Change Heat Transfer in Laser Transformation Hardening by Moving Gaussian Rectangular Heat Source.* J. Phys. D: Appl. Phys. **34**, 3434-3441 (2001).

[21]. Brockmann R., Dickmann K., Geshev P., Matthes K.J., *Calculation of Temperature Field in a Thin Moving Sheet Heated with Laser Beam*. Int. J. Heat Mass Transfer, **46**, 717-723.
[22]. Couëdel D., Rogeon P., LemassonV, Carin M., Parpillon J.C., Bertet R., *2D-Heat Transfer Modelling Within Limited Regions Using Moving Sources: Application to Electron Bean Welding*. Int. J. Heat Mass Transfer, **46**, 4553-4559.
[23]. Rosenthal D., *The Theory of Moving Sources of Heat and its Application to Metal Treatments*. Trans. ASME, **68**, 3515-3528 (1946).
[24]. Patankar S.V., *Numerical Heat Transfer and Fluid Flow*. Hemisphere Publishing Corporation, 1980.
[25]. Almeida De S.M., Hinds B.K., *Finite Difference Solution to the Problem of Temperature Distribution Under a Moving Heat Source, Using the Concept of a Quasi-Steady State*. Numeric. Heat Transfer, **6**, 17-27 (1983).
[26]. Nardini S., Manca O., Naso V., *Analytical Solution to the Temperature Distribution in a Finite Depth Solid with a Moving Heat Source*. Proc. IV Brazilian Thermal Science Meeting,, 287-291 (1992).
[27]. Bianco N., Manca O., Nardini S., Tamburrino S., *Transient Heat Conduction in Solids Irradiated by a Moving Heat Source*. Diffusion in Solids and Liquids IV. Defect and Diffusion Forum Vols., 283-286 (2009).
[28]. Bianco N., Manca O., Nardini S., Tamburrino S., *Effect of Solids Thickness on Transient Heat Conduction in Workpieces Irradiated by a Moving Heat Source*, 2009.
[29]. Minea A.A., Manca O., Nardini S., Tamburrino S., *Transient Heat Conduction in Solids Irradiated by a Moving Heat Source with Combined Donut and Gaussian Distributions*, 2009.
[30]. ** *Metals Handbook*, 9th Ed. ASM, Metal Park, OH, (1981).

ANALIZA NUMERICĂ A UNUI CURENT DE ÎMPINGERE ASUPRA CONDUCŢIEI TERMICE ÎN PIESELE IRADIATE DE O SURSĂ DE CĂLDURĂ MOBILĂ

(Rezumat)

În această lucrare s-a elaborat un model tridimensional de transfer termic pentru cazul încălzirii unei piese cu ajutorul laserului. Modelul a fost elaborat folosind programul de simulare-modelare CFD Comsol Multhiphysics. Sursa laser, având definită repartiţia de putere, loveşte suprafaţa materialului şi se mişcă cu o viteză uniformă în direcţia pozitivă x. În partea de simulare s-au realizat unele presupuneri, cum ar fi: dimensiunea solidului în direcţia de mişcare s-a presupus a fi infinite, în timp ce s-au luat în consideraţie valori finite pentru grosime (s) şi lăţime. Mai mult, proprietăţile termice au fost considerate dependente de temperatură, iar materialul a fost presupus isotropic. În calcul au fost considerate şi pierderile de căldură către mediul extern. Au fost considerate şi câteva valori ale fluxului convectiv la suprafaţa exterioară

în considerarea numerelor Reynolds şi Peclet dar cu neglijarea efectelor radiaţiei. Rezultatele au fost oferite grafic, pentru diferite valori ale numărului Re, în termeni de profil termic necesar pentru evaluarea efectului dimensiunilor piesei precum şi a coeficientului global de schimb termic.

BULETINUL INSTITUTULUI POLITEHNIC DIN IAŞI
Publicat de
Universitatea Tehnică „Gheorghe Asachi" din Iaşi
Tomul LVII (LXI), Fasc. 4, 2011
Secţia
ŞTIINŢA ŞI INGINERIA MATERIALELOR

USE OF MAGHMITE AND ITS DERIVATES AS NANOPARTICLES FOR WASTEWATER TREATMENT

BY

ECATERINA MATEI[1*], ANDRA PREDESCU[1], EUGENIU VASILE[2] and CRISTIAN PREDESCU[1]

[1]POLITEHNICA University of Bucharest,
[2] METAV CD Bucharest

Received: April 14, 2011
Accepted for publication: June 27, 2011

Abstract. Nano-sized crystals of maghemite iron oxide (γ-Fe2O3) were synthesized, with an average of 10 nm. Subsequently, a nano-composite from γ-Fe2O3 with AMBERLITE cationic exchange resin was synthesized. The products have been subjected for thorough characterization with several spectroscopic techniques as well as transmission electron microscopic measurements or X-ray diffraction analysis. These investigations confirm the formation of maghemite nanoparticles on resin surface. The nano-composite showed remarkable adsorption efficiency in removal of some toxic metal ions as Zn, Ni, Cu, Cd, Cr.

Key words: nanomaterials, maghemite, catonic resin, heavy metal ions.

1. Introduction

The industrial waste water effluents contains mainly the various heavy metals, which are a real threat to the environment and public health, because their toxicity and persistence in the environment (Hu *et al.,* 2007). The removal of some toxic metals such as chromium, cadmium, copper, lead, nickel, mercury and zinc from waste waters became a necessity due to their toxicity and carcinogenicity. There are many removal techniques such as adsorption, chemical precipitation, ion

* Corresponding author e-mail: predescu@ecomet.pub.ro

exchange, filtration, membrane separation, and reverse osmosis in order to diminish the pollution impact of these metals. Also, due the development in nano technology, nanoscale iron oxides have became a raw material for treating the waste waters and soils, accelerating the coagulation of sewage, removing radionuclides, adsorbing organic dyes and cleaning up the contaminated soils (Lo *et al.,* 2009). There are many types of nanomaterials with these characteristics, but magnetic iron oxide nanoparticles are an efficient adsorbent, which couples magnetic separation with ionic exchange capacity for removal of heavy metals pollutants (Wang *et al.,* 2009). Nano-iron oxides, such as magnetite (Fe_3O_4) and maghemite (γ-Fe_2O_3), and also different ferrite compounds are known as materials used in different biological and industrial application. These materials have unique magnetic and electronic properties. Due their chemical stability, biocompatibility and heating ability, ferrofluids of maghemite nanoparticles can be used for ferrofluids hyperthermia in tumor treatment (Sun *et al.,* 2004).

In this paper the preparation by chemical coprecipitation and characterization of maghemite (γ-Fe_2O_3) and a nano-composite from γ-Fe_2O_3 with AMBERLITE cationic exchange resin batch adsorption/desorption studies are described.

2. Experimental

2.1. Preparation and Characterization of Maghemite (γ-Fe_2O_3) and Nano-Compsite Maghemite – Cationic Resin (γ-Fe_2O_3 – R-H) Nanoparticles

There are various methods for preparation of γ-Fe2O3, using different reagents for synthesis. In this paper the nanoparticles were prepared by coprecipitation of ferrous ion (Fe^{2+}) and ferric ion (Fe^{3+}) with NaOH solution. D-sorbitol was used to prevent the agglomeration between the nanoparticles (Predescu, 2010). The iron solutions were strongly stirred in water, after adding NaOH solution. The precipitates were separated by magnetic decantation or slow filtration after which it was washed several times with distilled water and ethanol.

The magnetite nanoparticles were dried into oven at 60°C. In order to obtain maghemite (γ-Fe_2O_3), the magnetite nanoparticles was heated at 200°C, for 3 hours and finally, red-brown maghemite nanoparticles were collected. The nanocomposite was obtained after 24 ore time contact between maghemite nanoparticles and AMBERLITE cationic resin, under mechanical stirring. After, water washing the new nanocomposite was analyzed with the same methods as initial maghemite nanoparticles.

The structure and morphology of the γ-Fe_2O_3 nanoparticles was characterized by X-ray powder diffraction, which was carried out in a SHIMADZU diffractometer with high-intensity Cu Kα radiation (λ = 1.54065 Å) with the 2θ range from 10° to 90°. The particle size and distribution were detected by transmission electron microscopy (TEM).

The energy dispersive X-ray (EDX) and selected area electron diffraction (SAED) spectra were recorded with a TECNAI F30 G^2 high resolution transmison electron micrsoscope with 1Å line resolution and with an EDX detector with 133 eV resolution.

2.2. Batch Adsorption and Recovery Studies

The metal solutions were prepared from Merck stock standard solutions, consisting of dissolved metal into nitric acid, in case of zinc, cadmium, nickel, and copper and from potassium chromate (K_2CrO_4) salt dissolved into distilled water in case of chromium. Each initial metal standard solution concentration was 1000 mg/L. The initial standard solutions were used in order to evaluate the maximum quantity adsorbed at pH 2.5. The metal solutions with the same concentrations were mixed together and resulted a multi-component system (Zn, Cd, Ni, Cu, Cr) had resulted. The evaluation took place by analyis from 20 to 20 minutes, during 2 hours.

The time for recovery was 24 hours and all maghemite nanoparticles and nanocomposite were recycled by magnetic separation. All samples containing hexavalent chromium was analyzed by diphenylcarbazide method with a molecular absorption spectrometer (Cintra 202 GBC) with spectral domain between 190 and 1000 nm. Total chromium quantity and the others metals were measured with an atomic absorption spectrometer (GBC 932 AB Plus) with spectral domain between 185 and 900 nm.

3. Results and Discussions

3.1. Characterization of Magnetite (Fe_3O_4) Nanoparticles

The obtained samples were analyzed by X-ray diffraction (XRD) using a diffractometer with high-intensity Cu Kα radiation (λ = 1.54065 Å). The diffraction pattern for maghemite is shown into Fig. 1.

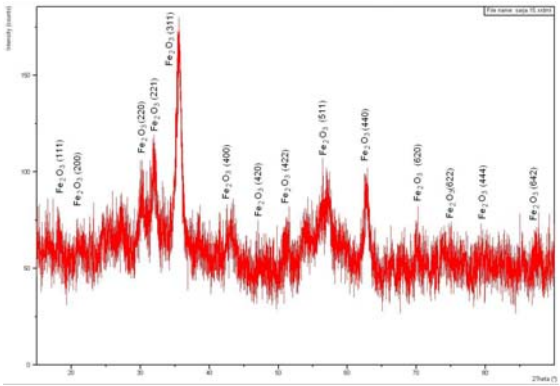

Fig. 1 – XRD patterns for γ-Fe_2O_3 nanoparticles.

The diffraction peaks reveal a cubic spinel structure with no others phases presented in the sample. The morphology and structure of the maghemite samples were investigated by transmission electron microscopy through bright field (TEMBF) and image is presented in the Fig. 2*a*. Spherical particles with a reduced size and a good dispersion can be observed in this figure.

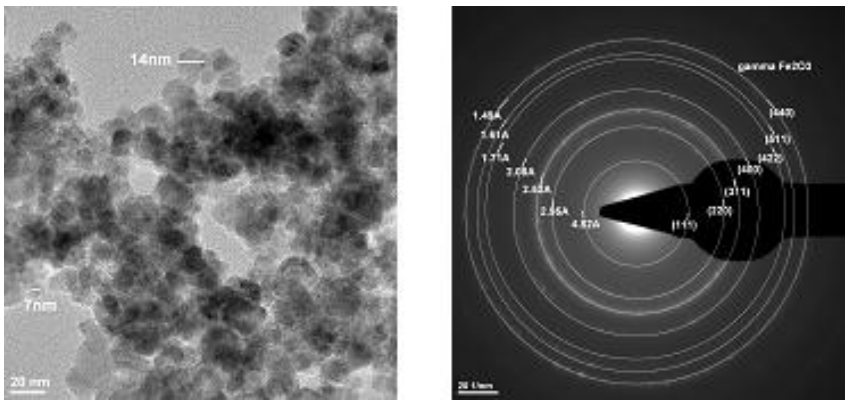

a *b*

Fig. 2 – *a* – Transmission electronic microscopy through bright field (TEMBF) for γ-Fe_2O_3; *b* – Selected area electron diffraction (SAED) image associated to the sample from figure (*a*).

Also, in order to identify the plans associated with the maximum values for the nanoparticles was used as method selected area electron diffraction (SAED), the image being presented in the Figure 2(b). The SAED diffraction peaks corresponding to the (440), (511), (422), (400), (311), (220) and (110) planes for γ-Fe_2O_3 match with the XRD pattern.

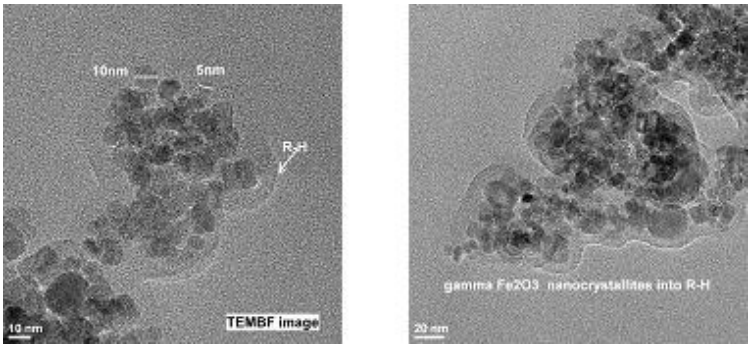

a *b*

Fig. 3 – *a* – Transmission electronic microscopy through bright field (TEMBF) for Fe_3O_4; *b* – Selected area electron diffraction (SAED) image associated to the sample from figure (*a*).

The SAED image confirmed the formation of the γ-Fe_2O_3 nanoparticles. These nanoparticles have been used as adsorption material for pollutants from wastewaters, in accordance with their small particle size and high specific surface area.

The morphology and structure of the maghemite into cationic resin samples were investigated by transmission electron microscopy through bright field (TEMBF). The TEMBF image is presented in the Fig. 3 *a*. Spherical particles with a reduced size and a good dispersion can be observed in this figure, covered by a layer of resin (R-H). Also, another image at about 20 nm for maghemite nanoparticles into resin is shown in the Fig. 3*b*).

3.2. Batch Adsorption and Recovery Studies

Fifty milliliters of 1000 mg/L multi-component solution and 1 g/L γ-Fe_2O_3 nanoparticles were mixed at pH of 2.5. Also, the same concentration was used for mixture with 1 g/L γ-Fe_2O_3-R-H. An important characteristic for maghemite was the value for the surface charge which is 6.3 at the zero point of charge (pHpzc) (Hu *et al.,* 2005). This value was not obtained as experimental data, only from literature. Below this value, the adsorbent surface is positively charged and the anions are adsorbed by electrostatic attraction. Above this value of pHpzc, the adsorbent surface is negative charged and the cations are adsorbed on the maghemite (Hu *et al.,* 2005). For example, with the increase in pH, the uptake of Cr (VI) ions decreased, because in the aqueous phase, the surface of the metal oxides is covered with hydroxyl groups that vary at different pH values. Hexavalent chromium in wastewaters is presented in forms as chromates (CrO_4^{2-}), dichromates ($Cr_2O_7^{2-}$) and bichromates ($HCrO_4^-$), in these conditions, the OH^- groups from mixture will compete with chromium species for adsorptions sites. Also, if the adsorption surface is negatively charged, the electrostatic repulsions increase between negatively charged Cr (VI) species and negatively charged nanoparticles, leading to the removal of some adsorbed species such as bichromates ($HCrO_4^-$) or chromates (CrO_4^{2-}) (Hu *et al.,* 2005). In the environment, at acidic pH value, the metal ions can appear in the following oxidation states: Ni^{2+}, $NiSO_4^0$, Cu^{2+}, Zn^{2+} (Loon &, Duffy, 2005). With these information, regarding the distribution of the ions can be achieved an assessment of the metal species presented into water environment. For the analyzed aqueous solutions the samples were analyzed during of 120 minutes, from 20 to 20 minutes. The evolution in time of the removal efficiency using γ-Fe_2O_3 is presented in Fig. 4.

It was observed that after first minute of the reaction, almost 70% from hexavalent chromium is removed and the quantity remains almost the same at 120 minutes. In case of the others metal ions, the efficiency was lower due the presence of the metals as cations (Zn^{2+}, Ni^{2+}, Cu^{2+}, Cd^{2+}) which is diminished by the pHpzc value for maghemite. In this case, the removal efficiency is not

higher than 35%. The variation of the removal efficiency remains the same in the case of the nano-composite consists of the maghemite and AMBERLITE cationic resin (γ-Fe_2O_3-R-H) but the removed quantity of the metals is significantly higher compared with the maghemite nanoasorbent. This situation is due the double effect of the exchange resin and the adsorption of the maghemite. The high efficiency for all metal ions can be observed in the Fig. 5.

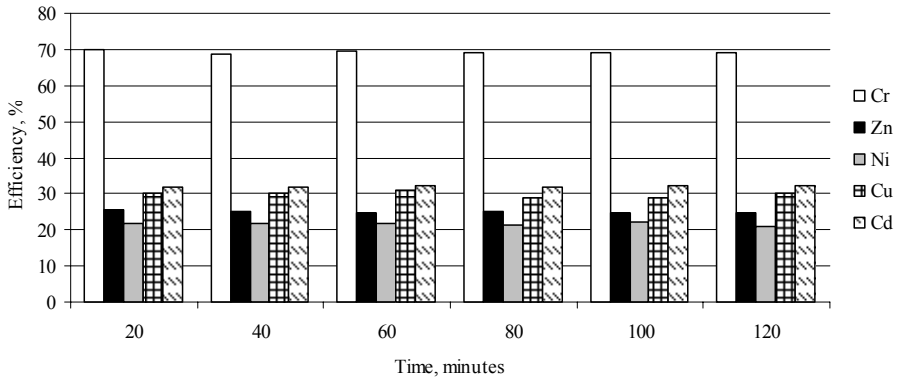

Fig. 4 – The removal efficiency using γ-Fe_2O_3 as adsorbent for metal ions, at pH 2.5.

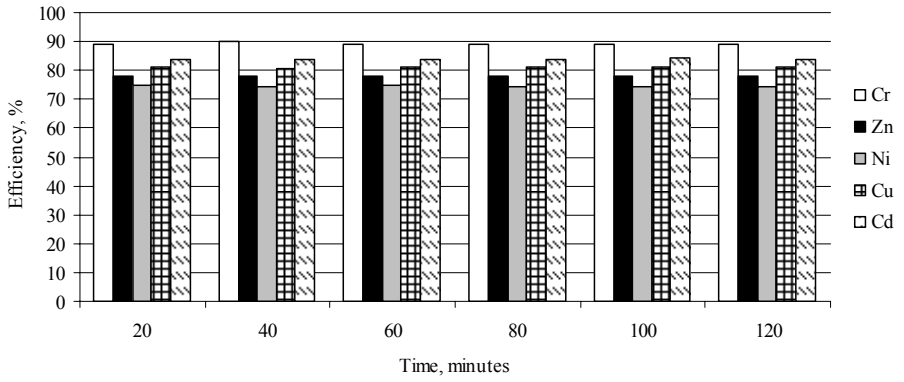

Fig. 5 – The removal efficiency using γ-Fe_2O_3-R-H as adsorbent for metal ions at pH 2.5.

The amount adsorbed at equilibrium, q_e, was calculated with the following formula expressed as:

$$q_e = \frac{(C_0 - C_e) \cdot V}{m} \tag{1}$$

where: C_0 – initial concentration, mg/L; C_e – equilibrium concentration, mg/L; V – volume of solution, L; m – adsorbent quantity, g.

The effect of time as function of adsorbed quantity is shown in Fig. 6, for maghemite nano-adsorbent. It can be seen the rapid adsorption of metal on maghemite nanoparticles, initially quite high, followed by a much slower removal rate this leading to an equilibrium state. It can be assumed that after first 20 minutes the adsorbed quantity reaches at a maximum. The quantity is quite different function by type of the metal. The highest quantity is for hexavalent chromium 55mg/g, a high value compared with common adsorbents from the literature: 11.5 mg/g for diatomite and 15.47 mg/g for activated carbon, respectively (Hu *et al.,* 2005).

For the others metals, the adsorbed quantities are different from 15.9 mg/g for Cd and 15 mg/g for Cu to 12.75 mg/g for Zn. The lowest value as adsorbed quantity is for Ni: 10.9 mg/g.

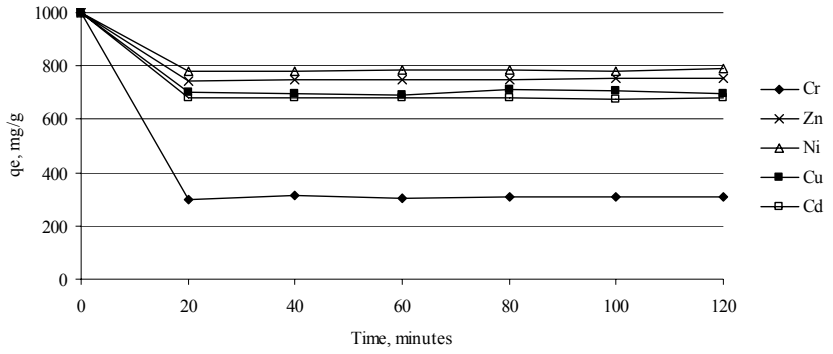

Fig. 6 – Effect of time on the removal of metal ions on maghemite nanoparticles.

In case of maghemite with AMBERLITE cationic resin, the adsorbed quantities significantly increase, emphasized by the exchange effect of the resin. The adsorbed quantity as function of time is shown in the Fig. 7.

The tendency of the adsorption remains the same as in case of the maghemite nanoparticles, but the adsorbed quantities are higher. In this case, the adsorbed quantity of the hexavalent chromium onto 1 g of γ-Fe_2O_3-R-H nano-adsorbent is 44.6 mg/g. Lower quantities are adsorbed for Cd: 42 mg/g, Cu: 40.5 mg/g, Zn: 39 mg/g or Ni: 37.5 mg/g, but more higher than in case of adsorption onto maghemite nanoparticles. All measurements for metals, before and after adsorption process, were made by flame atomic absorption spectrometry (FAAS) and presented results are an average of 10 measurements. For hexavalent chromium, two analysis methods were chosen: FAAS for total

chromium and molecular absorption spectrometry for hexavalent state. Comparing the results, it can be observed that the oxidation state of the hexavalent chromium remains the same, this indicating that no redox reaction occurs during the adsorption process. The chromium valence in solution never changes after the adsorption process. Dissolved hexavalent chromium formed a color complex with diphenylcarbazide detected by absorbance at 530 nm. As comparison, from Fig. 8, the difference between initial and final concentration, after the adsorption onto maghemite and maghemite with cationic resin, can be observed.

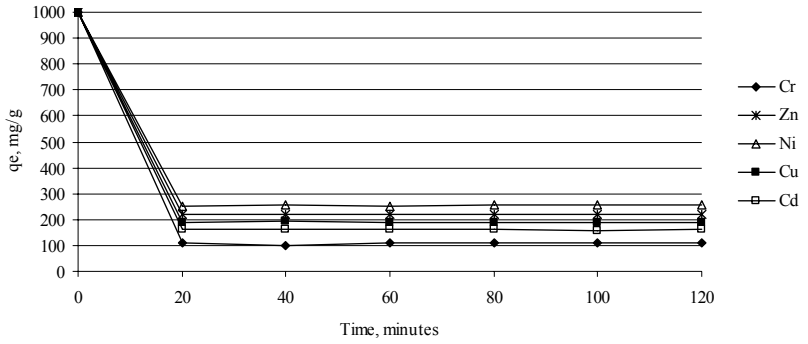

Fig. 7 – Effect of time on the removal of metal ions on maghemite nanoparticles.

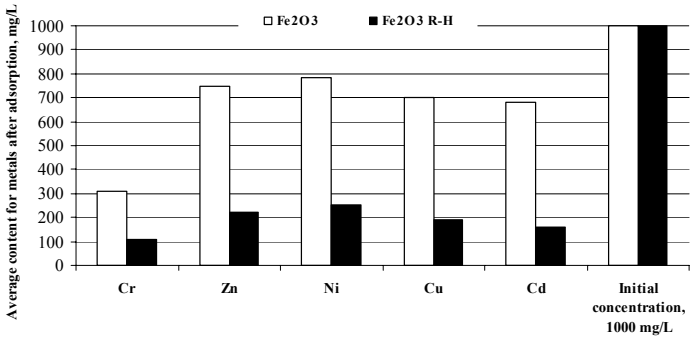

Fig. 8 – Comparison between the initial and final concentration of the metals adsorbed onto nanoaprticles as maghemite and maghemite with cationic resin.

It can be observed the highest efficiency for hexavalent chromium adsorbtion in case of the two nano-adsorbents and a higher tendency of adsorption for maghemite covered by cationic resin, the composite which lead a exchange capacity and adsorption characteristics for the new material. The adsorption is a reversible process, being possible the reuse of the adsorbent, after the regeneration. By washing the adsorbents with NaOH (1 N) solution,

after magnetic separation of the maghemite and maghemite with cationic resin, followed by washing with ultrapure water, the recovered quantity was 0.96 g (the rate of recovery was 96%) for the two adsorbents but these are only a preliminary results and future experiments will be made in oreder to evaluate the regeneration capacity for these adsorbents.

4. Conclusion

The maghemite nanoparticles with an average diameter of 10 nm were synthesized using coprecipitation method. Also, a nanocomposite with average diameter for maghemite of 10 nm was obtained by covering the maghemite nanoparticles with AMBERITE cationic resin. These nanoparticles were successfully tested for the removal of some toxic metals from synthetic aqueous solutions, such as hexavalent chromium, zinc, nickel, copper and cadmium. The adsorption process was conducted into acidic environment, at pH 2.54. The obtained adsorption data indicated a good adsorption capacity for metal ions removal especially in case of maghemite into cationic resin (γ-Fe_2O_3-R-H) and a higher adsorption tendency for hexavalent chromium in comparison with the others metal ions. Also, the regeneration of the adsorbents was investigated with good results, in presence of sodium hydroxide solution. The adsorption study showed that the electrostatic attraction was responsible for the metal removal in case of maghemite nanoparticles and a double effect of electrostatic attraction during the adsorption process and ionic exchange was observed for maghemite covered cationic resin (γ-Fe_2O_3-R-H).

The obtained data represents only the preliminary result obtained for the achieving a systematic study regarding the removal of heavy metals from wastewaters using as adsorbents the nanoparticles with high capacity of adsorption due theirs high surface area.

Acknowledgements. Authors recognize financial support from the European Social Fund through POSDRU/89/1.5/S/54785 project: "Postdoctoral Program for Advanced Research in the field of nanomaterials".

REFERENCES

Hu J., Chen G., Lo M.C.I., *Removal and Recovery of Cr (VI) from Wastewater by Maghemite Nanoparticles*, Water Research, **39**, 4528 – 4536 (2005).

Hu J., Lo M.C.I., Chen G., *Comparative Study of Various Magnetic Nanoparticles for Cr (VI) Removal*. Separation and Purification Technology, **56**, 249 – 256 (2007).

Lo M.C.I., Hu J., Chen G., *Iron-Based Magnetic Nanoparticles for Removal of Heavy Metals from Electroplating and Metal-Finishing Wastewater*, In: Nanotechnologies for Water Environment Applications. Zhang C.T., Surampali Y.R., Lai K.C.K, Hu Z., Tyagi R.D., Lo M.C.I. (Eds.), American Society of Civil Engineers, Virginia, 213-264 (2009).

Loon G.W., Duffy S.J., *Environmental Chemistry,* Oxford University Press (2005).

Predescu A., *Researches Regarding the Dimension and Distribution of Magnetic Iron Oxide Nanopowders and Theirs Characterization.* (In Romanian), Bul. Inst. Polit. Iaşi, **LVI (LX)**, 95 – 102 (2010).

Sun Y.–K., Ma M., Zhang Y., Gu N., *Colloids and Surfaces A: Physicochem. Eng. Aspects*, *245*, 15 (2004).

Wang X., Zhao C., Zhao P., Dou P., Ding Y., Xu P., *Gellan gel Beads Containing Magnetic Nanoparticles: An Effective Biosorbent for the Removal of Heavy Metals From Aqueous System*. Bioresource Technology, *100*, 2301-2304 (2009).

UTILIZAREA MAGHEMITEI ŞI DERIVAŢILOR SĂI CA NANOPARTICULE PENTRU EPURAREA APELOR UZATE

(Rezumat)

Nanocristale de maghemită (γ-Fe_2O_3) au fost sintetizate, la un diametru mediu de 10 nm. Ulterior, un nano-compozit format din γ-Fe_2O_3 cu răşină schimbătoare cationică de tip AMBERLITE a fost de asemenea sintetizat. Produsele au fost caracterizate prin tehnici spectroscopice ca de exemplu microscopie electronică de transmisie şi difracţie de raze X. Aceste investigaţii au confirmat formarea maghemitei prin sintetiză şi ulterior a compozitului. Acesta din urmă a prezentat o capacitate mare de adsorbţie pentru reţinerea unor metale toxice cum ar fi Zn, Ni, Cu, Cd, Cr.

BULETINUL INSTITUTULUI POLITEHNIC DIN IAŞI
Publicat de
Universitatea Tehnică „Gheorghe Asachi" din Iaşi
Tomul LVII (LXI), Fasc. 4, 2011
Secţia
ŞTIINŢA ŞI INGINERIA MATERIALELOR

SIMULATION OF A FLUID BED EQUIPMENT FOR DIFFERENT FLUIDIZATION RATES

BY

A. A. MINEA[1*], O. MANCA[2], M. ALEXANDRU[3] and A. DIMA[1]

[1] "Gheorghe Asachi" Technical University of Iaşi,
[2]Seconda Università degli studi di Napoli,
[3]Grupul Şcolar Ştefan Procopiu Iaşi

Received: April 14, 2011
Accepted for publication: June 27, 2011

Abstract. A fluidized bed is formed when a quantity of a solid particulate substance (usually present in a holding vessel) is placed under appropriate conditions to cause the solid/fluid mixture to behave as a fluid. This is usually achieved by the introduction of pressurized fluid through the particulate medium. This results in the medium then having many properties and characteristics of normal fluids; such as the ability to free-flow under gravity, or to be pumped using fluid type technologies. Fluidized beds are used for several purposes, such as fluidized bed reactors (types of chemical reactors), fluid catalytic cracking, fluidized bed combustion, heat or mass transfer or interface modification, such as applying a coating onto solid items. A fluidized bed consists of fluid-solid mixture that exhibits fluid-like properties. As such, the upper surface of the bed is relatively horizontal, which is analogous to hydrostatic behavior. The bed can be considered to be an inhomogeneous mixture of fluid and solid that can be represented by a single bulk density.

Key words: fluidization, fluid bed equipment, heat transfer rate.

[*] Corresponding author e-mail: aminea@tuiasi.ro

1. Introduction

The purpose of this article is to study the hydrodynamics and bubble formation in a fluidized bed over a period of time. It also demonstrates how to customize a drag law for granular gas-solid flow (Bejan, 2006, 1993). The default drag law in FLUENT is the Syamlal-O'Brien drag law (Tsotsas & Schlünder, 1990; Freiwald & Paterson, 1992; Landon *et al*., 1996; Stewart, 1965)

This law works for a large variety of problems, but has to be tuned properly for predicting the minimum fluidization conditions accurately.

This methodology demonstrates how to do the following:

- Customize a drag law for granular gas-solid flow.
- Use the Eulerian models to predict the pressure drop in an uniformly fluidized bed.
- Solve the case using appropriate solver settings.
- Postprocess the resulting data.

2. Methodology

The prediction of pressure drop in an uniformly fluidized bed is a problem of long standing interest in the process industry (Schwartz & Smith, 1953). The Eulerian models in FLUENT provide an important modeling tool for studying dense phase particulate flow involving complex inter-phase momentum transfer.

Despite rigorous mathematical modeling of the associated physics, the drag laws used in the model continue to be semi-empirical in nature. Therefore, it is crucial to use a drag law that correctly predicts the incipient or minimum fluidization conditions where the bed of particles is essentially in a state of suspension as a result of the balance between interfacial drag and body forces (Schertz & Bischoff, 1969).

The default Syamlal-O'brien is as follows: The fluid-solid exchange coefficient is.

$$k_{sl} = \frac{3\alpha_s \alpha_l \rho_l}{4 v_{r,s}^2 d_s} C_D \left(\frac{Re_s}{v_{r,s}} \right) \left| \vec{v}_s - \vec{v}_l \right| \tag{1}$$

where $v_{r,s}^2$ is the terminal velocity coefficient for the solid phase.

$$v_{r,s}^2 = 0,5\left(A - 0,06 Re_s + \sqrt{(Re_s)^2 + 0,12 Re_s (2B - A) + A^2} \right) \tag{2}$$

with $A = \alpha_l^{4,14}$ and $B = 0,8\alpha_l^{1,28}$ for $\alpha_l \leq 0,85$ and $B = \alpha_l^{2,65}$ for $\alpha_l > 0,85$ (Subagyo, 1998).

The default constants of 0.8 and 2.65 predict a minimum fluidization of 21 cm/s. The experimentally observed minimum fluidization for this particular case is 8 cm/s. Therefore, by changing the constants we can tune the drag law to predict minimum fluidization at 8 cm/s. After some mathematical manipulation, these constants come out to be 0.281632 and 9.07696 respectively. Therefore, these values have to be used to predict the correct bed behavior and are passed to the code through user-defined functions.

The problem considered is a 1m x 0.15m fluidized bed as shown in Fig. 1. The inlet air enters in at 0.25 m/s and the top is modeled as a pressure outlet. The bed is packed with granular solids at 0.55 volume fraction (close to packing).

The grid, as shown in Fig. 2, was checked and scaled according to initial data-s and it has 5544 quadrilater cells, 11 314 faces and 5771 nodes.

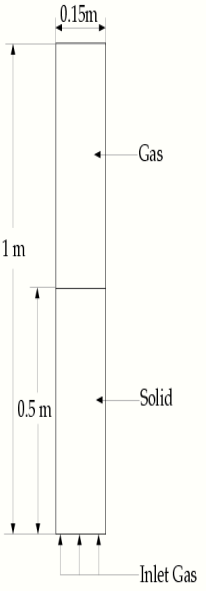

Fig. 1 – Simulation case.

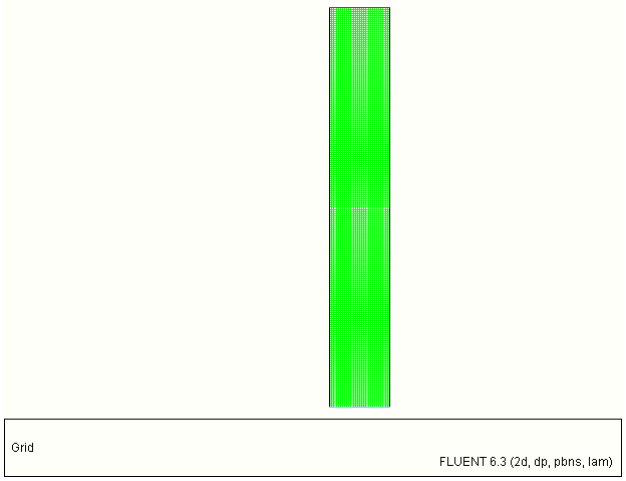

Fig. 2 – Grid.

2.1. Simulation Settings

We selected Pressure Based solver with 2D space and Unsteady time condition and the Eulerian multiphase model, as shown in Fig. 3.

For the fluidization we used air with some modified properties:1.2 kg/m^3 for density and 1.8e-05 kg/m-s for viscosity. Moreover a material called

solids was defined with: 2600 kg/m3 for Density and 1.7894e-05 kg/m-s for Viscosity.

Models

Model	Settings
Space	2D
Time	Unsteady, 1st-Order Implicit
Viscous	Laminar
Heat Transfer	Disabled
Solidification and Melting	Disabled
Species Transport	Disabled
Coupled Dispersed Phase	Disabled
Pollutants	Disabled
Pollutants	Disabled
Soot	Disabled

Fig. 3 – Solver settings.

For Operating Conditions we enabled Gravity and enter -9.81 m/s2 for Gravitational Acceleration in the Y direction and enabled Specified Operating Density, and enter 1.2 kg/m^3 for Operating Density.

3. Postprocessing

For checking the fluidization we displayed contours of volume fraction for solid at 0.2 sec (Fig. 4), 0.9 sec (Fig. 5), and 1.4 sec (Fig. 6).

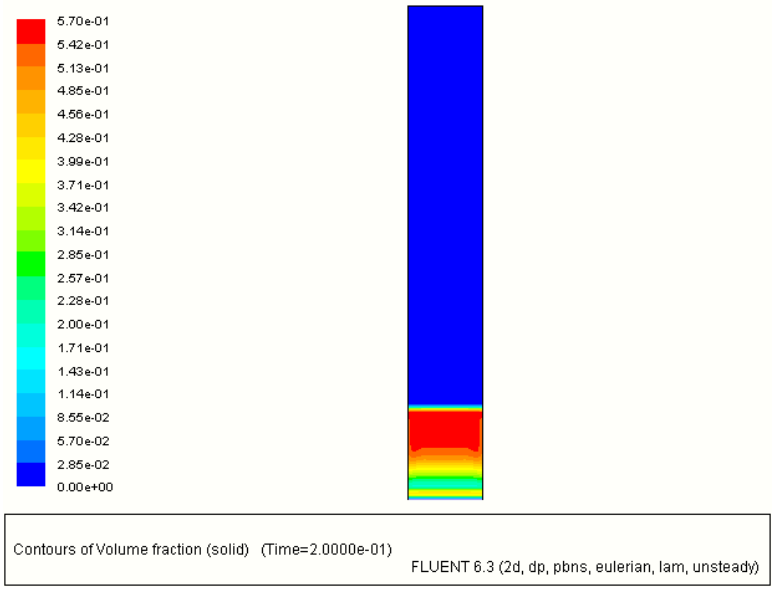

Fig. 4 – Contours of volume fraction (t = 0.2 s).

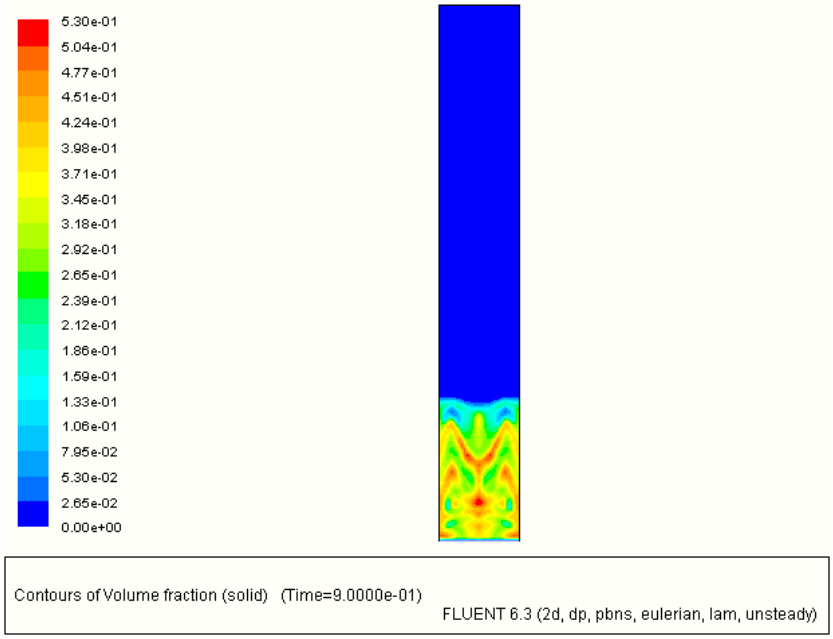

Fig. 5 – Contours of volume fraction (t = 0.9 s).

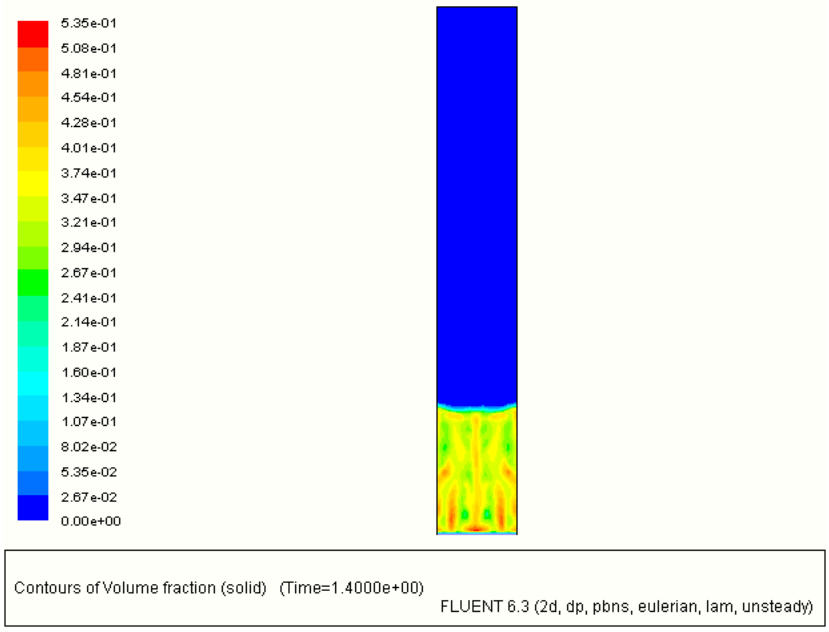

Fig. 6 – Contours of volume fraction (t = 1.4 s).

Moreover, simulation were made for different rates of fluidization and for 1000 seconds of bed functioning and the results obtained after data post processing are illustrated in Table 1 and in Fig. 7 are the velocity profiles on default interior.

Table 1
Simulation Results in Fluent

Case no.	Fluidization rate, m/s	Results on gas velocity magnitude, m/s	
		Default interior	Outlet
1	0.20	7.09	0.036
2	0.25	14.30	0.037
3	0.30	17.15	0.045
4	0.35	20.00	0.052
5	0.40	22.85	0.059

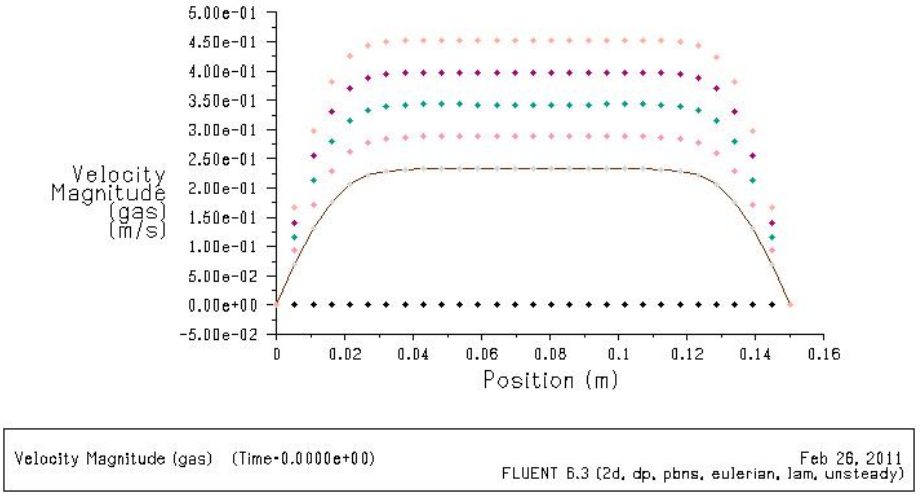

Fig. 7 – Velocity profiles on default interior for the 5 studied cases.

4. Conclusion

Typically, the constants set to 0.8 and 2.65 in the default drag law have to be modified to balance the interfacial drag with the weight of the bed at minimum fluidization. If this is not done, the correct bubbling pattern will not be predicted, leading to incorrect predictions of pressure drop which is the most important objective of such simulations.

Computational fluid dynamics (CFD) studies can improve understanding of fixed bed fluid flow and heat transfer. Our long-term objective

is to use the CFD results in the development of tractable reactor models that are based on a good understanding of the fluid flow phenomena.

The CFD simulations of fluid flow and heat transfer require verification to increase confidence in their use for model development.

A very good quantitative as well as an excellent qualitative fit in CFD simulation was obtained.

REFERENCES

Bejan A., *Advanced Engineering Thermodynamics.* Third Ed., Wiley, Hoboken, 2006.

Bejan A., *Heat Transfer*. Wiley, New York, 1993.

Tsotsas E., Schlünder E.-U., *Heat Transfer in Packed Beds with Fluid Flow: Remarks on the Meaning and the Calculation of a Heat Transfer Coefficient at the Wall.* Chem. Eng. Sci. **45**, 819–837 (1990).

Freiwald M.G., Paterson W.R., *Accuracy of Model Predictions and Reliability of Experimental Data for Heat Transfer in Packed Beds*. Chem. Eng. Sci. **47**, 1545–1560 (1992).

Landon V.G., Hebert L.A., Adams C.B., *Heat Transfer Measurement for Industrial Packed Bed Tubular Reactor Modeling and Design*. AIChE Symp. Ser. 92, 134–144 (1996).

Stewart W.E., *Transport Phenomena in Fixed-Bed Reactors*. Chem. Eng. Prog. Symp. Ser. **61**, 58-61(1965).

Schwartz C.E., Smith J.M., *Flow Distribution in Packed Beds.* Ind. Eng. Chem. **45**, 1209–1218 (1953).

Schertz W.W., Bischoff K.B., *Thermal and Material Transport in Nonisothermal Packed Beds*. AIChE J., **15**, 597–604 (1969).

Subagyo, Standish N., Brooks G.A., *A New Model of Velocity Distribution of a Single-Phase Fluid Flowing in Packed Beds*. Chem. Eng. Sci. **53**, 1375–1385 (1998).

SIMULAREA FUNCŢIONĂRII UNEI INSTALAŢII TIP PAT FLUIDIZAT, PENTRU DIVERSE VITEZE DE FLUIDIZARE

(Rezumat)

În această lucrare s-a elaborat un model bidimensional de transfer termic pentru cazul fluidizării în pat fluidizat, pentru diferite viteze de fluidizare. Fluidizarea este o tehnică de lucru avansată, cu largi aplicaţii industriale, prin care se pun în contact diferite faze pentru intensificarea proceselor de schimb de căldură şi de masă. Fazele puse în contact în timpul fluidizării sunt solide cu lichide şi solide cu gaze. Denumirea de strat fluidizat de particule solide se datorează asemănării formale cu comportarea unui lichid. Stratul fluidizat se realizează circulând un agent de fluidizare (gazos sau lichid) printr-un strat de particule solide, susţinute de un suport perforat (distribuitor), în direcţie ascendentă. La viteze mici, fluidul trece printre granulele stratului fără să-l

deplaseze şi stratul rămâne fix până când căderea de presiune devine egală cu presiunea exercitată de stratul granular. În acest moment, stratul se umflă (se afânează), frecarea dintre mediul fluid şi particule creşte în aşa măsură încât particulele sunt aruncat în sus într-o mişcare dezordonată. Aceasta este faza de *fluidizare liniştită*, în care particulele au o oarecare libertate de mişcare între ele, putându-se mişca în jurul unei poziţii medii. Stratul se comportă ca un lichid, putând curge şi exercita o presiune hidrostatică.

BULETINUL INSTITUTULUI POLITEHNIC DIN IAŞI
Publicat de
Universitatea Tehnică „Gheorghe Asachi" din Iaşi
Tomul LVII (LXI), Fasc. 4, 2011
Secţia
ŞTIINŢA ŞI INGINERIA MATERIALELOR

STAKEHOLDERS INVOLVEMENT AND ETHICAL ASPECTS OF OCCUPATIONAL HEALTH AND SAFETY MANAGEMENT IN ROMANIA

BY

ROLAND IOSIF MORARU[*] and GABRIEL BUJOR BĂBUŢ

University of Petroşani,
Mining Engineering and Industrial Safety Department

Received: March 25, 2011
Accepted for publication: June 27, 2011

Abstract. There is always an unexplored ethical dimension over and above the list of causes of occupational accidents. This results in a cascade of bad decisions being taken at the organizational, human and technical levels, which cause tragic accidents, often with loss of human life. To manage risks properly, it will not only be necessary to develop techniques but also to develop processes, at the personnel level as well as at the organizational level, which will take human nature into account. Appropriate mechanisms will also have to be set up to reconcile „public interest" and „risk management". It will thus be necessary to define, implement and improve a series of processes and most importantly, provide guidance to managers. It is necessary to continue improving the risk analysis methods, to continue training in the field of risk management for numerous stakeholders, to reinforce legislation on risk management and most importantly, to base risk management on ethical principles. The paper discusses values and principles applied in safety decision-making and actions. However, there is no straightforward answer to what is safe enough. Therefore, the purpose of this paper is to present some alternative and supplementing lines for reasoning around some fundamental questions of occupational health and safety management in the Romanian industry.

Key words: occupational health and safety, ethical aspects, stakeholders.

[*] Corresponding author e-mail: roland_moraru@yahoo.co; gabriel_babut@yahoo.com

1. Introduction

The challenge for safety management is being rational within accepted rules of facts and logic on one hand, and considering values and opinions of the public on the other hand. We can make a make a similar distinction between the domain of technical risks (the expert sphere) and the domain of perceived risk (the public sphere). The increased concern about the ethical aspect of safety is revealed at different levels and domains by:

- the activities of popular movements as a driving force for a safety agenda,
- mass media publicity, and an issue in political debates,
- legislation and standardization, control and certifying activities at both national and international levels, based on moral obligations and/or on market needs.

A fundamental aspect of safety management is to take care of basic human values, e.g. protection of individuals' life and health, property, human dignity, personal freedom and needs adjusted to requirements for a sustainable development, etc. (Døderlein, 1987). In dealing with risk issues, moral questions are inevitable. The main questions remain the same: „What causes the occupational accidents?" And more importantly, what can be done to avert them? Is it necessary to develop new ways to manage risks? Is it necessary to develop or look further into new methods of risk analysis? Is it necessary to adopt more stringent legislation in the field of risk management? Undoubtedly, what is required is a little of everything mentioned above but, nonetheless, these measures would still not be sufficient.

This paper explores various facets of risk management, the technical aspects as well as the human aspects. Indeed, all accidents have human nature as a basis, which implies that no matter how many laws, regulations and standards are set up, major and minor industrial accidents will always occur since human beings are not infallible. To individual level, as well as at the organizational level, this will take into account the human nature aspect.

2. Review of the Major Occupational Risk Categories

Human error is the most frequent cause of accidents according to many scientific papers (www.csb.gov/assets/document/CSBFinalReportBP.pdf; Hollnagel, 1999; Lee *et al.,* 2004; Moraru *et al.,* 2010; Reason, 1990). But human error is hard to define, as seen in the Major Accident Hazards Bureau database, where 40 % of accidents are classified as „Cause: Human" (http://mahbsrv.jrc.it/mars/Default.html). Some of the conditions that typically lead to human errors are described below:

- inadequate personnel qualifications or training;

- inefficient safety programs and operating instructions;
- ineffective implementation of safety and operating instructions;
- poor housekeeping practices and cleanliness;
- deficient maintenance systems and practices;
- flawed planning and execution of modifications to procedures, operating parameters and equipment etc.

These faults, which are closely related to organizational type errors such as lack of employee training, are common and unfortunately are still the cause of too many accidents.

Technological failures are also often quoted in scientific papers as causes of accidents, especially in the context of leading-edge technologies, as was the case in the accidents of the two space shuttles (Hall, 2003; Pidgeon & O'Leary, 2000). These technological failures are real, but, in several cases several managers had raised numerous red flags that, for various reasons that probably seemed worthwhile at the time, were not given proper attention.
Some of the conditions that may lead to technological failures are described below:

- increased complexity of systems, equipment and procedures;
- flawed process studies;
- faulty equipment design and construction;
- poor control of data processing.

These failures are also strongly related to human and organizational errors.

Organizational failures are also frequently the cause of major accidents. In its web publication „A Management Approach to Creating a Strong Process Safety Culture", the Center for Chemical Process Safety (www.aiche.org/ccps) lists the following key organizational culture findings:

- maintain sense of vulnerability;
- combat normalization of deviance;
- establish an imperative for safety;
- perform valid/timely hazard/risk assessments;
- ensure open and frank communications;
- learn and advance the culture.

Some recommendations to counter organizational failures will necessarily include:

- process safety leadership within the organization;
- integrated and comprehensive process safety management: identify, reduce and manage process safety risks;
- appropriate level of process safety knowledge and expertise for all personnel;
- process safety culture: involve all relevant stakeholders in the development of a positive, trusting and open safety culture (Moraru *et al.*, 2009);

- clearly defined expectations and accountability for process safety at all levels within the organization;
- support for line management at all levels in the organization;
- leading and lagging performance indicators for process safety: develop, implement, maintain and update indicators;
- process safety auditing: establish and implement an effective review system;
- board monitoring: monitor implementation of recommendations.

3. The Influence of Regulations on OHS Risk Management

The objective of laws and regulations is to prevent or limit occupational accidents and illnesses. However, it is important to note that this legislation does not have all of the intended effects and industrial accidents still occur in spite of increasingly abundant and strict regulations, as suggested in Fig. 1. An increase in the amount of legislation did not have the anticipated effect of decreasing the number of accidents.

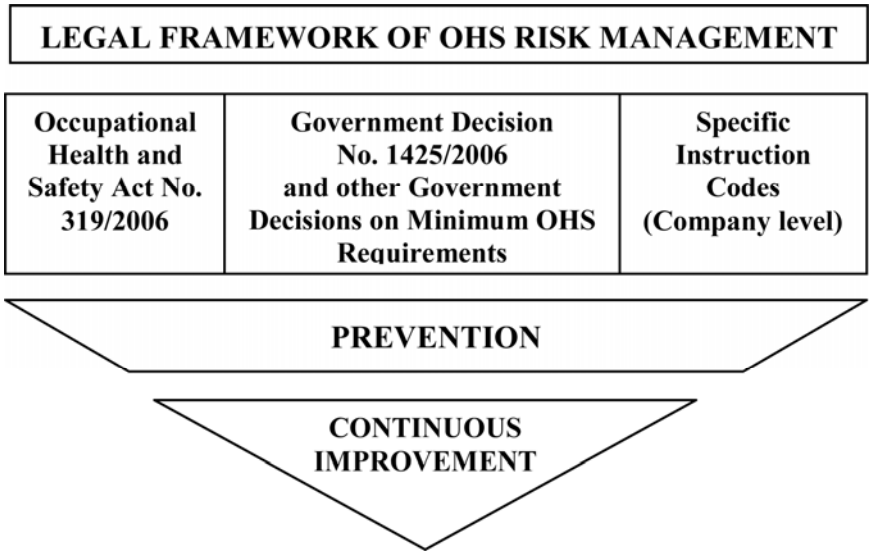

Fig. 1 – Legal framework of OHS risk management in Romania.

Various examples illustrate the limitations of one of the key stakeholders and one of the key mechanisms in the field of risk management:

- The Occupational Safety and Health Act nr. 319/2006 (OSHA)'s national focus on inspecting facilities with high personnel injury rates, while important, has resulted in reduced attention being given to preventing less frequent but catastrophic safety incidents.

- OSHA's capability to inspect highly hazardous facilities and to enforce process safety regulations is insufficient; very few comprehensive process safety inspections were conducted prior to the ISOM incident and "only a limited number of OSHA inspectors have the specialized training and experience needed to perform these complex examinations" (www.csb.gov/assets/document/CSBFinalReportBP.pdf).

4. Comparison Between the Management and Ethical Process for Problem Solving

As seen so far, organizations have implemented systems to manage risk but they must be reinforced to prevent accidents. One other major stakeholder, the government, has also put in place several key mechanisms in the field of risk management, *i.e.* major laws and regulations in the field of environment, occupational health and safety, asset protection, etc., but these mechanisms must also be reinforced. This section presents the responsibility of the other major stakeholder, the human being, *i.e*. employees and supervisor who work in these organizations.

How should managers „think outside the box" when referring to risk management in the organization? These steps are listed below and are then briefly described. They are also illustrated in Fig. 2, which compares the problem solving process to the ethical reasoning process.

Identifying the issue

The identification of the issue will be centered on the manager and the moral dilemma that has to be resolved. It will also include the main elements that must be taken into consideration.

Trusting initial impressions

What appears with one's initial impression when faced with similar situations is often the moral attitude or a start of conscientiousness, a spontaneous attitude that is a mix of competency and social responsibility. This initial impression must undoubtedly be checked and eventually modified, but it would be wrong to dismiss it too quickly under the weight of pressures and constraints.

Speaking, informing, communicating, discussing, negotiating when arguments presented need to be prioritized

Absence and even fear of communication are often observed in companies. The culture of secrecy and silence dominates. But that should not be used as a pretext to subscribe to the phenomenon. This vicious circle must be broken at the risk management level for the company and, through laws and regulations for the public.

The function of communication in all forms is very broad with regards to risk management. It can allow the validation of a technical point of view, identify organizational and personal resistance to responsible risk management,

facilitate management of emotions by expressing them, confront and clarify values, test solutions, etc. It can take various shapes: formal or informal seeking counter-expertise and advice among friends or people with different perspectives. No one can claim to possess good judgement while remaining isolated and deprived of relevant information from other viewpoints.

Communication in different forms is often essential to ethical risk management. At this stage, it is important to pay close attention to arguments used to justify one particular position or another. These arguments are not all on the same level; it may be preferable to sort and prioritize them and treat them on a hierarchical basis (http://ark.cdlib.org/ark:/13030/ ft3n39n8s1/).

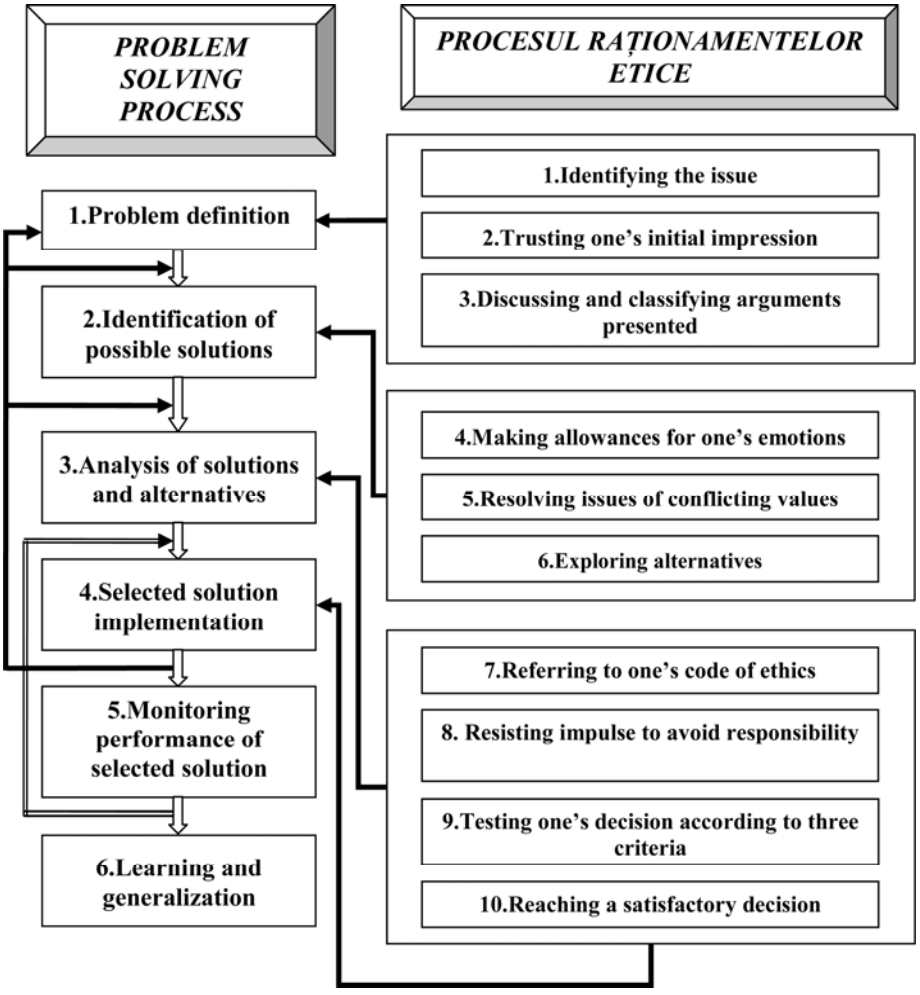

Fig. 2 – Problem solving process and ethical reasoning process (Lacoursiere *et al.*, 2003).

Becoming aware of emotions to better manage them

Managers are not robots. Their emotions play a certain part in their managerial decisions and it would be wrong to deny this. It is advantageous to become aware of one's feelings and emotions, and to speak to reliable people about them when need be, to be able to manage them with greater clarity.

Identifying any conflicting values and identifying the values which must have priority

A good way for clarifying things is to determine which value must have priority, but this determination is often a difficult operation. In the OHS case, this operation is facilitated by the existence of a multitude of rules and regulations, not to mention the various codes of ethics that are found in many professions.

Knowing laws, regulations and code of ethics and recognizing situations where they apply

Our use of the knowledge of laws and regulations is more „practical" than legal, starting from its underlying values. From this point of view, two aspects deserve to be mentioned: First of all there is the importance given to risk management by various laws and regulations. Secondly, in the eyes of the legislator, the manager is the person in charge, the guard of public safety.

Identifying all possible alternatives with their advantages and disadvantages

A frequent error in our personal life as in our professional one is to neglect to adequately explore the whole field of possible alternatives. This is often the case when a decision is made in the throes of emotions, in an emergency situation or in a climate of conflict.

Resisting the impulse to avoid responsibility

The reactive discourse in which company problems, or this or that type of culture are prominent features, but individual responsibility in problem solving is never mentioned.

Testing decisions according to three criteria

- *Criterion of transparency:* It is usually agreed that an ethical decision can be recognized and can even be made public. Reasonable and well-informed individuals cannot blame the honesty or good faith of the ones who reached the decision, even if they do not necessarily share it. In the case of a decision requiring confidentiality, a committee obliged to discretion would come to the same conclusion.
- *Criterion of exemplarity:* An ethical decision can usually serve as a model, all things considered and in similar cases, whether in engineering or in other professions (Racine *et al.,* 1991).
- *Criterion of reciprocity:* This criterion is universal and is found in all great religious or philosophical traditions. It is seen, for example, in the Gospel in a well-known form: „do onto others as you would have others do on to you". An ethical decision must be fair or all at least reasonable for all parties involved.

5. Reaching Satisfactory Decisions by Making a Clear Distinction Between „Options" and „Methods"

Why speak of an acceptable decision and not of an ethical decision? Because, from the ethical point of view adopted here, the acceptability of a decision and its ethical character are the same thing. Why not speak of a decision that is actually accepted? To take into account the limit of what can be done. An ethical solution is not an ideal decision that necessarily has unanimous support and, whether or not it is accepted does not solely depend on the decision maker.

6. Conclusion

In discussions on risk issues it is also important to be aware of the two main approaches for defending moral actions: 1) ethics of the mind - focusing on the purpose, meaning or intention of the action. 2) ethics of the consequence - focusing on the good or bad results of an action. The moral guides and regulates behavior. Decisions may be difficult for a number of reasons. Safety is an unequally distributed benefit in society, *e.g.* employees in construction and in traditional industry are more exposed to accidents than the total work force. Only small amounts of money are used to prevent the enormous amount of accidents among the increasing number of old people. A little money extra to this work would have maximum impact on the fatal accident statistics. But is the modest effort based on implicit economic considerations of the value of human lives? In industry people at high risk are usually low-income workers, in other words; they have negative risk compensation. They have also very often higher risk exposure in traffic, at home and local community, *i.e.* a risk concentration which support the doctrines of the sociology of stratification.

The concept of saving „statistical lives" is a logical contradiction. Death is inevitable. But expectations of an increase in average length of life, is a performance measure for investments and priorities of resources in a framework of utility and cost-effectiveness. Most people will apply a completely different ethics of reasoning when it comes to identified individuals at extreme danger both regarding priorities on rescue operations in accidents and on medical treatment of deadly diseases, *i.e.* an obligation to do whatever possible at whatever cost to save the person.

With an increase in the complex structure of society, trade and industry, communication, political and administrative systems, technical systems and technological change etc., it is getting more and more important to relate to different ethical and political arguments to keep an image of being in control and for being trusted.

For all of us, it is necessary to continue the whole process, to continue improving risk analysis methods, to continue training in the field of risk

management for numerous stakeholders, it is necessary to continue reinforcing legislation to structure and make risk management compulsory, and at the organizational and business levels, it is necessary to set up a real „division of powers", based on ethical principles that allow dialogue. All stakeholders - companies, organizations, governments, managers - must strengthen their roles to avoid major accidents.

REFERENCES

*** CCPS, *A Management Approach to Creating a Strong Process Safety Culture* (*20 Elements for Success*), American Institute of Chemical Engineers - AIChE, Centre for Chemical Process Safety – CCPS, 2005 (www.aiche.org/ccps).

*** CSB, *Refinery Explosion and Fire (BP, Texas City, Texas, March 23, 2005) - Report Investigation No. 2005-04-I-TX*, US Chemical Safety and Hazard Investigation Board, 2007 (www.csb.gov/assets/document/CSBFinalReportBP.pdf).

*** MAHB, *MARS - Major Accident Reporting System.* Major Accident Hazards Bureau - MAHB (http://mahbsrv.jrc.it/mars/Default.html).

Døderlein J., *Introduction to Risk and Decisions*, In W.T. Singleton & J. Hovden (Eds.) Risk and Decisions, Wiley, Chichester, 1987.

Hall J.L., *Columbia and Challenger: Organizational Failure at NASA.* Space Policy, **19**, *4*, 239-247 (2003).

Hollnagel E., Kaarstad M., Lee H-C., *Error mode prediction*, Ergonomics, **42**, *11*, 1457-1471 (1999).

Lacoursiere J-P., Dastous P-A., Racine L., Lafontaine G., Legault G.A., *Notes de Cours Pour la Formation Intensive en Gestion des Risques Pour Ingenieurs et Autres Specialists*. Université de Sherbrooke, Québec, Canada, 2003.

Lee Y.S., Kim Y., Kim S.H., Kim C., Chung C.H., Jung W.D., *Analysis of Human Error and Organizational Deficiency in Events Considering Risk Significance.* Nuclear Engineering and Design, **230**, 61-67 (2004).

Moraru R,. Băbuţ G., Cioca L.I., *Adressing the Human Error Assessment and Management*. Archives of Mining Sciences, **55**, *4*, 873-878 (2010).

Moraru R.I., Băbuţ G.B, Cioca L.I., *Risk Interpretation and Decision Making in Occupational Risk Management.* Annals of the University of Petroşani - Mining Engineering, **10** (**XXXVII**), Universitas Publishing House, Petroşani, 223-230 (2009).

Pidgeon N., O'Leary M., *Man-Made Disasters: Why Technology and Organizations* (*Sometimes*) *Fail.* Safety Science, **34**, *1-3*, 15-30 (2000).

Racine L., Legault G.A., Begin L., *Éthique et ingénierie*. Éditions McGraw-Hill, Montréal, Québec, Canada, 1991.

Reason J., *The Contribution of Latent Human Failures to the Breakdown of Complex Systems*. Philosophical Transactions of the Royal Society of London, Series **B**. *327*, 475-484 (1990).

Shrader-Frechette K.S., *Risk and Rationality. Philosophical Foundations for Populist Reforms*. University of California Press, Berkeley, USA, 1991 (http://ark.cdlib.org/ark:/13030/ ft3n39n8s1/).

IMPLICAREA FACTORILOR INTERESAŢI ŞI ASPECTELE ETICE ALE MANAGEMENTULUI SECURITĂŢII ŞI SĂNĂTĂŢII ÎN MUNCĂ ÎN ROMÂNIA

(Rezumat)

Există întotdeauna o dimensiune etică insuficient explorată care transcede simpla inventariere a cauzelor accidentelor de muncă. Aceasta conduce la o cascadă de decizii inadecvate, adoptate la nivel organizaţional, uman şi tehnic, deseori consecinţele materializându-se în accidente tragice, de multe ori soldate cu pierderi de vieţi omeneşti. Pentru a gestiona riscurile în mod corespunzător, nu va fi necesară doar dezvoltarea de tehnici specifice, ci şi elaborarea şi dezvoltarea de procese, atât la nivelul lucrătorilor, cât şi la nivel organizaţional, procese care trebuie să ia în considerare natura umană. Mecanisme adecvate vor trebui, de asemenea, implementate, în vederea reconcilierii „interesului public" cu „managementul riscurilor". Va fi astfel necesară definirea, implementarea şi îmbunătăţirea unei succesiuni de procese şi, cel mai important, furnizarea de îndrumare pentru manageri. Se impune îmbunătăţirea, în continuare, a metodelor de analiză a riscurilor, perfecţionarea formării în domeniul gestiunii riscurilor a factorilor interesaţi, consolidarea legislaţiei şi fundamentarea managementului riscurilor pe principii de ordin moral. Lucrarea îşi propune să introducă în atenţia specialiştilor români din domeniu valorile şi principiile care ar trebui aplicate în adoptarea şi materializarea deciziilor privind securitatea şi sănătatea în muncă. Desigur, nu există un răspuns unic sau simplu referitor la ceea ce poate fi considerat drept sigur. Ca urmare, scopul prezentei lucrări este de a sugera o abordare alternativă şi de a furniza un tip diferit de raţionament în ceea ce priveşte întrebările fundamentale care îi preocupă pe specialiştii români din domeniul managementului securităţii şi sănătăţii în muncă.

BULETINUL INSTITUTULUI POLITEHNIC DIN IAŞI
Publicat de
Universitatea Tehnică „Gheorghe Asachi" din Iaşi
Tomul LVII (LXI), Fasc. 4, 2011
Secţia
ŞTIINŢA ŞI INGINERIA MATERIALELOR

HEAT RECOVERY OF FLUE GAS EXHAUSTED FROM HEATING FURNACES

BY

DORIAN MUŞAT*, MIHAI UDRIŞTE and AUREL GABA

Valahia University of Targovişte

Received: April 14, 2011
Accepted for publication: June 27, 2011

Abstract. This paper presents solutions for the recovery of the physical heat in the flue gas exhausted from heating furnaces in the metallic materials industry. Technological recovery solutions and preheating installations based on flue gas are presented. In order to determine the size of the air pre-heaters recovering the flue gas heat, a mathematical model transcribed in C_{++} has been used.

This computer program has been used for sizing an air pre-heater recovering the heat of flue gas exhausted from a pusher furnace. Sizing was done in conditions simulating the operation of the pre-heater with different thicknesses of the layer of particles deposited on the side of the flue gas. Following the simulation possibilities through the use of the computer program, it was possible to size the pre-heater in order to obtain a maximum efficiency of the recovery of the flue gas heat exhausted from the heating furnace.

The experimental results obtained on this air pre-heater are consistent with those obtained by simulating the operation with the software.

Key words: recovery, flue gas heat, heating furnace.

1. Introduction

In the context of the general actions meant to optimize the specific energy consumptions, a special attention is given, in the metallic materials

* Corresponding author e-mail: dormus60@yahoo.com

industry, to the recovery of secondary heat resources. An important secondary energy resource is the physical heat of the flue gas exhausted from heating furnaces. These heating furnaces work at temperatures ranging from 700 to 1400ºC and heat semi-products for a subsequent hot deformation.

The most common heating furnaces are (Brunklaus, 1977):

- Fixed hearth furnaces;
- Mobile hearth furnaces;
- Bogie hearth furnaces;
- Walking been furnaces;
- Pusher furnaces;
- Pit furnaces.

Burned exhaust gas temperature can reach temperatures up to 1450°C.

Due to significant heat losses mainly from the physical heat of the flue gas discharged, the efficiency of many heating furnaces does not go over 30%, while fuel consumption rate is between 15-60% (Mediokritskii *et al.,* 1997).

The recovery of the physical heat of the flue gas exhausted from heating furnaces can be carried out in the technological direction and in the energy-recovery direction. The technological recovery is done through the preheating of the combustion air, through the preheating of the low calorific gas fuel and through the pre-heating of the semi-products using a ventilator that takes the flue gas off the air pre-heater and sends it, through some nozzles arranged equidistantly, in which speeds of about 80 m/s are obtained, onto the surface of the melting stock. The recovery in the energy-recovery direction results in the production of thermal energy, usually under the form of steam (Gaba, 1990).

In Table 1, are presented the main types of heat recovery used to preheat the combustion air, with the temperature ranges of the flue gases within which they can be used (Brunklaus, 1977; Popa *et al.,* 1977; Ghia, 1978).

Table 1

Main Heat Recovery Types Used for Preheating the Combustion Air

Heat recovery		Temperature ranges of the flue gas	Temperatures of the preheated air
Convection recovery	-With plain steel tubes -With acicular prominences	• 400-900ºC • 500-800ºC	200-600ºC 300-450ºC
Thermo-bloc recovery		700-1150ºC	220-450ºC
Radiation recovery		800-1600ºC	500-800ºC
Mixed recovery		700-1200ºC	500-700ºC

Given the low thermal efficiency of the heating furnaces, the heat recovery should take place in the technological direction, by achieving performance recovery, the combustion air being heated to temperatures as high as possible. In integrated steel mill plants, where heating furnaces are supplied

with combustible waste gases with low calorific value (blast furnace gas mixed with coke oven gas or natural gas), the preheating in special pre-heaters placed after the combustion air heaters becomes interesting from an economical viewpoint. The solution of preheating the semi -products is rarely used, because of the high investment required (Popa *et al.,* 1977).

As in iron and steel works, walking been furnaces and pusher furnaces are widely used, evacuating flue gases at temperatures of 700-950ºC, for which it is advisable to use convection air pre-heaters, we undertook the realization of a mathematical model and of a computer program for sizing them.

2. Description of the Mathematical Model Used for Sizing the Convection Pre-Heaters

The mathematical model used for sizing the convection pre-heaters was conceived to obtain a maximum efficiency in the recovery of the heat of the flue gases throughout the area of the heating furnace. For different operating regimes, the mathematical model takes into account the values pertaining to: fuel flow, DC, fuel nature and makeup, flue gas temperature, TGI, air excess coefficient at the exit of the oven, α_i , air excess coefficient at the entrance in the burner, α, air temperature at the entrance in the pre-heater, TAI, ambient air temperature, TAM. At the same times, other input variables are introduced as well, deriving from the pre-heater's construction model, such as:

- $\Delta\alpha$ - value of the air coefficient increase from the entrance to the exit of the pre-heater;
- DI [m] - inner diameter of pipe;
- DE [m] – outer diameter of pipe;
- LT [m] - pipe length by one passing;
- LV [m] - height tube plate;
- LO [m] - length tube plate;
- PV [m] - spacing between pipes on vertical;
- PO [m] - spacing between pipes on horizontal;
- DV [m] - vertical distance from the wall;
- DO [m] - horizontal distance from the wall;
- NTR - number of passes;
- PRES [bar] -pressure;
- GF [m] - soot layer thickness;
- LAF [W/m/ ºC] - soot layer conductivity;
- LAMDAO [W/m/ ºC] - steel conductivity.

Also as input data are introduced:

- flow regime of the two fluids (same sense current, counter current, crossed current);
- position of pipes;
- ways of circulation of the two fluids.

For a start, the mathematical model calculates the air flow and the flue gas flow at the entrance in the pre-heater, respectively DAI and DGAI, in respectively [m^3_N air /h] and [m^3_N flue gas /h], after which it determines the heat quantity contained by the air at the entrance in the pre-heater, QAI and the heat quantity contained by the flue gas at the entrance in the pre-heater, QGI, in [W]. The temperature of the flue gas at the exit from the pre-heater, TGE, is determined through successive approximations from the relation describing the energy balance of the two fluids, taking into account the heat losses in the ambient air and the preheating temperature of the combustion air, TAE.

The flow scheme of the two fluids allows the calculation of the logarithmic mean temperature difference, ΔTMED and the average air temperatures, TMA and the average flue gas temperatures, TMG. The equivalent hydraulic equivalent is calculated and the sections and speeds of the fluids, having as input data the pipes' inner and outer diameter and the geometry of the heat exchanger with the distances between pipes.

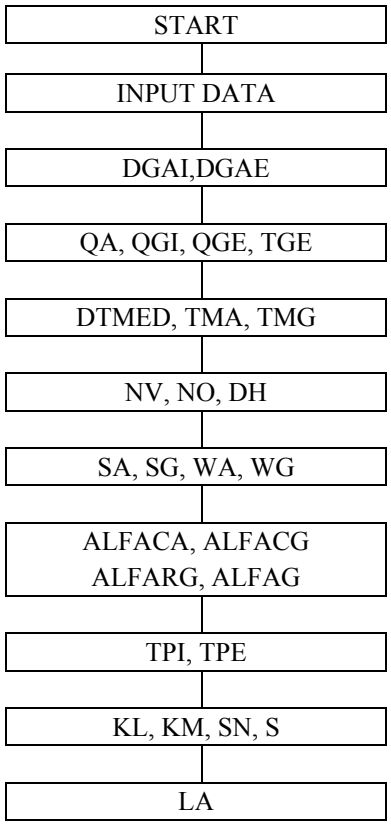

Fig. 1- Algorithm of the mathematical model for sizing the convection pre-heaters.

The convection coefficient for air and flue gas is calculated using the relations with invariants given according to the value of Reynolds invariant, type of flow, etc.

The radiation coefficient for gases is calculated from the Stephan - Boltzmann relation using the emissivity coefficients, which depend on the average gas temperature, the pipe wall temperature and the partial pressure of gases, CO_2 and H_2O, multiplied by the gas layer thickness.

The required heat exchange surface is determined on the basis of the global heat transfer coefficient and then is compared to the geometric surface of the heat exchanger chosen, until the moment when, by successive modifications of the heat exchanger's geometry, a maximal difference of 0.3% is reached.

The algorithm of the mathematical model for sizing the convection pre-heaters is presented in Fig. 1.

3. Application for Sizing a Convection Air Pre-Heater

The application was carried out for sizing a convection air pre-heater of a pusher furnace.

The computer program was run for different functioning regimes of the pusher furnace, given by the natural gas flow, the temperature and the flue gas makeup at the exit of the furnace. The maximal preheating temperature was imposed by the burner, being TAE=490°C.

A computer listing obtained for this sizing is shown in Table.2.

Table 2

Computer Listing Obtained for Sizing a Convection Air Furnace Using Propulsion

No	Notation	Symbol	U.M.	Value
	Inlet data			
	Composition of fuel			
1	Carbon dioxide	CO_2	m^3N/ m^3N	0.0
2	Carbon oxide	CO	m^3N/ m^3N	0.0
3	Hydrogen	H_2	m^3N/ m^3N	0.0
4	Hydrogen sulfide	H_2S	m^3N/ m^3N	0.0
5	Methane	CH_4	m^3N/ m^3N	0.98
6	Acetylene	C_2H_2	m^3N/ m^3N	0.0
7	Ethane	C_2H_6	m^3N/ m^3N	0.01
8	Propene	C_3H_2	m^3N/ m^3N	0.0
9	Propane	C_3H_8	m^3N/ m^3N	0.0
10	C_4H_8	C_4H_8	m^3N/ m^3N	0.0
11	Butane	C_4H_{10}	m^3N/ m^3N	0.0
12	Pentane	C_5H_{12}	m^3N/ m^3N	0.0
13	Nitrogen	N_2	m^3N/ m^3N	0.01
14	Oxygen	O_2	m^3N/ m^3N	0
15	Fuel Flow	DC	m^3N/h	3800

Tables 2 (Continuation)

No	Notation	Symbol	U.M.	Value
16	Air Flow	DA	kg/h	41462.005
17	Inlet air temp.	TAI	º C	10
18	Outlet air temp.	TAE	º C	490
19	Heat exchanger efficiency	ETA	-	0.98
20	Air excess coefficient to burner	ALF	-	1.13
21	Ambient temperature	TAM	ºC	10
22	Inlet exhaust gases temperature	TGI	ºC	900
23	Inner diameter of pipe	DI	m	0.0428
24	Outer diameter of pipe	DE	m	0.048
25	Pipe length by one passing	LT	m	1.35
26	Height tube plate	LV	m	0.68
27	Length tube plate	LO	m	6.76
28	Spacing between pipes on vertical	PV	m	0.08
29	Spacing between pipes on horizontal	PO	m	0.098
30	Vertical distance to the wall	DV	m	0.05
31	Horizontal distance to the wall	DO	m	0.05
32	Passes number	NTR	-	4
33	Pressure	p	barr	1
34	Thickness of soot layer	GF	m	0.0
35	Soot thermal conductivity	LAF	W/(m ºC)	0.1
36	Steel thermal conductivity	LAMDAO	W/(m ºC)	50
	Outlet data			
37	Inlet exhaust gases flow	DGAI	m^3N/h	45281.005
38	Outlet exhaust gases flow	DGAE	m^3N/h	45281.005
39	Mean caloric capacity of the inlet gases	CPI	kJ/ (m^3N ºC)	1.5271679
40	Mean caloric capacity of the outlet gases	CPE	kJ/ (m^3N ºC)	1.4661095
41	Heat included in the inlet gases	QGI	W	17287924
42	Heat included in the outlet gases	QGE	W	9559561.4
43	Outlet exhaust gases temperature	TGE	ºC	518.39166
44	Mean temperature difference	DTMED	ºC	448.28489
45	Mean temperature of gases	TMG	ºC	709.19583
46	Mean temperature of air	TMA	ºC	260.91094
47	Absorbed heat of air	QA	W	7573795.7
48	Pipes number on a line by one vertical passing	NV	-	7
49	Pipes number on a line by one horizontal passing	NO	-	68
50	Gas flow section	SG	m^2	4.7196
51	Air flow section	SA	m^2	0.68483412
52	Gas velocity	WG	m/s	9.5883484
53	Air velocity	WA	m/s	32.890357
54	Gas convection heat transfer coefficient	ALFACG	W/(m^2 ºC)	65.258761

Tables 2 (Continuation)

No	Notation	Symbol	U.M.	Value
55	Air convection heat transfer coefficient	ALFACA	W/(m^2 ºC)	117.85501
56	Thickness of gases layer	LG	m	0.14406167
57	Radiation coefficient	ALFARG	W/(m^2 ºC)	12.672184
58	Convection heat transfer coefficient from gases	ALFAG	W/(m^2 ºC)	77.930946
59	Overall heat transfer coefficient	KL	W/(m ºC)	6.576321
60	Overall surface heat transfer coefficient	KM	W/(m^2 ºC)	46.106673
61	Length of the device	LA	m	1.3493032
62	Heat transfer surface	S	m^2	366.65933
63	Necessary heat transfer surface	SN	m^2	366.43394
64	Air pressure losses	PA	N/m^2	4189.4701
65	Gas pressure losses	PGA	N/m^2	204.06471

As during the operation of the furnace, some of its parameters change (the fuel flow, the discharge temperature of the flue gas), which triggers the modification of the air pre-heater, the program was run taking into account the different values of the inlet data. In this way, it was possible to choose the most efficient air pre-heater. For this pre-heater, the program was run taking into account the thickness of the soot layer, GF and the air excess coefficient of the flue gas, α_i . The result led to the determination of the influence of the soot layer, GF and of the air excess coefficient of the flue gas, α_i, on the preheating temperature of the combustion air, TAE, which is presented in Table 3.

Table 3

Influence of the Soot Layer, GF and of the Air Excess Coefficient of the Flue Gas, α_i, on the Preheating Temperature of the Combustion Air, TAE

Nr. crt.	α_i	DGAI m^{3}N/h	TGI °C	GF mm	TAE °C
0	1	2	3	4	5
1	1,13	45000	900	4	490
	1,13	45000	900	0	450
	1,13	45000	900	0,3	405
2	1,26	50000	820	0,8	450
	1,26	50000	820	0	417
	1,26	50000	820	0,3	372
3	1,4	55000	750	0	419
	1,4	55000	750	0,3	388
	1,4	55000	750	0,8	345

4. Experimental Results

As the heat recovery installation has been set up recently, we have been able to take over exploitation data for the functioning of the pre-heater without soot deposits, and also for different discharge temperatures, TGI and diverse air excess coefficients of the exhausted flue gas, α_i.

These values obtained experimentally are noted as dots in Fig. 2, where there are presented, under the form of curves, the variation of the preheating temperature of the combustion air, depending on the thickness of the soot layer GF and on the air excess coefficient of the exhausted flue gas, α_i.

A good consistency can be noticed between the experimental values and the values obtained on the basis of the mathematical model.

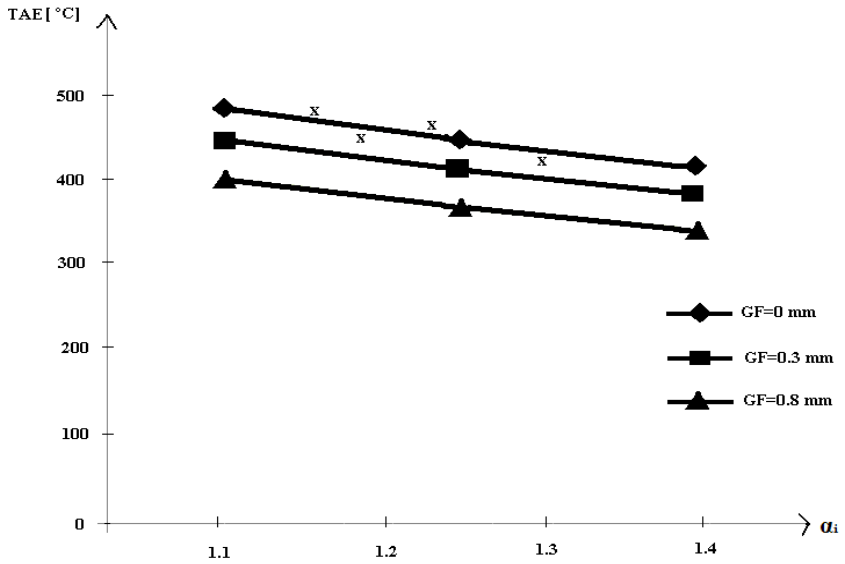

Fig. 2 – Variation of the preheating temperature of the combustion air, TAE, taking into account the thickness of soot layer, GF and the air excess coefficient of exhausted flue gas, α_i.

- values obtained using the mathematical model – continuous line;
-experimentally obtained values – dots marked under the form of "x"-es.

3. Conclusion

The recovery of the physical heat of the flue gas exhausted from furnaces in the metallic materials industry can be carried out in the technological direction, by preheating the combustion air, by preheating the gaseous fuel with

a low calorific power and by preheating the semi-products and in the energy direction, usually under the form of steam. Taking into account the low efficiency of the furnaces, the technological recovery should be preferred, through the realization of a high-performance recovery, using installations able to heat the combustion air at temperatures as much as possible

In order to determine the size of the air pre-heaters recovering the flue gas heat, a mathematical model transcribed in C_{++} has been used.

This computer program has been used for sizing an air pre-heater recovering the heat of flue gas exhausted from a pusher furnace. Sizing was done in conditions simulating the operation of the pre-heater with different thicknesses of the layer of particles deposited on the side of the flue gas. Following the simulation possibilities through the use of the computer program, it was possible to size the pre-heater in order to obtain a maximum efficiency of the recovery of the flue gas heat exhausted from the heating furnace.

The experimental results obtained on this air pre-heater are consistent with those obtained by computer simulation.

REFERENCES

Brunklaus J.H., *Cuptoare industriale*. Bucureşti, Ed. Tehnică 1977.

Mediokritskii E.I., Gaponov V.I., Loginov V.E., Journal of Engineering Physics and Thermophysics, **70**, *1*, 1997.

Gaba A., *Consideraţii asupra recuperării căldurii fizice a gazelor arse evacuate din cuptoarele adânci*. Bucureşti,Energetica, **38**, *3-4*, 1990.

Popa B. *et al., Schimbatoare de caldura industriale.* Bucuresti, Editura Tehnica 1977.

Ghia V., *Récupérateurs et régénérateurs de chaleur*. Ed. Eyrolles, Paris, 1978.

CONSIDERAŢII ASUPRA RECUPERĂRII CĂLDURII GAZELOR ARSE EVACUATE DIN CUPTOARELE DE ÎNCĂLZIRE DIN INDUSTRIA MATERIALELOR METALICE

(Rezumat)

Lucrarea prezintă soluţiile de recuperare a căldurii fizice a gazelor arse evacuate din cuptoarele de încălzire din industria materialelor metalice. Sunt prezentate soluţii de recuperare în direcţie tehnologică şi instalaţii de preâncălzire a aerului de combustie. Pentru dimensionarea preăncălzitoarelor de aer ce recuperează căldura gazelor arse evacuate din cuptoarele de încălzire s-a realizat un model matematic ce a fost transcris în C_{++}.

Acest program de calcul a fost utilizat în dimensionarea unui preâncălzitor de aer ce recuperează căldura gazelor arse evacuate dintr-un cuptor cu propulsie.

Dimensionarea s-a făcut în condiţiile simulării funcţionării preâncălzitorului cu diverse grosimi ale stratului de depunere de particule pe partea gazelor arse evacuate. Ca urmare a posibilităţilor de simulare prin utilizarea programului de calculator, s-a putut dimensiona preâncălzitorul, pentru a obţine o eficienţă maximă a recuperării gazelor arse evacuate din cuptorul de încălzire.

Rezultatele experimentale obţinute pe aceast preâncălzitor de aer sunt în concordanţă cu cele obţinute prin simularea funcţionării cu ajutorul programului de calculator.

BULETINUL INSTITUTULUI POLITEHNIC DIN IAŞI
Publicat de
Universitatea Tehnică „Gheorghe Asachi” din Iaşi
Tomul LVII (LXI), Fasc. 4, 2011
Secţia
ŞTIINŢA ŞI INGINERIA MATERIALELOR

COMPARATIVE ANALYSIS BETWEEN EOLIAN AND KINETIC MINIHIDROTURBINE

BY

EUGEN-VLAD NĂSTASE* and DORU CĂLĂRAŞU

"Gheorghe Asachi" Technical University of Iaşi,
Department of Fluid Mechanics

Received: April 14, 2011
Accepted for publication: June 27, 2011

Abstract. The purpose of this paper is to conduct a comparative analysis between eolian and kinetic minihidroturbine. The paper will trace the advantages and disadvantages of the two types of turbines. Will also pursue the possibility of applying the theory of wind turbine design for kinetic minihidroturbine.

Key words: turbine, renewable energy, hydropower.

1. Introduction

The energy has made a significant contribution to human development and technological achievement through history. With an ever increasing demand for energy resources, and global concern about pollution and environmental damage arising from fossil fuels; renewable energy may begin to assert an ever increasing role during this century and beyond. By 2020 renewable energy should account for 20% of the EU's final energy consumption. To meet this common target, each Member State, including Romania, needs to increase its production and use of renewable energy in electricity, heating and cooling and

* Corresponding author e-mail: nastase_eugenvlad@yahoo.com

transport. Renewable energy is basically the energy that comes from natural sources such as wind, sunlight, tides, rain, and geothermal heat. An important resource of renewable energy for Romania is water (http://www.enreg-expo.com). In our country it operates only a third of the hydropower potential. Romania has a significant potential of small hydro turbines. In developed countries, is testing this new technology - the conversion of kinetic energy of water currents - the technology that does not require dams, large areas of water accumulation and is considered more advanced and cleaner (Niet, 2001). The technology is similar to the modern technology of wind energy conversion of wind turbines.

2. Mathematical Model

Turbines extract only a part of the kinetic energy of fluid flow. To estimate the extracted power from the fluid current is considered the model presented in the below Fig. 1. In this model the turbine is considered as a disc, 1 is upstream section and 2 is downstream section:

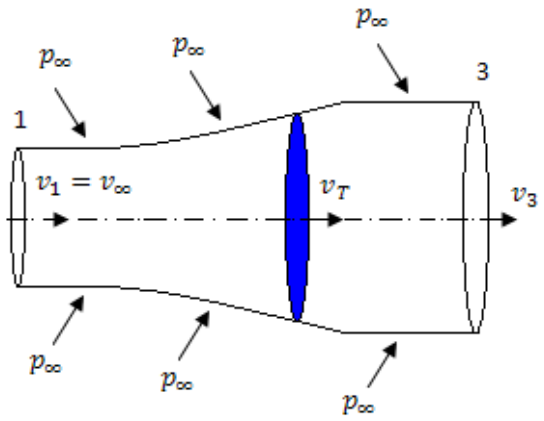

Fig. 1 – Control volume for the idealised actuator-disk analysis.

$$P = \rho Q\left(\frac{v_1^2}{2} - \frac{v_3^2}{2}\right) \text{ - extracted power} \quad (1)$$

$$F_a = \rho Q(v_1 - v_3) \text{ - axial force} \quad (2)$$

$$P = F_a v_T \quad (3)$$

$$Q = v_T S = v_1 S_1 = v_3 S_3 \text{ - flow} \quad (4)$$

From relations (3), (1) and (2) we have:

$$v_T = \frac{P}{F_a} = \frac{\rho Q (v_1^2 - v_3^2)}{2\rho Q (v_1 - v_3)} = \frac{v_1 + v_3}{2}$$ - current velocity on the turbine (5)

Using these relationships are further defined in the following coefficients:

$$K_{VT} = \frac{v_T}{v_1}$$ - turbine speed coefficient (6)

$$K_{V3} = \frac{v_3}{v_1}$$ - downstream speed coefficient (7)

Given equation (5) turbine speed coefficient becomes:

$$K_{VT} = \frac{v_1 + v_3}{2v_1} = \frac{1}{2}\left(1 + \frac{v_3}{v_1}\right) = \frac{1}{2}(1 + K_{V3})$$ (8)

Power coefficient and axial force coefficient can be expressed as:

$$C_p = \frac{1}{2}(1 + k_{v3})(1 - k_{v3}^2)$$ (9)

Noting $k_{v3} = t$ our expression for the coefficient of power:

$$C_p(t) = -\frac{1}{2}t^3 - \frac{1}{2}t^2 + \frac{1}{2}t + \frac{1}{2}$$ (10)

The extreme condition for power coefficient have its maximum value is 0,59. This model provides a good indication for the efficiency of a propeller, but not the blade design because does not take into account the shape of the propeller. Estimate the axial and tangential efforts are using blade element theory (Fig. 2):

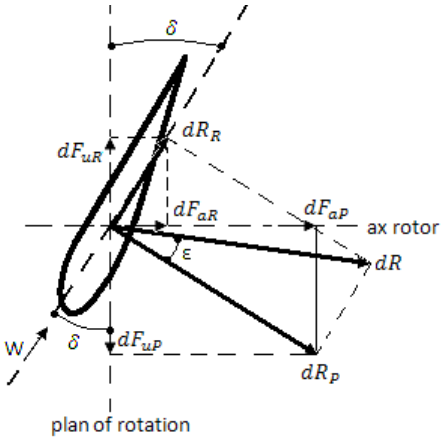

Fig. 2 – Blade cross-section diagram used to derive forces.

In the figure above were noted: w - fluid velocity at far upstream, δ - angle between the direction of the flow and the rotor plane, dR_P - element of lift force, dR_R - element of drag force.

3. Conclusion

The main conclusions of the present paper are the following:

Exploitation of renewable energy is an overriding goal to be achieved, because in this way diminishes the disadvantages of using fossil fuels for energy purposes. Using the kinetic energy of rivers does not require special construction (dams or powerhouse). This means that the environment is less affected and the costs are reduced. Advantage of using turbines that convert the kinetic energy of water is much higher power density compared to a wind turbine the same size. Wind turbine design technology can be successfully applied in the case of turbine that uses the kinetic energy of water.

REFERENCES

Coiro D.P., Maisto U., Scherillo F., Melone,S., Grasso F., *Horizontal Axis Tidal Current Turbine: Numerical and Experimental Investigations.* Owemes, Civitavecchia, Italy, 2006.

Gaden D.L.F., *An Investigation of River Kinetic Turbines: Performance Enhancements, Turbine Modelling Techniques, and an Assessment of Turbulence Models*. University of Manitoba, Canada, 2007.

Niet T.A., *Modelling Renewable Energy at Race Rocks*. University of Victoria, 2001.

Sobor I., Kobîleaţkii N., *Tendinţe moderne în tehnologia de conversie a energiei eoliene şi a energiei cinetice a curenţilor de apă*. Conferinta Tehnico – Stiintifică Jubiliară a Colaboratorilor, Doctoranzilor si Studenţilor, 8-9 oct./Univ. Teh. a Moldovei. Chişinău, Editura UTM, 299-302 (2004).

* * * http://www.enreg- expo.com/fileadmin/Renewable_Energy_in_Romania.ppt.pdf

ANALIZĂ COMPARATIVĂ ÎNTRE TURBINELE EOLIENE ŞI MINIHIDROTURBINELE CINETICE

(Rezumat)

În acestă lucrare se realizează o analiză comparativă între turbinele eoliene şi minihidroturbinele cinetice. Se au în vedere avantajele şi dezavantajele celor două tipuri de turbine şi de asemenea, posibilitatea de a aplica teoria de proiectare a turbinelor eoliene pentru minihidroturbine cinetice.

BULETINUL INSTITUTULUI POLITEHNIC DIN IAŞI
Publicat de
Universitatea Tehnică „Gheorghe Asachi" din Iaşi
Tomul LVII (LXI), Fasc. 4, 2011
Secţia
ŞTIINŢA ŞI INGINERIA MATERIALELOR

FLOW SIMULATION FOR KINETIC MINIHIDROTURBINE

BY

EUGEN-VLAD NĂSTASE* and DORU CĂLĂRAŞU

"Gheorghe Asachi" Technical University of Iaşi,
Department of Fluid Mechanics

Received: April 14, 2011
Accepted for publication: June 27, 2011

Abstract. In the field of hydraulic machinery, flow simulation is used in research and development as well as in the design phase. The simulation offers the possibility of viewing flow fluid during operation what gives a picture of how the turbine works and how it could be improved. The simulation leads to the unsteady pressure distribution especially on blades. From this results the dynamic forces can be evaluated. By applying a structural analysis also the dynamic stresses can be obtained. The purpose of this paper is to achieve a turbine flow kinetic simulation has been tested experimentally. Since for this geometry detailed measurements are available, the computational results can be compared with experimental data.

Key words: simulation, flow simulation, modelling, computational fluid dynamics turbine, renewable energy, hydropower.

1. Introduction

The present energetic context leads to the research of renewable energy sources. The diminution of conventional energy resources, the increasing of the oil price and the problems regarding the pollution also, made together the interest in the renewable energy sources. The conversion of water energy to useful energy involves two processes: the primary process of extracting kinetic energy from

* Corresponding author e-mail: nastase_eugenvlad@yahoo.com

water and conversion to mechanical energy at the rotor axis, and the secondary process of the conversion into useful energy (mostly electrical, but also mechanical for water pumps or chemical for water desalination). The type of water turbines employed can be characterized by their rotational axis orientation with regard to the water flow direction. The Axial Flow Water Turbine (AFWT) has an axis of rotation parallel to the current direction and its rotor must be controlled to follow the current direction, in order to increase the power conversion efficiency. Otherwise, if the rotational axis is perpendicular to the current, the turbine can operate whatever the flow direction. These turbines are known as Cross Flow Water Turbine (CFWT) (Molland *et al*., 2004). Lift and drag forces along with the angle of attack are the important parameters in a water turbine system. These parameters decide the efficiency of the kinetic hydraulic turbine.

Lift on a body is defined as the force on the body in a direction normal to the flow direction. Lift will only be present if the fluid incorporates a circulatory flow about the body such as that which exists about a spinning cylinder. The velocity above the body is increased and so the static pressure is reduced. The velocity beneath is slowed down, giving an increase in static pressure. So, there is a normal force upwards called the lift force. The drag on a body in an oncoming flow is defined as the force on the body in a direction parallel to the flow direction. For a windmill to operate efficiently the lift force should be high and drag force should be low. For small angles of attack, lift force is high and drag force is low. If the angles of attack (α) increases beyond a certain value, the lift force decreases and the drag force increases. So, the angle of attack plays a vital role. These parameters have a significant influence on turbine efficiency.

The aim of this paper is to study these parameters and to validate the experimental model. In this purpose we use an analysis of the flow with CosmosFloWorks.

2. General Information

Experimental model for the turbine to be carried out determinations is presented in the following figure:

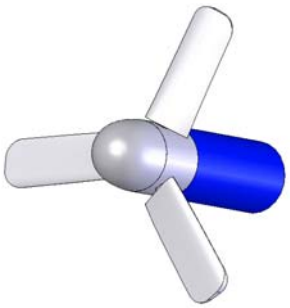

Fig. 1 – The experimental miniturbine.

For experimental testing of the miniturbine is using channel glazed of the fluid mechanics laboratory. The figure below presents a picture of miniturbine installed in order to make determinations.

Fig. 2 – The experimental miniturbine located in the channel.

For experimental testing, the movement of the miniturbine shaft is passed through a flexible cable. This flexible cable rotates a shaft which is mounted a wheel with known radius.

Fig. 3 – Miniturbine running for different tasks.

The relationship for calculating the turbine shaft torque is:

$$Me_i = Fe_i * r \quad (1)$$

where:

$$Fe_i = m_{ti} * g(1 + c_f) \tag{2}$$

r =0.02 [m] – radius wheel in meter; c_f=0.35 - friction coefficient; m_p = 0.133 [Kg]- mass pan; m_i - mass added to the pan; m_{ti}= m_p+ m_i - total mass; g = 9.81- gravitational acceleration.

In the above figure can be seen running with a load on the turbine.

3. Results and Discussion

After attempts to obtain experimental data in the table below:

Table 1
Experimental Measurements

i	m_i [Kg]	n_i $\left[\frac{rot}{min}\right]$	i	m_i [Kg]	n_i $\left[\frac{rot}{min}\right]$
1	0	138	14	0.6500	54
2	0.0500	128	15	0.7000	48
3	0.1000	122	16	0.7500	43
4	0.1500	113	17	0.8000	37
5	0.2000	107	18	0.8500	32
6	0.2500	103	19	0.9000	27
7	0.3000	98	20	0.9500	24
8	0.3500	91	21	0.9600	23
9	0.4000	86	22	0.9700	19
10	0.4500	84	23	0.9900	18
11	0.5000	70	24	1.0100	15
12	0.5500	61	25	1.0300	13.5
13	0.6000	58	26	1.0500	12

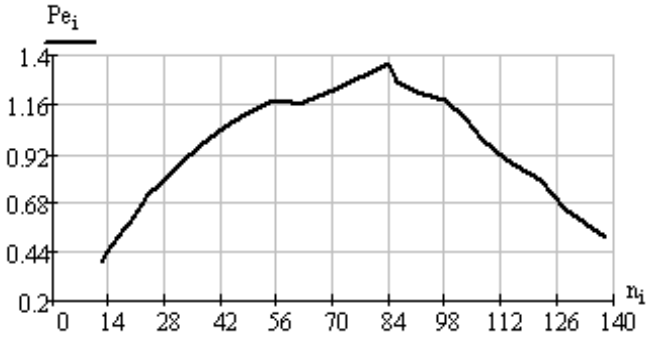

Fig. 4 – Power from the miniturbine shaft.

Data from experimental tests are used to trace the relation of power and angular speed obtained from the miniturbine shaft. The evolution of this dependence can be seen in the picture below.

Also we traced the dependence between miniturbine shaft torque and different angular speeds. This dependence can be seen in the picture below:

Fig. 5 – Miniturbine shaft torque.

The experimental data in Table 1 can also calculate the average torque for the miniturbine shaft:

$$Me_m = \frac{\sum_{i=1}^{28} Me_i}{28} \tag{3}$$

For the average torque value is obtained:

$$Me_m = 0.201\ [Nm] \tag{4}$$

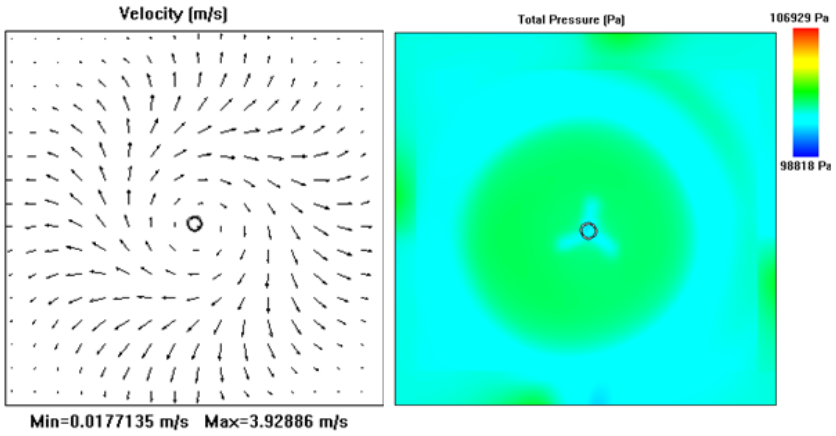

Fig. 6 – Velocity field and total pressure in the cross section.

The results of experimental data will be compared with simulation results.

In the Fig. 6 below can be observed velocity and total pressure in the cross section.

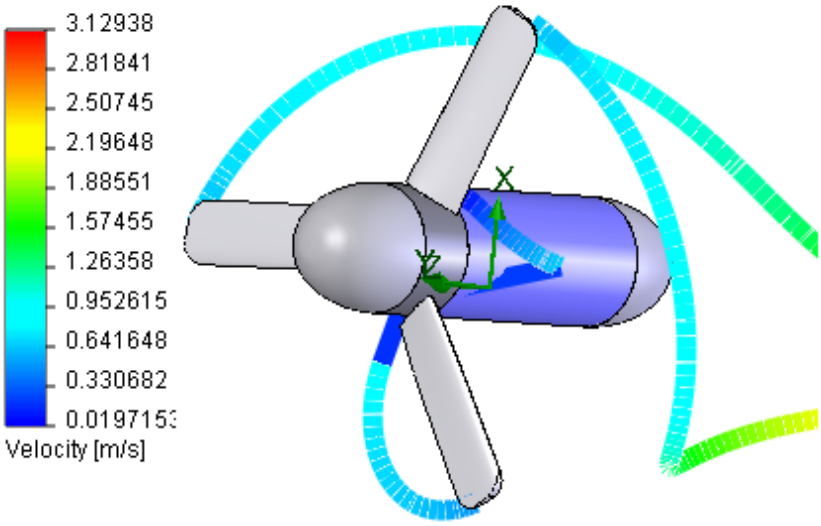

Fig. 7 – Flow on turbine blades.

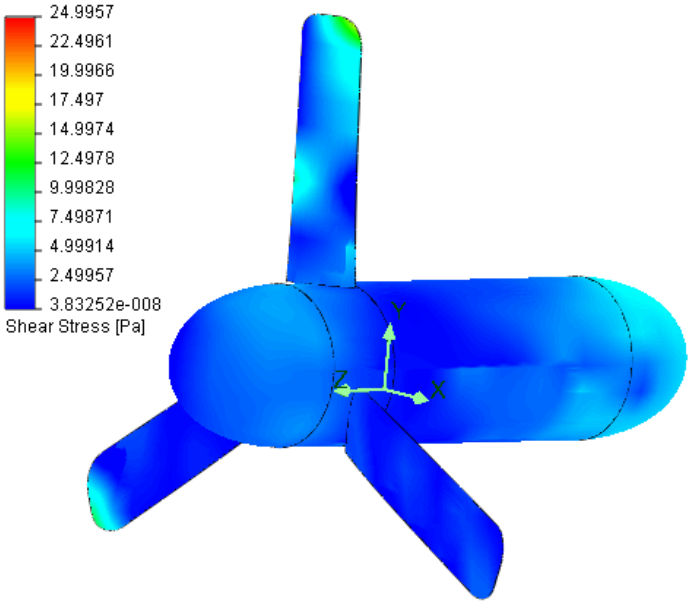

Fig. 8 – The picture with shear stress.

In the picture above you can see the flow trajectory and how speed variation.

In the next figure we can see the shear forces on the blades.

After simulation, the average torque obtained from the turbine shaft is:

$$M_m = 0,4 \text{ [Nm]} \tag{5}$$

The differences in torque for the two variants may occur in these cases:

- fluid velocity was considered constant in the simulation;
- no account was taken of the channel wall roughness.

4. Conclusion

Experimental model may be considered valid and the methodology used for design is correct.

Is obtain a higher torque in the case of simulation because some conditions were omitted: variation of speed, roughness, type of flow.

Other of the possible reasons for this difference is the turbulence level intensity developed in the channel and a series of friction losses.

In future simulations will take into consideration these issues.

REFERENCES

[1]. Chew J., Doherty J., Gillian M., Hills N., *Practical Applications of Automated Design and Optimisation Techniques Using CFD*. Automated Design & Optimisation Techniques Using CFD, IMechE, London, 2006.

[2]. Coiro D.P., Maisto S., Melone S., Grasso F., *Horizontal axis tidal current turbine: numerical and experimental investigations*. Civitavecchia, Italy, 2006.

[3]. Dellinger N., Imbault D., Tourabi A., *Caractérisation des efforts hydrodynamiques sur une maquette d'hydrolienne à axe vertical*. Congrès Français de Mécanique, Grenoble, France, 2007.

[4]. Gaden D., *An Investigation of River Kinetic Turbines: Performance Enhancements, Turbine Modelling Techniques, and an Assessment of Turbulence Models.* University of Manitoba, Canada, 2007.

[5]. Molland A.F., Bahaj A.S., Chaplin J.R., Batten W.M.J., *Measurements and Predictions of Forces, Pressures and Cavitation on 2-d Sections Suitable for Marine Current Turbines.* Proc. Institute of Mechanical Engineers, 218(M), 127-138 (2004).

SIMULAREA CURGERII PENTRU MINIHIDROTURBINELE CINETICE

(Rezumat)

În această lucrare s-a realizat simularea curgerii apei în jurul unei turbine cinetice care a fost testată experimental. Rezultatele obţinute în urma simulării au fost comparate cu datele experimentale. În urma acestor încercări s-a ajuns la concluzia că modelul poate fi considerat valid.

BULETINUL INSTITUTULUI POLITEHNIC DIN IAŞI
Publicat de
Universitatea Tehnică „Gheorghe Asachi” din Iaşi
Tomul LVII (LXI), Fasc. 4, 2011
Secţia
ŞTIINŢA ŞI INGINERIA MATERIALELOR

ROUGHNESS DETERMINATION FOR THE DEPOSITED LAYERS ON THE CAST IRON AND STEEL BY ESD METHOD

BY

CARMEN NEJNERU*, MANUELA CRISTINA PERJU, ANCA ELENA LĂRGEANU and MIHAI AXINTE

“Gheorghe Asachi” Technical University of Iaşi,

Received: April 14, 2011
Accepted for publication: June 27, 2011

Abstract. This paper aims to determine the roughness for the deposited layers using the ESD method on the grey cast iron and low alloy steel. The roughness testing has an major importance in the coating processes. If the roughness is too small, the consequence is a reduced adherence for the coating to the substrate, if the roughness is too high, there is the danger that the peaks for the surface profile are uncovered allowing the emergence of the rust or can lead to an unjustified paint consumption.

Key words: thin layers, EDS method, roughness.

1. Introduction

Roughness represents measuring at a smaller scale, variations in height of a natural area (as surface metrology). This measurement is opposed to large scale variations in surface geometry that or undesirable irregularities. Surface roughness can be undesirable because it causes friction and wear, but may also

* Corresponding author e-mail: cryss_ela@yahoo.com

be beneficial because it allows lubricant attachment and prevents the surfaces welding. After deposition a lower roughness can be obtained by applying the grinding operation, an operation that can be done manually, mechanically (by grinding machines) or by electrical sparks in the reversal condition of electrodes.

The ESD grinding method is carried out with the electrode used for hardening, but with a heavy jet cooling emulsion. After grinding the hardness does not change and the remaining micropores improve lubrication for the joining parts and increase the wear resistance.

This paper presents an analysis of roughness variation depending on the type of electrode used to deposit and the number of layers deposited on both gray cast iron support and the support of low-alloy steel.

2. Results and Discussions

For the experiment the following base materials were used:

- Grey cast iron, STAS 568/82;
- Low alloy steel 42CrMo4, STAS EN 10083-1.

Chemical compositions of base materials are presented in Tables 1 and 2, compositions were determined by Foundry Master spectrometer. Ti and Ni electrodes deposition materials were used. We used the method of thin films ESD (electrospark deposition).

Table 1
The chemical Composition of Gray Iron, %

Element	Fe	C	Si	Mn	P	S	Cr	Ni	Cu
Cast iron	91.8	4.50	1.54	1.03	0.620	0.140	0.096	0.057	0.148

Table 2
The Chemical Composition of Low Alloy Steel 42CrMo4, %

Element	Fe	C	Si	Mn	P	Cr	Mo	Ni	Al
Steel	95,7	0,477	0,185	0,331	0,0230	1,20	0,193	1,36	0,239

Surface roughness measurement was made before deposition on the samples of iron and steel processed by grinding and covered by ESD method with single or combined layers. Measurements were made with a Surtronic 3 + roughness testing device, and the interpretation was made using Talyprof software.

In ESD deposition method the roughness depends on the base material, mechanical processing and electrode type used for deposition.

2.1. Roughness Determination for the Deposited Layers on Gray Cast Iron Support

Following measurements to determine roughness values have been accumulated in Table 3. Ra and Rz values presented in Tables 3 and 4, represents:

- Ra - average ordinates (y1, y2,..., yn) points to the actual profile of the average line profile: $R_a = \frac{1}{l}\int_0^l |y\ |d_x$;
- Rz - the difference between the arithmetic average of five points ordinate the highest peak and the arithmetic mean of the ordinates of the lower profile of the bottom five points respectively between inner and outer lines:

$$R_z = \frac{(R_1 + R_3 + R_5 + R_7 + R_9) - (R_2 + R_4 + R_6 + R_8 + R_{10})}{5}.$$

Studying comparative analysis (Fig. 1) regarding roughness with the type of ESD deposition method shows that the roughness of the base material has a low value compared with all types of depositions. When submitting a Ni layer the roughness Ra = 3.308 mm is much smaller than the two layers Ni deposition where Ra = 5.716 mm, which is due mainly to the formation of the layer. On the simple layer appears uncovering graphite slides, due to high surface tension of molten Ni microbath droplets formed from melted metal electrode. On the double layer plays a lesser role in substrate diffusion and the presence of both iron deposition leads to low system conductivity, also appears irregularities in the layer, like unmelted drops, cracks and bumps, creating the premises for increased roughness.

Table 3

Roughness Values for Deposition by ESD on Gray Cast Iron Support

Material	Ra	Rz
Base material: cast iron	1,911 μm	14,323 μm
Deposition Ti 1 layer	5,058 μm	26,806 μm
Deposition Ti 2 layers	4,712 μm	23,527 μm
Deposition Ni 1 layer	3,308 μm	21,110 μm
Deposition Ni 2 layers	5,716 μm	31,252 μm
Deposition Ni/Ti	5,291 μm	26,429 μm
Deposition Ti/ Ni	4,664 μm	27,699 μm
Deposition Ni/Ti/Ni	5,530 μm	29,433 μm
Deposition Ti/Ni/Ti	7,588 μm	38,926 μm

The Ti one layer deposition roughness is higher than the deposition with one layer of Ni, since Ti has a melting point of 400°C higher that of Ni, leading to a rapid solidification of the droplet falling on the hot base material and droplets form preserves on the outer layer. This leads to a high roughness Ra=5.058 mm. The two-layer Ti deposition has a slightly lower roughness Ra=4.712 mm due to irregularities on the surface remelting due to low conductivities (we have two materials: Ti and iron) layer stays hot longer. For doubles combined deposition cases is observed that Ni/Ti has a roughness greater than Ti/Ni deposition, this is explained by the fact that Ni is deposited evenly, while more liquid remains on the surface as it melts more easily and easily disseminates.

The triple layer roughness increases, is still a good value for Ti and Ni coating interface, where Ra = 5.530 mm.

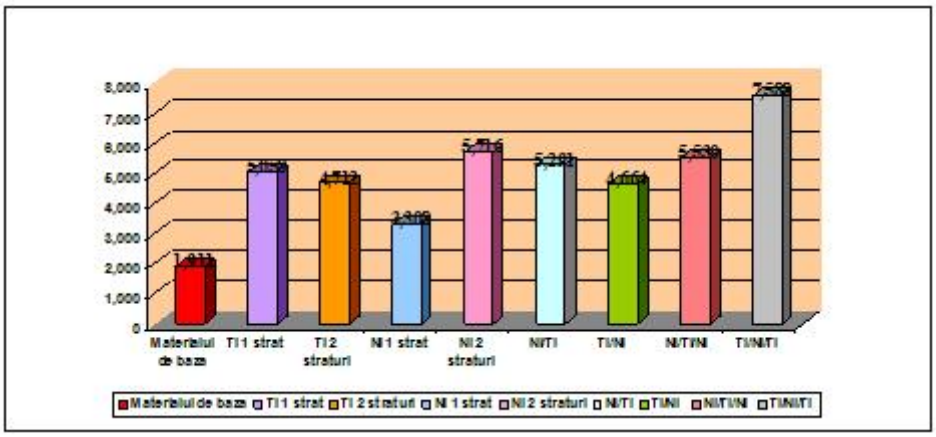

Fig. 1 – Comparative analysis for deposited on iron support layers roughness.

A high roughness was observed for triple layer Ti/Ni/Ti, Ra = 7.588 mm, justifying the predominant effect of the Ti.

2.2. Roughness Determination for the Deposited Layers on a Low-Alloy Steel Support.

Roughness depends on the material quality and processing mode (casting, cold or hot forming, grinding, finishing, superfinishing etc.).

The material was processed by coating. Previous it was processed by milling, being obtained a base roughness Ra = 2.09 mm (Table 4). In the case of depositing a layer of Ti we have a roughness Ra = 4, 303 mm, a value lower than the submission of Ni electrode, with roughness Ra = 5.649 mm. Double deposition with Ti has relatively low value for roughness Ra = 4.636 mm.

Table 4

Roughness Values for the ESD Deposition on Low-Alloy Steel Support

Material	Ra	Rz
Base material: Steel	2,09 μm	18,375 μm
Deposition Ti 1 layer	4,303 μm	19,844 μm
Deposition Ti 2 layers	4,636 μm	19,381 μm
Deposition Ni 1 layer	5,649 μm	24,934 μm
Deposition Ni 2 layers	6,093 μm	21,714 μm
Deposition Ni/Ti	4,803 μm	20,091 μm
Deposition Ti/ Ni	5,794 μm	24,346 μm
Deposition Ni/Ti/Ni	4,496 μm	16,158 μm
Deposition Ti/Ni/Ti	4,994 μm	23,073 μm

Deposition with double-layer Ni electrode, has a relatively high value of roughness Ra = 6.093 mm (the largest in the whole range of values). The explanation lies in the fact that titanium has excellent qualities of adhesion to the steel sample surface, without formation of duplication of material, pulling the electrode stuck to the part and no major cracks. In the case of double heterogeneous deposition Ti coating deposition have lower roughness (Ra = 4.803 mm), thanks to the properties of titanium to create smooth deposit on, while Ni surfaces creates strong irregularities.

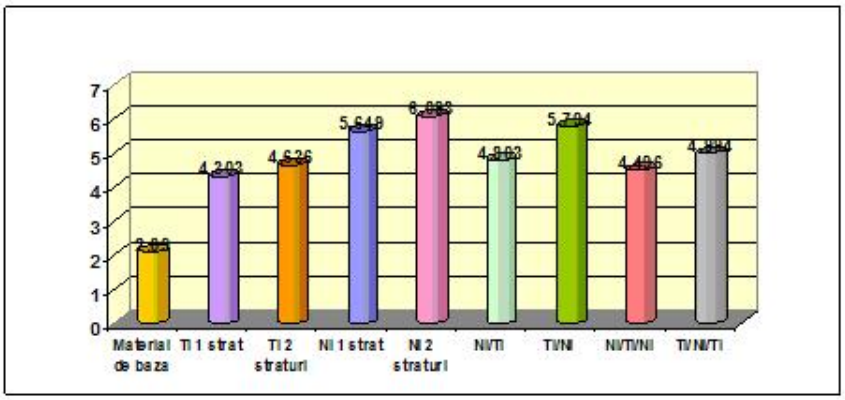

Fig. 2 – Comparative Analysis for deposited layers roughness on steel support.

For triple deposition layer coating the roughness is greater than for single and double deposits heterogeneous and homogeneous depositions.

3. Conclusion

1. Given the possibility for superfinishing made parts, roughness does not pose a major inconvenience, since after correction by reducing peaks, the

layer remains hard.

2. Roughness of deposited layers is much higher than the base material, iron or steel (which was processed by turning). It is noted that the highest roughness is obtained at the double and triple layers in both deposition cases, both the iron and steel.

3. In the case of cast iron deposition the lowest roughness is the Ni layer deposition (Ra = 3.308 mm) but high enough for 2 layers deposition of Ni (Ra = 5.716 mm), which is due to irregularities occurred, namely electrode melt drops and adhesions. Among the multiple layers the lowest roughness is the Ti/Ni (Ra = 5.664 mm) layer deposition due to a uniformity of Ni layer deposited by titanium intake, which leads to cracking and remelting adhesion zones.

4. In the case of the steel deposition we notice that they have the lowest surface roughness for Ti one layer deposition (Ra = 4.303 mm) and two layers (Ra = 4.636 mm) and for combined deposits Ni/Ti (Ra = 4.803 m) and Ni/Ti/Ni (Ra = 4.496 mm).

REFERENCES

[1]. Ciobanu D., Teză de doctorat, *Cercetări privind măsurarea durabilităţii organelor de lucru ale maşinilor şi instalaţiilor din agricultură şi industria alimentară, folosind tratamente termice*. Iaşi, 2009.

[2]. Gadelmawla E.S., Koura M.M., Maksoud T.M.A., Elewa I.M., Soliman H.H. *Roughness parameters*. Journal of Materials Processing Technology, **123**, *1*, 133-145 (2002).

[3]. Perju M.C., Găluşcă D.G., Nejneru C., Agop M., *Straturi subţiri: descărcări în impuls*. Editura Ars Longa, 339 (2010).

[4]. Ribalko Alexander V., Sahin Orhan, Korkmaz Kemal, *A Modified electrospark Alloying Method for Low Surface Roughness*. Surface & Coatings Technology, *203*, 3509–3515 (2009).

DETERMINAREA RUGOZITĂŢII PENTRU STRATURILE DEPUSE PRIN METODA ESD PE SUPORT DE FONTĂ ŞI OŢEL

(Rezumat)

Lucrarea are ca scop determinarea rugozităţii straturilor obţinute prin depunere utilizând metoda ESD pe suport de fontă cenuşie şi oţel slab aliat. Verificarea rugozităţii are o importanţă deosebită în procesele de acoperire. Dacă rugozitatea este prea mică, aceasta are ca şi consecinţă diminuarea aderenţei învelişului la substrat, iar dacă rugozitatea este prea mare, există pericolul ca vârfurile profilului suprafeţei să rămână neacoperite, permiţând astfel apariţia ruginii sau poate duce la un consum nejustificat de vopsea.